

Institut für theoretische Physik

ELECTROMAGNETIC PROBES
IN HEAVY-ION COLLISIONS

Dissertation
zur Erlangung des Doktorgrades
der Naturwissenschaften

vorgelegt beim Fachbereich Physik
der Johann Wolfgang Goethe-Universität
in Frankfurt am Main

von

Moritz Greif

aus Frankfurt am Main

Frankfurt am Main
(D30)

Vom Fachbereich Physik (13) der Johann Wolfgang Goethe-Universität Frankfurt als
Dissertation angenommen.

Dekan: Prof. Dr. Owe Philipsen

Gutachten: Prof. Dr. Carsten Greiner
Zweitgutachten: Prof. Dr. Hannah Elfner

Datum der Disputation:

Contents

List of Figures	V
Deutschsprachige Zusammenfassung	VIII
Overview	XVI
1. Introduction	1
1.1. Standardmodel of particle physics	1
1.2. Properties of strongly interacting matter	3
1.2.1. Asymptotic freedom	3
1.2.2. Color confinement	4
1.3. Detection of hot QCD matter	5
1.3.1. The detection of quark-gluon plasma signatures at SPS	5
1.3.2. From SPS to RHIC to LHC	6
1.3.3. Hydrodynamic behavior and shear viscosity	7
1.4. Electromagnetic observables	9
1.4.1. Photons	9
1.4.2. Dileptons	13
1.5. Units	16
2. Electric and diffusion properties of QCD matter	17
2.1. Electric conductivity of the QGP	18
2.2. Electric conductivity of the hot hadron gas	18
2.2.1. Basic definitions	19
2.2.2. Linear response to the electric field	21
2.2.3. General calculation with linearized collision term	21
2.2.4. Results	25
2.2.5. Massless particles and constant isotropic cross sections	25
2.3. Diffusion processes	32
2.3.1. Chemical composition and choice of cross sections	34
2.3.2. Results for the complete diffusion matrix	36
2.4. Conclusion and phenomenological consequences	43
3. Magnetic fields	47
3.1. Fields from Spectators	47
3.1.1. Geometry	47
3.1.2. Field strengths	48
3.2. Magnetic field influence on the QGP dynamics	52
3.2.1. Simple model without collisions	53
3.2.2. Results of the collisionless model	56
3.2.3. The effect of collisions	57
3.3. Conclusion and outlook	63
3.3.1. Propagating fields in the QGP	63
3.3.2. Algorithm for simultaneously solving the Maxwell and Boltzmann equation	63

3.3.3. Testcase for dynamically propagating fields-conducting wire	65
4. Modeling of heavy-ion collisions	69
4.1. Hydrodynamics	69
4.2. Transport theory	72
4.3. The partonic cascade Boltzmann Approach to Multiparton Scatterings . . .	72
4.3.1. Elastic cross sections	73
4.3.2. Radiative cross sections	74
4.3.3. Selected results from BAMPS	75
5. Theoretical foundations	77
5.1. Basic definitions	77
5.1.1. Propagators	78
5.1.2. Scalar field theory	78
5.1.3. Spectral density	79
5.1.4. Self energy	80
5.2. Thermal emission rate of photons	80
5.3. Optical theorem and cutting rules	81
6. Microscopic photon production	85
6.1. Construction of photon production processes	85
6.1.1. One-loop contribution	86
6.1.2. Two-loop contribution and symmetric cuts	87
6.2. Binary photon rates	90
6.2.1. Semi-analytic evaluation of a screened photon rate	92
6.2.2. Screening of soft momentum transfers	95
6.2.3. Correction of the distribution functions	97
6.3. Bremsstrahlung, LPM effect and inelastic photon production	98
6.3.1. Parametric estimates of higher order photon production	98
6.3.2. Landau-Pomeranchuk-Migdal effect	100
6.3.3. Interference effects in transport models	102
6.4. Radiative photon production	103
6.4.1. Photon rate at nontrivial quark fugacities	108
6.4.2. Running Coupling	109
7. Photon radiation using thermal resummed rates	113
7.1. Caveats in evaluating differential photon rates	113
7.2. Gluon and photon splitting in the AMY formalism	114
7.2.1. From thermal photon rates to jet transition rates	114
7.2.2. Numerical implementation of AMY emission rates in BAMPS	118
7.2.3. Gluon emission rates	119
8. Differential kinematics of photon production	123
8.1. Boosted particle production rates	123
8.2. Analytically computed thermal average	124
8.3. Photonic elliptic flow from multiple sources	126
8.4. Elliptic flow of photons originating from parton jets	127
8.4.1. Box calculation of photon leakage effect	127
8.5. Angular structure	128
8.5.1. Jet photon conversion and angular structure with microscopic $2 \rightarrow 3$ matrix elements	129

8.5.2. Phenomenological consequences	130
9. Photons from heavy-ion collisions	135
9.1. Background chemistry in BAMPS	136
9.1.1. Temperature	137
9.1.2. Velocity	139
9.1.3. Energy density	140
9.1.4. Particle density and fugacity	142
9.2. Photon yield from heavy-ion collisions	145
9.2.1. Prompt photons in literature	146
9.2.2. Spectra and elliptic flow at LHC from BAMPS	150
9.2.3. Spectra and elliptic flow at RHIC from BAMPS	151
9.2.4. Running coupling	154
9.3. Artificial equilibration scenario	157
9.4. Comparison to other models	158
9.5. Conclusion	159
10. Dileptons in heavy-ion collisions	161
10.1. Perturbative dilepton rates	161
10.1.1. Higher order rates	162
10.2. Temperature fits	162
10.3. Conclusion	164
11. Initial and final state effects in p+Pb collisions	167
11.1. Overview of experimental results	167
11.1.1. Multiplicity classes	168
11.1.2. Experimental results	168
11.2. Purpose of the present study	170
11.3. Initial state & phase-space distribution	171
11.4. Final state interactions	172
11.5. Evolution of azimuthal anisotropies	173
11.6. Multiplicity selection and fragmentation	178
11.7. Conclusions	182
12. Summary, conclusion and outlook	183
12.1. Summary	183
12.2. Conclusion and outlook	186
Appendices	191
A. Cutting rules for bremsstrahlung	191
A.1. Two-loop contribution and non-symmetric cuts	191
A.1.1. Three-loop contribution and symmetric cuts	191
B. Matrix elements for bremsstrahlung	195
B.1. Bremsstrahlung diagrams for quark-quark scattering	195
B.1.1. Matrix elements	195
B.1.2. Amplitude	196
B.1.3. Symmetry-factor	197
B.1.4. Algorithm to determine specific mean free paths	197
B.1.5. Verification of the bremsstrahlung process and kinematics	198

C. Calculations for hadronic conductivity	201
C.1. Calculations of the collision integrals	201
C.2. Cross sections for pion-isotriplett elastic scattering via ρ resonances	202
D. Lorentz invariance	203
D.1. Lorentz invariance of phase-space measures and distribution functions	203
D.1.1. Momentum space measure	203
D.1.2. Lorentz invariant distribution function	204
D.2. Boltzmann equation and stochastic collisions	205
Bibliography	207

List of Figures

1.1. Standardmodel particle species	3
1.2. Running strong coupling	5
1.3. Heavy-ion collision scheme	7
1.4. Elliptic flow for identified particles	8
1.5. Shear viscosity to entropy ratio	8
1.6. Direct photons at RHIC	11
1.7. Direct photon elliptic flow at RHIC	12
1.8. Direct photon elliptic flow at LHC	12
1.9. Low mass dilepton enhancement	15
1.10. Examples of dilepton spectra	15
2.1. Electric conductivity in the QGP	19
2.2. Convergence of analytic solution of the conductivity	26
2.3. Mass dependence of the electric conductivity	27
2.4. Electric conductivity from only pions	29
2.5. Electric conductivity with constant cross sections and only pions	30
2.6. Employed resonance cross sections	31
2.7. Electric conductivity including pions, kaons and nucleons	32
2.8. Diffusion coefficient matrix	37
2.9. Baryon-Baryon diffusion coefficient	38
2.10. Baryon-Electric diffusion coefficient	39
2.11. Negative Baryon-Strange diffusion coefficient	39
2.12. Electric-Electric diffusion coefficient	40
2.13. Strange-Electric diffusion coefficient	41
2.14. Electric conductivity for different μ_B	42
2.15. Electric conductivity in $T - \mu_B$ -plane	42
2.16. Strange-Strange diffusion coefficient	43
3.1. Sampling of nucleon positions	48
3.2. Magnetic fields at RHIC and LHC	50
3.3. Electric fields at RHIC and LHC	51
3.4. Magnetic field geoemtry	52
3.5. Magnetic field parameterization	54
3.6. Increase of v_2 due to momentum change	55
3.7. Change of spectra due to magnetic fields	56
3.8. Integrated final v_2 after magnetic field influence	57
3.9. Differential v_2 of partons without formation times	58
3.10. Differential v_2 of partons with formation times	58
3.11. Transverse momentum spectra of quarks under the influence of a magnetic field	59
3.12. p_T -differential v_2 for different times	60
3.13. p_T -differential v_2 for different magnetic fields	61
3.14. Photon compared to quark v_2	62

3.15. Magnetic field for relativistic charge	64
3.16. Magnetic field from straight conductor	67
6.1. Photon self energy at one-loop	86
6.2. Two-loop photon self energy with gluon loop	87
6.3. Two-loop photon self energy with gluon rung	87
6.4. Compton scattering and pair annihilation diagrams	88
6.5. Interference between s- and u-channel of Compton scattering	89
6.6. Interference between u- and t-channel of pair annihilation	90
6.7. Analytic vs numerical binary photon rates	96
6.8. Verification of numerically obtained binary photon rate	97
6.9. Vacuum diagrams for radiative scattering	98
6.10. Multiple independent radiative photon emission	101
6.11. Multiple interferent radiative photon emission	102
6.12. Kinematics in a photon radiation process	102
6.13. Photon self energy for leading order rates	103
6.14. LPM interference effect in $2 \rightarrow 3$ processes	104
6.15. Specific mean free path for a quark	105
6.16. Bremsstrahlung rate from BAMPS compared to analytic form	107
6.17. Photon rate dependence on quark fugacity	109
6.18. Fugacity λ_q scaling of m_D and density	110
6.19. Temperature dependence of gluon Debye mass	111
7.1. Verification of AMY radiation kernel in BAMPS	119
7.2. Thermal photon rates from AMY kernel emission in BAMPS	120
8.1. Boosted production rate of particles	124
8.2. Transfer of momentum anisotropy from equilibrium	126
8.3. Box calculation for leakage effect	128
8.4. Photon spectra of quark jets	131
8.5. Angular photon spectra of quark jets for different processes	132
8.6. Angular photon spectra of quark jets for different photon energies	133
8.7. Photon spectra for high energy quark and gluon jets	134
9.1. Time evolution of effective temperature in heavy-ion collisions	138
9.2. Comparison of temperature profiles	139
9.3. Time evolution of background boost velocity in heavy-ion collisions	140
9.4. Time evolution of energy density in heavy-ion collisions	141
9.5. Time evolution of particle density at the LHC	142
9.6. Time evolution of particle density at the RHIC	143
9.7. Time evolution of fugacity in heavy-ion collisions	144
9.8. Schematic diagram of prompt photon production	147
9.9. Comparison of prompt photon calculations at RHIC	149
9.10. Direct photons from BAMPS for LHC	151
9.11. Elliptic flow from BAMPS for LHC	152
9.12. Direct photon spectra from BAMPS for RHIC	153
9.13. Elliptic flow of direct photons from BAMPS for RHIC	154
9.14. Effect of running coupling for photon spectrum	155
9.15. Effect of running coupling for elliptic flow	156
9.16. Fugacity evolution in artificial equilibration scenario	157
9.17. Photon spectra from artificial equilibration scenario	158

9.18. World comparison of direct photon spectra at RHIC	160
10.1. Born dilepton production rate from BAMPS	163
10.2. Fit of invariant mass spectrum of dileptons	164
10.3. Time evolution of dilepton spectra	165
11.1. Experimental two-particle correlation function $1/N_{\text{trig}}dN^{\text{pair}}/d\Delta\eta\Delta\phi$	170
11.2. Time evolution of gluon $v_2\{2PC\}(p_T)$	174
11.3. Initial and final two-particle $v_2(p_T)$ in random azimuth scenario	176
11.4. Eccentricity plane $v_2(p_T)$	177
11.5. Evolution of the p_T integrated $v_2\{2PC\}$	178
11.6. Gluon $v_2\{2PC\}(p_T)$ from BAMPS compared to CMS	179
11.7. Initial and final $v_2\{2PC\}$ from BAMPS compared to CMS	180
11.8. Hadronic $v_2\{2PC\}$ from BAMPS	181
12.1. Word cloud	183
A.1. Non-symmetric cuts in two-loop photon self energy	191
A.2. Three-loop photon self energy	192
A.3. Different symmetric cuts to the three-loop photon self energy	193
B.1. Scatter plot of photon radiation in $k_T - y$ plane	199
B.2. Rapidity differential cross section of photon radiation	200
B.3. k_T differential cross section of photon radiation	200

Deutschsprachige Zusammenfassung

Einführung

Die Wechselwirkungen aller Objekte der Natur wird durch die vier Grundkräfte der Physik beschrieben, die Gravitationskraft, die elektromagnetische Kraft, die schwache Kraft und die starke Kraft.

Wir untersuchen in dieser Arbeit die Auswirkungen der starken und elektromagnetischen Kraft. Quarks und Gluonen, die Bestandteile der Hadronen, sind an die starke Kraft gebunden, wobei das Gluon ihr Austauschteilchen ist. Quarks sind elektrisch geladen, und unterliegen zudem der elektromagnetischen Kraft, können also mit Photonen wechselwirken. Leptonen unterliegen ausschließlich der elektromagnetischen Kraft.

Zur Untersuchung dieser kleinsten Teilchen in der Natur bedient sich der Mensch Hochenergieexperimenten. Die bekanntesten ihrer Art sind der Large Hadron Collider (LHC) am CERN Kernforschungszentrum, Schweiz, und der Relativistic Heavy-Ion Collider (RHIC) am Brookhaven National Lab, USA. Dort werden u.a. Protonen mit Protonen zur Kollision gebracht, Protonen mit schweren Ionen (Blei oder Gold) oder zwei schwere Ionen. Die erreichten Energien sind so groß, dass man inzwischen davon ausgeht, dass die Nukleonen beim Stoß zerstört werden, und, für mehr oder weniger lange Zeiträume ein Plasmazustand aus freien Quarks und Gluonen entsteht. Dieses sogenannte Quark-Gluonen Plasma (QGP) ist Gegenstand zahlreicher experimenteller und theoretischer Untersuchungen. Die zugrundeliegende Theorie ist die Quanten Chromodynamik (QCD), bei beteiligten Photonen und Elektronen zusätzlich die Quanten Elektrodynamik (QED). Experimente sind in der Lage, hadronische Spektren, deren azimuthale Winkelabhängigkeit, einzelne hochenergetische hadronische "Jets" und Spektren von Photonen und Dileptonen zu messen.

Der Vergleich von theoretischen Modellen mit experimentellen Daten bestätigte das Standard-Bild der Evolution von Schwerionenkollisionen: Zunächst entsteht in der meist mandelförmigen Kollisionszone des Schwerionenstoßes ein Nichtgleichgewichts-Zustand extrem hoher Dichte und Temperatur, bestehend aus stark wechselwirkenden Quarks und Gluonen. Dieses Gas equilibriert schnell, dehnt sich dabei aus und kühlt ab. Ab einer inzwischen sehr genau bestimmten Temperatur findet ein Phasenübergang zu normaler, hadronischer Materie statt. Das hadronische Gas wechselwirkt immer noch stark, dehnt sich weiter aus und kühlt weiter ab. Ab einem bestimmten Zeitpunkt hören auch die hadronischen Stöße auf, und die Produkte fliegen auf geraden Bahnen zum Detektor. Sowohl beim ersten Kern-Kern Kontakt als auch während der gesamten QGP Phase und hadronischen Evolution werden Photonen und Dileptonen produziert.

Eine der interessantesten Eigenschaften des QGPs sind sein geringes Verhältnis von Scherviskosität zu Entropie, was Nahe am theoretischen unteren Minimum liegt. Das QGP bildet damit fast eine ideale Flüssigkeit. Die Zustandsgleichung bei verschwindendem chemischen Potential ist hinreichend bekannt, sie zeigt einen auffälligen Sprung beim Phasenübergang, jedoch gibt es nur Vermutungen über das Verhalten bei endlichem chemischen Potential. Inzwischen gibt es weiterführende Vermutungen über die Volumenviskosität, die thermische als auch die elektrische Leitfähigkeit. Diese Transportkoeffizienten charakterisieren die Eigenschaften des QGP auf interessante Art, und man kann Rückschlüsse auf die mikroskopischen QCD Interaktionen zwischen Quarks und Gluonen ziehen. Bei niedrigeren Schwerpunktsenergien vermutet man höhere chemische Potentia-

le der dominanten Ladungen (elektrische, baryonische und seltsame Ladung). Inzwischen sind auch die Diffusionskoeffizienten und deren Kopplungen bekannt.

Neben Transportkoeffizienten sind Spektren von elektromagnetischen Observablen wertvolle Informationsquellen, die vor allem die Evolution des Feuerballes beschreiben: Temperaturverlauf, Expansionsgeschwindigkeit und relative Dichten von Quarks und Gluonen sind dabei die wichtigsten Kenngrößen.

Elektrische Leitfähigkeit und Diffusionseigenschaften von QCD Materie

In dieser Arbeit entwickeln wir einen Formalismus zur (semi-analytischen) Bestimmung der elektrischen Leitfähigkeit von relativistischer Materie. Nach ausführlichen Tests benutzen wir diese Methode für ein hadronisches Modellsystem bei Temperaturen knapp unter der Phasenübergangstemperatur. Wir berechnen die elektrische Leitfähigkeit für ein Gas bestehend aus mehreren Hadronen, wobei Pionen die wichtigsten Spezies darstellen (da sie am häufigsten auftreten). Als theoretische Basis benutzen wir die Boltzmann Transportgleichung mit linearisiertem Kollisionsterm, bei dem wir, soweit bekannt, binäre Resonanz-Streuquerschnitte annehmen. Unbekannte Hadron-Hadron Streuquerschnitte nehmen wir als isotrop und konstant an und untersuchen die Sensitivität zu Veränderung dieser Konstanten. Wir finden das erwartete abfallende Verhalten des Verhältnisses von elektrischer Leitfähigkeit über Temperatur mit steigender Temperatur, und vergleichen u.a. mit Literaturwerten aus Gitterfeldtheorie, anderen Transportmodellen und chiraler Störungstheorie. Unsere Ergebnisse liegen zwischen den teilweise stark abweichenden Literaturwerten. Wir erhalten etwa eine Größenordnung höhere Leitfähigkeit als gitterfeldtheoretische Rechnungen. Hierbei merken wir an, dass bisher die gitterfeldtheoretischen Rechnungen nur bei höheren Temperaturen verlässlich funktionieren. Chirale Störungstheorie ergibt etwa ein Drittel schwächere Leitfähigkeiten, mit einem sehr ähnlichen Temperaturverlauf wie unsere Rechnung. Kurz über dem Phasenübergang treffen wir mit den meisten Ergebnissen der Gitterfeldtheorie zusammen.

Wir haben weiterhin untersucht, wie der elektrische, baryonische und seltsame Strom aufgrund von Gradienten in thermischen Potentialen (chemisches Potential geteilt durch Temperatur) entstehen, und sich gegenseitig beeinflussen. Wir stellen eine symmetrische Matrix aus Diffusionskoeffizienten auf, die klassische, diagonale Diffusionskoeffizienten (Baryon Diffusionskoeffizient, Elektrischer Diffusionskoeffizient und Seltsamkeits Diffusionskoeffizient) enthalten, als auch drei Kreuz-Diffusionskoeffizienten, die die Diffusionsströme einer Ladung aufgrund von Gradienten einer anderen Ladung beschreiben.

Für Temperaturen über dem Phasenübergang benutzen wir ein vereinfachtes Modell mit masselosen Quarks und Gluonen mit konstanten isotropen Streuquerschnitten, die allerdings temperaturabhängig sind. Wir wählen eine Beschreibung bei der das Verhältnis von Scherviskosität zu Entropie das theoretische untere Minimum annimmt. Die Diffusionskoeffizienten sind relativ konstant über diese Temperaturen im QGP.

Für Temperaturen unter dem Phasenübergang benutzen wir 19 verschiedene baryonische und mesonische Spezies mit Massen bis zum Lambda-Baryon. Wie bei der elektrischen Leitfähigkeit benutzen wir teilweise gemessene Resonanzquerschnitte, oder Modellierungen und Parametrisierungen von Streuquerschnitten für die Wechselwirkungen der Spezies untereinander. Die Temperaturabhängigkeit der sechs unabhängigen Diffusionskoeffizienten variiert stark mit dem baryon chemischen Potential. Wir finden, dass in den meisten Fällen unsere vereinfachte Annahme der Streuquerschnitte ausreicht, um eine ungefähre Annäherung der hadronischen und der QGP Rechnung im Bereich des Phasenübergangs zu gewährleisten. Eine Ausnahme ist der Elektrisch-Baryonische Kopplungs-

koeffizient, der bei verschwindendem chemischen Potential im QGP ganz verschwindet. Die bei weitem stärkste Diffusion ist die Seltsamkeits-Diffusion, der entsprechende Koeffizient liegt bis zu einer Größenordnung über den anderen Koeffizienten. Interessant ist auch der Seltsamkeits-Baryon Kopplungskoeffizient, der negativ ist. Das bedeutet, dass ein baryonischer Gradient in thermischen Potential einen negativen Seltsamkeits-Strom hervorruft, der zudem im hadronischen stark vom baryon chemischen Potential abhängt. Wie erwartet, ist die Abhängigkeit der nicht-baryonischen (Kopplungs-) Koeffizienten vom baryon chemischen Potential gering.

Es bleibt zu zeigen, inwieweit diese Diffusionskoeffizientenmatrix eine phänomenologische Relevanz hat. Zukünftige Studien werden zeigen, ob beispielsweise der starke longitudinale Gradient in baryon thermischen Potential eine Erhöhung der Seltsamkeit bei zentraler Rapidität hervorruft, und welche Rolle die elektrische Ladung spielt. Es ist bisher nicht bekannt, ob sich durch die starken Kopplungskoeffizienten verschiedene Ströme aufheben, sodass beobachtbare Effekte klein sind. Eine Möglichkeit dies zu untersuchen sind hydrodynamische Modelle mit mehreren erhaltenen Strömen, die sich im Moment aber noch im Aufbau befinden.

Das verwendete Modell zur Beschreibung von Schwerionenstößen

Das in dieser Arbeit verwendete theoretische Modell zur numerischen Beschreibung des Plasmazustandes in Schwerionenstößen basiert auf der Lösung der relativistischen Boltzmann Transportgleichung (Boltzmann Approach to Multi-Parton Scatterings, BAMPS). Dazu teilen wir das betreffende Volumen in Zellen auf und simulieren die Verteilungsfunktion der Partonen als Ensemble von Einzelteilchen. Für den Anfangszustand wird hierzu das Modell Pythia 6 und IP-Glasma für verschiedene Zwecke benutzt. Nach dem Generieren eines Anfangszustandes aus Quark und Gluon Orts- und Impulsvektoren werden in diskreten Zeitschritten Kollisionswahrscheinlichkeiten berechnet und die Teilchenensembles durch binäre und radiative Stöße weiterentwickelt. Dies stellt eine numerisch exakte Lösung der Boltzmann-Gleichung dar. Nachdem die Energiedichte lokal auf einen kritischen Wert gefallen ist, wird die Evolution unterbrochen und die Partonenspektren analysiert. Dieses Modell dient in der vorliegenden Arbeit als Basis für die Untersuchung des Einflusses von Magnetfeldern, für die Implementation und Analyse von Photonen- und Dileptonenproduktionsprozessen und ein Projekt zum Einfluss des Anfangszustandes bei Proton-Blei Systemen.

Magnetische Felder in Schwerionenkollisionen und ihre dynamischen Auswirkungen

Es ist bekannt, dass sich im Zentrum der Schwerionenkollision extrem starke elektrische und magnetische Felder aufbauen. Diese entstehen durch das schnelle Vorbeifliegen der Ladungen der nicht-teilnehmenden Nukleonen in peripheren Kollisionen. Im Rahmen dieser Arbeit wurde untersucht, wie sich die extremen Felder auf die Dynamik innerhalb des QGPs auswirken. Durch die Geometrie des Problems zeigen die Magnetfelder fast ausschließlich in die Richtung senkrecht zur Ereignisebene und die Lorentzkraft zwingt die elektrisch geladenen Partonen (Quarks) auf Kreisbahnen. Nachdem wir verschiedene Magnetfeldkonfigurationen betrachtet haben, untersuchen wir inwieweit sich der Effekt der elektromagnetischen Kraft auf Observablen wie Spektren oder elliptischen Fluss auswirken. Wir beschreiben genau, welche kinematischen Regionen der Parton-Ensembles Effekte

hervorrufen. Das Ergebnis ist eine merkliche Erhöhung des elliptischen Flusses bei extrem niedrigen transversalen Impulsen, die auch in näherer Zukunft nicht messbar sein werden. Bei diesen Skalen spielen außerdem Effekte eine Rolle, die nicht im Rahmen des Modells erfasst werden können, wie u.a. die wenig erforschte Hadronisierung.

Photonenproduktion in Schwerionenkollisionen

Das Hauptaugenmerk dieser Thesis liegt auf der Untersuchung von photonischen Observablen. Seit den ersten Messungen von direkten Photonen am RHIC versuchen Theoretiker, bisher wenig zufriedenstellend, deren gemessene Spektren und den elliptischen Fluss zu beschreiben. Direkt bedeutet hierbei Photonen, die nicht aus späten Zerfällen, z.B. von Pionen, stammen, sondern thermisch im QGP und Hadronengas erzeugt werden, oder aber bei den initialen harten Nukleon-Nukleon Stößen am Anfang der Kollision. Die meisten Untersuchungen dazu wurden mit Hilfe von hydrodynamischen Modellen ausgeführt, wobei Gleichgewichtsraten zur Photonproduktion mit dem Temperaturverlauf gefaltet werden. In unserem Modell müssen durch mikroskopische Parton-Parton Stöße Photonen erzeugt werden. Dies hat den Vorteil, dass es auch im Nichtgleichgewicht funktioniert, bzw. es keinen Unterschied macht, inwieweit das Medium equilibriert ist. Der Nachteil ist, dass die entsprechenden Matrixelemente kompliziert zu konstruieren sind. Hierbei besteht das Problem, dass die Gleichgewichtsraten der Photonproduktion zu führender Ordnung nicht nur Matrixelemente zu führender Ordnung in den Vertizes (Baumdiagramme) enthalten, sondern eine unendliche Resummation von radiativen Prozessen, die miteinander interferieren. Dieses, als Landau-Pomeranchuk-Migdal Effekt bekannte Verhalten ist sehr schwer mikroskopisch zu modellieren.

Auch bei binärer Photonproduktion besteht das Problem, dass thermisch berechnete Gleichgewichtsraten nicht unmittelbar mit mikroskopisch generierten Raten übereinstimmen, selbst wenn die gleichen Prozesse benutzt werden (Compton-Streuung und Quark-Antiquark Annihilation). Dies liegt an der Abschirmung der off-shell Propagatoren innerhalb des Plasmas. Wir benutzen die Ein-Schleifen Quark-Selbstenergie, in der partonischen Kaskade dynamisch berechnet (Debye Masse), und fügen einen Anpassungsfaktor hinzu, der, im thermischen und chemischen Gleichgewicht, an analytisch berechnete Raten angepasst wird (die mit Hard-Thermal-Loop Theorie konsistent berechnet wurden). Wir korrigieren zudem mit einem weiteren Faktor die fehlende Quantenstatistik des Modells. Damit stellen wir zunächst sicher, dass sich die binäre Rate in BAMPS sehr ähnlich der korrekten analytischen Rate verhält.

Im radiativen Fall muss ein ähnliches Verfahren angewendet werden. Wir approximieren daher das Verhalten der radiativen Prozesse und des LPM Effektes auf zwei verschiedene Weisen.

Zunächst berechnen wir ein $2 \rightarrow 3$ Matrixelement mit effektiven Quark und Gluon Propagatoren, wobei die zusätzliche kollineare Divergenz zunächst willkürlich abgeschnitten wird. Hierbei wird die Formationszeit des Photons mit einer effektiven freien Weglänge verglichen. Im thermischen und chemischen Gleichgewicht kann die so mikroskopisch erzeugte Rate mit der analytischen Form verglichen werden. Hier wenden wir nur einen äußeren Anpassungsfaktor an, der die ungefähre Gleichheit der absoluten Rate in einem phänomenologisch interessanten Energiebereich sicherstellt.

Die zweite Variante der radiativen Photonproduktion, die im Rahmen dieser Arbeit untersucht wurde, ist die Verwendung eines Streukernels, der mit Hilfe von thermischer Feldtheorie aus der Literatur bekannt ist. Diese Methode beruht darauf, dass aufgrund von Impulsen einzelner Quarks und einer Hintergrund-Temperatur die Wahrscheinlichkeit berechnet wird, in einem Zeitschritt ein Photon mit einer bestimmten Energie auszusenden.

den. Wird dieses Photon erzeugt, so fliegt es exakt kollinear zum Quark. Die entstehenden Raten im Gleichgewicht sind ohne Annahmen nahezu identisch den analytischen Parametrisierungen aus der Literatur, allerdings benötigt man einen Temperaturbegriff des Hintergrunds. Wir verwenden hier daher einen Temperaturbegriff, der unabhängig von der Fugazität ist und als Quotient zwischen zwei Momenten der Verteilungsfunktion errechnet wird. Dies ist eine sinnvolle, allerdings willkürliche Wahl. Desweiteren kann mit dieser Methode nicht abschließend geklärt werden, wie sich der Strahlungskern im chemischen Nichtgleichgewicht verhält, da sich die internen effektiven Propagatoren bei Fugazitäten verändern werden.

Wir untersuchen in einem weiteren Kapitel, inwieweit elliptischer Fluss eines partonischen Hintergrunds auf Photonen übertragen wird. Durch einen rein kinematischen Effekt verringert sich diese Impuls-Asymmetrie deutlich.

Im vielleicht wichtigsten Teil dieser Arbeit werden die oben beschriebenen Methoden der Photonenproduktion auf realistische Szenarien in peripheren Schwerionenkollisionen angewendet. Dazu berechnen wir für vier Zentralitäten bei RHIC und drei Zentralitäten für LHC die QGP Photonenspektren mit BAMPS.

Für LHC Simulationen benutzen wir prompte Photonenspektren aus der Literatur und summieren diese zu dem QGP Anteil, um im höheren Teil der transversalen Impulse einen Vergleich zum experimentell gemessenen, direkten Photonenspektrum zu ermöglichen. Der Vergleich wird zu höheren Impulsen etwas präziser, wobei der QGP Anteil als sehr gering auffällt. Die beiden Methoden der radiativen Photonenproduktion unterscheiden sich mit geringer Impulsabhängigkeit. Diese Differenz kann als systematische Unsicherheit gewertet werden.

Für RHIC Simulationen benutzen wir verfügbare hadronische und prompte Photonenspektren, und summieren diese zu den QGP Spektren aus BAMPS. Damit sind wir in der Lage, mit experimentellen Ergebnissen zu vergleichen. Die Übereinstimmung ist gut bei hohen und niedrigen transversalen Impulsen, aber im mittleren Impulsbereich, wo das QGP eine dominante Rolle einnehmen sollte, unterschätzen wir die Experimente etwas. Dies ist bei uns auf die niedrige Anzahl an Quarks zurückzuführen (Quark Fugazitäten unter Eins).

Wir berechnen weiterhin den elliptischen Fluss für RHIC und LHC. Dabei ist zu beachten, dass elliptischer Fluss von Photonen aus mehreren Quellen ein gewichtetes Mittel ist, bei dem der Fluss aus den Quellen mit dem Spektrum gewichtet wird. Wir benutzen daher zusätzlich zu den Ergebnissen aus BAMPS aus der Literatur (Hydrodynamik) bekannte Ergebnisse von hadronischem elliptischen Fluss und Spektrum, zusammen mit dem prompten Spektrum (und verschwindendem Fluss) um den elliptischen Fluss von direkten Photonen am PHENIX Experiment am RHIC für zwei Zentralitätsklassen zu berechnen. Bis zu einem Transversalimpuls von etwa 1.5 GeV werden die Daten relativ gut beschrieben, danach unterschätzt unser Modell die Daten signifikant. Da für LHC keine hadronischen Einzelergebnisse aus der Hydrodynamik verfügbar sind, können wir keinen echten Vergleich mit dem Experiment anstellen. Wir stellen hier jedoch fest, dass die exakt kollineare Emission der Raten berechnet mit dem direkten Streukern für RHIC und LHC einen deutlich höheren elliptischen Fluss erzeugt. Die nicht-kollineare Emission aus den Matrixelementen, mit der etwas anderen Gewichtung (hier wird keine effektive Temperatur benutzt) lässt den elliptischen Fluss fast identisch verschwinden.

Wir zeigen weiterhin, dass eine laufende starke Kopplung das Photonenspektrum um bis zu einen Faktor 1.7 vergrößern kann. Hierbei benutzen wir verschiedene Skalen bei denen die Kopplung ausgewertet wird. An den Streuvertizes ist dies der Impulstransfer (Mandelstam Variablen), und innerhalb der effektiven Propagatoren ist das Quadrat einer effektiven Temperatur eher gerechtfertigt.

Da wir im Vorigen sahen, dass die Fugazitätsentwicklung eine wichtige Rolle spielt, untersuchen wir die Sensitivität darauf indem wir einen künstlichen Faktor auf die Quark-Antiquark Produktionsquerschnitte multiplizieren. Wir zeigen, wie sich die Fugazität bei einem Faktor von 10 und 100 deutlich schneller erhöht, und bis zu einem Wert von 3 steigt. In diesen künstlichen Szenarien erhöht sich die Photonenzahl über weite Bereiche in transversalem Impuls, was unsere Annahme der Sensitivität auf Fugazität bestätigt und quantifiziert.

Wir vergleichen mit einem anderen Transportmodell (PHSD) und einem hydrodynamischen Modell (MUSIC), da diese beiden Modelle ebenfalls ausführliche Studien zu direkten Photonen in Schwerionenkollisionen ausgeführt haben. Es fällt auf, dass der QGP Anteil an den Spektren sich in allen drei verglichenen Modellen stark unterscheidet. BAMPS zeigt das flachste (härteste) Spektrum, was allerdings von der Größenordnung her für niedrigere transversale Impulse unter den anderen beiden Modellen verbleibt. PHSD ist einen Faktor 2 unter den Ergebnissen von MUSIC, dafür zeigt PHSD einen höheren hadronischen Anteil im Spektrum. Die Unterschiede sind hauptsächlich auf den unterschiedlichen Anfangszustand zurückzuführen, als auch auf unterschiedliche hadronische Raten. Die Zukunft wird zeigen, welches Modell durch kleine Modifikationen am nächsten an die Daten kommen wird. Diese werden sicherlich auch noch präziser. Unser Modell betont die Wichtigkeit des chemischen Nichtgleichgewichts und es ist davon auszugehen, dass die Lösung des “Photonen-Puzzles” eine delikate Mischung aus verschiedenen kleinen Verbesserungen der Modelle sein wird.

Studie zur Dynamik von kleinen Systemen und ihrer Sensitivität zu initialem Zustand und finalen Interaktionen

Im letzten Kapitel dieser Arbeit untersuchen wir das etwas separate Problem der azimuthalen Korrelationen in kleinen Systemen, was allerdings in der Community der Schwerionenphysik in den letzten Jahren starkes Interesse gefunden hat. Die gemessenen azimuthalen Impuls-Anisotropien in Schwerionenkollisionen wurden durch Event-by-Event Hydrodynamik ausreichend beschrieben. In kleineren Systemen, z.B. p+Pb oder p+p Stößen wurden ähnliche Beobachtungen von Anisotropien in Vielteilchen-Korrelationsfunktionen gemacht. Hydrodynamik und auch alternative Modelle mit reinem anisotropen Anfangszustand konnten viele dieser Beobachtungen erklären. Allerdings ist die klassische relativistische Hydrodynamik in kleineren Systemen zunehmend schlechter anwendbar, da die Gradienten zu stark werden. Bisher wurden alle Studien zu Vielteilchenkorrelationen entweder zum reinen Anfangszustand oder aber zum reinen Endzustand ausgeführt. Wir präsentieren hier die erste Studie die sowohl Anfangszustand als auch Interaktionen zu späteren Zeiten enthält. Dazu kombinieren wir zwei etablierte Modelle: Zunächst benutzen wir ein Modell für den Anfangszustand der p+Pb Kollision, das sog. IP-Glasma Modell. Es basiert auf dem Farbglass-Kondensat (“color glass condensate”, CGC), und löst die klassischen Yang-Mills Gleichungen numerisch mit Anfangsbedingungen aus einem fluktuierenden Proton-Modell. Wir extrahieren die Gluonen Wigner-Verteilungen und (nach Schmieren für Positivität) generieren einzelne Gluonen im Phasenraum anhand der (transversalen) Verteilung. Diese Gluon-Verteilungen sind anisotrop im (transversalen) Impuls- und Ortsraum, enthalten also die intrinsischen Impulskorrelationen des CGCs. Wir evolvieren die Verteilungen anhand der Boltzmann-Gleichung mithilfe von BAMPS. Dabei benutzen wir elastische und radiative pQCD Streuquerschnitte. Am Ende der Evolution analysieren wir den elliptischen Fluss per Zwei-Teilchen-Korrelations Methode. Wir benutzen zunächst zwei, später mehrere Multiplizitätsklassen um zu verstehen, welchen relativen Einfluss der Anfangs- und Endzustand auf die Observablen haben. Insbesonde-

re inwieweit Signale des Anfangszustandes die späteren Wechselwirkungen der Teilchen überleben um am Ende in Observablen sichtbar zu bleiben ist hier von Interesse.

Wir können zeigen, dass speziell bei niedrigen Multiplizitäten der Anfangszustand sehr wichtig für den am Ende beobachteten elliptischen Fluss ist. Wir führen aus, welche Abhängigkeit vom transversalen Impuls diese Aussage hat, denn bei niedrigen Impulsen beobachten wir auch bei niedrigen Multiplizitäten eine sichtbare Veränderung des Flusses durch die späten Interaktionen. Der impulsintegrierte elliptische Fluss zeigt ein interessantes dynamisches Verhalten. Nach der Yang-Mills Evolution nimmt der Fluss zunächst für einige Zeit ab, da die pQCD Streuungen die Impulse isotropisieren, und sich die Symmetrieachse neu ausrichtet. Danach setzt die Antwort auf die entstandenen Druckgradienten ein, die, wie bei Schwerionenkollisionen, für eine ansteigende Impulsasymmetrie verantwortlich sind. Dieses wechselnde Verhalten ist bei hohen Multiplizitäten deutlich ausgeprägter.

Angesichts der langen Diskussion ob Anfangs- oder Endzustand ausschlaggebend sind in kleinen Systemen, schlagen wir einen Paradigmenwechsel vor, indem wir betonen dass beide Stadien wichtig sind. Wir schlagen vor, dass eine differentielle Untersuchung von azimuthalen Korrelationen in mehreren Multiplizitätsklassen deutlichen Wissenszuwachs über den Anfangszustand und die frühe Nichtgleichgewichtsphase von hochenergetischen Kollisionen bringen wird. Wir unternehmen erste Schritte in diese Richtung, und zeigen, dass eine Fragmentierung der finalen Partonen eine Methode sein kann, hadronische Observablen zu generieren, die mit dem Experiment verglichen werden können. In Zukunft wäre sicherlich eine mikroskopische Hadronisierung im Rahmen von BAMPS wünschenswert.

Ausblick

Diese Arbeit behandelt mehrere Themen der Hochenergiephysik, mit einem Fokus auf der theoretischen Beschreibung von Schwerionenkollisionen und Proton-Blei Kollisionen. Wir haben zunächst einige wichtige Transportkoeffizienten des heißen Hadronengases und des Quark-Gluon Plasmas berechnet, mit deren Hilfe in Zukunft weitere effektive Modelle noch genauere Vorhersagen treffen können. Dies wird insbesondere für Kollisionen bei niedrigeren Energien relevant sein, die das primäre Ziel verfolgen, das $T - \mu_B$ -Phasendiagramm der QCD zu kartieren.

Wir haben den Einfluss von externen Magnetfeldern untersucht, mit dem zusammenfassenden Ergebnis, dass die Felder zu kurzlebig sind, um in messbaren Observablen eine Rolle zu spielen. Weitere Studien, die auch interne Magnetfelder in Betracht ziehen, können darauf aufbauend neue Einsichten bringen.

Das Photonen-Puzzle in Schwerionenkollisionen am RHIC und LHC ist durch die ungenaue Datenlage oft schwer zu erfassen. Wir arbeiten mit einem neuen Modell, das explizit partonische Fugazitäten und eine Nichtgleichgewichtsevolution des Quark-Gluon Plasmas enthält. Die differentielle Analyse der Spektren und des elliptischen Flusses kann die Daten nur in einigen Bereichen erklären, und unterschätzt die Daten in den anderen. Dies deutet darauf hin, dass ein bislang unbekannter Baustein im Modell fehlt. Ein Vergleich mit anderen Modellen in der Literatur bringt keine weitere Information, da auch diese Modelle die Daten unterschätzen. Es erscheint vielversprechend, dass eine Kombination aus dem richtigen Anfangszustand, laufender Kopplung, exakten Photonenproduktionsraten auch bei chemischem Nichtgleichgewicht im QGP als auch im Hadronengas sowie präziseren experimentellen Ergebnissen die Spannung zwischen Theorie und Experiment verringert.

Wir haben weiterhin ein Projekt verfolgt, welches die relative Wichtigkeit des Anfangs- und Endzustandes in kleinen Kollisionssystemen untersucht. Dieses Modell sollte in Zukunft mit einer etwas genaueren Hadronisierung ausgestattet werden und verspricht dann, durch systematische Vergleiche mit dem Experiment, viel über die Natur des Anfangs-

zustandes von Schwerionenkollisionen und das zugrundeliegende “color glass condensate” Bild herauszufinden, sowie eine genauere Einschränkung der Natur der partonischen Interaktionen.

Overview

Abstract

In this thesis we work on the theoretical description of relativistic heavy-ion collisions, focussing on electromagnetic probes. We present mainly four topics: electric conductivity and diffusion properties of the hot plasma and hadronic matter, response of the quark-gluon plasma to external magnetic fields, direct photon production in the quark-gluon plasma and a study about initial and final state effects in small systems. The latter topic aims, i.a., at a better understanding of the initial state, which is crucial for electromagnetic probes. In all research areas we make use of the Boltzmann transport equation, whereby the presented methods provide analytical and numerical solutions. We pay particular attention to the construction of complete leading order photon production processes in numerical transport simulations of the quark-gluon plasma.

To begin with, our findings are the complete conserved charge diffusion matrix and electric conductivity. Those properties are important ingredients, e.g., for future simulations of baryon rich collisions. Next, we find that the influence of external magnetic fields to the QGP dynamics is not quantifiable in observables. We present results for a variety of direct photon observables and we can partly explain experimental data. We emphasize the importance of the chemical composition and non-equilibrium nature of the medium to the direct photon puzzle. Lastly, we observe the interesting dynamic behavior of azimuthal correlations in small systems and identify signatures of the initial state in final observables. This will also be of interest for more precise simulations of electromagnetic probes and allows for various future studies.

Outline of this thesis

After introducing the theoretical and experimental background in Chap. 1, we present in the next chapter the first project of this thesis about electric conductivity and diffusion coefficients of hot quark-gluon and hadronic matter. The chapter is partly reproduced from and based on Refs. [1, 2]. The following chapter presents a calculation of external magnetic fields from spectators in peripheral heavy-ion collisions. We use a numerical solution of the Boltzmann equation to investigate the kinetic influence of these fields to the QGP dynamics. The chapter is partly reproduced from and based on Ref. [3]. The next chapter gives an introduction to the theoretical modelling of heavy-ion collisions, with a focus on transport models. In Chap. 5 we summarize the theoretical foundations of thermal field theory. We conclude the chapter by the optical theorem and cutting rules which will be needed in the following. The next four chapters aim at the theoretical description of direct photons in heavy-ion collisions. Parts of these chapters are extensions and improvements of the methods and results published in Ref. [4]. Chap. 6 deals with microscopic photon production in transport models. We construct a consistent leading order photon production algorithm including binary and radiative scattering.

In the following Chap. 7 we present a to date unpublished method within BAMPS to compute photon radiation and compare it with the method from Chap. 6 before.

In Chap. 8 we investigate more closely the implementation of boosted production rates

and the translation of elliptic flow from the background to photons. Furthermore we take a closer look to emission angles and energy spectra of photons radiated by single quarks. In Chap. 9 we present an update of the direct photon results from BAMPS for RHIC and LHC and compare to data. The subsequent Chap. 10 deals briefly with the principle of QGP dilepton emission in transport theory with temperature extraction as an application. We then come in Chap. 11 to the last project, dealing with initial and final state effects in small systems. This somewhat segregated topic is interesting by itself, but will in future help to find more precise answers to the questions of the previous chapters, especially regarding the initial state of heavy-ion collisions. To this end we first give an overview of experimental results, introduce the new model (combining two existing models and an event-by-event analysis) and present the results. This chapter is partly reproduced from and based on Ref. [5]. Lastly, we summarize, conclude and give an overall outlook of future projects.

1. Introduction

A small fraction of our universe’s mass is “bright matter”, meaning it is visible, and clustered in galaxies, dust or gas clouds. Most of this matter whose existence we claim to know participates in the strong force, described by the fundamental theory of Quantum Chromodynamics (QCD).

QCD is a nearly complete quantum theory of matter, with the only parameters being the masses of the current quarks and the strong coupling constant [6]. Matter properties of quarks, gluons and hadrons arise from the complicated dynamics of QCD. The interactions among the constituents of the theory play the most important role, but due to its complexity it is extremely difficult to solve. Adding Quantum Electrodynamics (QED) into the theory, also the interactions among leptons and photons with quarks (and each other) add to the problem.

QCD has a perturbative limit, which is in most cases reached if large energy scales are involved. For this reason one thrives with the help of high-energy experiments to unravel properties and parameters of QCD and QED; however, several outstanding questions remain. In many experiments, the number of involved constituents (partons or hadrons) is large. This multi-particle dynamics of QCD is both a virtue and a vice. It has the disadvantage, that individual properties of partons and their mutual interactions are hidden in the ensemble and must be disentangled by laborious experimental and theoretical effort. It is however also a virtue, since ensembles of particles can be described traditionally by a few macroscopic thermodynamic properties such as temperature or transport coefficients. Albeit not in a first-principle sense, such descriptions can be surprisingly precise.

In the following, we review the standard model of QCD and QED (omitting the electroweak sector), and outline important properties of strongly interacting matter. We then turn to a selection of high-energy experiments which were crucial for the modern understanding of particle physics.

1.1. Standard model of particle physics

Quantum Electrodynamics, the theory of interacting leptons and photons, is based on the Lagrange density

$$\mathcal{L}_{\text{QED}} = \bar{\psi}_l(i\cancel{\not{D}} - m_l)\psi_l - e\bar{\psi}_l\cancel{A}\psi_l - \frac{1}{4}F_{\mu\nu}F^{\mu\nu}, \quad (1.1)$$

where ψ_l denotes the lepton spinor, m_l its mass, and the electromagnetic field strength tensor is

$$F^{\mu\nu} = \partial^\mu A^\nu - \partial^\nu A^\mu. \quad (1.2)$$

Slashed quantities are defined as $\cancel{D} = \gamma^\mu a_\mu$ with Dirac gamma matrices γ_μ [7]. The (classic) electromagnetic vector potential A^μ takes the role of the photon in the quantized theory. The Lagrange density has the unit of an energy density (i.e. energy⁴), the field strength tensor the unit energy². The latter incorporates the measurable components of the electric field \vec{E} and magnetic induction¹ \vec{B} . QED is an Abelian field theory, i.e. the photon fields

¹In vacuum, or in a medium with negligible magnetization, the magnetic induction is equal to the magnetic field \vec{H} .

A^μ commute. Quantum effects in QED loose importance as one probes lower and lower energy scales, such that in many traditional applications, the classical limit of the theory (classical electrodynamics) is sufficient. It is based on the Maxwell equation,

$$\partial_\mu F^{\mu\nu} = j^\nu \quad (1.3)$$

and the Jacobi identity $\partial_\alpha F_{\mu\nu} + \partial_\mu F_{\nu\alpha} + \partial_\nu F_{\alpha\mu} = 0$. The electric current density j^ν is classically defined as a boost of the local rest frame electric charge density ρ_0 , $j^\nu = \rho_0 u^\mu$ with four-velocity u^μ . Note that in quantized electrodynamics (after promoting all quantities to operators) the equations of motion are the Maxwell equation, Eq. (1.3), coupled with the Dirac equation,

$$(i\cancel{D} - e\cancel{A} - m_l)\psi_l = 0. \quad (1.4)$$

More precise, Eq. (1.4) is the original Dirac equation plus an interaction term with an external electromagnetic potential. The only possible microscopic process is the emission or absorption of a photon from a lepton.

Quantum Chromodynamics is the theory of quarks and gluons. It is a non-Abelian theory, which is the most important difference to QED with a number of striking consequences. Quark fields ψ_q^n transform under a representation of the SU(3) group, where the corresponding non-Abelian charge is labeled as *color*, $n = 1 \dots 3$. Gluons couple to quark currents and transform under the adjoint representation of SU(3), that means they belong to a color octet. Defining a fundamental representation λ^a of the SU(3) algebra, $[\lambda^a, \lambda^b] = if^{abc}\lambda^c$, $\text{Tr}(\lambda^a\lambda^b) = 1/2\delta^{ab}$ with structure constants f^{abc} characterizing the algebra, one can define a covariant derivative for the quark fields $D^\mu = \partial^\mu + ig\lambda^a A_\mu^a$. Likewise, one can define a covariant derivative for the adjoint fields D_A^μ . The field strength tensor in QCD carries the adjoint color index $a = 1 \dots 8$,

$$F_{\mu\nu}^a = \partial_\mu A_\nu^a - \partial_\nu A_\mu^a - gf^{abc}A_\mu^b A_\nu^c. \quad (1.5)$$

We can now write down the QCD Lagrangian,

$$\mathcal{L}_{\text{QCD}} = \bar{\psi}_q^m (i\cancel{D}_{mn} - m_q\delta_{mn})\psi_q^n - \frac{1}{4}F_{\mu\nu}^a F_a^{\mu\nu}, \quad (1.6)$$

where m_q is the mass of the quark and we explicitly wrote down color indices.

Similar as in QED, the dynamics is determined by the Dirac equation $(i\cancel{D} - m_q)\psi_q = 0$ coupled with the Yang-Mills equation, (which takes the role of the Maxwell equation in QED),

$$[D_\mu, F_a^{\mu\nu}] = g\bar{\psi}_q\gamma^\mu\lambda^a\psi. \quad (1.7)$$

Possible processes in QCD are quark-gluon absorption or emission, gluon-gluon absorption or emission and gluon-gluon scattering. Due to its complicated structure, analytic solutions of the theory are intractable. It is however possible to use approximation schemes, such as perturbative techniques, in order to solve for certain observables. Another common approximation is space-time discretization, with subsequent numerical evaluation of observables of the theory, referred to as lattice QCD (lQCD) [8]. Effective theories, integrating out certain degrees of freedom (which are less relevant at the scales of interest) help in some cases to obtain answers from QCD.

The Standardmodel of particle physics nowadays combines QED, QCD and the electroweak theory in a common framework. The fundamental degrees of freedom are leptons (neutrinos, electrons, myons, tauons), quarks, gauge bosons (photons, gluons, Z bosons, W bosons) and the scalar Higgs boson. In Fig. 1.1 all participants are summarized.

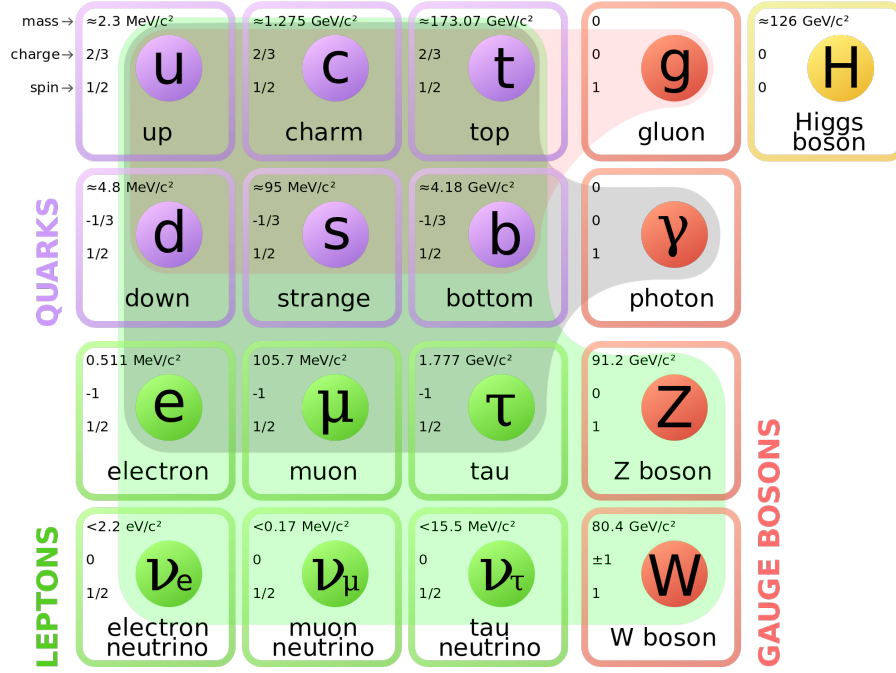


Figure 1.1.: Figure from Ref. [9]. Overview of the fundamental particle species in the Standard Model of particle physics to date. The red, grey and green shading groups the particles interacting strongly (QCD), electromagnetically (QED) and weakly.

1.2. Properties of strongly interacting matter

QCD is a renormalizable quantum field theory, that means that all bare (i.e. non renormalized) fields and parameters can be rescaled in order to absorb unphysical divergences. There are many different renormalization schemes, all of which involve a renormalization point μ , which is an arbitrary energy scale. Physical observables must not depend on μ , whereas internal quantities, such as quark masses or coupling constants depend on μ . Typically one first regularizes divergent integrals (e.g. using dimensional regularization), then redefines fields and parameters (renormalization; e.g. minimal subtraction scheme \overline{MS} [10]). Physical observables must not depend on the regularization prescription.

1.2.1. Asymptotic freedom

The dimensional regularization is intimately connected to the the running of the strong coupling constant α_s . One lifts the requirement of four spacetime dimensions, introducing $D = 4 - 2\epsilon$ dimensions, such that the action is $S = \int d^D x \mathcal{L}(x)$ where the Lagrangian has now D energy dimensions. By this procedure, the regularized coupling g_R has ϵ energy dimensions - a feature that will translate into the running of $\alpha_s = g^2/4\pi$. The requirement that the bare coupling g_{bare} be independent of μ leads to the flow equation (or renormalization group equation),

$$\mu^2 \frac{d\alpha_s(\mu^2)}{d\mu^2} = \beta(\alpha_s), \quad \beta(\alpha_s) = -\frac{[\alpha_s(\mu^2)]^2}{4\pi} \left(11 - \frac{2}{3} N_f \right). \quad (1.8)$$

This differential equation can be solved with boundary condition² $\alpha_s(\Lambda_{\text{QCD}}^2) \rightarrow \infty$, with solution

$$\alpha_s(\mu^2) = \frac{1}{4\pi\beta_0 \log(\mu^2/\Lambda_{\text{QCD}}^2)}, \quad \beta_0 = \frac{1}{(4\pi)^2} \left(11 - \frac{2}{3}N_f \right). \quad (1.9)$$

The value of Λ_{QCD} depends on the subtraction scheme and the number of flavors, but must be determined from experiments. The world average of Λ_{QCD} at $N_f = 3$ quark flavors is [6, 11]

$$\Lambda_{\text{QCD},\overline{MS}}^{N_f=3} = (332 \pm 17) \text{ MeV}. \quad (1.10)$$

The corresponding value for 4, 5 and 6 flavors is (292 ± 16) MeV, (210 ± 14) MeV and (89 ± 6) MeV, respectively. The right hand side of Eq. (1.8) is the 1-loop approximation of the β -function, however; it is known up to 4-loop order. In QED, where the coupling constant $e = \sqrt{4\pi\alpha_{\text{EM}}}$ is widely known as the fundamental electric charge, the β -function is positive at all orders,

$$\beta_{\text{QED}}(e) = \frac{e^3}{12\pi^2} + \frac{e^5}{64\pi^4} + \dots \quad (1.11)$$

The coupling α_{EM} increases for higher values of the energy scale Q , due to the positivity of the β -function, however; in practice this dependence becomes only relevant at energy scales as high as the mass of the Z-boson $m_Z = 91$ GeV. At lower energies, $\alpha_{\text{EM}}(0) \approx 1/137$, whereas $\alpha_{\text{EM}}(m_Z) \approx 1/128$. In heavy-ion collisions, the typical energy scales are of the order of the temperature $T \lesssim 600$ MeV, thus in this thesis we fix for all applications $\alpha_{\text{EM}} \equiv 1/137$. The renormalization scale μ is unphysical, and the fact that the coupling $\alpha_s(\mu^2)$ depends on μ indicates that α_s itself is no observable. Observables, such as collision cross sections, depend on α_s and a renormalization scale dependent matrix element, and their dependences on μ should cancel. As an example, taking the renormalization scale as the momentum transfer in a scattering process, $\mu \sim Q$, the effective interaction strength is $\alpha_s(Q^2)$. In Fig. 1.2 we show the world collection of measurements of $\alpha_s(Q^2)$ from Ref. [11]. The described effect is known under the term asymptotic freedom, and was found by Gross, Wilczek and Polizer [12, 13].

1.2.2. Color confinement

Color charge can not be observed. No measurement will yield a color charge other than white (=“color + anticolor” or “red+blue+green”). The reason is, that color charged particles, i.e., quarks and gluons, are usually bound to white objects called hadrons. A rare special case are relativistic plasmas, such as the quark-gluon plasma (QGP), where quarks and gluons are free and unbound. However, any attempt to observe color charged objects within the plasma will first cause the *hadronization* of partons into white hadrons, whose electric charge, position, momentum or mass can be measured. This phenomenon is called confinement. It is postulated, and so far consistent with existing research, but its reasons and existence not yet rigorously proven. Phenomenologically, the strong force between a pair of colored partons is constant over distance, such that the energy increases with increasing distance. At some point, this energy suffices to generate a new pair of colored partons in between. This process is often depicted as a “flux tube” breaking. Color confinement belongs to one of the seven Millenium problems defined by the Clay Mathematics Institute in Cambridge, Massachusetts, US.

²The boundary condition is given in terms of the perturbatively defined coupling constant. At its scale, non-perturbative physics dominates.

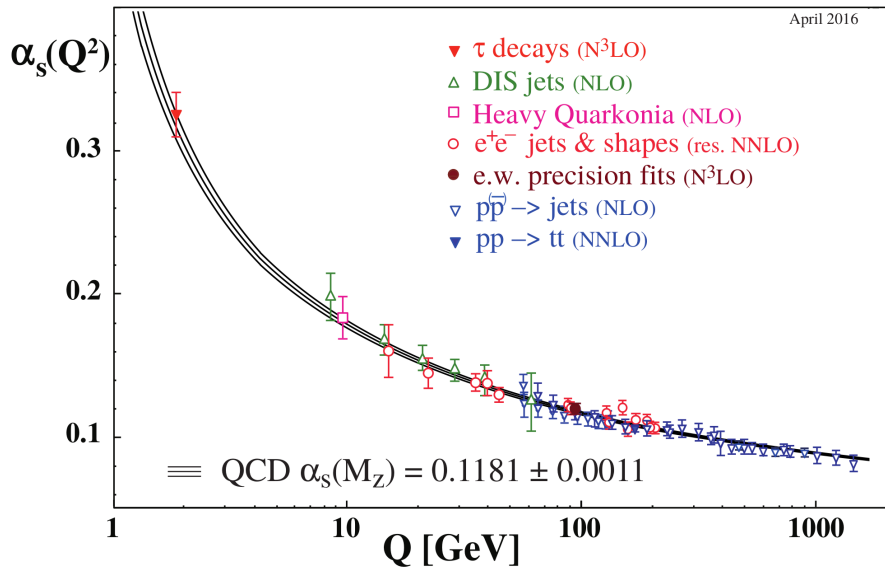


Figure 1.2.: Figure reproduced from Ref. [6]. World data on the running coupling constant dependent on the momentum scale Q . As a reference value, the world average of $\alpha_s(M_Z)$ with the mass of the Z-boson $Q \equiv M_Z$, is given.

1.3. Detection of hot QCD matter

The most important experiments for studying vacuum QCD are hadronic collisions. Thermodynamic properties and multi-particle dynamics is probed by nucleus-nucleus collisions. Today, in Au+Au collisions at the Relativistic Heavy Ion Collider (RHIC) at BNL or in Pb+Pb collisions at the Large Hadron Collider (LHC) at CERN, matter is highly dynamic, and temporarily the energy density is high enough such that a QGP is formed [14–17].

1.3.1. The detection of quark-gluon plasma signatures at SPS

Since 1975 it was proposed, that nuclear matter undergoes a phase transition from hadronic matter to deconfined quark-gluon matter [18, 19]. The picture became more concrete around ten years later [20–23]. In 1994, the Super Proton Synchrotron (SPS) at CERN carried out the first heavy-ion collisions which were powerful enough such that the search for evidence of the new state of matter, the QGP, seemed reasonable. In fact, seven experiments took part (NA44, NA45, NA49, NA50, NA52, NA57, WA98), and multiple datasets hinted to the formation of strongly interacting matter which was likely not only a hot hadronic gas - however, evidences were only indirect or remained inconclusive [24].

At center-of-mass energies per colliding nucleon pair of $\sqrt{s_{NN}} = 17.2$ GeV, the expansion rate of the fireball reached more than half the speed of light at freeze-out temperatures of $T \sim 120$ MeV [25]. Particle multiplicities could consistently be described with statistical hadronization models [26–28], assuming a nearly thermal particle production at a chemical freeze-out temperature of $T \sim 140$ MeV. It was also found, that heavy-ion collisions (Pb+Pb) build up significant collective transverse flow [28] (more to collective flow in Sec. 1.3.3). Furtheron, J/ψ -suppression could be measured [29–31], which was long before predicted to be a significant evidence for a transient existence of quark-gluon plasma [21]. Free color charges are able to screen the charm-anticharm potential inside a plasma such that the initially produced J/ψ bound states dissolve³. In the case of char-

³Central Pb-Pb collisions at SPS produce 1-2 J/ψ initially, at top RHIC energy about 7 – 10, at LHC

monium suppression, alternative hadronic models could also describe the data and their interpretation remained inconclusive [32]. Relative to proton-proton collisions, hadrons containing strange particles (probed by, e.g., the K^+/π -ratio) are enhanced by a factor of two in lead-lead collisions [26, 33]; however, deconfinement models could neither be ruled out nor proven by these results, and purely hadronic rescattering explained some of the data.

One of the best direct evidences for a quark-gluon plasma is the measurement of direct photons or dileptons from a thermal QGP phase. At the SPS facility, the background was too strong to give conclusive answers, however, a significant direct photon signal was reported [34]. At the expected temperatures, a dilepton or photon signal from thermal radiation is very low. Some experiments have however seen an enhancement of the dilepton rates over the cocktail from hadronic production, which is believed to be of thermal origin [35, 36].

1.3.2. From SPS to RHIC to LHC

As outlined in the previous section, at SPS many studies supported the onset of deconfinement, and evidently higher collision energies had promised much clearer effects. Those came with the beginning of the Relativistic Heavy Ion Collider (RHIC) facility, and its four main experiments, BRAHMS [14], PHOBOS [16], PHENIX [37] and STAR [17]. To date, only PHENIX and STAR are still operative. Collisions at RHIC extend to $\sqrt{s_{NN}} = 200$ GeV, but the facility is capable to cover a range of collision energies ranging down to $\sqrt{s_{NN}} = 7.7$ GeV. For a review, see, e.g., Ref. [38].

The initial energy density at times $\tau \sim 0.1$ fm/c can be up to 1400 GeV/fm³ at central Pb+Pb events at $\sqrt{s_{NN}} = 2.76$ TeV [39], and around 500 GeV/fm³ at $\tau \sim 0.2$ fm/c for central Au+Au collisions at $\sqrt{s_{NN}} = 200$ GeV [40]. Even other, more conservative, estimates exceed the nuclear ground state energy density (~ 1 GeV/fm³, [41]), such that deconfinement should be possible. Also at RHIC, statistical hadronization could precisely describe the particle abundancies, using a freeze-out temperature of $T \sim 177$ MeV and baryon chemical potentials of a few tens of MeV only. This was the first time when such low net baryon densities had been produced, and the Bjorken picture is truly applicable (Ref. [22]; see Sec. 4.1).

Rather unexpected was the discovery of strong collective flow in peripheral collisions [42–44]. As depicted schematically in Fig. 1.3 in an off-central collision, the eccentric, dense fireball (blue shaded area) develops in the transverse plane an anisotropic angular momentum distribution (green arrows) due to pressure gradients building up. Such collective flow indicates a strongly interacting medium. The QGP appeared as a possible explanation for this behavior, which is dubbed “elliptic flow”, since the azimuthal momentum distribution has an elliptic shape (more precise definition is given later) and the collective motion of particles in the transverse plane can be described by hydrodynamic equations. Measurements of particle momentum anisotropies could be explained first by ideal hydrodynamics, later on the theory was refined and dissipative hydrodynamics became standard. With great accuracy, particle identified elliptic flow v_2 could be understood by hydrodynamics [45], see Fig. 1.4.

The high energies at RHIC initiated research involving so-called *hard probes*, namely jets of particles traversing the strongly interacting medium. In all participating experiments, it turned out that high-energetic particles ($p_T \gtrsim 10$ GeV) traversing portions of the strongly interacting central collision region lose significant amount of their energy. The most cited observable is the nuclear modification factor R_{AA} . It could be shown in experiments

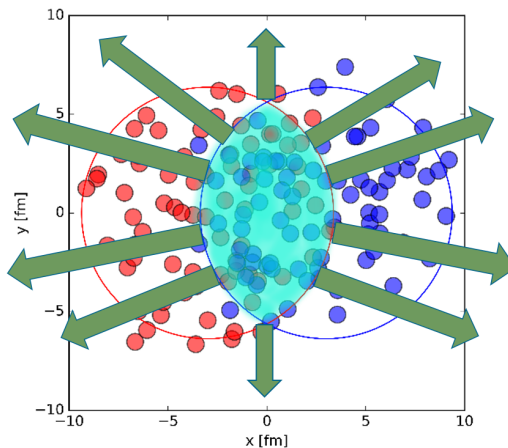


Figure 1.3.: A schematic picture of the transverse plane in a peripheral heavy-ion collision. Spatial eccentricity is translated into momentum anisotropy due to strong pressure gradients.

(compared to theory), that the energy loss of energetic particles occurs indeed due to final state interactions (in d-Au collisions the suppression is absent, [37, 46–48]). This is a further proof of a medium which interacts strongly with high energetic particles and consistent with QGP models [49].

1.3.3. Hydrodynamic behavior and shear viscosity

If two heavy ions collide, it is a priori not clear, if the system behaves as a collection of individual particles, or as a thermodynamic medium. The latter requires a sufficiently large number of particles and high interaction rates⁴ such that the ensemble is locally equilibrated. A locally (nearly) thermal system can meaningfully be described by averaged quantities like temperature, pressure, energy density, entropy density and several transport coefficients. If this is the case, hydrodynamic equations are applicable, which reduces the computational effort compared to microscopic descriptions. The equation of state is another key ingredient to describe the dynamics.

The standard picture of high-energy heavy-ion collisions is that the central energy density shortly after the collision is high enough such that matter deconfines into a quark-gluon plasma. The QGP quickly thermalizes (thermalization times are of the order of 1 fm/c). The QGP cools down and expands subsequently and trespasses the QGP-hadron gas transition at critical temperatures⁵ of about $T_c \sim 160 - 170$ MeV (at vanishing net baryon density). Thermal hadron yields are mostly fixed at this transition (“chemical freeze-out”) and statistical models are successful, assuming a freeze-out temperature and volume. Indeed, this temperature rises with increasing collision energy, but saturizes at T_c and excess energy heats up the QGP stage only.

Since the vast majority of studies have supported a transient QGP phase, it is important to determine its material properties. In relativistic fluids the most important quantities are shear- and bulk viscosities, diffusion coefficients and electric conductivity. The latter

⁴The inverse scattering rates should be much larger than the systems lifetime.

⁵The phase diagram of nuclear matter, featuring the phase transition, is only well defined in near-equilibrium systems.

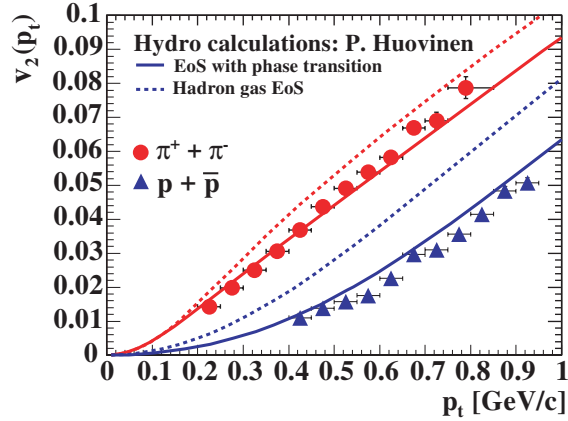


Figure 1.4.: Particle identified elliptic flow from the STAR experiment at RHIC (from Ref. [50]) compared to an ideal hydrodynamic model (from Ref. [45]) using a purely hadronic equation of state and one incorporating a phase transition. Clearly, the latter is more realistic. Figure from Ref. [51].

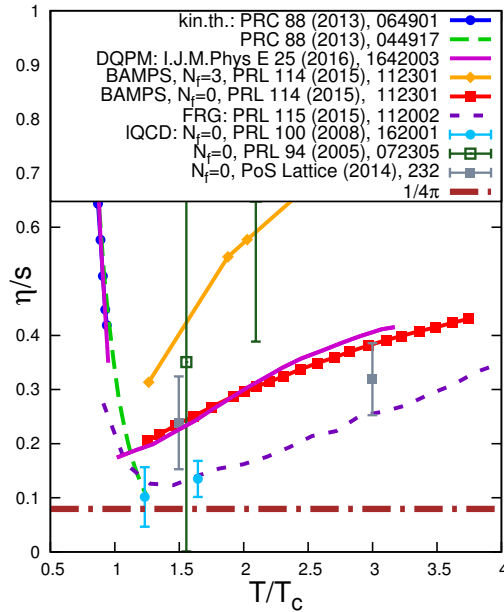


Figure 1.5.: Compilation of results to date for the shear viscosity to entropy ratio η/s .

two coefficients have gained little attention in literature so far but several new results will be presented in this thesis. Shear- and bulk viscosity are most important for dissipative hydrodynamic codes, because they influence the dynamical properties significantly.

Consider a fluid between two parallel walls. Simply, shear viscosity describes the proportionality between the shear stress (parallel force per area exerted to the walls resulting from drag) and the transverse velocity gradient within the fluid (more precise definition in Sec. 4.1). The determination of the shear viscosity in the QGP, at the phase boundary as well as the hadron gas has been a long standing problem, but some progress has been achieved. A theoretical lower bound of $\eta/s = 1/4\pi$ was given from AdS/CFT correspondence [52] (KSS bound).

It came as a surprise, that one had to assume a model with (nearly) zero viscosity, thus assuming an ideal fluid, in order to explain the experimental flow patterns at RHIC by

hydrodynamics [53–55], see Fig. 1.4. More precise parameterizations of $\eta/s(T)$ and fits to experimental data constrained the value of the shear viscosity to entropy ratio to below unity [56–60].

At $T \approx T_c$, it could be narrowed down to probably be close to the KSS bound $\eta/s \gtrsim 0.08$, but its temperature dependence plays a more important role the more differential datasets are explained. In Ref. [60] it was concluded, that the differential elliptic flow $v_2(p_T)$ at RHIC energies is almost independent to the value of η/s in the QGP but strongly sensitive to its behavior in the hadron gas, whereas at LHC the sensitivity to the value in the QGP is strong and results are independent of the hadronic value of η/s .

Even though intrinsically difficult, some attempts to determine η/s were done in lattice QCD [61–63]. Using perturbative QCD (pQCD), and solutions of the Boltzmann equation, the temperature dependence of η/s in the QGP was calculated numerically [64–67] and semi-analytically [68, 69]. The functional renormalization group approach has been exploited in Ref. [70], and a dynamical quasi-particle model is constructed in Ref. [71]. In the hadronic phase, kinetic theory estimations using resonance cross sections are done in Refs. [72, 73]. Recent results for η/s from the hadronic transport model SMASH are given in Ref. [74]. In Fig. 1.5 some of the results are summarized, and show the interesting trend, that η/s approaches a minimum at the phase transition temperature T_c . Indeed it was proposed, that the minimum of the shear viscosity to entropy ratio pinpoints the transition temperature [75].

1.4. Electromagnetic observables

So far, we were very brief about one of the most direct messengers of the heavy-ion collision: electromagnetic probes. Those are in most cases photons and electron-positron pairs, but also muon-antimuon pairs. Their mean free path exceeds by far the diameter of the collision fireball, such that they travel nearly undisturbed from the production point to the detector.

1.4.1. Photons

Photons have been used for decades as a valuable probe of the hot matter created in heavy-ion collisions. They are emitted from the initial nucleon-nucleon contacts (prompt photons), during the subsequent QGP phase and the hot hadron gas (HG) phase (thermal photons and jet-medium photons), by the fragmentation of jets outside the fireball, and finally by the decay of long lived resonances into real photons. The sum of all but the latter sources is called *direct* photon contribution, and experiments have succeeded in separating decay from direct photons (ALICE experiment at the LHC [76, 77], PHENIX experiment at RHIC [78–80]). The measurements extend down to transverse momenta $p_T = 0.4$ (0.9) GeV for RHIC (LHC), and both find an exponential excess above N_{coll} -scaled prompt photons, which indicates a strong additional source, most likely the shining QGP and hot HG. The decay background subtraction is done via different methods, and improvements of the direct photon data is expected in the future.

Direct photon yields

In experiment, after the extraction of a clean inclusive photon signal, i.e., the yield of all real photons, taking detector effects and non-photon signals into account, decay photons must be subtracted. Since the dominant⁶ number of particles which decay into real photons

⁶about 96 % [81]

are π^0 and η mesons, those two species must be identified and measured within the same experiment. Based on those data, the number of decay photons is calculated with Monte-Carlo algorithms. Finally, the direct photon spectrum (γ_{direct}) is the difference between the inclusive ($\gamma_{\text{inclusive}}$) and decay (γ_{decay}) yields. In practice, this subtraction would require unreachable accuracy of the components in order to achieve reasonable errors. Instead, a statistical subtraction method is applied, which can be schematically written as (here, π^0 denotes the mesonic spectrum),

$$\begin{aligned}\gamma_{\text{direct}} &= \gamma_{\text{inclusive}} - \gamma_{\text{decay}} = (1 - R^{-1}) \gamma_{\text{inclusive}} \\ R &= \frac{\gamma_{\text{inclusive}}}{\gamma_{\text{decay}}} = \frac{\{\gamma_{\text{inclusive}}/\pi^0\}^{\text{measured}}}{\{\gamma_{\text{decay}}/\pi^0\}^{\text{calculated}}}.\end{aligned}\quad (1.12)$$

The advantage of computing the double ratio R lies in the partial canceling of systematic errors. The measurements of $\gamma_{\text{inclusive}}$ and the mesonic spectrum (π^0 and η) both include similar systematic errors like energy scale nonlinearities which cancel out in the nominator. The spectrum of background photons in the denominator γ_{decay} is obtained from measured meson spectra and their simulated decay photons.

In Ref. [82] this method was applied for transverse momenta up to $p_T \approx 13$ GeV for Au+Au collisions in several centrality bins at $\sqrt{s_{NN}} = 200$ GeV. It turned out, that at these rather high momentum scales, the yield could satisfactorily be described by NLO pQCD calculations, scaled by the number of binary collisions N_{coll} . This is expected, if any thermal (QGP or HG) contribution is negligible, as direct photons in proton-proton collisions are explained rather precise by NLO pQCD calculations [83]. A breakthrough was achieved by the PHENIX experiment in 2010, when the enhancement of direct photons over the pQCD estimate became significant [78]. In Fig. 1.6 it can be seen, that below $p_T \sim 3$ GeV the direct photon signal is strongly enhanced with respect to N_{coll} -scaled pp results. This is interpreted as thermal photon emission from the QGP and hadron gas⁷. From now on, research in this direction focused on this low momentum region.

At the LHC, the ALICE experiment measures direct photons. The yield showed a significant thermal excess at $\sqrt{s_{NN}} = 2.76$ TeV [76].

Thermal photons are a an undimmed probe of the hot fireball itself and as such unique. Apart from the correct photon production, an accurate modeling of the heavy-ion background is necessary. Until now, popular descriptions of the spacetime evolution of heavy-ion collisions are given by fireball parameterizations [85, 86] or hydrodynamic simulations [57, 87–93]. Photon spectra can be obtained from those models by folding the spacetime evolution of temperature T and four-velocity u^μ over analytically known photon production rates $R(T, u^\mu)$ [85, 94–99].

Recently, much work is done concerning alternative rates (e.g. Ref. [100]) or rather ignored effects, such as viscous corrections (e.g. Ref. [101]) or unknown sources (e.g. Ref. [102]).

Anisotropic flow of photons

An asymmetry in the azimuthal distribution of direct photon momenta is produced by a radiating medium which itself flows asymmetrically. Unlike hadronic particle species, photons emitted isotropically, e.g. prompt photons, necessarily wash out any elliptic flow signal because the measured direct photon signal is always a sum of all contributions. Within the first fm/c, quark and gluon elliptic flow is built up, later it is translated into a hadronic phase. Photon flow is thus a spectrum-weighted average of the produced photons.

⁷ In Ref. [84] no significant low p_T enhancement was observed in d+Au collisions. This proved that the low p_T enhancement is indeed a thermal, and as such final state effect.

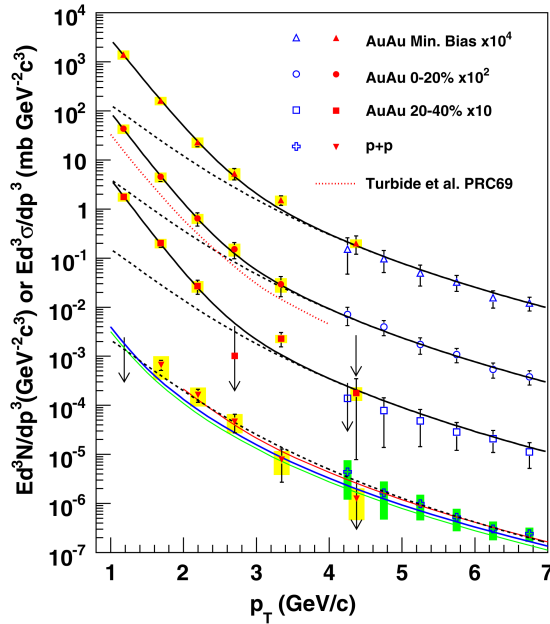


Figure 1.6.: Thermal enhancement of direct photons at RHIC, for two centrality classes and min bias events. Reproduced from Ref. [78].

There were suggestions, that elliptic flow can be enhanced by strong magnetic fields, but this is not yet widely accepted and questions remain open (see e.g. Ref. [103] and Ref. [3] and Chap. 3).

Recently, ALICE and PHENIX have measured elliptic and triangular flow of direct photons for several centrality classes (PHENIX, $\sqrt{s} = 200$ GeV: 0 – 20%, 20 – 40%, 40 – 60% [104], ALICE, $\sqrt{s} = 2.76$ TeV: 0 – 40% [105] and 0% – 20%, 20% – 40% [77]). Both experiments show unexpectedly large flow, however the measurement is extremely challenging and errorbars are still large. It is nearly impossible for experiments to disentangle the measured time-integrated photon spectra into their separate sources. Theoretical models however, compared to data, do not suffer from this problem.

The ultimate goal is the explanation of the measured photon spectra by the correct combination of photon production mechanisms of hard and soft quantum chromo/electrodynamical (QCD/QED) interactions and a suitable spacetime evolution of the high-energy heavy-ion collision.

It is furthermore desirable to explain the elliptic and triangular flow of photons in theoretical models. The explanation of elliptic flow for hadrons has required accurate modelling of the initial state and a correct treatment of the nearly hydrodynamic expansion of the medium with suitable viscosity [87, 93, 106–108].

The flow of photons is substantially different. Photons leave the fireball without any further scattering such that their flow originates solely from the production process. For now, the large elliptic flow of photons poses a formidable challenge for dynamical models, and the simultaneous description of the yield and the flow of direct photons remains an unsolved puzzle.

Photon studies within this thesis

Transport approaches, such as BAMPS [40], PHSD [109, 110] or UrQMD [111, 112] have two possibilities to study photon or dilepton production: “coarse-graining” of the particle ensemble [113] and obtaining a spacetime background which can be used in the same way

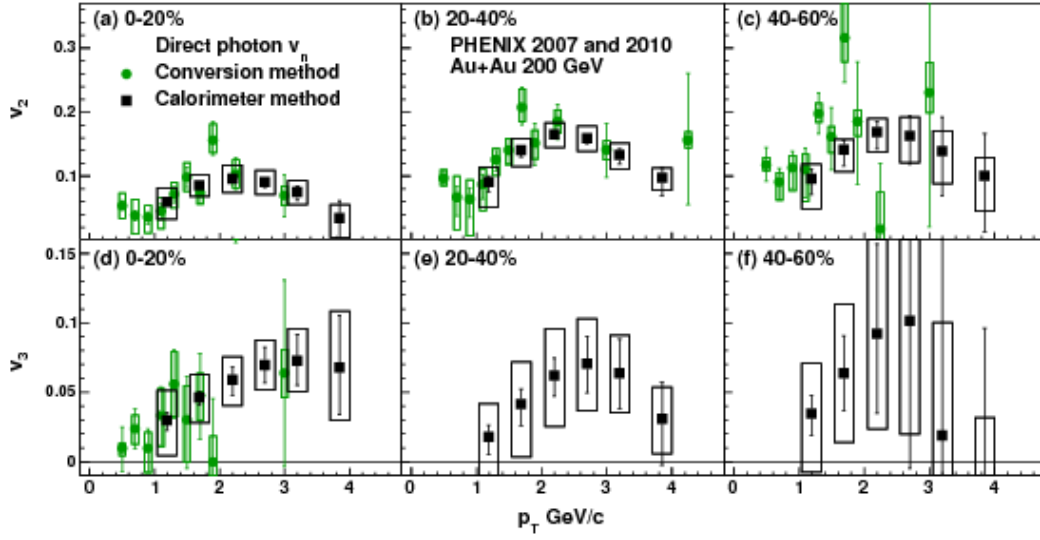


Figure 1.7.: Direct photon elliptic flow (top row) and triangular flow (bottom row) from the PHENIX experiment at RHIC for three different centrality classes. Reproduced from Ref. [104].

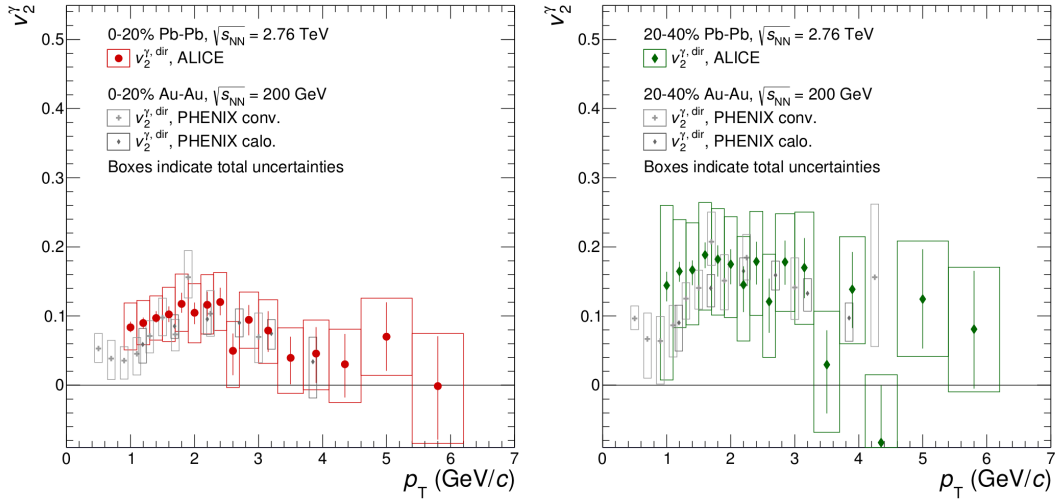


Figure 1.8.: Direct photon elliptic flow from the ALICE experiment for 0% – 20% (left) and 20% – 40% (right) centrality. Reproduced from Ref. [77].

as a hydrodynamic evolution as described above, or, using the microscopic cross sections for the desired photon production processes and generating photons within the transport framework directly. The latter method will be our choice in the *Boltzmann Approach to Multi-Parton Scatterings* (BAMPS) [4, 40], which is based on the numerical solution of the Boltzmann equation.

In this thesis we show how tree-level and radiative scattering diagrams can be implemented in dynamical transport simulations to nearly reproduce full leading order (LO) photon rates. To this end we introduce two separate methods to realize radiative scattering processes. Subsequently we compute results for the QGP phase of high energy nuclear reactions. The physical difference of our approach compared to hydro, fireball or coarse-graining approaches is the intrinsic non-equilibrium nature - high or low energetic jets and the non-, nearly- or full thermal medium is treated equally. Furthermore, spacetime dependent quark and gluon fugacities⁸ influence the photon rates by default. We investigate carefully the dependence of photon rates on parton fugacities.

As a main result, we claim that the photon yield of the QGP can be much smaller than previously thought, due to the small initial quark content of the fireball. Furthermore, the preequilibrium phase of the QGP does not contribute significantly to yield or elliptic flow of direct photons. Secondly, we show how important non-equilibrium photon production can be for the elliptic flow: energetic particles behave “jet-like”, and contribute negatively to the elliptic flow. These results provide necessary complementary aspects to hydrodynamic calculations, which in most cases does not include strong off-equilibrium dynamics. Supplied with hadronic and prompt contributions from elsewhere, we are able to explain experimental data only in limited regions of transverse momentum.

1.4.2. Dileptons

Correlated pairs of leptons (dileptons, or virtual photons) are a very differential observable, and several physical effects have to be taken into account which do not exist in direct real photon measurements. With energy q_0 and momentum \vec{q} of the dilepton pair, the invariant mass is defined as $M = \sqrt{q_0^2 - \vec{q}^2}$. Typically, spectra are measured in transverse momentum q_T or invariant mass M . Compared to real photons, dileptons benefit from a better signal to background ratio (due to the additional variable M). Dileptons, once produced, leave the fireball without further interactions, they are however, produced during all stages in heavy-ion collisions of all energies (like real photons). Even before the nuclei touch, the Coulomb field of the approaching but decelerating nuclei produce dileptons by coherent bremsstrahlung. It was shown in Ref. [114], that this contribution is negligible and thus not further studies are currently under way. The equivalent of prompt photon production, the hard production of dileptons in the very first moment of the nuclear overlap, is called Drell-Yan process [115]. Hard quark-antiquark pairs from colliding hadrons produce dileptons with invariant masses beyond $M \gtrsim 3$ GeV. They are rather well understood and shall be of no further interest here. Also in a partonic phase, quark-antiquark annihilation leads to dilepton emission. Assuming a rapid thermalization, production rates can be computed by perturbative thermal quantum field theory. A very important dilepton contribution stems from thermal hadronic radiation. As one of the most important processes, pion-antipion annihilation forms resonances, such as a ρ -resonance, which decays into dileptons. After freeze-out, long-lived resonances such as heavy quarkonium states decay into dileptons. More dominantly however, π^0 , η and ω mesons decay into dileptons and photons (Dalitz decay). This populates the low mass re-

⁸For high energy reactions the number of quarks and antiquarks is very similar, so that it makes sense to speak of an absolute quark fugacity defined as $\lambda_q \equiv n_{q+\bar{q}}/n_{q+\bar{q}}^{\text{equilibrium}}$ with the density n .

gion, $M \lesssim 1$ GeV. Finally, there is the so-called open charm contribution, which consists of correlated $D\bar{D}$ -pairs which decay individually into dileptons. The last contribution is rather little understood and often remains as a conclusion in studies containing all other contributions. The spectrum of open charm decays appears in the smooth region below the mass of the J/ψ .

The motivation to study dileptons is manifold. A thermal signal constitutes a direct test of equilibrium quantum field theory. The medium properties like temperature and density can experimentally be accessed (see, e.g., Ref. [116]). Light vector mesons, formed as intermediate states in hadronic thermal dilepton production, are characterized by their spectral function which is modified by the surrounding finite temperature medium (nonzero baryon density plays a role, too). As an example, the ρ meson's spectral function broadens significantly for higher temperatures, and in-medium effects are also substantial for ω and ϕ mesons [109,117]. Conveniently, the invariant mass spectrum of dileptons, produced by vector meson decay, gives direct access to the spectral function of the vector mesons.

Compared to real photons, dilepton spectra show visible resonance peaks and thus offer several mass scales at which models can be restricted. The low mass region (LMR, $M < 1$ GeV), intermediate mass region (IMR, $1 < M/\text{GeV} < 3$) and high mass region (HMR, $M > 3$ GeV) have different sensitivity to the aforementioned dilepton contributions.

In this thesis, we merely show the possibility to include $2 \leftrightarrow 2$ dilepton production in partonic transport simulations. We prove the correct implementation of the corresponding dilepton rates and show, as an example, how an effective temperature can be extracted by a fit of dilepton spectra (see Chap. 10).

Experiments

Dileptons have been measured in ultrarelativistic heavy-ion collisions at CERN-SPS with the CERES/NA45 experiment [36,118]. Furthermore, the NA38 collaboration [119] and NA50 collaboration [120] have done several measurements at the end of the 90s.

At CERES, dielectron spectra in proton-nucleus collisions could be explained by hadron decay channels which were obtained by using measured hadron multiplicities and known decay mechanisms. This method (“cocktail”) however strongly underestimates parts of the spectrum in nucleus-nucleus collisions (e.g. sulphur-gold). It was suggested that $\pi^+\pi^- \rightarrow l^+l^-$ processes are the missing piece: this was true but more subtle than expected. Intermediate vector mesons had to be strongly medium modified in order to explain the data, otherwise the mass region $0.3 < M/\text{GeV} < 0.6$ was underestimated by several groups, see the comparison in Fig. 1.9. In the IMR, the spectrum is continuum-like, and the inverse slope of invariant mass spectra can yield the averaged medium temperature (see Chap. 10). Here, four-pion annihilation processes and also QGP contributions had to be taken into account (in the LMR, the QGP contributes only 10 – 20 % [123]).

From 2001 to 2004 the successor experiment at SPS was NA60, which measured with great accuracy dilepton spectra and excess over decay cocktails for In+In collisions [124]. Employing several theoretical improvements, the physical processes behind the data became more and more clear [117,125]. Apart from a detailed modeling of in-medium spectral functions of light vector mesons, also late ρ -meson decay at thermal freeze-out, primordial ρ mesons subject to energy loss, an improved Drell-Yan scheme and an improved thermal hadronic production rate, as well as a detailed investigation of the background dynamics (freeze-out temperatures, critical temperatures) led to a satisfactory explanation of the data [117,125]. Note that in these studies, decays of correlated $D\bar{D}$ pairs were taken into account without medium modifications by extrapolating experimental results from p-p collisions. An example of the successful description of NA60 data is shown in the left panel of Fig. 1.10.

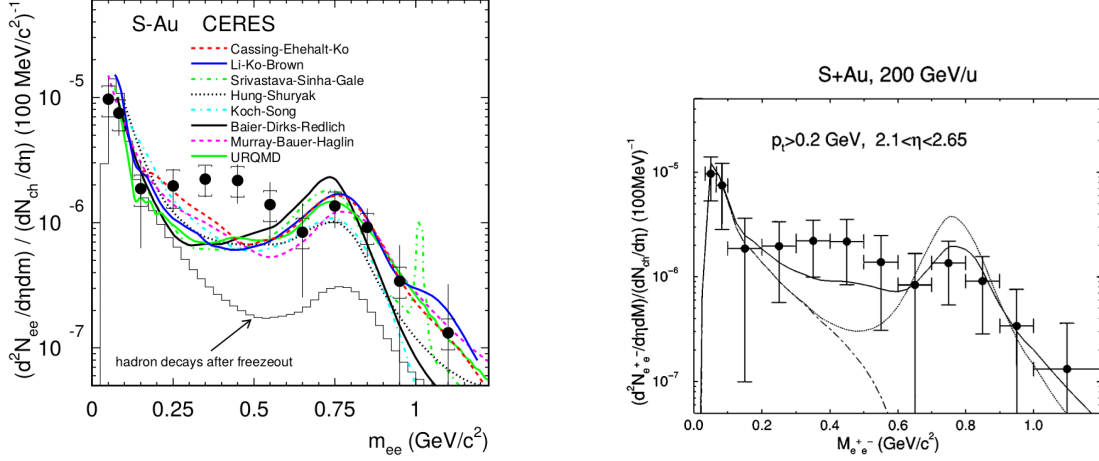


Figure 1.9.: Left: Low mass dilepton enhancement over the hadronic decay cocktail. Figure from Ref. [121]. Eight different models could not reproduce the enhancement. Right: Solution of the puzzle by employing realistic ρ meson in-medium modifications. Figure from Ref. [122].

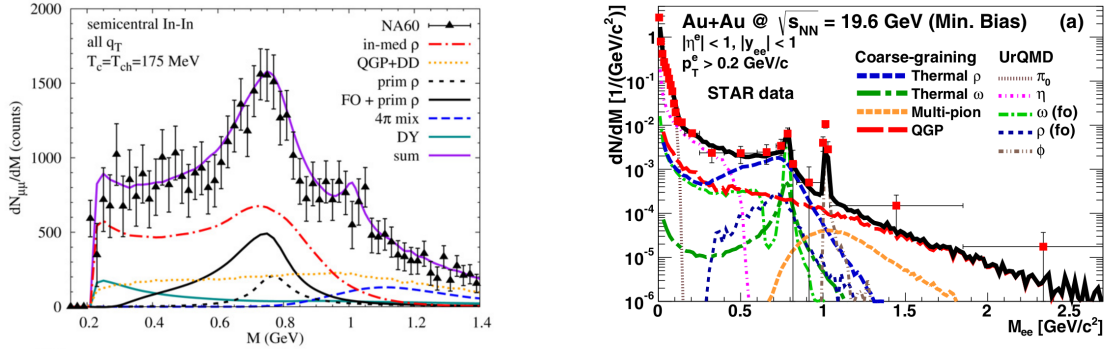


Figure 1.10.: Left: Dimuon spectrum with decay dileptons subtracted as measured by the NA60 collaboration at SPS compared to a model calculation including in-medium modified ρ mesons and several other contributions. Figure from Ref. [125]. Right: Dielectron spectra as measured at RHIC compared to a model calculation. Figure from Ref. [113].

Since 2013, the STAR collaboration published precise results from RHIC [126–128] and in 2016 PHENIX published improved dielectron results in Ref. [129]. The results of both experiments agree [113], however, the statistics from the PHENIX experiment is somewhat lower due to its construction. These new data could be explained by a coarse-graining approach within the hadronic transport model UrQMD [113]. Thermal hadronic and partonic dilepton emission with medium modification of the spectral functions account for the low mass excess above the decay cocktail. In the right panel of Fig. 1.10 an example of this study is shown, which retraces the STAR data with great accuracy, and also depicts the different contributions.

1.5. Units

In this thesis we use natural units, $c = k_B = \hbar = 1$. The metric tensor takes the form $(g^{\mu\nu}) = \text{diag}(1, -1, -1, -1)$. We use megaelectronvolt (MeV) or gigaelectronvolt (GeV) as energy units (1 GeV = 1000 MeV), and femtometer (fm) as length unit (1 fm = 10^{-15} m). By convention, times will be given in units of fm/c. Length and energy units are connected via

$$1 \text{ GeV} = \frac{1}{0.197 \text{ fm}}. \quad (1.13)$$

2. Electric and diffusion properties of QCD matter

In high energy collider facilities one strives to pin down properties of QCD matter around the phase transition from the partonic to the hadronic phase.

If the collision energy is sufficiently high, in the core of the fireball the quark-gluon plasma (QGP) is produced [14–17] which cools down and undergoes a phase transition into a hadronic phase [130].

The hadron gas (HG) produced at the late stages of the collision is still hot and hadrons can still collide multiple times before they stream freely into the detector. If the collision energy is lower, instantly after the passing of the nuclei a hot hadron gas is produced, which can also have temperatures of $T \lesssim 160$ GeV [131]. The characterization of the hot medium often relies on the local rest frame temperature T , which can be obtained by thermal fits [132] or through hydrodynamic simulations [56–59]. Also the flow velocity is computed by hydrodynamics. More information about the fundamental properties of the hot matter lies in its transport coefficients, such as viscosities (shear and bulk viscosity) and conductivities (heat conductivity or conductivities of conserved charges). As material constants, they are interesting by themselves to characterize the hot matter produced in hadronic collisions, and should in principle be calculable from first principles, i.e., the QCD Lagrangian. They depend strongly on the degrees of freedom and their mutual interactions as well as the temperature. One expects extrema at the phase transition [75]. To this end, the temperature dependence is important. Those transport coefficients are furthermore popular quantities employed in order to compare effective models and it is also customary to use them as fit parameters in dynamical models, such as hydrodynamics [56–59] or Langevin transport [133,134]. In the past, the shear viscosity over entropy ratio η/s was the prime coefficient as it has a dominant influence in dissipative hydrodynamic calculations [60,135]. Since the advent of precision modeling of heavy-ion collisions, also the bulk viscosity has gained increasing interest [136–143].

The influence of magnetic fields in the evolution of QGP has drawn attention to the electric conductivity; several studies on the lattice [144–149], in perturbative QCD (pQCD) [68,69,150,151], Dyson-Schwinger calculations [152] and other theories [153–155] have been carried out. Most of these calculations aim at the value of σ_{el} in the QGP phase, some extend below the transition temperature towards the HG. In general, the results differ over several orders of magnitude, and comparisons among different approaches are often intriguing. The electric conductivity can be related to the diffusion of magnetic fields in a medium [155–157] and the soft dilepton production rate [149,158,159] of a hot thermal medium. This is a measurable quantity, however, experimental constraints would e.g. require an accurate modeling of heavy-ion collisions, and the theoretical understanding of dilepton yields is still subject of ongoing research [113].

Apart from the electric conductivity, diffusion coefficients of QCD matter have been neglected thus far. In gaseous systems, density gradients will always generate diffusion currents, characterized by the diffusion constant and the gradient. As for the baryon diffusion coefficients, apart from the holographic calculation in Ref. [160], and simple relaxation time estimates [161,162], to our knowledge, not much was known about its magnitude or temperature dependence. For other conserved quantities, such as strangeness or electric

charge, even less work had been done. Diffusion coefficients will be very important input in hydrodynamic calculations including conserved currents. Those models are needed to explain current and future low energy collision systems, where the baryon chemical potential, and, possibly, also strange and electric chemical potential is large.

In this chapter we begin with a sketch of the calculation of the electric conductivity in the QGP phase applying pQCD, which summarizes the results from Ref. [150]. Next, we present a calculation of the electric conductivity in a realistic hadron gas model in detail. Large parts of this calculation and results were published in Ref. [1]. The following section deals with diffusion processes, where we focus on cross-diffusion among different charge types, such as electric, baryon and strange charges. We apply the developed formalism to diffusion processes, and compute the full diffusion matrix of baryon, strangeness and electric diffusion in the HG and QGP, for several values of baryon chemical potential. Those results were published in Ref. [2].

2.1. Electric conductivity of the QGP

The strongly interacting weakly coupled quark-gluon plasma has a typical shear viscosity to entropy ratio η/s close to the theoretical lower bound in AdS/CFT, $\eta/s = 1/(4\pi)$. This is the result of many theoretical studies, see the compilation in Fig. 1.5. Such extreme matter is expected to also show a very small electric conductivity. The longitudinal static electric conductivity σ_{el} relates the response of the electric current¹ \vec{j} to the externally applied static electric field \vec{E} ,

$$\vec{j} = \sigma_{\text{el}} \vec{E}. \quad (2.1)$$

At very high collision energies of interacting particles, or very high temperatures in thermal systems, perturbative QCD (pQCD) is a good approximation of QCD. However, owing to the lack of alternative methodology, it is customary to extrapolate pQCD down to temperatures close to the quark-hadron phase transition. In Ref. [150] we use pQCD scattering matrix elements (NLO in the scattering vertices) within the full collision term of the Boltzmann equation to extract estimates of the electric conductivity of the QGP. This numerical study (within the transport approach BAMPS) uses two different Monte-Carlo methods in a thermal system of massless quarks and gluons. The result is shown in Fig. 2.1, where we compare to different other results (see references in the caption). Clearly, the running of the strong coupling constant $\alpha_s(Q^2)$ is responsible for the temperature dependence of σ_{el}/T , whereas the inclusion of radiative processes ($2 \leftrightarrow 3$) decreases the overall conductivity. In general, the perturbative result is larger than most other results, especially those from the lattice. We refer to Ref. [150] for more details to the calculation.

2.2. Electric conductivity of the hot hadron gas

In the HG there has been so far no analytic computation of the electric conductivity from pure kinetic theory, this is what we will provide in this work.

Extending the analytic developments from Refs. [72, 169, 170], we investigated how an equilibrated relativistic gas of electrically charged particles, governed by the BE, behaves upon the influence of a small, static, electric field that is turned on. Assuming that the total system is electrically neutral, naturally an electric current will develop and eventually reach a static value (in an infinitely large system or setting periodic boundary conditions). We can thereby compute σ_{el} for a given set of (massive or massless) particle species in the

¹More precise, the electrically charged particle diffusion current density

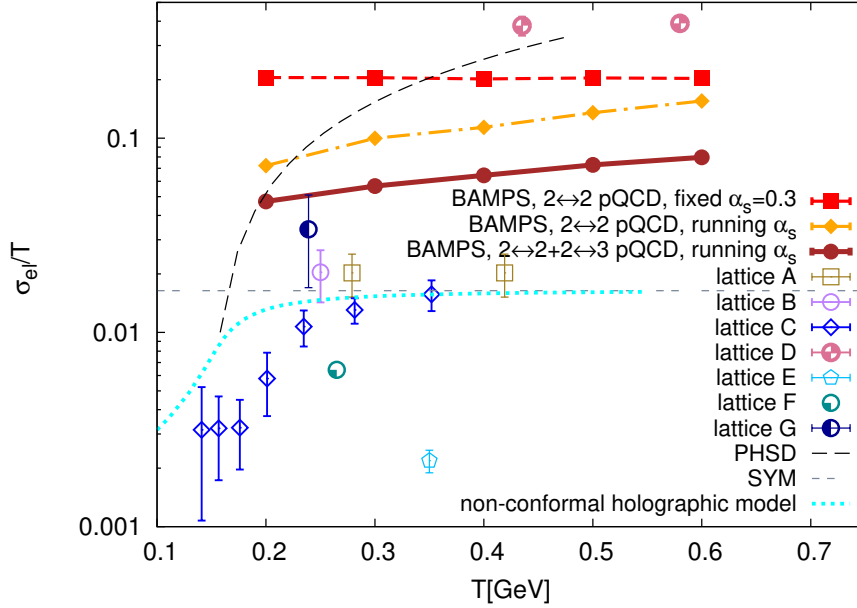


Figure 2.1.: Figure reproduced from Ref. [150]. Numerical results for the electric conductivity from BAMPS [150] (filled symbols) compared to recent results from literature. The open symbols represent results from lattice QCD. PHSD: [163], SYM: [164], non-conformal holographic model: [154], lattice A: [165], lattice B: [166], lattice C: [167], lattice D: [144], lattice E: [145], lattice F: [146], lattice G: [168]. The electric charge is explicitly multiplied out, $e^2 = 4\pi/137$. Around $T = 0.3$ GeV results from Ref. [152] (not shown), using a Dyson-Schwinger approach, are consistent with the results from Ref. [167].

system and the given set of their mutual, elastic, collision cross section. In this study we restrict ourselves on classical statistics. This is basically an extension to the well-known Drude formula for the electric conductivity (see Sec. 2.2.3) for a hadron resonance gas.

We investigate the influence of masses, average total cross sections, and different species. We finally state the temperature dependent electric conductivity of a hadron gas with well justified approximations. Indeed, the framework can give a very precise answer from kinetic theory for any (charge neutral) elastic particle system, and is not restricted to the results considered here.

In Sec. 2.2.1 we give basic definitions regarding the relativistic formulation for the fluid dynamical quantities. In Sec. 2.2.2 we derive the algorithm for the computation of the conductivity from linear response, and continue in Sec. 2.2.4 with our results. First, we reproduce previously published numerical results and show the convergence of the method in Sec. 2.2.5, then we show the influence of masses systematically in Sec.2.2.5, followed by the results for a realistic Pion gas in Sec. 2.2.5, a Pion-Nucleon-Kaon gas with fixed cross sections (Sec. 2.2.5) and realistic cross sections (Sec. 2.2.5).

2.2.1. Basic definitions

We consider a dilute gas consisting of N_{species} particle species, with the i -th particle species having electric charge q_i and degeneracy g_i . This system is in the presence of an external electromagnetic field, given by an electromagnetic field strength $F^{\mu\nu}$, and its net-electric charge density is assumed to be approximately zero at all space-time points. The state of the system is characterized by the single particle distribution function of each parti-

cle species, $f_i(x, p)$. The time evolution equation satisfied by $f_i(x, p)$ is the Boltzmann equation, which we repeat here for clarity,

$$k^\mu \frac{\partial}{\partial x^\mu} f_{\mathbf{k}}^i + k_\nu q_i F^{\mu\nu} \frac{\partial}{\partial k^\mu} f_{\mathbf{k}}^i = \sum_{j=1}^{N_{\text{species}}} C_{ij}(x^\mu, k^\mu), \quad (2.2)$$

where C_{ij} is the collision term, that will be specified later in this work. Since our goal is to calculate the electric conductivity of this system, we shall consider the case of a homogeneous, but time-dependent electric field.

The energy-momentum tensor and net electric charge four-current are expressed as the following momentum integrals of the single-particle distribution function

$$T^{\mu\nu} = \sum_{i=1}^{N_{\text{species}}} \langle k^\mu k^\nu \rangle_i, \quad N_q^\mu = \sum_{i=1}^{N_{\text{species}}} q_i \langle k^\mu \rangle_i, \quad (2.3)$$

where we employ the following notation

$$\langle \dots \rangle_i \equiv g_i \int \frac{d^3 k}{(2\pi)^3 k^0} (\dots) f_{\mathbf{k}}^i. \quad (2.4)$$

These currents are associated to conserved quantities and satisfy the continuity equations, $\partial_\mu T^{\mu\nu} = 0$ and $\partial_\mu N_q^\mu = 0$. Here we also refer the interested reader to the later section about hydrodynamics, Sec. 4.1.

It is convenient to decompose $T^{\mu\nu}$ and N_q^μ in terms of the fluid's collective velocity field, u^μ . Without loss of generality, these currents are re-expressed as

$$T^{\mu\nu} = \epsilon u^\mu u^\nu - \Delta^{\mu\nu} (P_0 + \Pi) + \pi^{\mu\nu}, \quad (2.5)$$

$$N_q^\mu(x) = n_q u^\mu + j_q^\mu. \quad (2.6)$$

Above, we introduced the energy density ϵ , the thermodynamic pressure P_0 , the bulk viscous pressure Π , the shear stress tensor $\pi^{\mu\nu}$, the net electric charge density n_q , and the net electric charge diffusion current j_q^μ (which we will further investigate in Sec. 2.3). We also defined the spatial projector $\Delta^{\mu\nu} = g^{\mu\nu} - u^\mu u^\nu$ and employed Landau's definition of the fluid velocity as an eigenvector of $T^{\mu\nu}$ with eigenvalue ϵ , that is, $T^{\mu\nu} u_\nu = \epsilon u^\mu$. In this scheme, each new variable introduced is expressed by a given contraction/projection of the currents with u^μ and $\Delta^{\mu\nu}$,

$$\epsilon = u_\mu u_\nu T^{\mu\nu}, \quad P_0 + \Pi = -\frac{1}{3} \Delta_{\mu\nu} T^{\mu\nu}, \quad (2.7)$$

$$\pi^{\mu\nu} = \Delta_{\alpha\beta}^{\mu\nu} T^{\alpha\beta}, \quad n_q = u_\mu N_q^\mu, \quad j_q^\mu = N_q^{\langle\mu\rangle}. \quad (2.8)$$

For convenience, we adopt the notation $A^{\langle\mu\rangle} \equiv \Delta_\nu^\mu A^\nu$ and $A^{\langle\mu\nu\rangle} \equiv \Delta_{\alpha\beta}^{\mu\nu} A^{\alpha\beta}$. The latter definition used the double, traceless, symmetric projection operator $\Delta_{\alpha\beta}^{\mu\nu} = (\Delta_\alpha^\mu \Delta_\beta^\nu + \Delta_\alpha^\nu \Delta_\beta^\mu)/2 - \Delta^{\mu\nu} \Delta_{\alpha\beta}/3$. Since our goal will be to compute the electric conductivity coefficient of a gas, most of the dissipative currents introduced above will play no role in our calculation. Nevertheless, we introduced them above for the sake of completeness.

We can define a temperature and chemical potential for this system using the traditional matching conditions,

$$\epsilon = \epsilon^{\text{eq}}(T, \mu_q), \quad n_q = n_q^{\text{eq}}(T, \mu_q). \quad (2.9)$$

where ϵ^{eq} and n_q^{eq} are the energy density and net electric charge density of a system in thermodynamic equilibrium with temperature T and chemical potential μ_q . The values

of temperature and chemical potential must be inverted from the above equations. With these definitions, we can introduce the local equilibrium distribution function for Boltzmann statistics,

$$f_{0,\mathbf{k}}^i = g_i \exp(-u_\mu k^\mu / T + q_i \mu_q / T), \quad (2.10)$$

and the deviation from equilibrium $\delta f_{\mathbf{k}}^i = f_{\mathbf{k}}^i - f_{0,\mathbf{k}}^i$, where, $\mu_i = q_i \mu_q$ is the chemical potential of the i -th species. Momentum integrals over these distribution functions will be expressed using the following notation

$$\langle \dots \rangle_{i,0} \equiv g_i \int \frac{d^3 k}{(2\pi)^3 k^0} (\dots) f_{0,\mathbf{k}}^i, \quad \langle \dots \rangle_{i,\delta} \equiv g_i \int \frac{d^3 k}{(2\pi)^3 k^0} (\dots) \delta f_{\mathbf{k}}^i. \quad (2.11)$$

The electric net charge diffusion current then is (omitting the index q for now)

$$j^\mu \equiv N_q^{(\mu)} = \Delta_\nu^\mu \sum_{i=1}^{N_{\text{species}}} q_i \langle k^\nu \rangle_{i,\delta}. \quad (2.12)$$

2.2.2. Linear response to the electric field

The scenario we want to consider here is that of a thermal 'brick' of matter, in which the temperature $T \equiv \beta_0^{-1}$ and chemical potential $\mu_q \equiv \alpha_0^q / \beta_0$ do not vary in space nor time. We generalize the methods proposed in [72, 170, 171] to calculate retarded Green's function associated to the response of a multi-component system to an external electric field. We present the general calculation first, using the full linearized collision term, and show afterwards that the formalism reduces to the well-known Drude formula in the relaxation time approximation. In all remaining computations we use the full linearized collision term.

2.2.3. General calculation with linearized collision term

We consider a system initially in thermal equilibrium, with $f_{\mathbf{k}}^i = f_{0,\mathbf{k}}^i$ and $F^{\mu\nu} = 0$. We then suddenly turn on a small external electric field. No external magnetic fields are present and we neglect the effect of any induced field. The distribution function acquires an off-equilibrium part, $f_{\mathbf{k}}^i = f_{0,\mathbf{k}}^i + \delta f_{\mathbf{k}}^i$, and the field strength tensor becomes

$$F^{\mu\nu} \rightarrow \delta F^{\mu\nu} = E^\mu u^\nu - E^\nu u^\mu, \quad (2.13)$$

where $E^\mu = u_\nu F^{\mu\nu}$ is the electric field. We write down the linearized BE (similar to [72]), neglecting any term that is second order in δf , $\delta F^{\mu\nu}$, or their product,

$$k^\mu \frac{\partial}{\partial x^\mu} f_{0,\mathbf{k}}^i + k^\mu \frac{\partial}{\partial x^\mu} \delta f_{\mathbf{k}}^i + k_\nu q_i \delta F^{\mu\nu} \frac{\partial}{\partial k^\mu} f_{0,\mathbf{k}}^i = \sum_{j=1}^{N_{\text{species}}} C_{ij}^{(l)}(x^\mu, k^\mu), \quad (2.14)$$

with $C_{ij}^{(l)}(x^\mu, k^\mu)$ being the linearized collision term. Without loss of generality, we carry out all computations in the local rest frame of the fluid, $u^\mu = (1, 0, 0, 0)$. Since E^μ is orthogonal to the velocity, $u_\mu E^\mu = 0$, we replace $k_\nu E^\nu \rightarrow k_{\langle\nu} E^{\nu\rangle}$. Then we have

$$k^\mu \frac{\partial}{\partial x^\mu} \delta f_{\mathbf{k}}^i + \frac{q_i}{T} f_{0,\mathbf{k}}^i k_{\langle\nu} E^{\nu\rangle} = \sum_{j=1}^{N_{\text{species}}} C_{ij}^{(l)}(x^\mu, k^\mu). \quad (2.15)$$

The linearized collision term can be written as an operator \hat{C} acting on δf ,

$$C_{ij}^{(l)}(x^\mu, k^\mu) \equiv \hat{C} \delta f_{\mathbf{k}}^i = \int dK' dP dP' \gamma_{ij} W_{\mathbf{k}\mathbf{k}' \rightarrow \mathbf{p}\mathbf{p}'}^{ij} f_{0,\mathbf{k}}^i f_{0,\mathbf{k}'}^j \left(\frac{\delta f_{\mathbf{p}}^i}{f_{0,\mathbf{p}}^i} + \frac{\delta f_{\mathbf{p}'}^j}{f_{0,\mathbf{p}'}^j} - \frac{\delta f_{\mathbf{k}}^i}{f_{0,\mathbf{k}}^i} - \frac{\delta f_{\mathbf{k}'}^j}{f_{0,\mathbf{k}'}^j} \right) \quad (2.16)$$

where we use the notation $dK \equiv d^3k / [(2\pi)^3 k^0]$, $\gamma_{ij} = 1 - 1/2\delta_{ij}$ and $W_{\mathbf{k}\mathbf{k}' \rightarrow \mathbf{p}\mathbf{p}'}^{ij} = s\sigma_{ij}(s, \Theta)(2\pi)^6 \delta^{(4)}(k^\mu + k'^\mu - p^\mu - p'^\mu)$. Above, we only considered elastic 2-to-2 collisions. The total cross section $\sigma_{\text{tot},ij}(s)$ is related to the differential cross section $\sigma_{ij}(s, \Theta)$ in the following way,

$$\sigma_{\text{tot},ij}(s) = 2\pi\gamma_{ij} \int d\Theta \sin \Theta \sigma_{ij}(s, \Theta), \quad \cos \Theta = \frac{(k - k')(p - p')}{(k - k')^2}, \quad s = (k + k')^2. \quad (2.17)$$

We take the Fourier transform of the Eq. (2.15), and divide it by the energy $E_{\mathbf{k}} = \sqrt{\mathbf{k}^2 + m^2}$, leading to the following equation for the Fourier transform of the non-equilibrium distribution function, $\delta \tilde{f}_{\mathbf{k}}^i$,

$$\begin{aligned} -i\omega \delta \tilde{f}_{\mathbf{k}}^i + i \frac{\mathbf{k}}{E_{\mathbf{k}}} \cdot \mathbf{q} \delta \tilde{f}_{\mathbf{k}}^i - \sum_{j=1}^{N_{\text{species}}} \frac{1}{E_{\mathbf{k}}} \hat{C}_{ij} \delta \tilde{f}_{\mathbf{k}}^j &= -\frac{q_i}{T E_{\mathbf{k}}} f_{0,\mathbf{k}}^{i(\nu)} \tilde{E}_\nu \\ \Rightarrow \delta \tilde{f}_{\mathbf{k}}^i &= -\frac{1}{T} \frac{q_i}{-i\omega + i \frac{\mathbf{k}}{E_{\mathbf{k}}} \cdot \mathbf{q} - \sum_{j=1}^{N_{\text{species}}} \frac{1}{E_{\mathbf{k}}} \hat{C}_{ij}} f_{0,\mathbf{k}}^{i(\nu)} \frac{k^{(\nu)}}{E_{\mathbf{k}}} \tilde{E}_\nu, \end{aligned} \quad (2.18)$$

where \tilde{E}_ν is the Fourier transform of E_ν and the last equation is the formal solution for the distribution function in Fourier space. Using the formal solution derived for $\delta \tilde{f}_{\mathbf{k}}^i$ in Eq. (2.18), we can express the Fourier transform of the net electric charge current in the following simple form

$$\tilde{j}^\mu = - \sum_{i=1}^{N_{\text{species}}} \frac{q_i}{T} \int dK k^{(\mu)} \frac{q_i}{-i\omega + i \frac{\mathbf{k}}{E_{\mathbf{k}}} \cdot \mathbf{q} - \sum_{j=1}^{N_{\text{species}}} \frac{1}{E_{\mathbf{k}}} \hat{C}_{ij}} f_{0,\mathbf{k}}^{i(\nu)} \frac{k^{(\nu)}}{E_{\mathbf{k}}} \tilde{E}_\nu \equiv \tilde{G}_R^{\mu\nu}(\omega, \mathbf{q}) \tilde{E}_\nu, \quad (2.19)$$

where we introduced the retarded Green's Function $\tilde{G}_R^{\mu\nu}(\omega, \mathbf{q})$.

In order to compute the static electric conductivity, it will be enough to compute the retarded Greens function $\tilde{G}_R^{\mu\nu}(\omega, \mathbf{q})$ at vanishing frequency and wavenumber, $\tilde{G}_R^{\mu\nu}(0, \mathbf{0})$. For this purpose, we introduce a vector $B_i^\alpha(Q, K_i)$, which satisfies the following integro-differential equation

$$\left[-i\omega + i \frac{\mathbf{k}}{E_{\mathbf{k}}} \cdot \mathbf{q} - \sum_{j=1}^{N_{\text{species}}} \frac{1}{E_{\mathbf{k}}} \hat{C}_{ij} \right] B_i^\alpha(Q, K_i) = q_i f_{0,\mathbf{k}}^i \frac{k^{(\alpha)}}{E_{\mathbf{k}}}. \quad (2.20)$$

Once B^α is known, the solution for $\tilde{G}_R^{\mu\nu}(\omega, \mathbf{q})$ follows trivially as

$$\tilde{G}_R^{\mu\nu}(\omega, \mathbf{q}) = - \sum_{i=1}^{N_{\text{species}}} \frac{q_i}{T} \int dK k^{(\mu)} B_i^{(\nu)}(Q, K_i). \quad (2.21)$$

Strictly speaking, B^α is a general function of $Q = (\omega, \mathbf{k})$, however, since we will need it only at vanishing Q , it is sufficient to only consider its dependence on the 4-momentum K , that is, $B_i^\alpha(Q = 0, K_i)$. We know that $B_i^\alpha(K)$ is a 4-vector orthogonal to u^μ and its tensor structure must be constructed from combinations of u^μ , k^μ , and $g^{\mu\nu}$. Therefore, it must be a tensor of the following form, $B_i^\alpha(K) \sim k^{(\alpha)}$, with the proportionality factors

being functions of the scalars μ_q , T , and $E_{\mathbf{k}}$. It is convenient to express it as an expansion in powers of the energy,

$$B_i^\alpha(K) = f_{0,\mathbf{k}}^i k^{(\alpha)} \sum_{n=0}^{\infty} a_n^{(i)} E_{\mathbf{k}}^n, \quad (2.22)$$

where $a_n^{(i)}$ are the expansion coefficients. Using the well-known relation

$$\int dK k^{(\mu)} k^{(\nu)} E_{i,\mathbf{k}}^n f_{0,\mathbf{k}}^i = \frac{1}{3} \Delta^{\mu\nu} \int dK E_{\mathbf{k}}^n f_{0,\mathbf{k}}^i \Delta_{\alpha\beta} k^\alpha k^\beta, \quad (2.23)$$

together with Eqs. (2.21) and (2.22), it is possible to express the retarded Green's function in terms of the coefficients $a_n^{(i)}$,

$$\tilde{G}_R^{\mu\nu}(0, \mathbf{0}) = -\Delta^{\mu\nu} \sum_{i=1}^{N_{\text{species}}} \sum_{n=0}^{\infty} \frac{q_i}{3T} a_n^{(i)} \int dK f_{0,\mathbf{k}}^i E_{\mathbf{k}}^n \Delta_{\alpha\beta} k^\alpha k^\beta \equiv \Delta^{\mu\nu} \tilde{G}_R. \quad (2.24)$$

Above, we defined the scalar retarded Green's function

$$\tilde{G}_R = - \sum_{i=1}^{N_{\text{species}}} \sum_{n=0}^{\infty} \frac{q_i}{3T} a_n^{(i)} \int dK E_{\mathbf{k}}^n (\Delta_{\mu\nu} k^\mu k^\nu) f_{0,\mathbf{k}}^i,$$

which can be used to express the linear relation between current and driving electric field at $Q = 0$ as

$$\tilde{j}^\mu = \tilde{G}_R \tilde{E}^\mu.$$

The above relation allows us to identify the electric conductivity as $\sigma_{\text{el}} \equiv \tilde{G}_R$.

Naturally, the expansion (2.22) must be truncated at some point and we will discuss the convergence of our results to the order of the truncation. We note that, even at the lowest possible order of truncation, the resulting transport coefficients are expected to be accurate up to 10 %, see, e.g., [169, 172]. Our next step is the determination of the expansion coefficients $a_n^{(i)}$. Multiplying Eq. (2.20) with $E_{\mathbf{k}}^m k^{(\beta)}$ and integrating over momentum we get an equation for $a_n^{(i)}$,

$$\sum_{n=0}^{\infty} \int dK_i E_{\mathbf{k}}^{m-1} k^{(\beta)} \left[- \sum_{j=1}^{N_{\text{species}}} \hat{C}_{ij} f_{0,\mathbf{k}}^j E_{\mathbf{k}}^n k^{(\alpha)} a_n^{(i)} \right] = q_i \int dK_i E_{\mathbf{k}}^{m-1} k^{(\alpha)} k^{(\beta)} f_{0,\mathbf{k}}^i.$$

Using straightforward manipulations of this equation and the above definition of the collision term, Eq. (2.16), we can rewrite it in the following form,

$$\sum_{n=0}^{\infty} \sum_{j=1}^{N_{\text{species}}} [\mathcal{A}_{mn}^i \delta^{ij} + \mathcal{C}_{mn}^{ij}] a_n^{(j)} = b_m^i, \quad (2.25)$$

where we defined

$$\begin{aligned} \mathcal{A}_{mn}^i &= \sum_{j=1}^{N_{\text{species}}} \int dK_i dK_j' dP_i dP_j' \gamma_{ij} W_{\mathbf{k}\mathbf{k}' \rightarrow \mathbf{p}\mathbf{p}'}^{ij} f_{0,\mathbf{k}}^i f_{0,\mathbf{k}'}^j E_{i,\mathbf{k}}^{m-1} k^{(\alpha)} \left(E_{i,\mathbf{p}}^n p^{(\alpha)} - E_{i,\mathbf{k}}^n k^{(\alpha)} \right), \\ \mathcal{C}_{mn}^{ij} &= \int dK_i dK_j' dP_i dP_j' \gamma_{ij} W_{\mathbf{k}\mathbf{k}' \rightarrow \mathbf{p}\mathbf{p}'}^{ij} f_{0,\mathbf{k}}^i f_{0,\mathbf{k}'}^j E_{i,\mathbf{k}}^{m-1} k^{(\alpha)} \left(E_{j,\mathbf{p}'}^n p'^{(\alpha)} - E_{i,\mathbf{k}'}^n k'^{(\alpha)} \right), \\ b_m^i &= q_i \int dK E_{\mathbf{k}}^{m-1} (-\Delta^{\mu\nu} k_\mu k_\nu) f_{0,\mathbf{k}}^i. \end{aligned} \quad (2.26)$$

For later use we denote the above matrix in particle species space and expansion space as

$$\mathcal{N}_{mn}^{ij} \equiv \mathcal{A}_{mn}^i \delta^{ij} + \mathcal{C}_{mn}^{ij}. \quad (2.27)$$

Note that there is no sum over i implied. The Landau matching condition can also be expressed as

$$\Delta_\nu^\lambda u_\mu T^{\mu\nu} = \sum_{i=1}^{N_{\text{species}}} \int dK u_\nu k^\nu k^{\langle\mu} \delta f_{\mathbf{k}}^i = -\frac{1}{3T} \sum_{i=1}^{N_{\text{species}}} \sum_{n=0}^{\infty} a_n^{(i)} \int dK f_{0,\mathbf{k}}^i E_{\mathbf{k}}^{n+1} (\Delta^{\alpha\beta} k_\alpha k_\beta) \tilde{E}^\mu = 0.$$

Since this should be true for any electric field and any of its components, we obtain a constraint that must be satisfied by the coefficients $a_n^{(i)}$,

$$\begin{aligned} \sum_{i=1}^{N_{\text{species}}} \sum_{n=0}^{\infty} a_n^{(i)} \left[\int dK f_{0,\mathbf{k}}^i E_{\mathbf{k}}^{n+1} (\Delta^{\alpha\beta} k_\alpha k_\beta) \right] &= 0 \\ \Rightarrow \sum_{i=1}^{N_{\text{species}}} \sum_{n=0}^{\infty} a_n^{(i)} d_n^i &= 0 \quad \text{with} \quad d_n^i \equiv \int dK f_{0,\mathbf{k}}^i E_{\mathbf{k}}^{n+1} (\Delta^{\alpha\beta} k_\alpha k_\beta). \end{aligned} \quad (2.28)$$

Solving the integrals in Eq. (2.26) for a given set of species and cross sections allows us to obtain the unknown coefficients $a_n^{(i)}$ by inverting the matrix $\mathcal{A}_{mn}^i \delta^{ij} + \mathcal{C}_{mn}^{ij}$ along with condition (2.28). In practice, this amounts to removing one line and column from the matrix \mathcal{N}_{mn}^{ij} .

Relaxation time limit

Nonrelativistically, the Drude formula for the electric conductivity $\sigma_{\text{el,nr}}$ of a single charge carrying species (e.g. electrons) with charge q_e , density n_e and mass m_e reads [173]

$$\sigma_{\text{el,nr}} = \frac{n_e q_e^2 \tau}{m_e}, \quad (2.29)$$

where τ is the mean time between collisions of the charge carriers (e.g. electrons) with, e.g., atomic cores. The Boltzmann equation can be solved analytically in the relaxation time approximation, which corresponds to a simplistic model for the collision term,

$$p^\mu \partial_\mu f_q + q F^{\alpha\beta} p_\beta \frac{\partial f_q}{\partial p^\alpha} = -\frac{p^\mu u_\mu}{\tau} (f_q - f_{\text{eq},q}). \quad (2.30)$$

It allows for a straightforward calculation of the charged particle distribution f_q after applying an external electric field. The uncharged particle distribution remains thermal $f_{q=0} = f_{\text{eq},q=0}$ and is not affected by the electric field,

$$\sigma_{\text{el}} = \frac{1}{3T} \sum_{i=1}^{N_{\text{species}}} q_i^2 n_i \tau. \quad (2.31)$$

Here, τ is the mean time between collisions of particles, independent of the particle type; for more details, see, e.g., Ref. [150]. Using Eq. (2.21) with a relaxation time collision

operator we recover the relaxation time answer, Eq. (2.31), for the electric conductivity,

$$\begin{aligned}
\tilde{j}^\mu &= \sum_{i=1}^{N_{\text{species}}} \frac{(q_i)^2}{T} \int dK k^{(\mu)} \frac{1}{-\sum_{j=1}^{N_{\text{species}}} \hat{C}_{ij}} f_{0,\mathbf{k}}^i k^{(\nu)} \tilde{E}_\nu \\
&= \sum_{i=1}^{N_{\text{species}}} \frac{(q_i)^2}{T} \int dK k^{(\mu)} \frac{\tau}{E_{\mathbf{k}}} f_{0,\mathbf{k}}^i k^{(\nu)} \tilde{E}_\nu \\
&= \sum_{i=1}^{N_{\text{species}}} \frac{(q_i)^2 \tau}{3T} \left[\int dK \frac{1}{E_{\mathbf{k}}} (\Delta^{\alpha\beta} k_\alpha k_\beta) f_{0,\mathbf{k}}^i \right] \tilde{E}^\mu \\
&= \sum_{i=1}^{N_{\text{species}}} \frac{(q_i)^2 \tau}{3T} n_{0,i} \tilde{E}^\mu.
\end{aligned} \tag{2.32}$$

2.2.4. Results

Our main goal is to calculate the electric conductivity of a hadron gas characterized by (measured) hadron-hadron cross sections (e.g. Breit-Wigner peaked resonances). In practice we have to limit the calculation to the dominant hadron species, such as pions, protons, neutrons, kaons. To understand the results and to cross check our method, we work systematically and include more species, masses and cross sections step-by-step. The use of simplified hadronic cross sections is common practise, e.g. in Ref. [174] the authors model a multicomponent hadron gas with species dependent constant cross sections in order to compute shear viscous phase space corrections. The authors of Ref. [72] compute the hadronic shear viscosity over entropy ratio using different constant cross sections for meson-meson, meson-baryon and baryon-baryon scattering.

2.2.5. Massless particles and constant isotropic cross sections

As a first step, we compute the electric conductivity for a massless gas of charged and uncharged particles, colliding with a fixed value of the cross section σ_{tot} , which is assumed to be constant. We give the result for the matrix in Eq. (2.27), which we truncate at $n = 2$. We define $\bar{n}_{ij} = (\delta_{ij} n_i n_T - n_i n_j)$, with $n_T = \sum_i^{N_{\text{species}}} n_i$ being the total particle density. The matrix is

$$\begin{aligned}
\mathcal{N}_{mn}^{ij} &= \begin{pmatrix} \mathcal{N}_{00}^{ij} & \mathcal{N}_{10}^{ij} & \mathcal{N}_{12}^{ij} \\ \mathcal{N}_{10}^{ij} & \mathcal{N}_{11}^{ij} & \mathcal{N}_{12}^{ij} \\ \mathcal{N}_{20}^{ij} & \mathcal{N}_{21}^{ij} & \mathcal{N}_{22}^{ij} \end{pmatrix} \\
&= \sigma_{\text{tot}} \begin{pmatrix} \frac{15}{2} T^2 \bar{n}_{ij} & 36 T^3 \bar{n}_{ij} & 210 T^4 \bar{n}_{ij} \\ 36 T^3 \bar{n}_{ij} & T^4 (216 \delta_{ij} n_i n_T - 192 n_i n_j) & T^5 (1520 \delta_{ij} n_i n_T - 1240 n_i n_j) \\ 210 T^4 \bar{n}_{ij} & T^5 (1520 \delta_{ij} n_i n_T - 1240 n_i n_j) & T^6 (12510 \delta_{ij} n_i n_T - 8850 n_i n_j) \end{pmatrix}.
\end{aligned} \tag{2.33}$$

This is the key information to obtain the electric conductivity at order $0 + 1 + 2$ in the above energy expansion for arbitrary many massless particle species. In order to compare with previously published numerical solutions of the BE, we give the explicit result for a gas of seven species, with electric charges (in units of e) $q_{1,3} = 1/3, q_{2,4} = -1/3, q_5 = 2/3, q_6 = -2/3, q_7 = 0$ and degeneracys $g_{1,2,3,4,5,6} = 6, g_7 = 16$, which mimic a quark-gluon

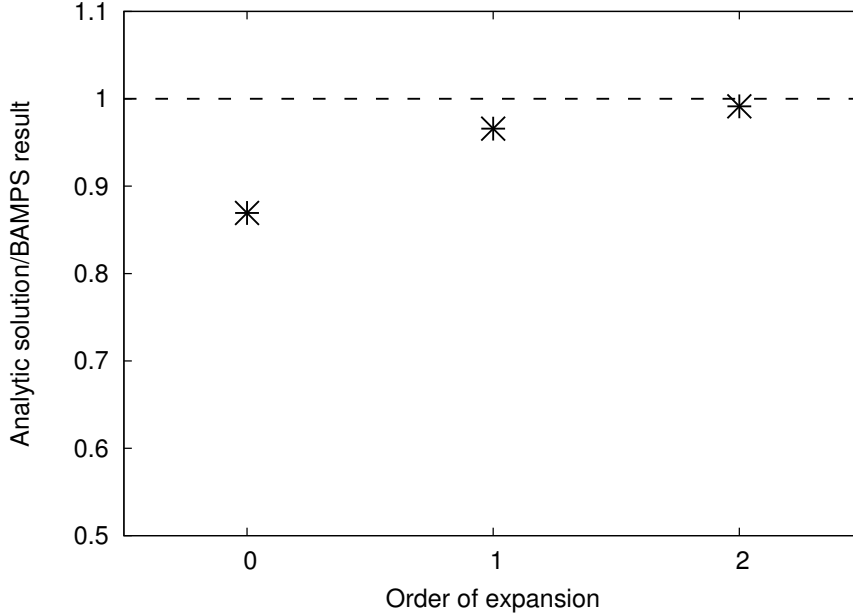


Figure 2.2.: Convergence of the analytical computation for the electric conductivity for a massless quark-gluon gas towards the numerical value obtained by the partonic cascade BAMPS [150].

plasma. Using that $e^2 = 4\pi/137$, and considering a cross section of $\sigma_{\text{tot}} = 3 \text{ mb}$, we obtain the following value of conductivity for this system,

$$\sigma_{\text{el}}/T = \frac{\text{const.}}{\sigma_{\text{tot}}} = \frac{0.000832737 \text{ GeV}^2}{T^2}. \quad (2.34)$$

In Ref. [150] the ultrarelativistic BE was solved for exactly this configuration (using the partonic cascade BAMPS), and the result matches the analytic computation of this paper, Eq. (2.34), by about 99%. By changing the order of the expansion, we show in Fig. 6.8, that the result converges for the considered order in expansion (truncation of the sum in Eq. (2.22) at $n = 2$).

Influence of masses to the electric conductivity

In order to see the influence of sizeable masses to the electric conductivity, we consider an arbitrary, simplified scenario for illustrative purposes. There are three species present, one species with charge +1, degeneracy 1, one with charge -1, degeneracy 1, and one with zero charge and degeneracy 9. All particles have masses, and we vary the ratio of the mass of the charged species with respect to the mass of the uncharged species. In Fig. 2.3 we show the results for the electric conductivity over temperature depending on this ratio, for different absolute values of the mass of the charged species. There we fix the cross section to an arbitrary value (10 mb) and set the temperature to be 140 MeV and the chemical potential is $\mu_q = 0$. This is a useful exercise to illustrate the mass dependence. In thermal and chemical equilibrium, lower mass particles are more abundant than higher mass particles, and one sees clearly the dependence of the electric conductivity to the number-density ratio of charged to uncharged particles. The electric conductivity is clearly very dependent on both the mass (or density) ratio of charged/uncharged species, and also on the mass (or density) of the charge carrying species. However, the precise values need to be computed (finally via numerical integration) as explained in Sec. 2.2.2.

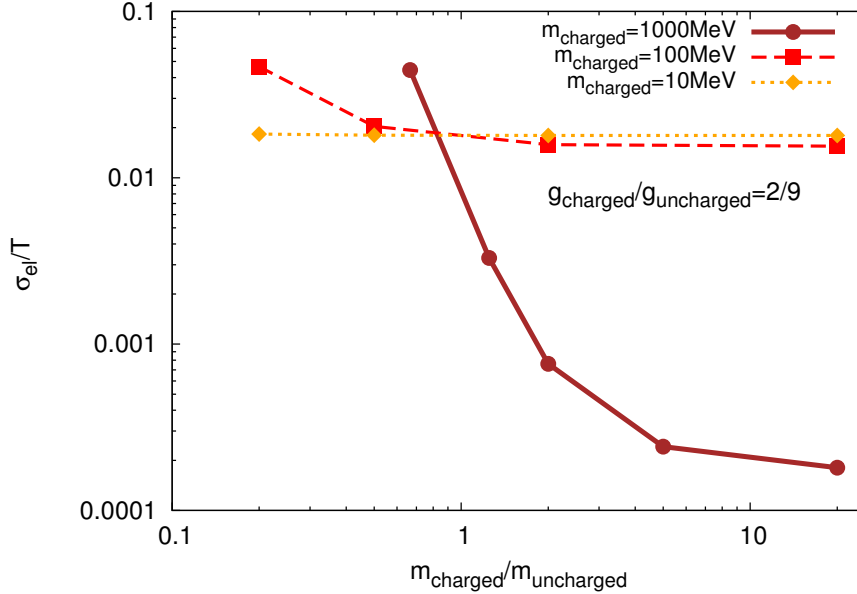


Figure 2.3.: The mass dependence of the electric conductivity for (three species of) interacting relativistic particles. The cross section was arbitrarily fixed to 10 mb, and the degeneracy ratio of charged/uncharged species is 2/9, the charges are $\pm 1, 0$. On the x-axis we vary the mass ratio of the charged to the uncharged species, and show results for different masses of the charged species. (color online)

Pion Gas

Pions are the most abundant hadrons in an equilibrated hadron gas. Therefore a pure pion gas can be considered a good starting point to understand some features of a realistic hadron gas. We set the chemical potential to zero for simplicity. Mainly, pions interact via the formation and decay of a ρ -resonance (see App. C.2). In the right panel of Fig. 2.4 we show three possible resonance cross sections. The blue solid curve includes all resonances as given in Ref. [175], whereas the gray dashed curve is a simple Breit-Wigner (BW) type parameterization, as well as the red dotted curve, which we adopt from Ref. [176]. The results from our calculation is given in the left panel of Fig. 2.4 for all three cross section parameterizations. Clearly, the two ρ -resonance parameterizations do not differ very much, however, the larger cross section which includes all resonances suppresses the conductivity strongly. The electric conductivity approaches a minimum below ~ 180 MeV. This can be physically motivated, as transport coefficients like the conductivity are expected to show a minimum in the QGP-hadron crossover region. This region is now believed to be in the vicinity of ~ 154 MeV [177]. Here we also compare to preliminary results from the hadronic transport model “Simulating Many Accelerated Strongly interacting Hadrons” (SMASH) [176]. This calculation applies the Green-Kubo formalism in an equilibrium setup. The agreement is good, but not entirely perfect. This may be attributed to some numerical uncertainty. In Fig. 2.5(a) we show the result using the simple BW parameterization of the ρ meson and compare our results with the results from different groups. The brown dash-dotted line represents calculations using Chiral Perturbation Theory (ChPT) [155] and include only pions. The ChpT-based analysis uses the Green-Kubo formula to extract the conductivity from the spectral function, identifying the dominant diagrams in a low energy and low temperature expansion and implementing unitarity of the partial waves in

the thermal width. The temperature dependence of the results from ChPT is very similar to those found in our results, although the overall magnitude of our electric conductivity is about a factor of ~ 1.6 higher. The blue open diamonds are results obtained from lattice QCD calculation for an 2+1d anisotropic and unquenched lattice, Ref. [147]. However, the authors discuss that the lattice data especially around the phase transition should be treated with caution (see Ref. [147] for details). The grey dashed line is the result obtained in a conformal Super-Yang Mills plasma [164]. In Ref. [154, 160], the authors used a non-conformal, bottom up holographic model to compute the electric conductivity (cyan dotted line). The full orange diamonds are results from the pQCD-based partonic cascade BAMPS [150], employing a running coupling, leading order, Debye-screened pQCD interactions including elastic and inelastic (radiative) scattering of gluons, up, down and strange quarks.

Pion-Kaon-Nucleon Gas with constant cross sections

Constant isotropic cross sections are often used to compare different models or theories. In Fig. 2.5(b) we show results for the electric conductivity for a gas of pions (π^+, π^-, π^0 ; $m = 138$ MeV), Kaons (K^0, \bar{K}^0, K^+, K^- ; $m = 496$ MeV) and nucleons (p, \bar{p}, n, \bar{n} ; $m = 938$ MeV), all interacting with a constant cross section σ_{tot} . The chemical potential is again zero. We tune this cross section, in order to meet other calculations at the transition temperature from hadrons to the QGP. Strongly coupled theories and 2+1d non-quenched lattice require cross section values of 30 – 110 mb, whereas the pQCD-based partonic cascade BAMPS needs a value of ~ 3.5 mb. These numbers should be taken with care, as we are dealing here with an oversimplified scenario of effective average cross sections. Especially as one approaches the crossover region, this concept is questionable, however it allows to gain some understanding about the effective coupling strength of different theories. In Fig.2.5(b), the purple open circles include only pions, and uses $\sigma_{\text{tot}} = 30$ mb. By comparing with the red solid squares (all species), one sees the influence of other, heavier species. Also the temperature dependence changes slightly. This is due to the fact, that the ratio of densities of different species is temperature dependent, as the mass enters here as an additional scale. Different contributing massive species can thus result in different temperature behavior of the conductivity. We expect, that the inclusion of even more species, albeit not very abundant, may decrease the electric conductivity. This may be true even in the case of realistic s -dependent cross sections, cf. Sec. 2.2.5.

Pion-Kaon-Nucleon Gas with experimental cross sections

The presented calculation procedure becomes gradually more complicated as more particle species are included, with the final numerical integrations becoming rather tedious and time consuming. Furthermore, all cross sections among all species have to be known, something quite problematic in the hadronic zoo. In order to get a rough picture of the electric conductivity in a hadron gas, we use pions, kaons and nucleons as in the previous section, but include now as realistic cross sections as possible, as shown in Tab.2.1. Many of them are approximated by constant values, but we include different resonances. The $\pi + \pi$ scattering resonance is that from the right panel of Fig. 2.4 (simple BW), whereas all non constant resonances are taken from the Particle Data Group [6, 11], as shown in Fig. 2.6. The result for zero chemical potential is shown in Fig. 2.7. In order to get a handle on the uncertainty introduced by using approximated constant cross sections σ_{const} , we multiply these with a factor k , $\sigma_{\text{const.}} \rightarrow \sigma_{\text{const.}} k$, and vary $k = 0.5, 1, 2$. The change of the conductivity is visible but not dramatic.

As can be seen by comparing with Fig. 2.5(b), the overall magnitude in our case is

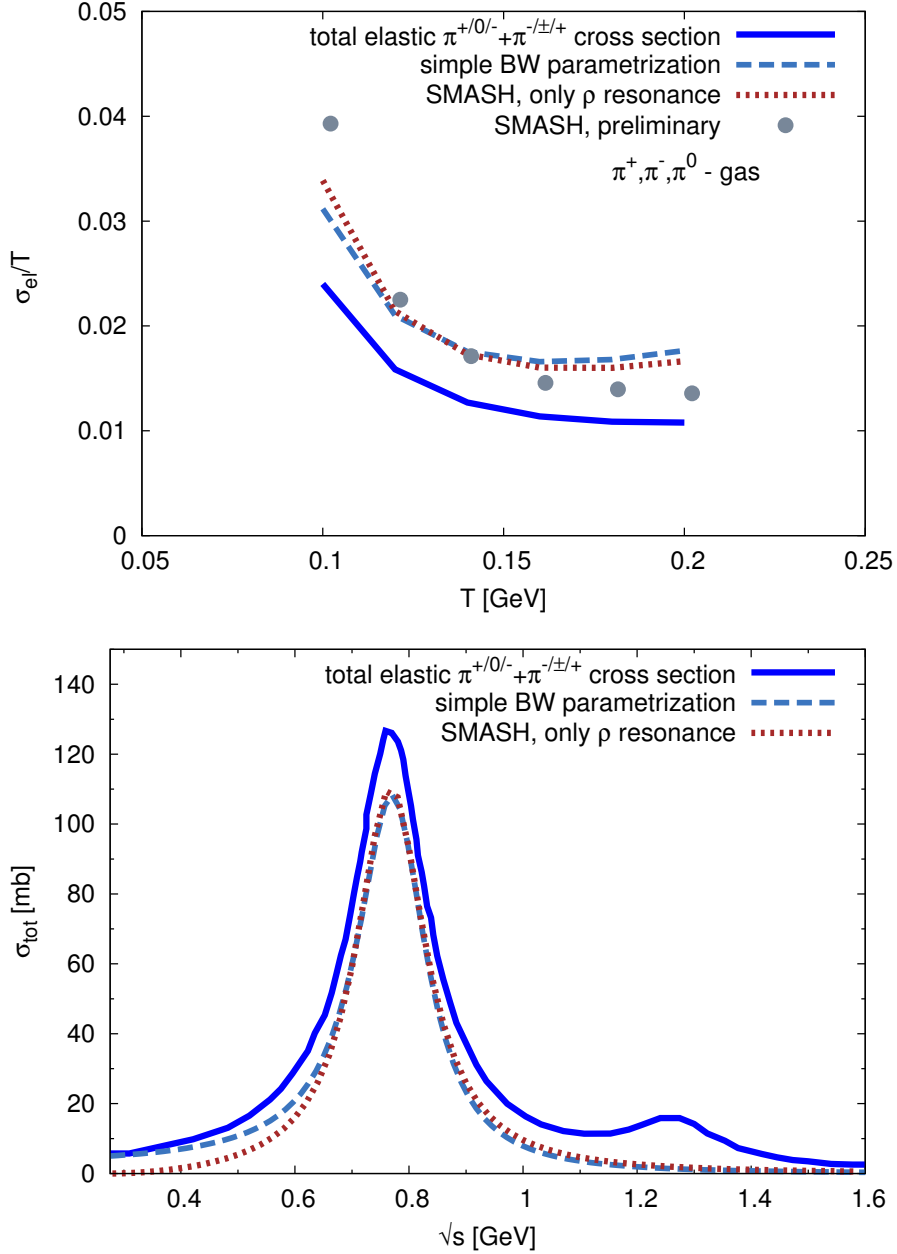
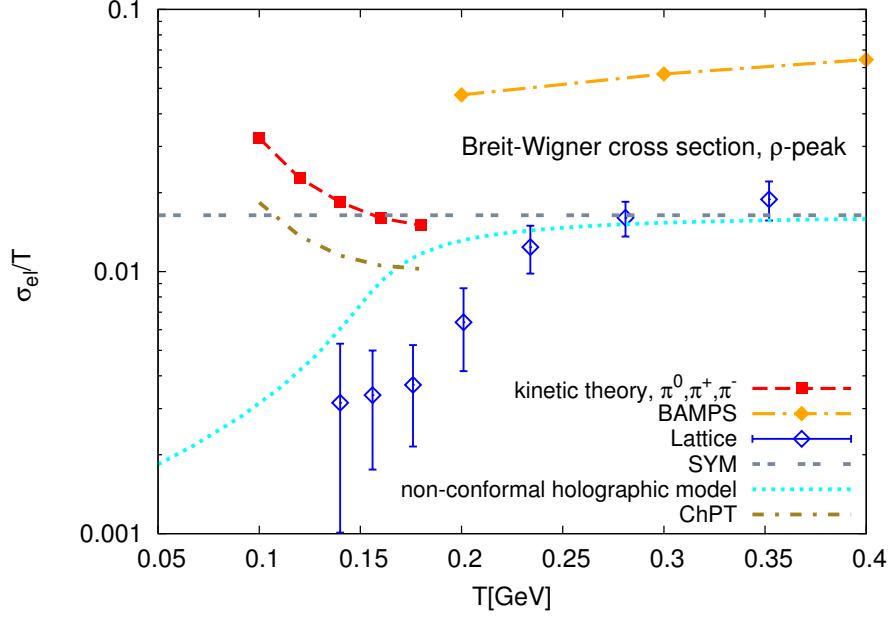


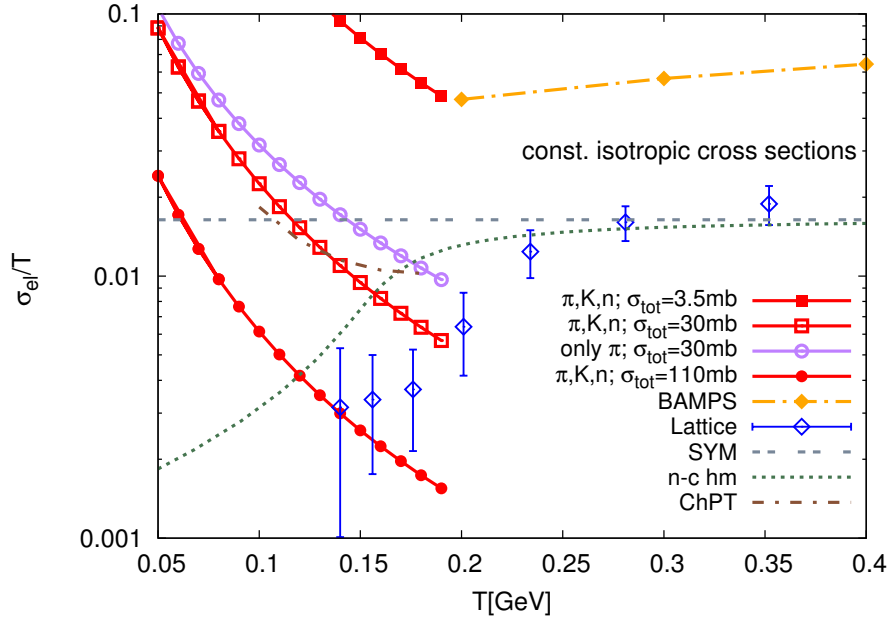
Figure 2.4.: Top: Results for the electric conductivity from this work including only pions, compared to preliminary Monte-Carlo results from a hadronic transport model Ref. [176]. Bottom: The three different resonance cross sections used for the lines in the left plot. SMASH uses the red dotted cross section parametrization with only the ρ resonance for the grey spheres in the left figure.

dominated by the constant cross section values, mostly ~ 10 mb in the important channels. Although results have to be taken with care due to the uncertainties in the cross sections, they are (to our knowledge) the first (semi-)analytic kinetic computation of the electric conductivity in the hadronic sector for multiple species.

In Fig. 2.7 we also compare to results from the Parton-Hadron-String Dynamics (PHSD) approach [163, 179] (open squares). PHSD is in the hadronic sector a covariant extension to the Boltzmann-Uehling-Uhlenbeck model [180]. The authors apply an electric current to the numerical simulation in thermal equilibrium and observe a static current in order to



(a) Interacting pion gas (red squares) in equilibrium for different temperatures. The pions interact via the ρ -resonance-scattering.



(b) The electric conductivity for interacting pions (π^+, π^-, π^0), Kaons (K^0, \bar{K}^0, K^+, K^-) and nucleons (p, \bar{p}, n, \bar{n}). The cross section σ_{tot} is constant and isotropic, and we show results for 4 different values. Results for a pure pion gas are shown for comparison.

Figure 2.5.: Results for the electric conductivity from this work and other theories. Parton transport BAMPS [150], Chiral Perturbation Theory ChPT [155], SYM theory [164], a non-conformal holographic model (n-c hm) [154] and lattice [147, 167] calculations are shown for comparison. These theories all require very different effective cross sections when compared to kinetic theory.

extract the electric conductivity. The hadronic sector contains several mesons and baryons

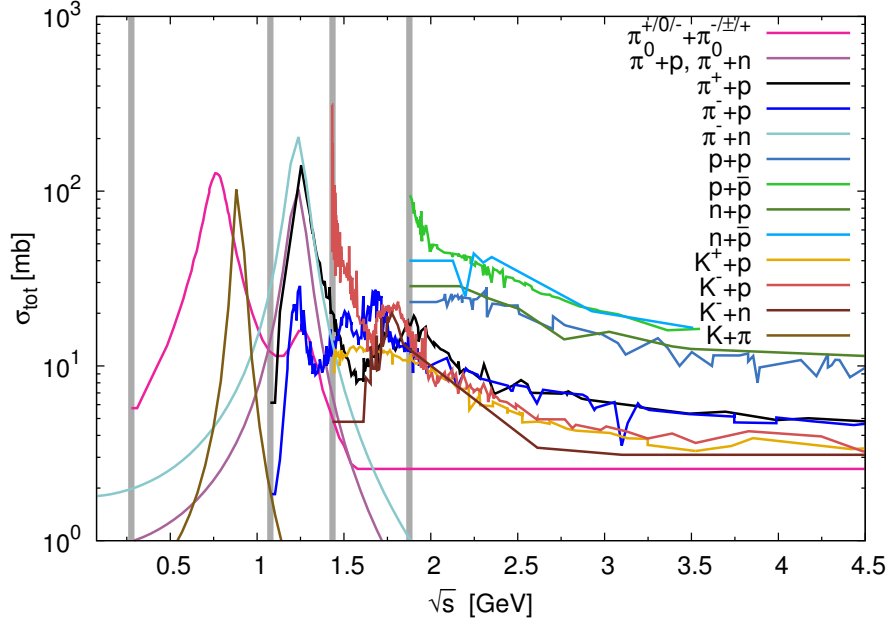


Figure 2.6.: The non constant cross sections which we use, involving at least one baryon. They are available from the Particle Data Group [6, 11]. The $\pi + K$, $\pi^0 + p$, n and the $\pi^- + n$ cross sections are simple parameterizations from Ref. [178]. For the numerical integrations, the curves are interpolated and sometimes extrapolated at the edges when the tables stop.

in mb	π^+	π^-	π^0	K^+	K^-	K^0	\bar{K}^0	p	n	\bar{p}	\bar{n}
π^+	10	res	res	10	10	res	10	res	10	10	res
π^-		10	res	res	10	10	res	res	res	res	10
π^0			5	res	10	res	res	res	res	res	res
K^+				10	10	10	50	res	10	20	10
K^-					10	50	10	res	res	6	10
K^0						10	50	6	6	20	20
\bar{K}^0							10	8	20	6	6
p								res	res	res	20
n									20	res	100
\bar{p}										10	10
\bar{n}											10

Table 2.1.: All elastic cross sections among all species. The constant cross sections are in units of mb, the label res refers to the tabulated or parametrized resonance cross sections we show in Fig. 2.6. We use constant cross sections where no resonance cross section was available.

with resonance cross sections.

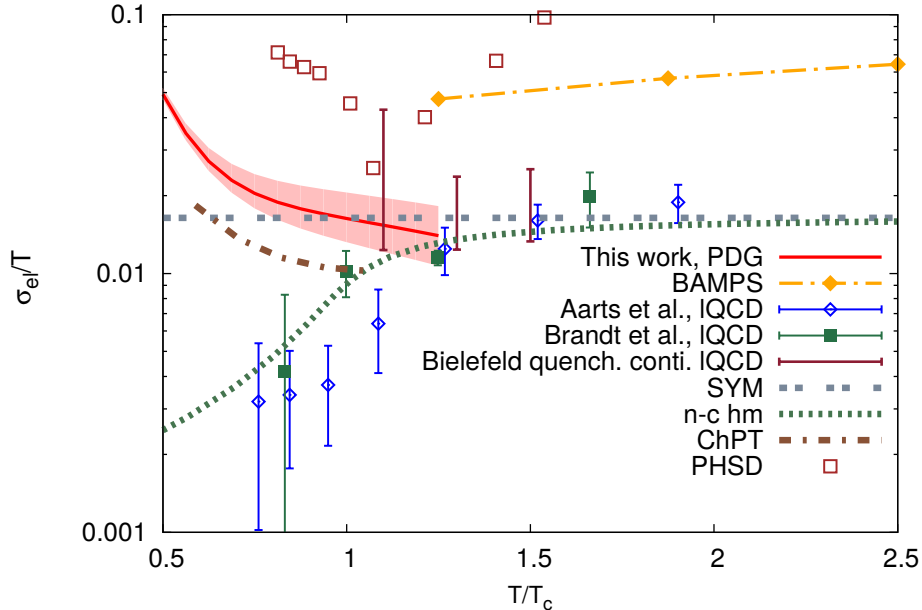


Figure 2.7.: Results for the electric conductivity from this work (red solid band), including pions, kaons and nucleons [1], compared to results from PHSD [163, 179] and all other theories as before. The band shows the uncertainty in the choice of the constant cross sections from Tab. 2.1, by multiplying all of them with a factor 0.5 and 2.

2.3. Diffusion processes

In high energy heavy-ion collisions, dissipative effects due to charge diffusion [181] are typically very small and experimental observation becomes difficult. The recently started beam energy scan (BES) program at the Relativistic Heavy-Ion Collider (RHIC) performs hadronic collisions at lower energies in order to investigate the phase diagram and transport properties of nuclear matter at finite net-baryon (and net-electric charge) density [182–184]. The Bjorken assumption of a flat shape of net baryon multiplicity $dN_{B-\bar{B}}/d\eta$ around mid-rapidity (central plateau) is not fulfilled at those low energies, such that strong gradients in the chemical potential of conserved charges are expected. At RHIC BES, beam energies reach down to $\sqrt{s_{NN}} = 7.7$ GeV, and the baryon chemical potential can reach values up to $\mu_B \sim 400$ MeV, which can be larger in magnitude than the local temperatures [131, 185]. This is the reason, why the high-density region of the phase diagram can be explored by low-energy collisions and furthermore, they are particularly useful to explore the properties of net-charge diffusion of nuclear matter.

Gradients of particle density generate particle currents due to diffusion. More precise, gradients of chemical potentials of a conserved charge generate net currents of this charge. Among the most important conserved charges in heavy-ion collisions are baryon charge (B), electric charge (Q) and strangeness (S).

In the relativistic Navier-Stokes-Fourier theory, a net-charge (q) diffusion 4-current, j_q^μ , is determined by the following constitutive relation,

$$j_q^\mu = \kappa_q \nabla^\mu \alpha_q, \quad (2.35)$$

where $\alpha_q \equiv \mu_q/T$ is the thermal potential, with μ_q being the charge chemical potential, T the temperature and κ_q the corresponding net-charge diffusion coefficient. We further defined the transverse gradient $\nabla^\mu \equiv \Delta^{\mu\nu} \partial_\nu$, and the projection operator $\Delta^{\mu\nu} \equiv g^{\mu\nu} -$

$u^\mu u^\nu$, where u^μ is the local fluid velocity and $g^{\mu\nu}$ the space-time metric. We remark that this relativistic constitutive relation does not only describe the effects of charge diffusion but also includes the effects of heat flow.

The constitutive relations satisfied by the diffusion 4-currents become different in the presence of more than one conserved charge. Since several hadrons (and quarks) carry more than one of the above mentioned B, Q or S charges, the diffusion current of each charge will no longer be solely proportional to the gradient of the thermal potential ($\nabla^\mu \alpha_q$) of that specific charge. Instead, there will be a mixing between the currents, with gradients of every single charge density being able to generate a diffusion current of any other charge. In general, one has

$$\begin{pmatrix} j_B^\mu \\ j_Q^\mu \\ j_S^\mu \end{pmatrix} = \begin{pmatrix} \kappa_{BB} & \kappa_{BQ} & \kappa_{BS} \\ \kappa_{QB} & \kappa_{QQ} & \kappa_{QS} \\ \kappa_{SB} & \kappa_{SQ} & \kappa_{SS} \end{pmatrix} \cdot \begin{pmatrix} \nabla^\mu \alpha_B \\ \nabla^\mu \alpha_Q \\ \nabla^\mu \alpha_S \end{pmatrix}, \quad (2.36)$$

where $\alpha_a \equiv \mu_a/T$, $q = B, Q, S$ is the ratio of charge chemical potential over temperature. The charge *conductivity* due to diffusion is defined by $\sigma_{qq'} \equiv \kappa_{qq'}/T$.

It is possible to include dissipative charge currents in relativistic hydrodynamic equations [161, 162, 186]. This will be relevant in the near future, when hydrodynamic simulations are needed for low energy experiments. The study of baryon, electric or strange diffusion coefficients ($\kappa_{BB}, \kappa_{QQ}, \kappa_{SS}$) is rather new and only very few publications give explicit values. In Ref. [160] the baryon diffusion constant was calculated in an holographic model of the strongly coupled quark-gluon plasma. In Ref. [161] the diffusion of quark number was given in the relaxation time approximation. The transport coefficient for baryon diffusion has been overlooked in the past, arguing that for collision energies $\sqrt{s_{NN}} \sim 0.2 - 2.76$ TeV at the Relativistic Heavy Ion Collider (RHIC) and Large Hadron Collider (LHC) μ_B/T and its gradients are only on the order of 1 – 5% [181]. At RHIC BES collisions at $\sqrt{s_{NN}} = 7.7$ GeV the thermal potential can be $\alpha \equiv \mu_B/T \sim 2.6$ [185] around the phase transition and diffusion effect might be important. In Ref. [181] the influence of baryon diffusion to hydrodynamical predictions for the net baryon rapidity distribution $dN_{B-\bar{B}}/dy$ were found to be significant, even for very low baryon diffusion constants and very small initial μ_B . It was seen (even for RHIC and LHC calculations), that the dissipative baryon current flows visibly due to a gradient in baryon chemical potential into the mid-rapidity region. It is expected that this effect is much more pronounced at low collision energies and a precise knowledge of the diffusion constants will be crucial to quantitatively understand experimental data.

The computation of the diffusion matrix is analogous to the electric conductivity presented in Sec. 2.2.3. The electric charge q_i of species i must now be replaced by the conserved charge under consideration, being baryon charge, electric or strange charge. An important difference in the calculation concerns the force term in the Boltzmann equation. Instead of Eq. (2.15), where the electric field drives the distribution function out of equilibrium, the source term is now a gradient in α_q of the conserved quantity q [170],

$$k_i^\mu \partial_\mu \delta f_{\mathbf{k}}^i + \sum_{q \in \{B, Q, S\}} f_{\mathbf{k}, 0}^i k_\mu \nabla^\mu \alpha_q \left(\frac{E_{i, \mathbf{k}} n_q}{\epsilon_0 + P_0} - q_i \right) = \sum_{j=1}^{N_{\text{species}}} C_{ij}(x^\mu, k^\mu), \quad (2.37)$$

with the total energy density ϵ_0 , isotropic pressure P_0 and

$$n_q = \sum_{i=1}^{N_{\text{species}}} q_i \langle E_{i, \mathbf{k}} \rangle_{i, 0} \quad (2.38)$$

is the net charge density. The deviation from equilibrium has an expansion, similar to Eqs. (2.18) and (2.22),

$$\delta f_{\mathbf{k}}^i = \sum_q k_i^\mu \nabla_\mu \alpha_q \sum_{m=0}^M a_{q,m}^i (E_{i,\mathbf{k}})^m, \quad (2.39)$$

where the integer M characterizes the truncation of the power series in energy, and the coefficients $a_{q,m}^i$ are calculated from Eq. (2.25), where one must replace the vector b_m^i (see the last definition in Eq. (2.26)), which must read now

$$b_m^i = \frac{n_B}{\epsilon_0 + P_0} \int dK E_{\mathbf{k}}^m (\Delta^{\mu\nu} k_\mu k_\nu) f_{0,\mathbf{k}}^i + q_i \int dK E_{\mathbf{k}}^{m-1} (-\Delta^{\mu\nu} k_\mu k_\nu) f_{0,\mathbf{k}}^i, \quad (2.40)$$

In the following we present our results for baryon, electric and strangeness diffusion as function of baryon chemical potential and temperature.

The q -th charge diffusion current is given as

$$j_q^\mu = \sum_{i=1}^{N_{\text{Species}}} q_i \int \frac{d^3 k_i}{(2\pi)^3 E_{i,\mathbf{k}}} \Delta_{\nu}^{\mu} k_i^{\nu} \delta f_{\mathbf{k}}^i. \quad (2.41)$$

Substituting the expansion for $\delta f_{\mathbf{k}}^i$ into Eq. (2.41), and comparing to Eq. (2.36), leads to the following expression for the diffusion coefficients

$$\begin{aligned} \kappa_{qq'} &= \frac{1}{3} \sum_{i=1}^{N_{\text{Species}}} q_i \sum_{m=0}^M a_{q',m}^i \\ &\quad \times \int \frac{d^3 k_i}{(2\pi)^3 E_{i,\mathbf{k}}} E_{i,\mathbf{k}}^m \Delta_{\mu\nu} k_i^\mu k_i^\nu f_{0,\mathbf{k}}^i. \end{aligned} \quad (2.42)$$

Therefore, calculating $\kappa_{qq'}$ is reduced to evaluating the integrals in Eq. (2.26) and Eq. (2.40) and then solving the set of linear equations satisfied by $a_{q',m}^i$ in Eq. (2.25). Both these tasks are performed numerically.

As a sidenote, in a simple relaxation time approximation, the baryon diffusion counter part of the ‘‘Drude’’ formula (electric conductivity) reads with relaxation time τ [162],

$$\kappa_{BB} = \tau n_B \left(\frac{1}{3} \coth(\alpha_B) - \frac{n_B T}{\epsilon + P_0} \right). \quad (2.43)$$

2.3.1. Chemical composition and choice of cross sections

We aim to fix the chemical composition of the system by requiring that the system resembles a (high energy) heavy-ion collisions. This means, for each conserved charge q we are free to either fix its net number N_q or its chemical potential μ_q . First, we require the total net strangeness to vanish, as this resembles probably the physical reality in heavy-ion collisions (strange quarks must be pairwise produced: $s + \bar{s}$). The chemical potential of baryon charge is fixed to different values (given in the plot legends), as this is common practice and allows for comparisons with other models. The electric charge depends on the specific collision (number of protons). For simplicity and comparability, we choose $\mu_Q \equiv 0$.

Quark-gluon plasma

In order to get an estimate for the scale of the diffusion constants found in the hadron resonance gas, we apply our method for a system, where the degrees of freedom are massless quarks and gluons. To this end we have seven species, u, d and s quarks with degeneracies $g_{1,2,3,4,5,6} = 6$ and gluons with degeneracy $g_7 = 16$ all with their corresponding baryon, electric and strange charge. For vanishing chemical potentials, using the matrix elements found in Ref [1], it is possible to derive analytic expressions for the six different $\kappa_{qq'}$.

However, it is worth looking again at the chemical composition of the QGP. We define quark chemical potentials $\mu_{\text{up}}, \mu_{\text{down}}, \mu_{\text{strange}}$ in such a way, that they are related to the usual (hadronic) chemical potentials μ_B, μ_Q, μ_S in the following way,

$$\begin{pmatrix} \mu_{\text{up}} \\ \mu_{\text{down}} \\ \mu_{\text{strange}} \end{pmatrix} = \begin{pmatrix} 1/3 & 2/3 & 0 \\ 1/3 & -1/3 & 0 \\ 1/3 & -1/3 & -1 \end{pmatrix} \cdot \begin{pmatrix} \mu_B \\ \mu_Q \\ \mu_S \end{pmatrix}, \quad (2.44)$$

As mentioned before, we want to fix the net strangeness to be zero, thus $\mu_{\text{strange}} = 0$. It is also reasonable to assume isospin symmetry (number of protons equals the number of neutrons), such that $\mu_{\text{up}} = \mu_{\text{down}}$. Solving Eq. (2.44) with these conditions leads to $\mu_B = 3\mu_{\text{up}} = 3\mu_{\text{down}}, \mu_Q = 0$ and $\mu_S = \mu_{\text{up}} = \mu_{\text{down}}$. Fixing μ_B to a given value means we must set $\mu_Q = 0$ and $\mu_S = \mu_B/3$. All results for the quark-gluon plasma will assume these chemical potentials.

For simplicity and feasibility we choose an unique, isotropic, total cross section σ_{tot} , so that the shear viscosity to entropy ratio has the theoretical lower bound, $\eta/s = 1/(4\pi)$ [52]. By using²

$$\eta = 1.2 \frac{T}{\sigma_{\text{tot}}}, \quad (2.45)$$

this leads for $\mu_B = \mu_Q = \mu_S = 0$ to $\sigma_{\text{tot}} = 0.72/T^2$, where the entropy is $s = 4n$, with total density n . At nonzero chemical potential, the entropy is $s = 4n - \mu_B/Tn_B - \mu_S/Tn_S - \mu_Q/Tn_Q$, and the cross section $\sigma_{\text{tot}} = 1.2T/(s\eta/s)$.

Hadronic gas

Assuming Isospin symmetry, we set $\mu_Q \equiv 0$ from now on. In this case the density of a hadronic species i is given by

$$n_i(T, \mu_B, \mu_S) = g_i T m_i^2 K_2(m_i/T) \exp\left(q_{S,i} \frac{\mu_S}{T} + q_{B,i} \frac{\mu_B}{T}\right). \quad (2.46)$$

For given μ_B we can solve to following equation for μ_S ,

$$\sum_{\text{species } i} q_{S,i} n_i(T, \mu_B, \mu_S) \equiv 0. \quad (2.47)$$

This fixes the chemistry, and all the results for the hadron gas will assume the so obtained chemical potentials, solved individually for each temperature. For the diffusion coefficients involving baryon and strangeness charge it will be relevant, and more realistic, to include also the Λ and Σ baryons. Since the cross sections involving strange baryons are largely unknown, we take the values from the UrQMD transport code, which are fixed cross sections, independent on the electric charge, as given in Table 2.2.

²The factor 1.2 (Israel-Stewart computation, [187]) was recalculated in the 41 moment DKR scheme, being 1.267 [169]. We will however use the Israel-Stewart value here.

in mb	Λ	Σ
π	23.1	5
K	18.5	3
p/n	34.7	10
Λ	30	10
Σ	10	10

Table 2.2.: The isotropic, elastic cross sections of strange baryons in units of mb, as used in Ref. [111,112].

2.3.2. Results for the complete diffusion matrix

We first remark that we checked that Onsager's theorem [188,189], which imposes that $\kappa_{qq'} = \kappa_{q'q}$, is fulfilled in all our calculations. We display our results for the diffusion coefficient matrix from Eq. (2.42) in Fig. 2.8 for $\mu_B = 0, 300, 600$ MeV. For the sake of presentation, we switch the degrees of freedom from hadronic to QGP at temperature $T = 160$ MeV.

Baryon diffusion

For the baryon diffusion current j_B^μ , we expect a strong dependence on both μ_B and T , and indeed this can be seen, e.g., from the functional behavior of the coefficient κ_{BB}/T^2 in Fig. 2.8. In Fig. 2.9 we show the coefficient κ_{BB}/T^2 in the T and μ_B plane. It becomes apparent that at high μ_B the temperature dependence weakens, and around $\mu_B \sim 400$ MeV and $T \sim 150$ MeV the coefficient takes a local maximum. For $\mu_B \lesssim 300$ MeV the coefficient rises rapidly with increasing temperature, as the system is less meson dominated at higher temperatures, and mesons act purely as a resistance for the diffusion of baryons. This effect is also visible in the off-diagonal coefficients $-\kappa_{SB}$ and κ_{QB} . In Fig. 2.10 we show the baryon-electric cross-diffusion coefficient κ_{QB}/T^2 in the $T - \mu_B$ plane for hadronic degrees of freedom, and in the bottom left panel of Fig. 2.8 we compare the hadronic and the QGP results. It is apparent, that κ_{QB}/T^2 is of the smallest magnitude, and exhibits a very strong μ_B dependence. Interestingly, for $\mu_B = 0$ and QGP degrees of freedom, it vanishes. This can be understood schematically by summing up the electric current due to a constant baryon gradient. The only difference among the quarks is their electric charge, thus,

$$\begin{aligned}
 j_Q^{\text{up-quark}} &\sim \underbrace{\begin{pmatrix} 2 \\ 3 \end{pmatrix} e}_{\text{electric charge}} \quad \underbrace{\begin{pmatrix} 1 \\ 3 \end{pmatrix}}_{\text{baryon charge}} \\
 j_Q^{\text{strange-quark}} = j_Q^{\text{down-quark}} &\sim \underbrace{\begin{pmatrix} -1 \\ 3 \end{pmatrix} e}_{\text{electric charge}} \quad \underbrace{\begin{pmatrix} 1 \\ 3 \end{pmatrix}}_{\text{baryon charge}} \\
 j_Q^{\text{net}} = j_Q^{\text{up-quark}} + j_Q^{\text{down-quark}} + j_Q^{\text{strange-quark}} &= 0.
 \end{aligned} \tag{2.48}$$

Since this is true for arbitrary gradients, the coefficient κ_{QB} must vanish with those specific particle species.

In Fig. 2.11 we show the strange-baryon cross-diffusion coefficient $-\kappa_{SB}/T^2$ in the $T - \mu_B$ plane for hadronic degrees of freedom, and in the bottom right panel of Fig. 2.8 we compare the hadronic and the QGP results. The negative sign of κ_{SB} indicates that gradients in strangeness act to reduce the baryon current. The reason for the negative

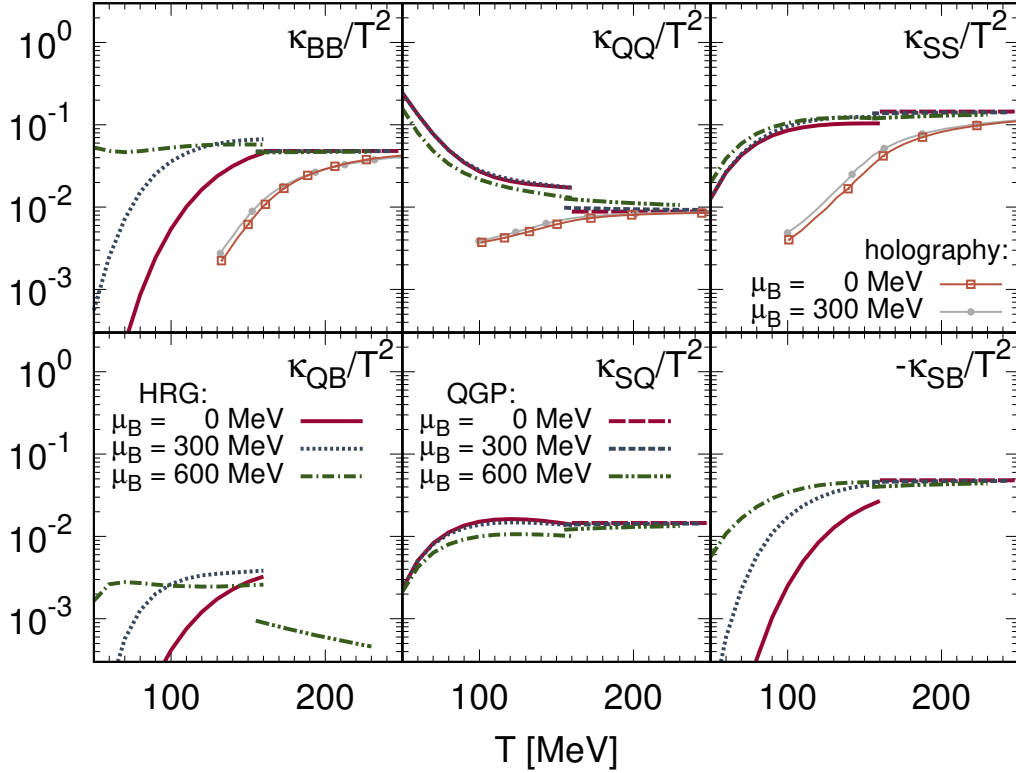


Figure 2.8.: All diffusion coefficients for baryon- electric and strangeness diffusion. The hadronic results include resonance cross sections of the lightest 19 hadronic species, whereas the QGP uses massless quarks and gluons with fixed $4\pi\eta/s = 1$. For illustrative purpose, we show the hadron resonance gas results for $T \leq 160$ MeV and above that the QGP calculation. We compare to holographic results from Ref. [160,190].

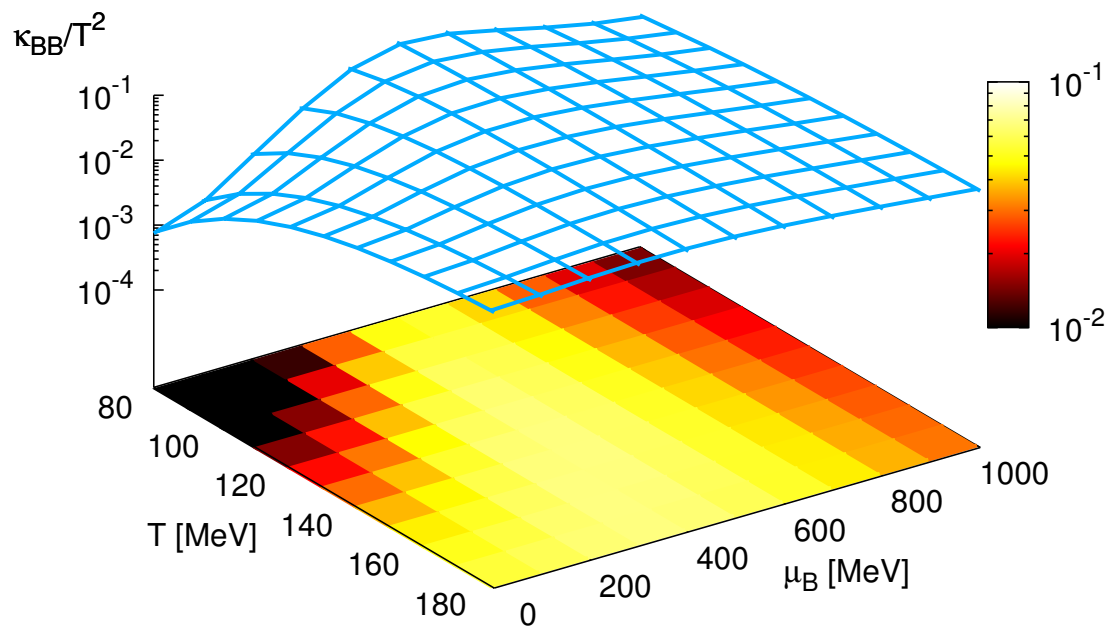


Figure 2.9.: Baryon-Baryon diffusion coefficient κ_{BB}/T^2 over temperature and baryon chemical potential for hadronic degrees of freedom. We plot up to $T = 180$ MeV.

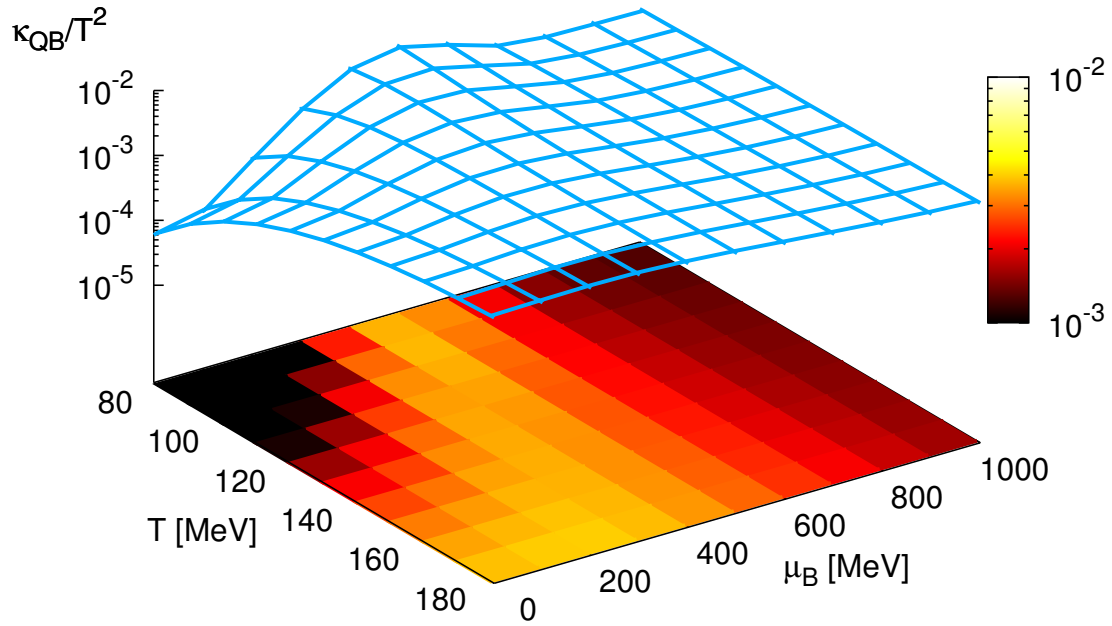


Figure 2.10.: Baryon-Electric diffusion coefficient κ_{QB}/T^2 over temperature and baryon chemical potential.

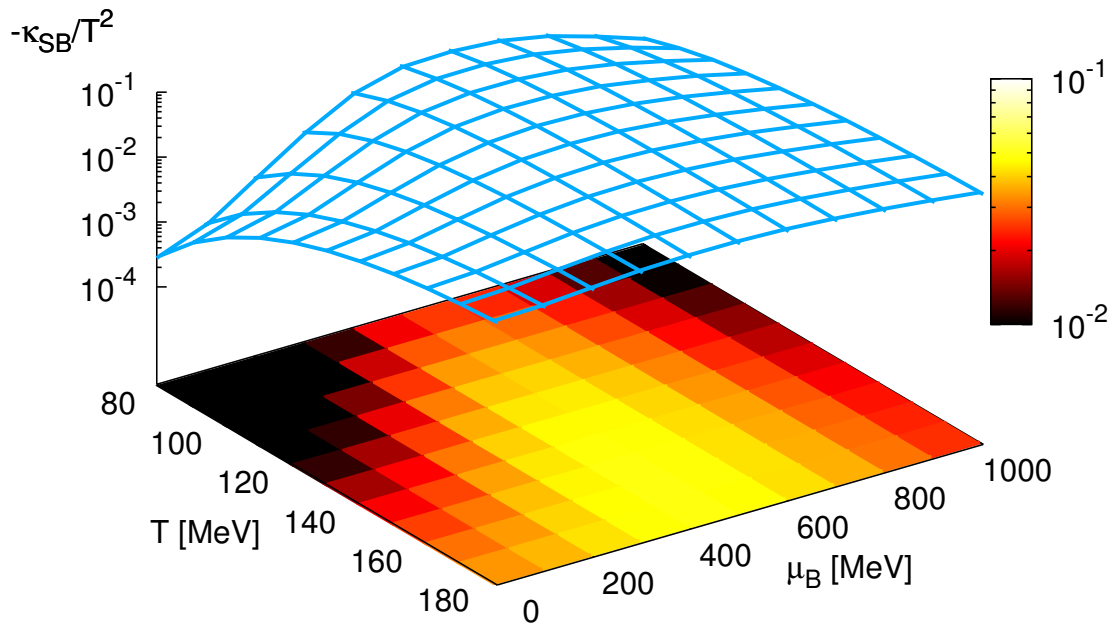


Figure 2.11.: Negative Baryon-Strange diffusion coefficient $-\kappa_{SB}/T^2$ over temperature and baryon chemical potential.

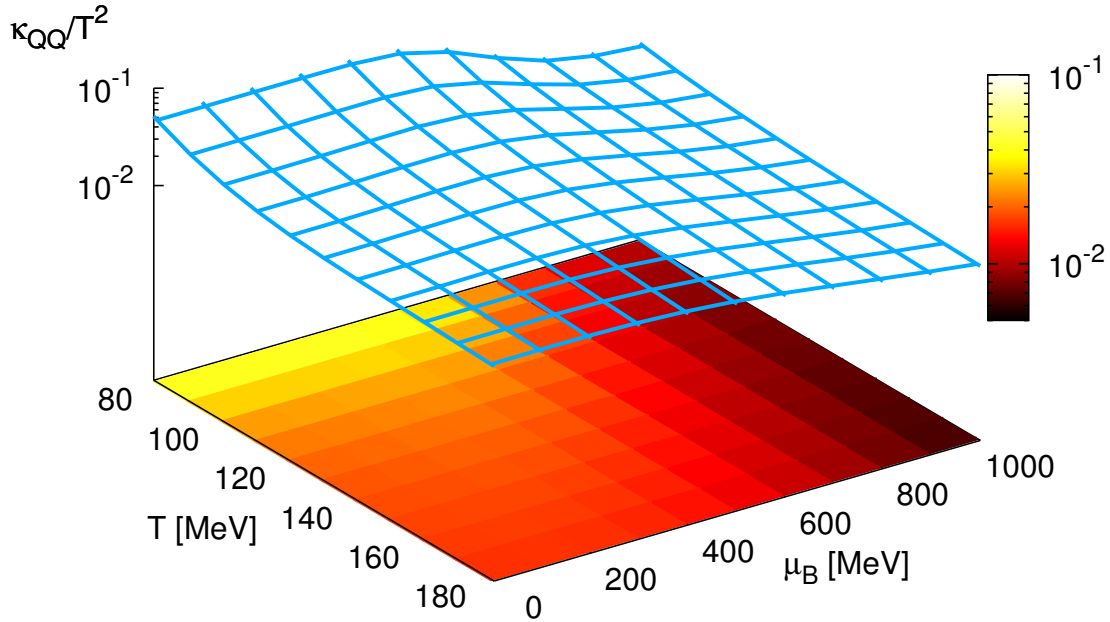


Figure 2.12.: Electric-Electric diffusion coefficient κ_{QQ}/T^2 over temperature and baryon chemical potential.

sign is the definition of negative strangeness of the strange quark. In the hadron phase the dependence on μ_B is very pronounced, indicating the important role of the hyperons.

Comparing κ_{QB} to κ_{BB} , in Fig. 2.8, we infer that the electric charge gradients contribute to the baryon diffusion current about an order of magnitude less than the baryonic gradients. In contrast, gradients in strangeness can be as important as gradients in the baryon charge, as can be seen in the bottom right panel from the magnitude of the coefficient $-\kappa_{SB}$, which is similar in magnitude to κ_{BB} . We remark that this is due to the hyperons, which carry both B and S charge.

In dynamical models, the coefficient κ_{BB}/T^2 is the only one that has been used to study baryon diffusion, e.g., in Ref. [162].

Electric charge diffusion

The coefficients $\kappa_{QQ}, \kappa_{SQ}, \kappa_{QB}$, characterize the diffusion of electric charges³.

In Fig. 2.12 we plot κ_{QQ}/T^2 depending on temperature and baryon chemical potential for hadronic degrees of freedom. We see that κ_{QQ}/T^2 decreases with temperature, and for increasing values of μ_B . This happens because the particle density grows, but the ratio of charged to uncharged species stays the same.

In the top middle panel of Fig. 2.8 we compare the hadronic result with the QGP result. We see that in the QGP at $\mu_B < 600$ MeV the coefficient does not exactly match the hadronic result. This is due to the fact that the QGP is treated only in an effective way. We remark, that only for the case $\mu_B = 0$ there are several other results available in literature, in particular also from the lattice, see Fig. 2.7. In general, they

³ at $\mu_B = 0$, κ_{QQ}/T^2 is equal to the electric conductivity σ_{el}/T

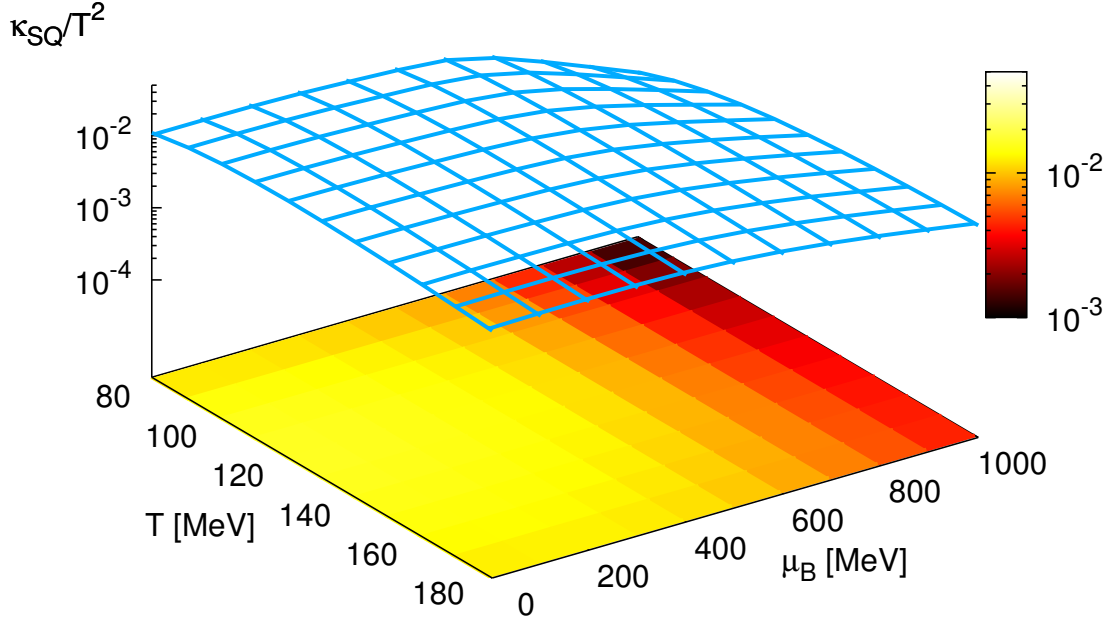


Figure 2.13.: Strange-Electric diffusion coefficient κ_{SQ}/T^2 over temperature and baryon chemical potential.

show an increasing behavior with rising temperature, hinting to the conjectured minimum of κ_{QQ}/T^2 at the phase transition.

In Fig. 2.13 we show the strange-electric cross-diffusion coefficient κ_{SQ}/T^2 again in the $T - \mu_B$ plane for hadronic degrees of freedom, and in the bottom middle panel of Fig. 2.8 we compare the hadronic and the QGP results. This coefficient shows a very small μ_B dependence, and its magnitude for $T \gtrsim 120$ MeV is of the same order of magnitude as κ_{QQ}/T^2 . The QGP and hadronic results match surprisingly well at the phase transition.

The small ratio κ_{QB}/κ_{QQ} indicates the little importance of baryon chemical potential gradients to the electric diffusion current, whereas κ_{SQ} is (for $T \gtrsim 100$ MeV) of the same order of magnitude as κ_{QQ} , indicating that strangeness gradients contribute significantly to the electric diffusion current.

We can again calculate the electric conductivity, taking also the strange baryons into account (see Tab. 2.2), for different baryon chemical potentials. This is an extension of the results in Fig. 2.7, shown in Figs. 2.14 and 2.15. The electric conductivity behaves similar to the electric charge diffusion, decreasing for higher temperature and higher chemical potential.

Strangeness diffusion

In Fig. 2.16 we plot the coefficient related to strangeness diffusion currents due to strangeness gradients, κ_{SS}/T^2 , depending on temperature and baryon chemical potential for hadronic degrees of freedom and in the top right panel of Fig. 2.8 we compare the hadronic with the QGP result. We find that κ_{SS} is larger than both $-\kappa_{SB}$ and κ_{SQ} (bottom right and middle panel in Fig. 2.8), being even larger in magnitude than the baryon diffusion coef-

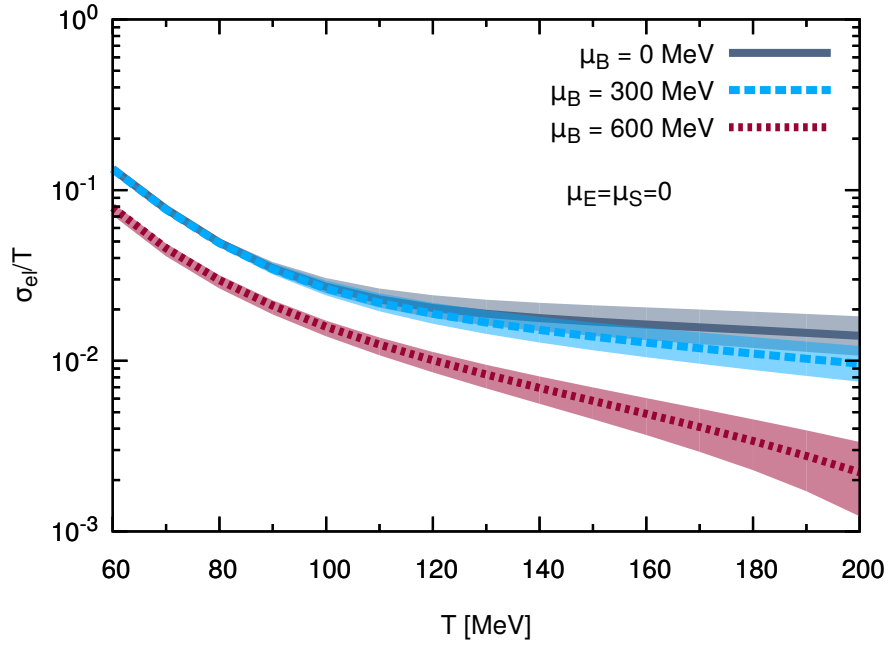


Figure 2.14.: Electric conductivity as before in Fig. 2.7, but now we change the baryon chemical potential which influences the chemical composition of the hadron gas. Bands indicate only the uncertainty in those cross sections which are approximated as constant, see Sec. 2.2.5.

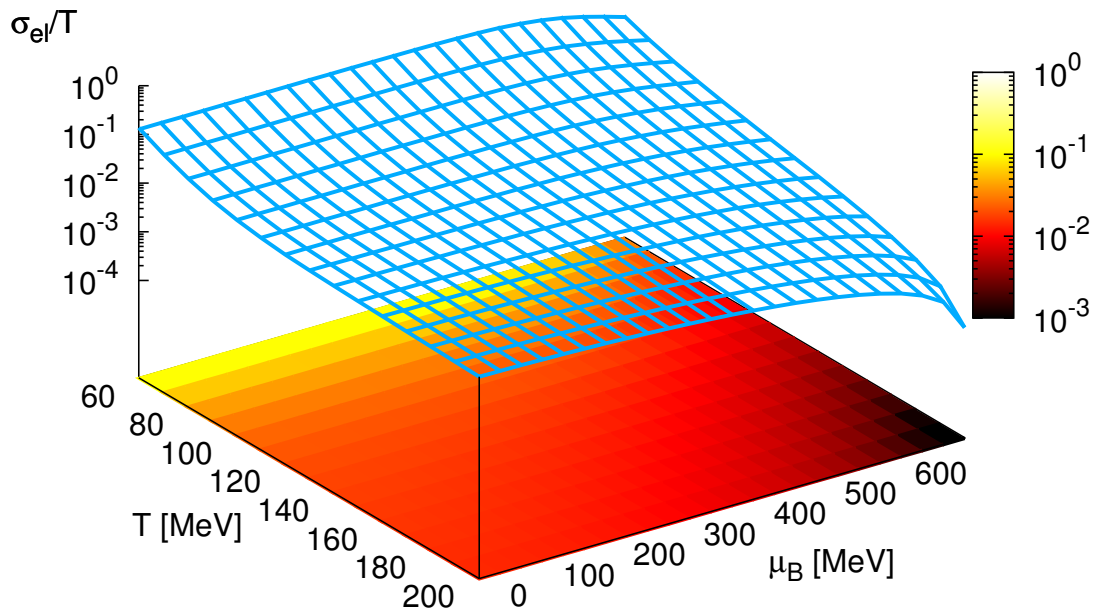


Figure 2.15.: Electric conductivity as function of temperature and baryon chemical potential. The cross sections are given in Tab. 2.1 and Fig. 2.6.

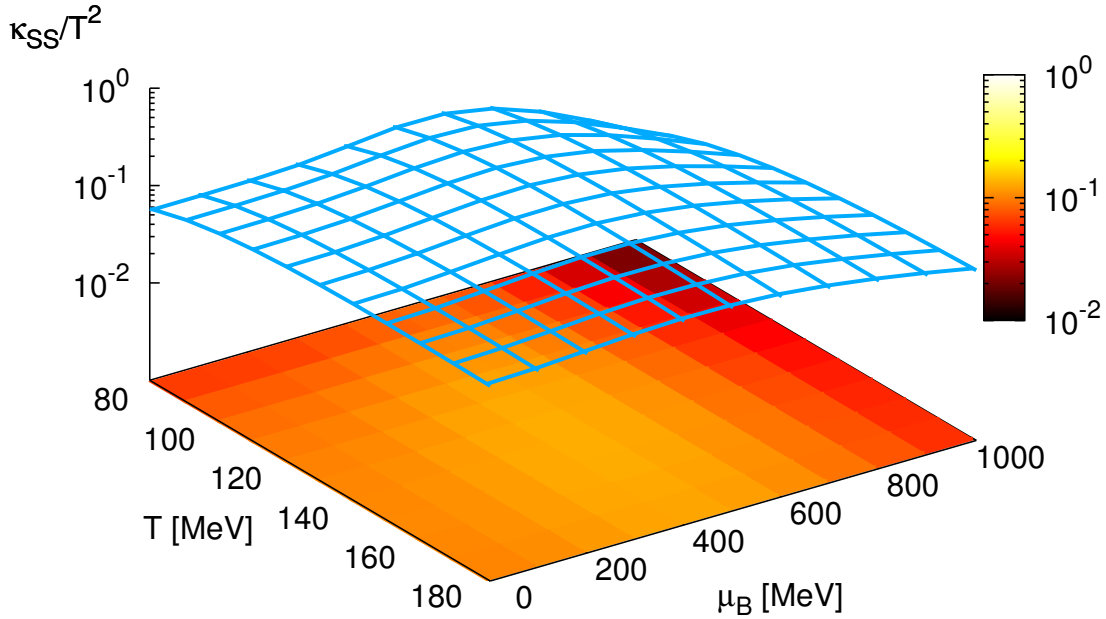


Figure 2.16.: Strange-Strange diffusion coefficient κ_{SS}/T^2 over temperature and baryon chemical potential.

ficient (except for very small values of temperature). Its μ_B dependence is weak, and the temperature dependence weak compared to the other coefficients.

We find that baryonic gradients act to significantly reduce strangeness currents in both the QGP and HRG, since κ_{SB} is negative and its magnitude is only about a factor two smaller than κ_{SS} . Therefore, it is possible that cancellation effects due to coupling between the currents can lead to small strangeness diffusion currents. On the other hand, κ_{SQ} is about an order of magnitude smaller than κ_{SS} , indicating that electric gradients are less important for strangeness transport. We remark that the μ_B dependence of κ_{SS} , κ_{QQ} and κ_{SQ} is very weak, however their dependence on μ_Q and μ_S can behave differently. κ_{SS} was only calculated before in Ref. [191] for a Kaon system.

2.4. Conclusion and phenomenological consequences

As a main result, we quoted the full matrix of diffusion coefficients for the relevant range of temperatures $T \sim 50 - 250$ MeV and chemical potentials $\mu_B \sim 0 - 600$ MeV. We switched the degrees of freedom at an approximate transition temperature, $T = 160$ MeV without any further calculation, keeping in mind, that this transition is probably more complicated, and there might be a mixed phase.

The six transport coefficients include the traditional baryon diffusion coefficient κ_{BB} , and the electric and strangeness diffusion coefficients κ_{QQ} and κ_{SS} , respectively. We present for the first time also the three off diagonal transport diffusion coefficients κ_{QB} , κ_{SB} and κ_{SQ} which describe the mixing between gradients and currents of different charge.

In our semi-analytic approach, we confine ourselves to classical statistics, elastic collisions and isotropic scattering, employing a Chapman-Enskog-type calculation [192, 193].

The calculations in the hadron gas phase are carried out including analytic resonance and measured elastic hadron-hadron cross sections, when available, taking into account hadrons up to the Σ baryons. This constitutes the most extensive result of the charge diffusion matrix in the HRG to date.

For calculations in the QGP phase, we employ a much simpler model, fixing η/s to be a constant and assume all up, down and strange quarks to be massless. It is in fact very interesting that most of the diffusion coefficients in the QGP match the HRG results quite well nearby the conjectured phase transition region. At this point it is unfeasible to assess the systematic uncertainties in a reliable way, thus physical interpretations of the discontinuity around the phase transition is difficult. It however hints to missing ingredients.

In brief words, our results emphasize that the mixing between gradients of the thermal potential of different charges is in general important and should not be neglected when simulating low energy heavy-ion collisions. For example, the contribution to the baryon diffusion current from gradients of baryon number density can be almost completely canceled by gradients in strangeness of comparable magnitude, whereas we found electric gradients to be almost negligible for baryon transport. Electric diffusion currents are mainly driven by electric and strangeness gradients. Strangeness diffusion is mostly affected by strangeness and baryon number gradients, with electric charge gradients being less important. The relevance of these effects for experimental observables remains to be investigated.

The diffusion coefficients can readily be used in dissipative hydrodynamic calculations for charge rich systems. Only then the true relevance of the three diffusion currents for experimental observables can be evaluated. Due to the growing interest in baryon rich experiments, like RHIC BES, NICA or FAIR, we expect that more work on diffusion phenomena will be undertaken in the near future.

The transport coefficients are matter properties, like $\eta/s, \sigma_{\text{el}}/T$ or the bulk viscosity over entropy ratio ζ/s , and as such it is instructive to compare them to different theories, with the goal to learn about microscopic interactions, or transition lines in the phase diagram of QCD. As an example, in Fig. 2.8 we compare to the holographic results from Ref. [160, 190] which match ours at high T (conformal limit). Their μ_B dependence for the diagonal coefficients is as weak as for our QGP results, but the coefficients are slightly lower in magnitude for temperatures $T \lesssim 150$ MeV. It is interesting how a simple kinetic calculation, that simply fixes $\eta/s = 1/4\pi$, is already capable of reproducing the basic trends of such holographic calculations. It would be interesting to see whether this holds for the off-diagonal coefficients.

It is furthermore desirable to compare our kinetic calculations with lattice QCD studies. Unfortunately, those calculations require a solution for the highly non-trivial inversion problem (analytic continuation). To date, lattice studies exist only (for vanishing chemical potentials) for the electric charge diffusion coefficient $\sigma_{\text{el}} = \kappa_{QQ}/T$ [147, 149, 194]. In the confined phase, the lattice results are extremely difficult to compute and thus not reliable. The holographic result for strongly coupled $\mathcal{N} = 4$ Yang-Mills theory is $2\pi TD = 1$, where $D \equiv \kappa_{QQ}/(T\chi_Q)$, with the electric charge susceptibility χ_Q . Those comparisons were already made in Sec. 2.2.5. The coefficients κ_{BB}, κ_{SS} and the off-diagonal diffusion coefficients have never been calculated on the lattice. All coefficients should also be accessible from hadronic transport models, or other dynamical approaches.

We plan to extend our work to quantum statistics, a more realistic description of the QGP and possibly more particle species to achieve a fully comprehensive framework of diffusion properties. Especially the use of non-isotropic cross sections (resonance p-wave scattering in the HRG or pQCD inspired matrix elements in the QGP) will be an inter-

esting possibility for the future.

The electric conductivity is a key ingredient of Maxwell's equations in medium, and as such a crucial ingredient for investigations of magnetohydrodynamics or other calculations of electromagnetic fields in the quark-gluon medium. A first step in this direction will be undertaken in the next chapter, where we look at the response of partons to external magnetic fields. The electric conductivity influences the dynamic behavior strongly, and we compare, i.a., the difference between a free streaming medium and a medium with finite electric conductivity, both under magnetic field influence.

3. Magnetic fields

In peripheral heavy-ion collisions, the passing nuclei generate very strong electromagnetic fields. They each carry 79 (Au nucleus) or 82 (Pb nucleus) protons, and the typical distance of the passing electric charges to the QGP is very small ($\mathcal{O}(1)$ fm). All charges, which fly outside the almond shaped overlap region contribute strongly to the magnetic field. Fields induced by spectators located inside the overlap region mostly cancel each other. In high energy experiments, the velocities of the nuclei reach nearly the speed of light, which, in addition to the geometry explained above, is the reason for electromagnetic fields which are at $eB \sim 10^{18}$ G among the largest in the Universe [195, 196]

A large part of this chapter was published in Ref. [3]. We first calculate the field strength of the electric and magnetic field at three different positions inside the almond-shaped transverse collision region, induced by the spectators. We then investigate the influence of these fields to the dynamics of the partons in the QGP, with and without collisions. After looking more differentially on the kinematic regions of interest, we find, that the elliptic flow v_2 at very low transverse momenta can be significantly enhanced. As an other example, we calculate the corresponding photon elliptic flow enhancement, which is also visible at low transverse momenta.

3.1. Fields from Spectators

For all the following studies it is a natural first step to calculate the magnetic field strength due to fast spectator nucleons at the time when both nuclei pass each other, $t \equiv 0$. In general, the solution of Maxwell's equations for N_{ch} charged particles with charge $Q_i = q_i e$ moving with constant speed \vec{v}_i reads

$$\begin{aligned} e\vec{E}(t, \vec{r}) &= \alpha_{\text{EM}} \sum_i^{N_{\text{ch}}} q_i \frac{\vec{R}_i}{\gamma^2 R_i^3 (1 - (\vec{R}_i \times \vec{v}_i)^2 / R_i^2)^{3/2}} \\ e\vec{B}(t, \vec{r}) &= \alpha_{\text{EM}} \sum_i^{N_{\text{ch}}} q_i \frac{\vec{v}_i \times \vec{R}_i}{\gamma^2 R_i^3 (1 - (\vec{R}_i \times \vec{v}_i)^2 / R_i^2)^{3/2}}, \end{aligned} \quad (3.1)$$

where $\vec{R}_i = \vec{r} - \vec{r}_i(t_R) = \vec{r} - \vec{r}_i(t - |\vec{r} - \vec{r}_i(t)|)$ is the relative distance between the observation point \vec{r} and the trajectory of the charged particle $\vec{r}_i(t)$ evaluated at the retarded time $t_R = t - R_n(t)$ with $R_n(t) = |\vec{r} - \vec{r}_n(t)|$. Numerically, it turns out to be more efficient to compute the fields rather at advanced times $t_A = t + R_n(t)$, such that the rhs of Eq. (3.1) must be evaluated at the present time t , $e\vec{E}(t_A, \vec{r})$, $e\vec{B}(t_A, \vec{r})$.

Since protons travel on straight lines, and stopping effects in high energy collisions are weak, we can assume that the velocity vector of the protons is $\vec{v} = (0, 0, \pm v_z)$, where the magnitude is given by the collision energy, $v_z^2 = 1 - (2m_p / \sqrt{s_{NN}})^2$ [157, 196], and $\gamma_p = \sqrt{s} / (2m_p)$.

3.1.1. Geometry

For the computation of the external fields one must precisely sample the positions of the charges. Inside each nucleus of charge number A , the particle density n at radius $|\vec{r}| = r$

from the nucleus' center is approximated by the Woods-Saxon distribution [197, 198],

$$n = \gamma_p \frac{n_0}{\exp((r - R_A)/d_A) + 1} \quad (3.2)$$

where the central density n_0 is obtained by solving $\int d^3 \vec{r} n(\vec{r}) \equiv A$. The radius of the nucleus is given by $R_A/\text{fm} = 1.12A^{1/3} - 0.86A^{-1/3}$ and the skin depth for an Au (Pb) nucleus is $d_A = 0.535$ fm (0.546 fm) [199]. It is straight forward to sample the transverse positions \vec{r}_i of the protons, and shift their positions by $\pm b/2$ for impact parameter b . In the right panel of Fig. 3.1 we show the result of such a sampling, whereas in the left panel the nucleon positions are sampled according to a homogeneous disc distribution,

$$n(r) = n_0 \Theta(r - R_A). \quad (3.3)$$

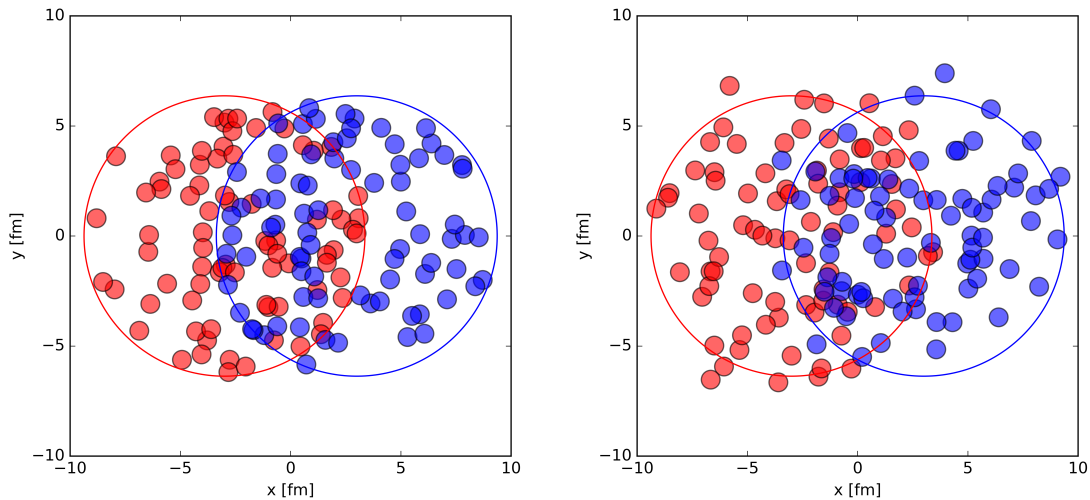


Figure 3.1.: Typical sampling of nucleon positions of two overlapping Au nuclei (impact parameter $b = 6$ fm). Shown are only the protons, as they generate the magnetic field. The positions are sampled uniformly across the disc (left), and along a realistic Woods-Saxon distribution (right).

3.1.2. Field strengths

We want to compute the fields at the moment of maximal overlap, $t = 0^+$ and we assume that due to the strong Lorentz contraction the nuclei are two dimensional pancakes, such that the distance of the charges to the computation point $\vec{R}_i = \vec{r} - \vec{r}_i$ lies entirely in the x-y-plane, $\vec{R}_i \equiv \vec{R}_{\perp,i}$. In this case, the field strengths reduce to [196, 200, 201]

$$\begin{aligned} e\vec{E} &= \alpha_{\text{EM}} \sum_i^{N_{\text{ch}}} q_i \frac{\vec{R}_{\perp,i}}{|\vec{R}_{\perp,i}|^3} \gamma_p, \\ e\vec{B} &= \alpha_{\text{EM}} \sum_i^{N_{\text{ch}}} q_i \frac{\vec{v}_i \times \vec{R}_{\perp,i}}{|\vec{R}_{\perp,i}|^3} \gamma_p. \end{aligned} \quad (3.4)$$

In Fig. 3.2 we show the magnetic field strength at $t = 0$ for Au+Au and Pb+Pb collisions at $\sqrt{s_{NN}} = 200$ GeV and $\sqrt{s_{NN}} = 2.76$ TeV in the center of the collision, at the side and the top of the almond-shaped overlap zone. We show separately the event averages $\langle B_{x,y} \rangle$ and the absolute value of the fields averaged, $\langle |B_{x,y}| \rangle$. The z -components are very small, so we omit them here. In Fig. 3.3 we do the same study for the electric field strengths $E_{x,y}$. The results in Figs. 3.2 and 3.3 are in qualitative agreement with previous studies [196, 200, 202]. The results of Ref. [196] are about a factor of 2 smaller than the results of Ref. [200] or ours.

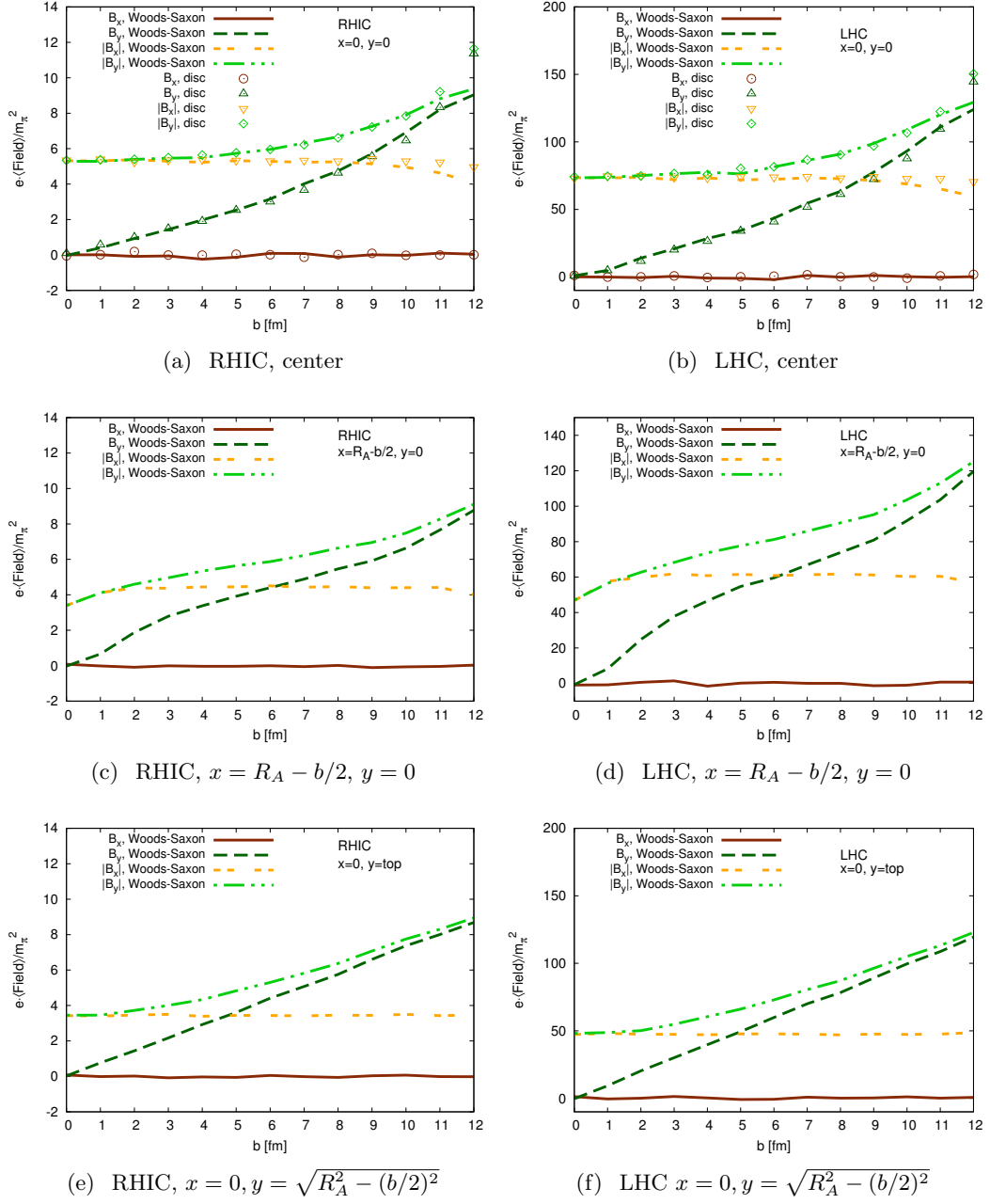


Figure 3.2.: Event averaged magnetic field components ($\langle B_x, B_y \rangle$) and averaged absolute fields ($\langle |B_x|, |B_y| \rangle$) at midrapidity for RHIC (Au+Au $\sqrt{s_{NN}} = 200$ GeV, left panels) and LHC (Pb+Pb $\sqrt{s_{NN}} = 2.76$ TeV, right panels) at the center of the fireball, at the side of the almond-shaped overlap zone, $x = R_A - b/2, y = 0$, and at its top, $x = 0, y = \sqrt{R_A^2 - (b/2)^2}$ at time $t = 0$.

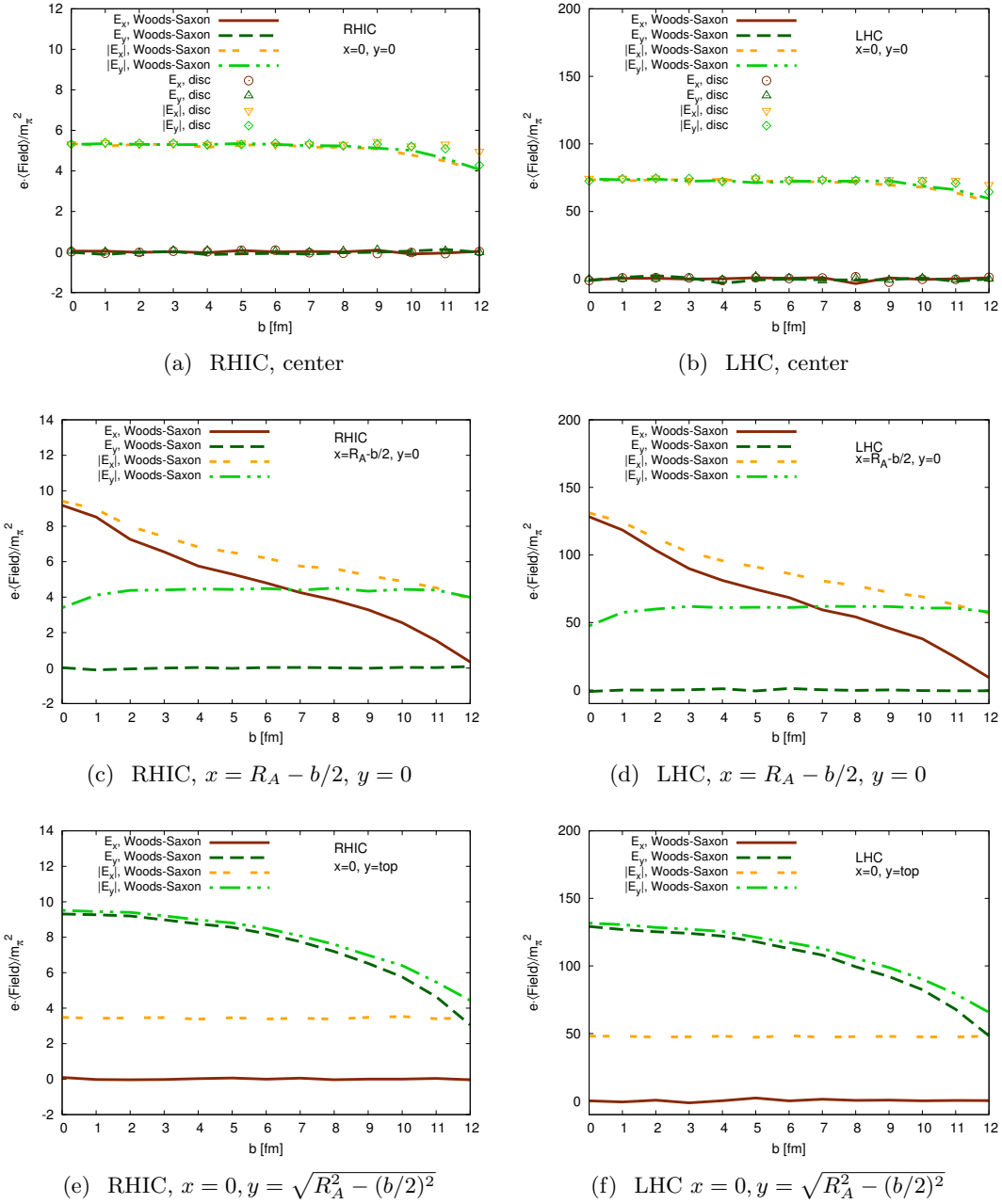


Figure 3.3.: Event averaged magnetic field components ($\langle B_x, B_y \rangle$) and averaged absolute fields ($\langle |B_x|, |B_y| \rangle$) at midrapidity for RHIC (Au+Au $\sqrt{s_{NN}} = 200$ GeV, left panels) and LHC (Pb+Pb $\sqrt{s_{NN}} = 2.76$ TeV, right panels) at the center of the fireball, at the side of the almond-shaped overlap zone, $x = R_A - b/2, y = 0$, and at its top, $x = 0, y = \sqrt{R_A^2 - (b/2)^2}$ at time $t = 0$.

3.2. Magnetic field influence on the QGP dynamics

In this section, we turn to a fundamental question which has not gained much attention in literature: will there be directly measurable effects of the electromagnetic Lorentz force in heavy-ion collisions? Early attempts [203] to model a hadron gas under the influence of magnetic fields did not show strong effects.

The authors of Ref. [204] have studied the charge dependent directed flow of pions and protons in a simplified analytic model, taking electric and magnetic fields into account. They find a very small signal, owing mainly to the currents induced by electric fields generated by the fast decaying magnetic fields (Faraday effect). For very low p_T however, they see a strong influence of the magnetic field itself (dubbed as ‘‘Hall’’ effect). In particular, the magnetic effect becomes important for the directed flow at transverse momenta $p_T \lesssim 0.25$ GeV for RHIC and LHC. We will later see the growing influence of the magnetic effect at low p_T .

Hydrodynamic calculations including magnetic fields are rare, and still under development [205,206]. Recently, it has been found that the directed flow of charm quarks is very sensitive to the magnetic and electric field [207]. Furthermore, it has been proposed, that the J/Ψ formation becomes anisotropic which leads, e.g., to a sizable elliptic flow at high transverse momenta [208].

We attempt an exploratory study of the early-time non-equilibrium dynamics of deconfined quarks and gluons including simple parametrizations of an external magnetic field. We find that the quark momenta rotate parallel to the event plane and develop a surprisingly large momentum anisotropy at mid- and forward rapidity for very low transverse momenta. This is roughly reminiscent to the Hall effect. The particle velocity stems mainly from the large boosts in beam direction (longitudinal expansion), whereas the magnetic field comes from the charged spectator nucleons.

We see furthermore that the spectra are also slightly enhanced at early times and we show explicitly how collisions damp both the effect of the flow and the spectra.

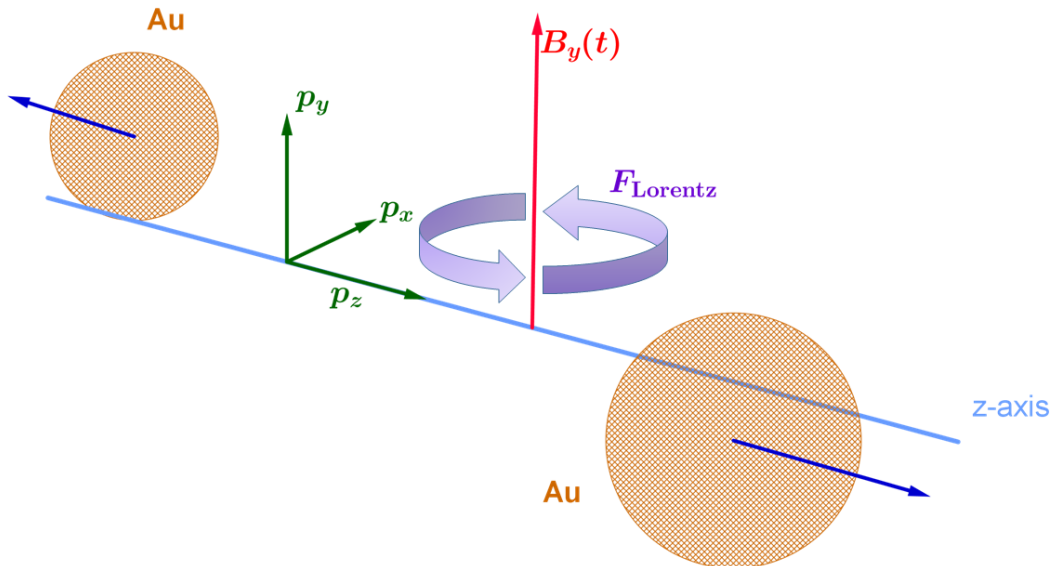


Figure 3.4.: Geometry of our model. The magnetic field is constant and homogeneous.

3.2.1. Simple model without collisions

We investigate how strong the effect of the Lorentz force alone can be on the particle distributions. To this end, we outline a simple model for the heavy-ion collision, neglecting parton-parton collisions in a first step. We consider the passing of two heavy nuclei along the z-axis. For simplicity, we assume the magnetic field \vec{B} to be constant and homogeneous, pointing in y-direction, $\vec{B} \equiv B_y \vec{e}_y$. The situation is depicted in Fig. 3.4. Here we neglect electro-dynamical induction effects. We assume that all events are symmetric and the impact parameter points in x-direction. In this geometry elliptic flow can be seen as an average $\langle \langle \cdot \rangle \rangle$ momentum asymmetry $\langle \langle (p_x^2 - p_y^2)/p_T^2 \rangle \rangle \equiv v_2$, where $p_T = \sqrt{p_x^2 + p_y^2}$.

Initial state and formation time

In this simple model setup we do not consider space-dependent effects, thus we sample only four-momenta of the particles. All particles are assumed to be massless. The p_T distribution is sampled according to a power law,

$$dN/dp_T = \left(\frac{n-1}{p_{T,\min}^{1-n}} \right) p_T^{-n}, \quad n = 2, 3, 4. \quad (3.5)$$

We choose a minimal value $p_{T,\min} = 0.01$ GeV. For all the following results we assume a constant distribution in rapidity, $y = 1/2 \log(E + p_z)/(E - p_z)$,

$$dN/dy = \text{const.}, \quad p_z = p_T \sinh y. \quad (3.6)$$

We find that the results are not dependent on the rapidity window in which we initialize the particles, as long as it is larger than the observed rapidity bins. For most studies, $-3 < y < 3$ is sufficient.

It is possible to use a formation time $\Delta t_f = \cosh(y)/p_T$ during which particles are still off-shell and do not interact, but propagate freely. This formation time has been used earlier in transport approaches using the Minijet model for the initial condition [209–211]. We can assume that the magnetic field will also not influence the partons within their formation time. However, as quarks carry their electric charge even off-shell, their classical interaction with magnetic fields is arguable, and the formation time could be irrelevant. As this point is conceptually uncertain, we show results for both options, assuming the particle-field interaction to be switched on immediately (no formation time), or, only after Δt_f , respectively. In this simplified collisionless scenario we only initialize quarks, carrying the electric charge $q = e/3$ or $q = 2e/3$, respectively. The exact quark and gluon content in the early phase of heavy-ion collisions is under debate. It is clear, that the more gluon dominated the system is, the less pronounced such electromagnetic effects will be.

Magnetic field parameterizations

The external magnetic field present at $t = 0^+$ after the collision is still subject to active research, and depends strongly on the geometric modeling of the nuclei as well as the electric conductivity and also possible non-equilibrium effects. Common to all the results in literature is the dominant B_y -component, perpendicular to the event plane, which is about an order of magnitude larger than the B_x -component, the B_z -component is nearly absent, see Sec. 3.1.2. The authors of Ref. [212] look explicitly at fluctuations of the direction of the magnetic field and find that for middle central collisions the field fluctuates less around the direction perpendicular to the event plane than for near central or very peripheral collisions. For the qualitative understanding of the dynamical effects to the

quark momenta, we adopt several simplified scenarios for the field strength B_y , and set $B_x = B_z = 0$. In Ref. [203] it was found that the spatial dependence over the overlap region is mild, so that we restrict ourselves here to a homogeneous field in space, parametrized as

param 1 $eB_y(t) = 4 m_\pi^2 \Theta(0.3 \text{ fm}/c - t)$

param 2 $eB_y(t) = eB_y^{t=0}(1 + t^2/t_c^2)^{-3/2}$ with $t_c = 0.065 \text{ fm}/c$.

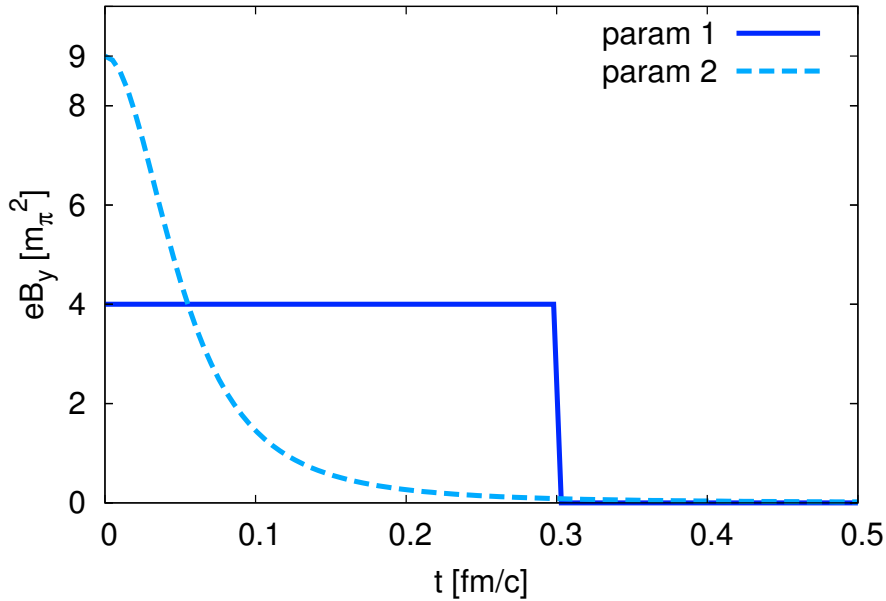


Figure 3.5.: The two simple parameterizations of the homogeneous magnetic field. Param 2 follows Ref. [196].

Param 2 is the parametrization of the results of Ref. [196] as given in Ref. [202]. We use it with parameters corresponding to RHIC collisions (Au+Au, $\sqrt{s_{NN}} = 200 \text{ GeV}$) at typical impact parameters of $\sim 8 \text{ fm}$ corresponding to 20 – 40% centrality (see also, e.g., Refs. [200, 213] for typical field strengths). In the very early stage, the medium is assumed to be gluon dominated, such that the electric conductivity can be neglected [202] (being roughly proportional to the sum of the electric charges squared, weighted by the densities of the charge-carrying species [1, 150]). The authors of Ref. [196, 202] approximate the total magnetic field thus by the external component produced by the charged nucleons passing each other. The full solution of the Maxwell- and Boltzmann equation will slow down the decay of the magnetic field, but so far, only little is known about the precise evolution. Parametrization 1 is an optimistic imitation of a strongly conducting medium, which would keep the magnetic field present for some time. We have tried even higher or longer field parametrizations, but for simplicity we restrict ourselves to an optimistic, and a realistic one.

Larmor movement

The magnetic field changes the direction of velocity of the particles by the Lorentz force, $\vec{F}_L = q\vec{v} \times \vec{B}$. In our geometry, particles will move in a circle around the y-direction, clockwise or anticlockwise depending on their charge q . Thereby, any momentum in z-direction will increase or decrease the momentum in x-direction, $p_x \rightarrow p_x + \Delta p_x$.

To analytically estimate the effect of increasing p_x components, we note that in the whole particle ensemble by symmetry $\langle p_x \rangle = 0, \langle p_y \rangle = 0$. We consider two same-charge particles with opposite p_x momentum components, $p_{x,1} = -p_{x,2}$ as representer of the (in total charge neutral) particle ensemble. Their p_y momenta are equal, and chosen in a way, that the initial momentum asymmetry v_2 takes a given value. The change $p_x \rightarrow p_x + \Delta p_x$ on the v_2 of the whole particle ensemble can then, in a simplified fashion, be estimated by

$$v_2(\Delta p_x) = \frac{1}{2} \left(\frac{(p_x + \Delta p_x)^2 - p_y^2}{(p_x + \Delta p_x)^2 + p_y^2} + \frac{(-p_x + \Delta p_x)^2 - p_y^2}{(-p_x + \Delta p_x)^2 + p_y^2} \right). \quad (3.7)$$

In Fig. 3.6 we show this momentum asymmetry for three choices of the initial v_2 , positive, zero and negative. Clearly, for zero initial v_2 , the increase of Δp_x must be larger than p_T in order to enhance the asymmetry. All cases show a minimum in v_2 for $\Delta p_x < p_T$, which can be strongly negative. Note that Eq. (3.7) is symmetric under the change of

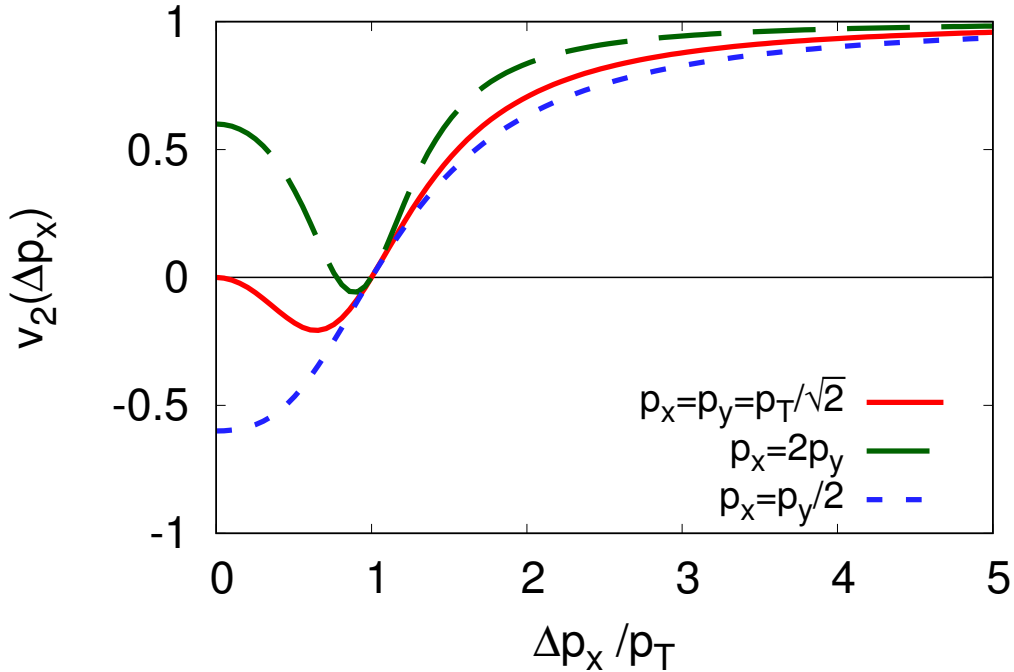


Figure 3.6.: After the increase of p_x , the momentum asymmetry v_2 is in all cases positive for $\Delta p_x > p_T$. The result is symmetric in Δp_x .

$\Delta p_x \rightarrow -\Delta p_x$, thus insensitive to the sign of the electric charge. An ensemble of particles with positive and negative charges, and momenta drawn from a distribution, can also give positive v_2 , this is what we will explore in the next section. The resulting v_2 of such ensembles is in principle an average like Eq. (3.7), just taken over a larger set of particles.

The radius of deflection due to the magnetic field is

$$r_{\text{Larmor}} = \frac{\sqrt{p_x^2 + p_z^2}}{qB_y}, \quad (3.8)$$

and the angle of the circular movement of time t is $\alpha_{\text{Larmor}} = t/r_{\text{Larmor}}$. The value of Δp_x depends on the momenta p_x and p_z of each particle, for a given magnetic field times its duration, $B_y t$.

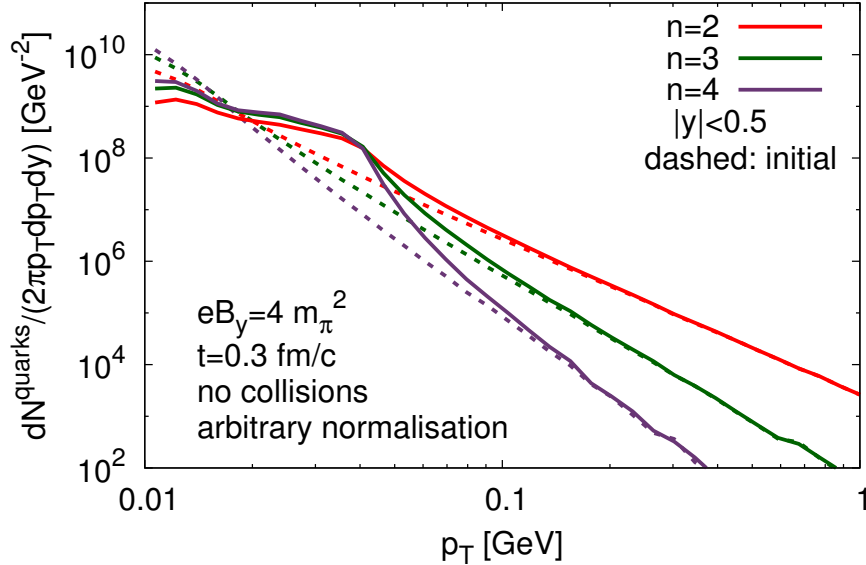


Figure 3.7.: For three different initial p_T -distributions (power-law exponent n) we show how the spectra change after 0.3 fm/c under the influence of a magnetic field. Here we use an arbitrary number of particles and magnetic field parametrization 1.

In this study, we do not include electromagnetic effects other than the Larmor movement. The reason is outlined in the following. The Faraday effect due to the time dependent magnetic flux $\varphi = B_y A$ through surface A generates an electric field,

$$-\frac{\partial \varphi}{\partial t} = \oint \nabla \vec{r} \cdot \vec{E}. \quad (3.9)$$

This electric field accelerates charges in the opposite direction than the Lorentz force $\vec{F}_L = q\vec{v} \times \vec{B}$. Assuming for a moment, that $\vec{F}_L \equiv 0$, the electric current due to the force $q\vec{E}$ will generate a magnetic field component B_{ind} counter balancing the decay of the field, $\vec{B}_{\text{ind}} \sim \partial \vec{B} / \partial t$, depending on the electric conductivity. On top of these effects, the electric fields generated by the spectators, albeit small in magnitude, has also an x -component [201], which is positive $E_x^{\text{spec}} > 0$ for $x > 0$ and negative $E_x^{\text{spec}} < 0$ for $x < 0$. All these 3 effects can cancel or enhance each other, and depend crucially on the assumed electric conductivity and parametrization of the bare spectator induced fields. Furthermore, the calculation of the magnetic flux as well as the electric fields would require a full space-time dependent (propagating) solution of the electromagnetic fields. This is why we restrict ourselves to show what maximum effect on the particle dynamics is expected from the magnetic field only.

3.2.2. Results of the collisionless model

First we show how p_T -spectra of quarks are influenced in the early time by a magnetic field in Fig. 3.7. Here, for parametrization 1 of the magnetic field, the spectrum is enhanced for $0.02 < p_T/\text{GeV} < 0.1$ due to the Larmor turn of p_z -momenta. In Fig. 3.6 we explained that the final momentum asymmetry depends strongly on the additional Δp_x . We explore which momentum space region (regions in rapidity) is necessary to gain sufficiently large values of Δp_x for the v_2 to change visibly. Here we differentiate between initial quantities,

and those after the circular Larmor-movement has been applied to the particle. For this purpose we show in Fig. 3.8 the final v_2 (after the Larmor movement had been applied for a time t) as function of initial rapidity y_{initial} . We split this up in a soft region, for final $p_T < 0.3$ GeV, where the averaged v_2 reaches large values, and the region of final $p_T > 0.3$ GeV, where the v_2 is consistent with zero. This ultrasoft p_T ranges can already be expected from the spectra, Fig. 3.7. Note that the saturation in Fig. 3.8 is due to the cuts in *final* p_T , which means, that, in the curve for final $p_T < 0.3$ GeV, the larger $\sinh(y)$, the smaller the values of p_T which contribute. Clearly, momentum rapidities

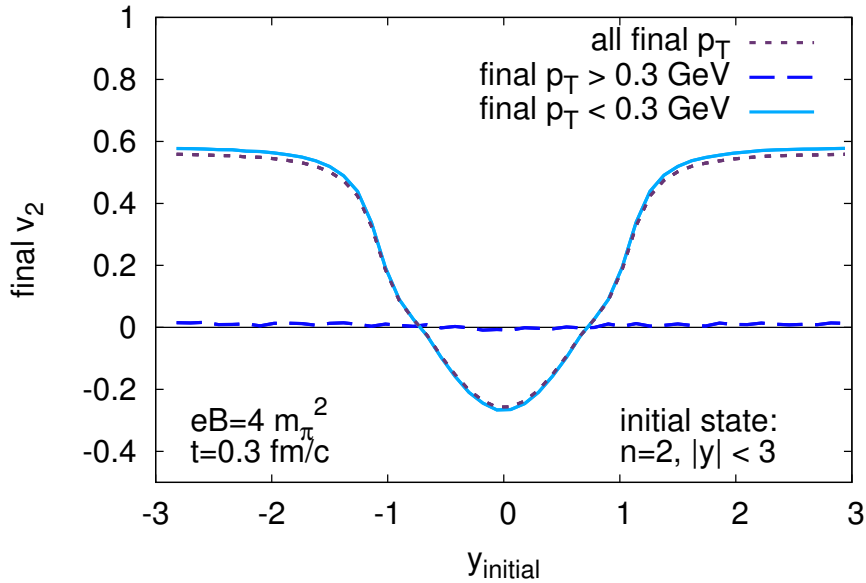


Figure 3.8.: Final average v_2 per particle for three different p_T ranges as function of *initial* rapidity y_{initial} of the particle. Here we use an initial state with power law exponent $n = 2$ and magnetic field parametrization 1. The result for $n = 3, 4$ looks very similar, only the maximal value of the final v_2 increases by up to 25%.

$y > 1$ are responsible for $\Delta p_x \gtrsim p_T$ and the average momentum asymmetries larger than zero. The three initial p_T -distributions show similar behavior, only the maximal value of v_2 increases with increasing n . Finally we turn to the differential v_2 . Using magnetic field parametrization 1, we show in Fig. 3.9 the resulting $v_2(p_T)$ without the use of the formation time, for mid- and forward rapidity and all three initial state parametrizations. The v_2 can be (temporary) up to 80 %. It is larger for forward rapidity. In Fig. 3.10 we show the result when the formation time $\Delta t_f = \cosh(y)/p_T$ was taken into account. This results in deleting all relevant interactions among the field and the particles, and the v_2 remains zero.

3.2.3. The effect of collisions

Next we want to consider the effect of particle collisions. To this end we employ the 3+1-dimensional transport approach BAMPS (Boltzmann Approach to Multi-Parton Scatterings), which solves the relativistic Boltzmann equation by Monte-Carlo techniques [40,214] for massless on-shell quarks and gluons¹ (See Chap. 4 for more details about the model).

¹corresponding to an ideal equation of state

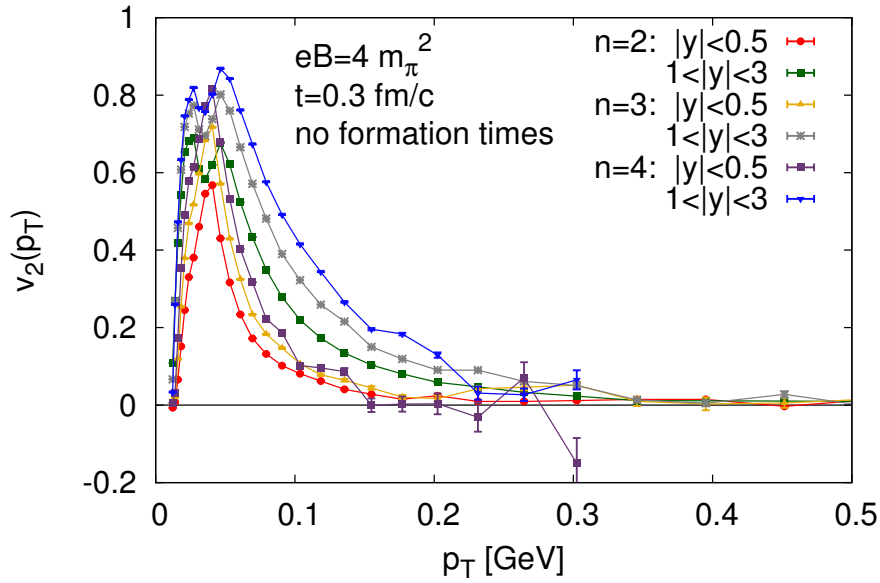


Figure 3.9.: The p_T -differential v_2 in a collisionless toy model for initial power law spectra with exponent $n = 2, 3, 4$. Here we do not assign formation times. We show results for forward- and midrapidity with magnetic field parametrization 1.

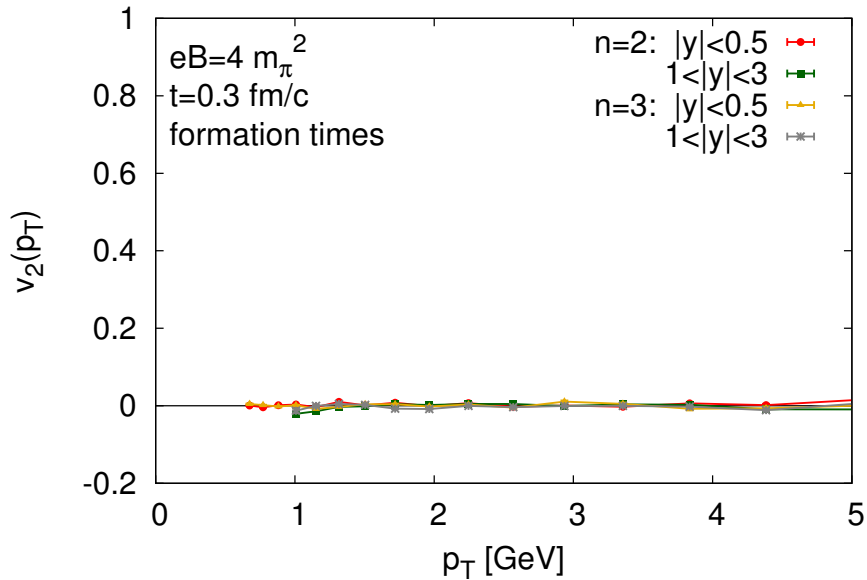


Figure 3.10.: Same as Fig. 3.9, but here formation times had been assigned. For the shown snapshot at $t = 0.3 \text{ fm}/c$, the minimum occurring momentum at midrapidity is $p_T \approx 0.66 \text{ GeV}$.

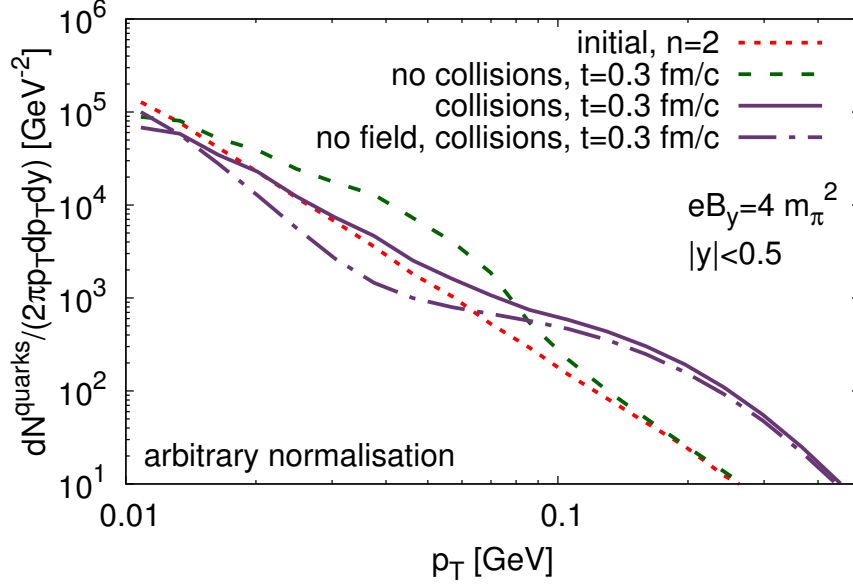


Figure 3.11.: Transverse momentum spectra of quarks under the influence of a magnetic field in a free streaming and a collisional medium. We use an arbitrary number of particles and magnetic field parametrization 1. Particles collide with constant isotropic cross sections, $\sigma_{\text{tot}} = 10$ mb.

The Boltzmann equation is ideally suited to study thermalization and isotropization processes [40, 215] and the electromagnetic fields enter by an external force term. With the phase-space distribution function $f^i(x, k) \equiv f_{\mathbf{k}}^i$ for particle species i , the Boltzmann equation reads

$$k^\mu \frac{\partial}{\partial x^\mu} f_{\mathbf{k}}^i + k_\nu q_i F^{\mu\nu} \frac{\partial}{\partial k^\mu} f_{\mathbf{k}}^i = \sum_{j=1}^{N_{\text{species}}} C_{ij}(x^\mu, k^\mu), \quad (3.10)$$

where C_{ij} is the collision term, and q_i the electric charge. The field strength tensor $F^{\mu\nu} = E^\mu u^\nu - E^\nu u^\mu - B^{\mu\nu}$, with $B^{\mu 0} = B^{0\nu} = 0$, $B^{ij} = -\epsilon^{ijk} B_k$ and $E^\mu = (0, \vec{E})$, introduces the electromagnetic forces to the charged particles [216]. For the BAMPS simulations we include 3 flavors of light quarks, antiquarks and gluons. Space is discretized in small cells with volume ΔV and particles scatter and propagate within timesteps Δt . In each cell, the probability for binary/inelastic scattering is

$$P_{22/23} = \frac{\sigma_{\text{tot},22/23}(s)}{N_{\text{test}}} v_{\text{rel}} \frac{\Delta t}{\Delta V}, \quad (3.11)$$

where $\sigma_{\text{tot}}(s)$ is the (in general Mandelstam s dependent) total cross section and v_{rel} the relative velocity. The inelastic backreaction works similar. In the simplest case, we employ constant and isotropic cross sections in BAMPS (later we will use the model with perturbative QCD (pQCD) cross sections [217, 218]). There is no qualitative difference when employing pQCD cross sections, so we restrict ourselves to constant and isotropic scattering in this study. As a new feature, we include the electromagnetic force, which within the Monte-Carlo framework reduces to the additional change of the particle momenta (for every computational timestep) by

$$d\vec{k}_i = \Delta t F_{\text{Lorentz}} = \Delta t q_i \left(\vec{E} + \vec{v} \times \vec{B} \right). \quad (3.12)$$

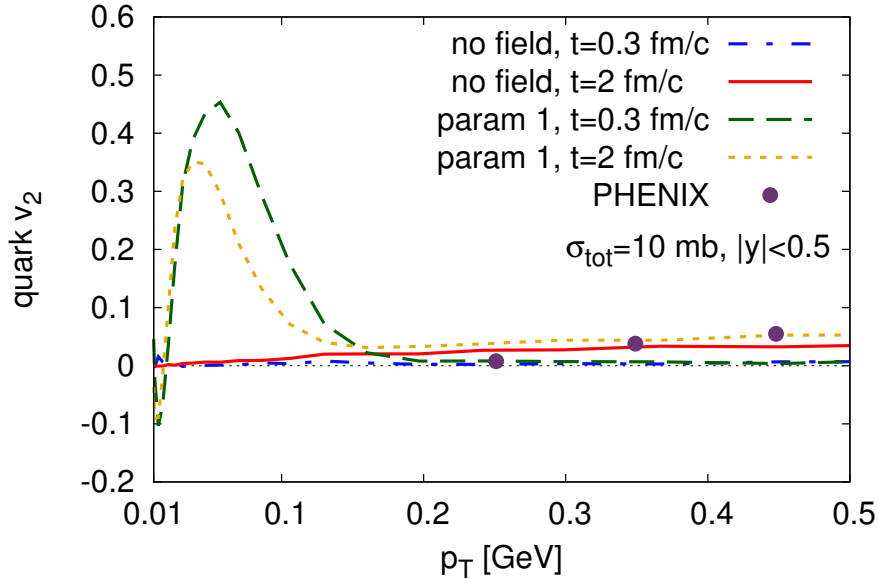


Figure 3.12.: The p_T -differential v_2 from BAMPS for the ultrasoft p_T range with and without magnetic field. The initial state is equivalent to Sec. 3.2.1, with exponent $n = 2$. The initial geometry is equivalent to an impact parameter of $b = 8.5 \text{ fm}$. We ignore formation times here. For a rough comparison we show data from PHENIX [221] (unidentified charged hadrons, $\sqrt{s_{NN}} = 200 \text{ GeV}$, 20% – 60% centrality, $|\eta| < 0.35$).

As mentioned before, we set $\vec{E} = 0$. The propagation of fields (by retarded Liénard-Wiechert potentials) generated by quarks would refine the picture, this will be mentioned later in Sec. 3.3.3. Nevertheless, electric currents appear by default in BAMPS, and the electric conductivity of the matter is built in naturally [150]. We use the same initial state in momentum space in BAMPS as in the simple model from Sec. 3.2.1, and use smooth a Glauber Monte-Carlo distribution of particle positions. Here we use an impact parameter of $b = 8.5 \text{ fm}$. The particle numbers are roughly equal to simulations performed in earlier studies using BAMPS for Au+Au collisions at $\sqrt{s_{NN}} = 200 \text{ GeV}$ [218–220]. Flavors for gluons and quarks ($N_f = 3$) are sampled randomly with probabilities $P_g = 16/52$, $P_q = 36/52$. We note that this setup is certainly rough, but it should suffice for our purpose of an optimistic upper estimate of the “Hall current” to the anisotropic flow.

We show in Fig. 3.11, how the spectra are affected by collisions. Here we see, that in the viscous case (including collisions, $\sigma_{\text{tot}} = 10 \text{ mb}$), the spectra influenced by the magnetic field for momenta $p_T \gtrsim 1 \text{ GeV}$ are very close to the field free case. Without fields, the medium thermalizes at timescales of $0.5 \sim 1 \text{ fm/c}$ (see Ref. [40]). Again, in the region of $0.01 \lesssim p_T/\text{GeV} \lesssim 0.1$ the spectra are enhanced compared to the field free spectra. The green dashed line shows the collisionless result, which is close to the initial power law for larger momenta, $p_T \gtrsim 1 \text{ GeV}$, and enhanced in the soft region.

In Fig. 3.12 we show the p_T -differential v_2 of light quarks from BAMPS, and turn the magnetic field on and off. Clearly, the field causes a strong momentum anisotropy below $p_T \sim 0.1 \text{ GeV}$, but has hardly any effect above this soft p_T -range. We see in comparison with Fig. 3.9, which shows the collisionless result, that the collisions damp the v_2 (about 20% lower v_2 at around $p_T = 40 - 60 \text{ MeV}$). Here we show results with parametrisation 1, which switches off the field at $t = 0.3 \text{ fm/c}$. After that time, the collisions isotropize this

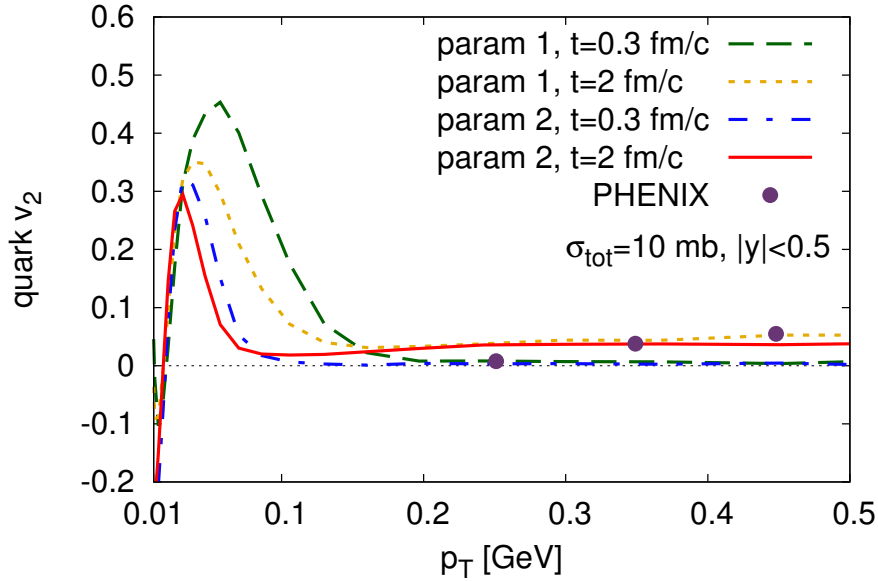


Figure 3.13.: Same as Fig. 3.12, but here we compare the magnetic field parametrizations 1 and 2.

initial flow, such that after $t = 2$ fm/c it is around 0.34 and the maximum is pushed to even lower p_T . In Fig. 3.13 we compare the effect of the two magnetic field parametrizations. Parametrization 2, probably more realistic, has a weaker effect than parametrization 1. The maximal flow is still about 30%, but, more importantly, it is shifted to much lower transverse momenta. For comparison we plot the softest points of experimentally measured unidentified charged particle flow. Unfortunately they are still measured at such high transverse momenta, that a detection of the presented magnetic field effect is unlikely at present. We need to recall at this point, that all strong elliptic flow signals appear only, when the formation time of quarks is neglected for the interaction among the field and the particles. This issue must be further addressed in future. We note, that we ignore for simplicity hadronization and the subsequent hadron gas evolution here, nevertheless, elliptic flow on the order of 30% is likely to survive to some degree. This remains subject for future work.

Photons are an ideal probe to test effects throughout the spacetime evolution of the medium, such as magnetic field induced flow, as they leave the fireball nearly undisturbed, once produced. Later in this thesis, and in Ref. [4], we present the implementation of leading order photon production rates for microscopic transport approaches such as BAMPS. As an application and example, we here anticipate the $2 \leftrightarrow 2$ photon production method (of Chap. 6) for the QGP influenced by magnetic fields.

At very low p_T (where all interesting magnetic effects happen), the microscopic photon production processes for collisions of two low p_T partons will have typical Mandelstam variables at magnitudes, where the concept of perturbative QCD methods is questionable ($s \lesssim \Lambda_{\text{QCD}}^2$). Nevertheless, we allow photons to be produced as we are mainly interested in the non-equilibrium effect of photon production from a flowing quark medium. In Fig. 3.12 we show the $v_2(p_T)$ of produced photons with that of the quarks at time $t = 2$ fm/c. Photons are produced during the whole collision, and observables are thus always spacetime averaged, weighted by the production yield. In the beginning of the collision, the medium is dense and the energy density is high, so many photons are produced, but

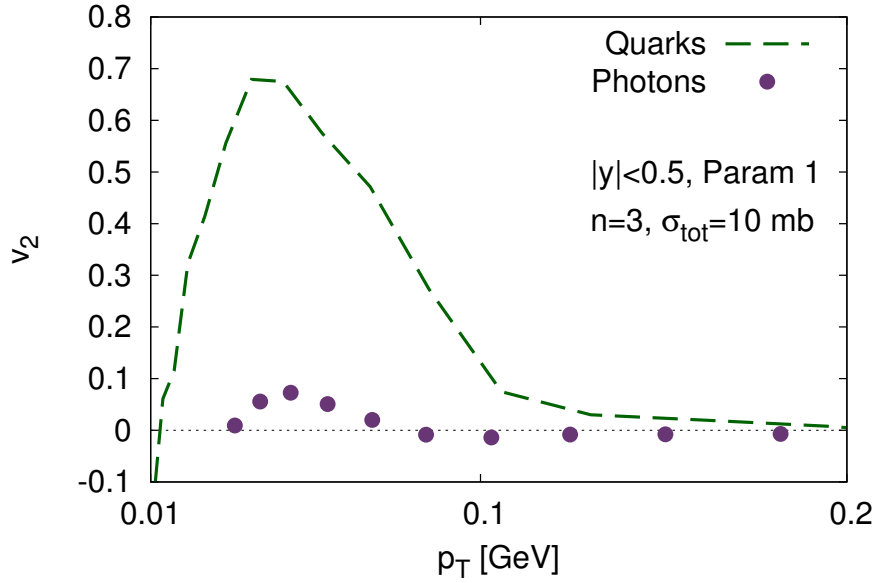


Figure 3.14.: Photon v_2 as function of p_T compared to quark v_2 for magnetic field parametrization 1. Here we use an initial state with power law exponent $n = 2$. Photons and quarks are evaluated at midrapidity $t = 2$ fm/c.

(in our simplified initial state) the flow is zero. Later, the photons inherit some of the flow, but their rate decreases steadily. This is the reason, why the observed photon flow is smaller than the pure quark flow. Below $p_T \lesssim 0.1$ GeV the photon flow is enhanced. It will be challenging to measure such an effect, considering that recent measurements of (direct) photon flow [105, 222] extend down to $p_T = 0.4$ GeV (PHENIX)/ $p_T = 1$ GeV (ALICE).

3.3. Conclusion and outlook

We have shown how the Lorentz force in heavy-ion collisions can affect observables. To this end, we have assumed two simple parametrizations for an external, homogeneous magnetic field, which is produced by the fast spectator nucleons. We investigate a free streaming, and a viscous medium (with collisions), employing the partonic transport simulation BAMPS. We use a simple boost invariant initial state, assuming a power-law in the transverse momentum distribution, and a peripheral Monte-Carlo Glauber geometry of the overlap zone. We have shown that the magnetic field will generate a strong elliptic flow only at very small transverse momenta due to the Larmor movement of the charged particles. In this very soft region, also the transverse momentum spectra are enhanced. We show that collisions will wash out both the enhancement of the spectra and the elliptic flow. However, the flow is still quite large, such that it could be measured, if experiments had access to ultrasoft transverse momenta. Assuming an initial formation time of the particles, within which the magnetic field can not act, all strong effects are deleted. The interaction of classical fields and unformed particles is however a difficult theoretical problem and must be clarified further. We emphasize, that the present study should only give an order-of-magnitude estimate of what can be expected from the magnetic Lorentz force (“Hall effect”) for light quarks. Apart of the experimental challenge, there might be other consequences. Especially final spectra of tomographic probes like photons or dileptons will inherit information of this strongly flowing but ultrasoft region. To get an idea of this effect we have shown that photons inherit a fraction of the elliptic flow from the quarks at nearly the same ultralow transverse momenta.

3.3.1. Propagating fields in the QGP

The most realistic description of a relativistic electromagnetic plasma includes propagating electromagnetic fields. Within the description of the plasma by the Boltzmann equation, an approximate solution of the Boltzmann and Maxwell equation simultaneously is possible. This would include a realistic space dependence of the external fields, and a full spacetime evolution of retarded fields including induction effects (similar to Ref. [203]). Here we shall give an outlook how this could be implemented, elaborate on the necessary algorithm and present results for fixed geometry. We assume the free quarks and gluons in the QGP to be massless. Massless quarks will however generate infinitely collimated fields, as one can see from Eq. (3.1). In Fig. 3.15 the absolute field strength around a single charged particle is plotted. One can observe how much the field is collimated perpendicular to the velocity vector. Massless charged particles emit magnetic fields only exactly transverse to their velocity, and electric fields only in the direction of it. For any practical calculation we must use a small mass for the emitting particles, in order to have a finite cone of field radiation. If the mass is small enough, it suffices to use it in the Liénard-Wiechert Potentials, and treat the particle propagation as for massless particles.

3.3.2. Algorithm for simultaneously solving the Maxwell and Boltzmann equation

In order to build an algorithm that is capable of propagating Liénard-Wiechert potentials, we have to simplify the situation. First, the fields from Eq. (3.1) depend strongly on the position of the particle and the observer (quadratic parametric dependence). We will need to discretize space into cells. This is natural to do, as the Boltzmann equation is also solved in discretized form (within BAMPS). For simplicity and consistency we should use the same space discretization for the solution of the Maxwell equation as for the

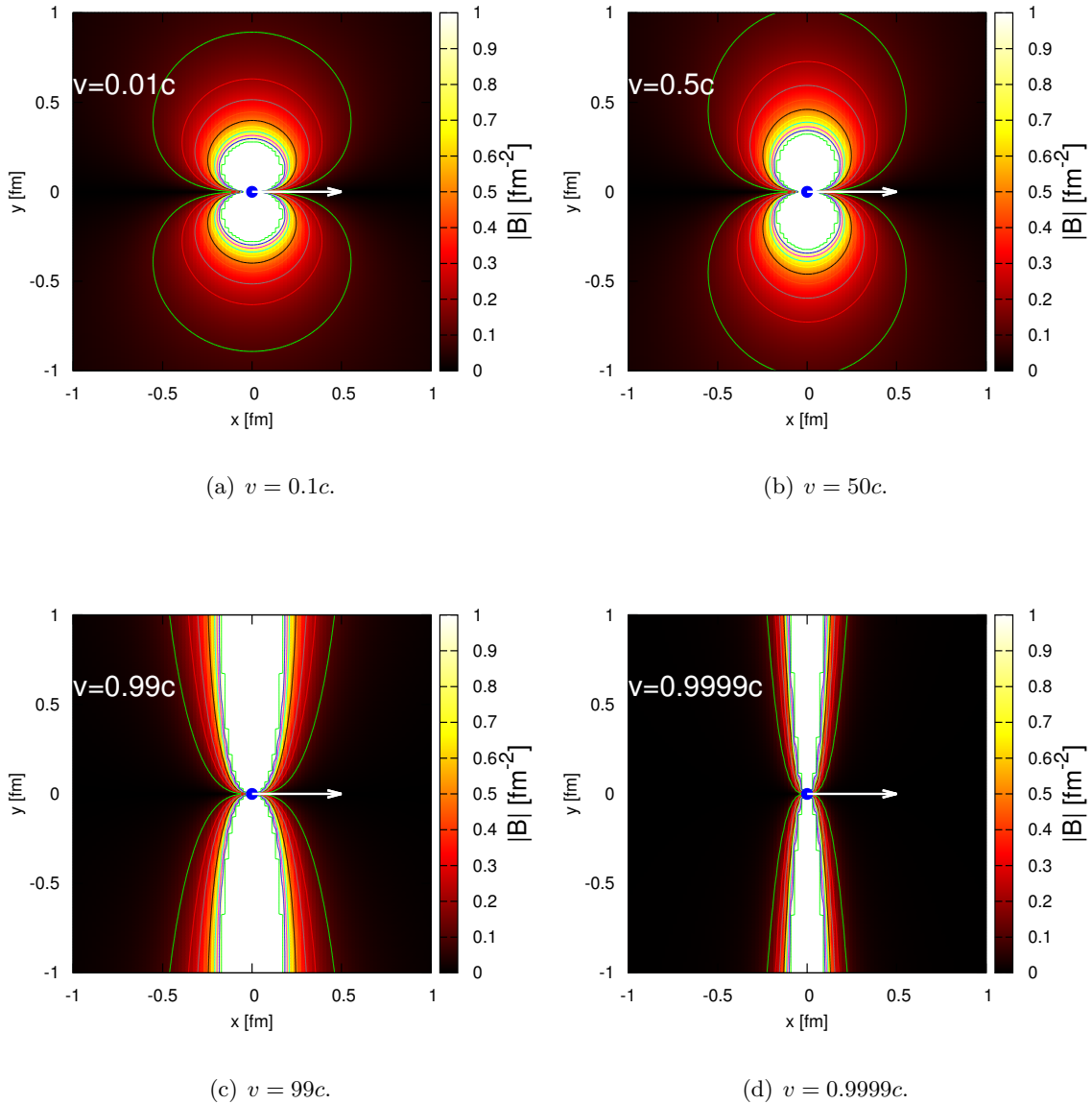


Figure 3.15.: Contour plot of the absolute field strength of the induced B -field around a charged particle (charge e) traveling with different velocities (white arrow indicates velocity direction). Clearly, at velocities close to the speed of light, the field is transversely collimated.

Boltzmann equation. Also time must be discretized. Next, the γ -factors in Eq. (3.1) must include a small mass, the dependence on this mass will be apparent in, e.g., Sec. 3.3.3. As mentioned before, we compute the fields in the future rather than recovering the past, as this is numerically better feasible. We propose the following algorithm for the propagating fields:

Algorithm 1: Propagating fields

Initialize fields $\vec{E}(\vec{r}, t), \vec{B}(\vec{r}, t) = \vec{0}$ for all future timesteps and all cell positions.

At each timestep t_i do:

for all particles j do

 get massive energy $E_j = \sqrt{\vec{p}_j^2 + m_j^2}$;

 get velocity $\vec{v}_j = \vec{p}_j/E_j$;

for all cells k do

 get cell position \vec{r}_{cell} ;

 get distance particle-cell R_{jk} ;

 compute advanced time $t_A = t_i + R_{jk}$;

 get index $\text{ind}(t_A)$ of timestep array;

 compute contribution $\Delta\vec{E}_j(R, v), \Delta\vec{B}_j(R, v)$ with Eq. (3.1);

 add $\Delta\vec{E}_j(R, v), \Delta\vec{B}_j(R, v)$ to $\vec{E}(\vec{r}_{\text{cell}}, \text{ind}(t_A)), \vec{B}(\vec{r}_{\text{cell}}, \text{ind}(t_A))$

The local induction effect should as well be evaluated from $\partial_t \vec{B}, \partial_t \vec{E}$. Before or after the propagation of the fields the collision algorithm from BAMPS must be applied, that is, calculating the collision probabilities, Eq. (3.11), colliding the particles, and sampling of the new momenta. Next, the evolution of all particles in BAMPS will be influenced by the fields at each timestep. At time t , all particles located in a cell with position vector \vec{r}_{cell} (pointing to the center of the cell) thus get the additional momentum

$$d\vec{k} = \Delta t q_i \left(\vec{E}(\vec{r}_{\text{cell}}, \text{ind}(t)) + \vec{v} \times \vec{B}(\vec{r}_{\text{cell}}, \text{ind}(t)) \right) \quad (3.13)$$

We will leave the full implementation of the simultaneous numerical solution of the Maxwell and Boltzmann equation and tests of those algorithms for a future project. The propagation of the fields from the above algorithm can however be tested by using a standard problem of electrodynamics, the magnetic field of a straight, conducting wire.

3.3.3. Testcase for dynamically propagating fields-conducting wire

In Ref. [201] it is shown that the angular component of the magnetic field around a particle with charge q with velocity v at transverse (to the velocity) distance r and longitudinal distance z at time t can be computed with

$$eB_\phi = \frac{q}{4\pi} \frac{v\gamma r}{\left(\gamma^2(vt - z)^2 + r^2\right)^{3/2}}. \quad (3.14)$$

We now assume a wire along the z-axis of length L carrying N_{ch} charges with fixed momentum $\vec{p} = (0, 0, p_z)$ and energy $E = \sqrt{p^2 - m^2}$ so that its one-dimensional charge density is $\sum_{i=1}^{N_{\text{ch}}} q_i/L$ and velocity $\vec{v} = \vec{p}/E$. We set the observer at $z = 0$ and integrate Eq. (3.14) over the longitudinal distance from $-L/2$ to $L/2$. One obtains the field strength of the magnetic field at $z = 0$ and $t = 0$ depending on the transverse distance only,

$$eB_\phi = \alpha_{\text{EM}} \left(\sum_{i=1}^{N_{\text{ch}}} q_i \right) \frac{1}{r} \frac{2v\gamma}{\sqrt{\gamma^2 L^2 + 4r^2}}. \quad (3.15)$$

It is instructive to compare to the non-relativistic result, which can be obtained by the Biot-Savart law,

$$\vec{B}(\vec{r}) = \frac{1}{4\pi} \int d^3\vec{r}' \vec{j}(\vec{r}') \times \frac{\vec{r} - \vec{r}'}{|\vec{r} - \vec{r}'|^3}, \quad (3.16)$$

with electric current $\vec{j} = qn_q\vec{v}$ for charge density n_q . The charge density in this case can be written as $n_q = \delta(x)\delta(y) \sum_{i=1}^{N_{\text{ch}}} q_i/L$. Using the same system as above, we find

$$eB_\phi = \alpha_{\text{EM}} \left(\sum_{i=1}^{N_{\text{ch}}} q_i \right) \frac{1}{r} \frac{2v}{\sqrt{L^2 + 4r^2}}, \quad (3.17)$$

which is identical to Eq. (3.15) when setting $\gamma = 1$.

As a testcase for the propagation of fields we initialize in BAMPS a straight conductor in vertical z-direction carrying a constant electric current. The current consists of a number $n_{\text{particles}}$ of single point particles with electric charge $+1e$ and momentum \vec{p} in z-direction. We impose periodic boundary conditions, that means particles moving out of the conductor at the top are inserted again at the bottom of the “wire”. We remark that the particles move without collisions. Around the conductor there is a vacuum. We then apply the algorithm in Sec. 3.3.2 for the propagating fields. At this point we include (for numerical reasons) a small “mass” *only* in the γ factor appearing in the computed fields from each charge, Eq. (3.1). Numerically, it does not make a difference if particles propagate with exact lightspeed or slightly slower due to a small mass that is why in the simulation it is sufficient to propagate them with velocity $v = 1$. It does however make it impossible numerically to compute infinitely collimated fields due to particles moving at lightspeed.

After enough time has passed, the magnetic fields close to the conductor become constant in time, and can be compared to the analytic formula.

In Fig. 3.16 we show the field strength in angular direction B_ϕ scaled by the transverse distance r and the number of particles $n_{\text{particles}}$, resulting from BAMPS and compared to Eq. (3.15) for 5 different values of the mass, from $m = 10 \text{ GeV} - 0.001 \text{ GeV}$. Clearly, the numerical results match the analytics very closely, and for $mr \lesssim 1$ the mass dependence is very small. The deviation of the numerical result extremely close to the wire ($r \lesssim 0.03 \text{ fm}$) is due to the finite cell sizes.

This shows how the correct propagation of fields can be achieved microscopically. It will be an important step for the near future to simulate a conducting medium, including collisions, where electric and magnetic fields propagate and influence the particles. Then, e.g., the Lenz effect of induction can be microscopically realized. To come to a conclusion, it will be possible with BAMPS to simulate microscopically all electromagnetic phenomena in vacuum and matter.

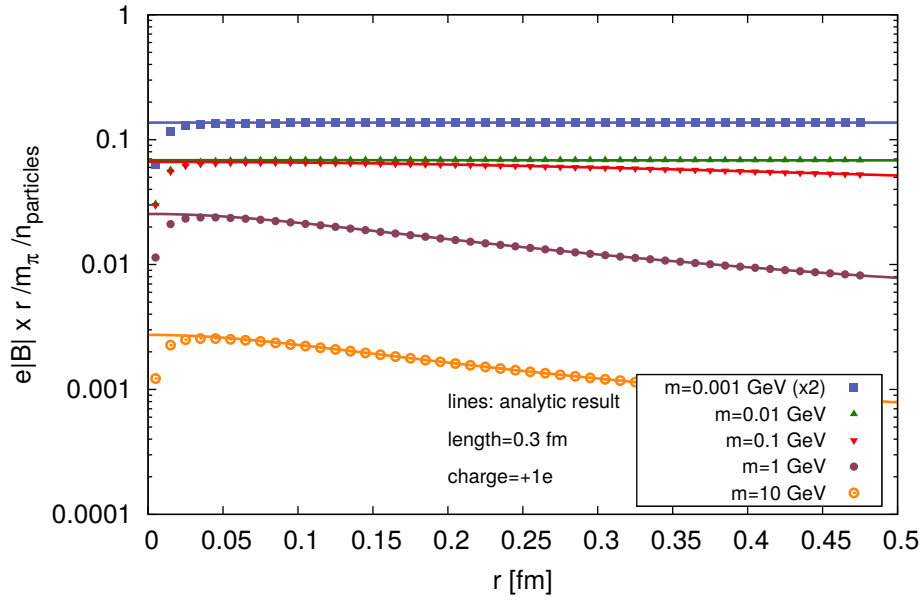


Figure 3.16.: Magnetic field strength $B \equiv B_\phi$ in angular direction induced by a conducting wire at transverse distance r from the wire for five different values of the charge carrier's mass. Symbols are results from BAMPS, using algorithm 1, and lines are the analytic result from Eq. (3.15). Here, the number of particles is $n_{\text{particles}} \equiv N_{\text{ch}}$.

4. Modeling of heavy-ion collisions

The theoretical description of heavy-ion collisions has a long history. One of the first theoretical studies about the dynamical description of high energy hadronic collisions, being essentially the spark initiating most of the modern models, was done by James Daniel Bjorken in 1982 [22]. In order to follow his arguments, let us start from a typical heavy-ion collision, say, two gold nuclei in a collider experiment with a large center of mass energy $\sqrt{s_{\text{NN}}}$. After the passing of the nuclei, which for high $\sqrt{s_{\text{NN}}}$ causes only little deceleration, a large amount of energy density is deposited at the collision point. Viewed from the center-of-mass (COM) frame, the receding nuclei are Lorentz-contracted pancakes which do not play any role in the following picture, but the central blob of energy density behaves nearly as an ideal fluid. Bjorken imposed a symmetry of this system, assuming that the fluid velocity in the beam direction (henceforth labeled longitudinal direction) is entirely given by the distance of the fluid element to the central point, z , and the time since the collision happened, t ,

$$v_z = \frac{z}{t}. \quad (4.1)$$

Due to this property, it is useful to introduce light cone coordinates or Bjorken coordinates,

$$t = \tau \cosh(\eta_s), \quad z = \tau \sinh(\eta_s), \quad \tau = \sqrt{t^2 - z^2}, \quad \eta_s = \frac{1}{2} \ln \frac{t+z}{t-z}, \quad (4.2)$$

where η_s is the space-time rapidity and τ the proper time. Similarly, we introduce the momentum rapidity y ,

$$y = \frac{1}{2} \ln \frac{E + p_z}{E - p_z}. \quad (4.3)$$

Evidently, for massless particles in the Bjorken picture, Eq. (4.1) implies $y = \eta_s$. It also implies that the initial condition after the passing of the nuclei, and the subsequent evolution is the same for all η_s 's, which is commonly referred to as boost invariance. Boost invariance reduces hydrodynamic equations to 2+1 dimensions. Central observable is the particle number with respect to rapidity, $dN/d\eta_s$, which shows a plateau structure around midrapidity, $\eta_s = 0$. In his seminal paper [22], Bjorken neglected any transverse expansion, and described only the longitudinal expansion of the system. In the next section, we show that a hydrodynamical description of this system can be for simpler cases even analytical.

4.1. Hydrodynamics

Undoubtedly the most prevalent methodology to model the dynamics of heavy-ion collisions lies in the solution of hydrodynamic equations, which rely on the assumption of local thermal equilibrium. They are direct reformulations of energy and momentum conservation and local conservation of particle number,

$$\partial_\mu T^{\mu\nu} = 0, \quad \partial_\mu N^\mu = 0. \quad (4.4)$$

In the context of heavy-ion physics, the hydrodynamic concept was initiated by the seminal papers, Refs. [223, 224] and later refined in, e.g., Ref. [225].

For the purpose of decomposing the energy-momentum tensor $T^{\mu\nu}$ and particle current N^μ , one defines, at first arbitrary, a time-like four vector u^μ , which is normalized to unity,

$$u^\mu u_\mu = 1. \quad (4.5)$$

Naturally, one can define a projection operator orthogonal to u^μ , $\Delta^{\mu\nu} u_\nu = 0$, $\Delta^{\mu\nu} = g^{\mu\nu} - u^\mu u^\nu$. It is then straightforward to decompose,

$$\begin{aligned} N^\mu &= n u^\mu + \nu^\mu \\ T^{\mu\nu} &= \epsilon u^\mu u^\nu - (p + \Pi) \Delta_{\mu\nu} + W^\mu u^\nu + W^\nu u^\mu + \pi^{\mu\nu}, \end{aligned} \quad (4.6)$$

where one can later identify the local rest frame (LRF) energy density ϵ , isotropic pressure p , bulk viscous pressure Π , energy flow W^μ as well as the shear stress tensor $\pi^{\mu\nu}$. The LRF particle density is n and the diffusion current ν^μ . The vector u^μ , which will be called four-velocity from now on, must be specified, where two choices are common: One can choose it to be either parallel to the particle number current N^μ , or to the energy flow $u_\nu T^{\mu\nu}$. The first choice, called Eckart frame or Eckart velocity, reads,

$$u^\mu = \frac{N^\mu}{\sqrt{N_\mu N^\mu}}. \quad (4.7)$$

By definition, the diffusion current ν^μ vanishes, and the heat flow $q^\mu = W^\mu - (\epsilon + p)/n u^\mu$ simplifies, $q^\mu = W^\mu$. This choice was, e.g., used in previous studies to extract the heat conductivity coefficient [226]. The second choice is the so-called Landau frame,

$$u^\mu = \frac{T^{\mu\nu} u_\nu}{\sqrt{u_\alpha T^{\alpha\beta} T_\beta^\gamma u_\gamma}}, \quad (4.8)$$

in which frame there is no flow of energy, $W^\mu = 0$, and heat flow is proportional to particle diffusion flow ν^μ . The Landau velocity is the four-velocity of the energy flow, whereas the Eckart velocity is the four-velocity of charge (or particle) flow. The shear viscosity coefficient η is defined in lowest order approximation (Navier-Stokes) by

$$\pi^{\mu\nu} = 2\eta (\nabla^\mu u^\nu - \nabla^\nu u^\mu). \quad (4.9)$$

So far, the hydrodynamic equations Eq. (4.4) have 14 unknowns for 5 linear independent equations. They must be supplemented with an underlying theory, which in almost all applications in high energy physics is kinetic theory, where the starting point is the Boltzmann equation,

$$p^\mu \partial_\mu f(\vec{x}, \vec{p}, t) = \mathcal{C}[f]. \quad (4.10)$$

Here, $\mathcal{C}[f]$ denotes schematically the collision operator and $f(\vec{x}, \vec{p}, t)$ the single particle distribution function. $\mathcal{C}[f]$ describes locally a rate of instantaneous momentum change of the particles and must be modeled in a way to represent the local, microscopic interactions of the system one wants to describe. In the case of QCD below or above the quark-hadron phase transition, the Boltzmann equation is often used to describe the medium effectively with an appropriate set of scattering cross sections in $\mathcal{C}[f]$.

In local thermal equilibrium, the solution of the Boltzmann equation is the equilibrium distribution function,

$$f_{\text{eq}}(x, p) = g \left[\exp \left(\frac{p_\mu u^\mu(x) - \mu(x)}{T(x)} \right) \pm 1 \right]^{-1}, \quad (4.11)$$

where g is the degeneracy of the particle species and μ the chemical potential. Temperature, velocity and chemical potential are in general dependent on the location. From kinetic theory, the energy momentum tensor and particle current are given by

$$\begin{aligned} T^{\mu\nu}(x) &= \int \frac{d^3\vec{p}}{(2\pi)^3} \frac{1}{2E} p^\mu p^\nu f(x, p) \\ N^\mu(x) &= \int \frac{d^3\vec{p}}{(2\pi)^3} \frac{1}{2E} p^\mu f(x, p), \end{aligned} \quad (4.12)$$

such that local charge density, energy density and pressure are given by

$$n = u_\mu N^\mu, \quad \epsilon = u_\mu u_\nu T^{\mu\nu}, \quad p = -\frac{1}{3} \Delta_{\mu\nu} T^{\mu\nu} - \Pi. \quad (4.13)$$

A strong assumption, that of the *ideal* fluid, consists in neglecting all dissipative currents, $\nu^\mu = W^\mu = \pi^{\mu\nu} = 0$. This forces strict local equilibrium, where the local scale is defined to be smaller than space-time gradients of T , ϵ and n [130]. Together with an equation of state $p = p(\epsilon, n)$, the 6 unknowns ϵ, p, n, u^μ are solved uniquely by 6 equations.

As an example, consider the Bjorken picture of only longitudinal expansion. The equations to solve reduce to

$$\begin{aligned} \partial_\tau \epsilon &= -\frac{\epsilon + p}{\tau} \\ \partial_\eta p &= 0 \\ \partial_\tau n &= -\frac{n}{\tau}, \end{aligned} \quad (4.14)$$

as well as the equation of state. For the ideal equation of state, $\epsilon = 3p$, the hydrodynamic evolution is analytic,

$$T(\tau) = T_0 \left(\frac{\tau_0}{\tau}\right)^{1/3}, \quad \epsilon(\tau) = \epsilon_0 \left(\frac{\tau_0}{\tau}\right)^{4/3}, \quad n(\tau) = n_0 \tau_0 / \tau, \quad (4.15)$$

where τ_0 is the initial time at which the temperature is T_0 , charge density n_0 and energy density ϵ_0 . We see that these quantities are independent of rapidity, consistent with the Bjorken picture.

If one assumes transverse hydrodynamic expansion, the equations are considerably more complicate and require a numerical solver for coupled differential equations. Introducing the transverse coordinate $\vec{x}_T = (x, y)$, the energy flow velocity $\tilde{v}_i = T^{\tau i} / T^{\tau\tau}$, the transport velocity $\bar{v}_i = v_i \cosh(\eta)$ and the scaled quantities $\tilde{p} = \tau p$, $\tilde{N}^\mu = \tau N^\mu$ and $\tilde{T}^{\mu\nu} = \tau T^{\mu\nu}$, the hydrodynamic equations can be written as [130],

$$\begin{aligned} \partial_\tau \tilde{T}^{\mu\nu} + \partial_x \left(\bar{v}_x \tilde{T}^{\tau\tau} \right) + \partial_y \left(\bar{v}_y \tilde{T}^{\tau\tau} \right) &= -p \\ \partial_\tau \tilde{T}^{\tau x} + \partial_x \left(\bar{v}_x \tilde{T}^{\tau x} \right) + \partial_y \left(\bar{v}_y \tilde{T}^{\tau x} \right) &= -\partial_x p \\ \partial_\tau \tilde{T}^{\tau y} + \partial_x \left(\bar{v}_x \tilde{T}^{\tau y} \right) + \partial_y \left(\bar{v}_y \tilde{T}^{\tau y} \right) &= -\partial_y p \\ \partial_\tau \tilde{N}^\tau + \partial_x \left(\bar{v}_x \tilde{N}^\tau \right) + \partial_y \left(\bar{v}_y \tilde{N}^\tau \right) &= 0. \end{aligned} \quad (4.16)$$

The relaxation of the ideal assumption leads to *dissipative* hydrodynamics. The equations are again more complicated, however nowadays widely used and common practice. Typically, the shear viscosity $\eta/s \sim 0.08 - 0.3$ [87, 135, 218] is of prime interest, and other transport coefficients are neglected (see also Chap. 2. Among the most successful and

important hydrodynamic calculations are, i.a., MUSIC [87, 227, 228], the Hydro framework from Refs. [60, 229] and Hirano’s Hydro [230] (selected Refs. only).

The transport coefficient of bulk viscosity has gained increasing interest [136–143]. The discrepancy between models and experimental data could be reduced by including a temperature dependent bulk viscosity, which was estimated to be around $\zeta/s \approx 0.3$ or larger at the phase transition temperature T_c [143].

4.2. Transport theory

The underlying assumption of any hydrodynamic simulation is that of local thermal equilibrium. Our goal is however the description of all stages of a heavy-ion collision, which does in general not fulfill this requirement. Especially the early to intermediate stage ($\tau \sim 0.2 - 1$ fm/c for central $Au + Au$ collisions) may not be thermal [40, 214, 231–236]. In the field of high energy physics, transport theory usually sets the focus on solving the Boltzmann equation. The formulation of the theory in Ref. [172] can be seen as a baseline, and most modern approaches follow these principles. The Boltzmann equation, Eq. (4.10) describes the spacetime evolution of the single particle distribution function $f(x, p)$ within a multiparticle system. It is valid under the assumption of the *Boltzmann Stoßzahlansatz*. It consists of two assumptions about the scattering processes in the gas:

1. Incoming particle momenta for each individual scattering process are uncorrelated, as well as the momenta of the outgoing particles. This is known as “Molecular Chaos”.
2. The mean free path of particles, i.e. the mean distance between the particles, is much larger than the typical distance where interaction potentials are relevant. In other words, the time it takes for the collision to take place is much shorter than the mean free time between collisions. This is the *dilute gas* assumption.

These conditions are in practice often challenged, and often pushed to their limits of applicability.

4.3. The partonic cascade Boltzmann Approach to Multiparton Scatterings

The main numerical framework of this thesis is called Boltzmann approach to multiparton scatterings (BAMPS), which simulates the partonic evolution of heavy-ion collisions [40, 214]. It is a full $(3 + 1)$ -dimensional transport approach which solves the relativistic Boltzmann equation by Monte Carlo techniques for on-shell quarks and gluons by using perturbative QCD (pQCD) scattering matrix elements including $2 \leftrightarrow 2$ and $2 \leftrightarrow 3$ (radiative) processes.

With the phase-space distribution function $f^i(x, k) \equiv f_{\mathbf{k}}^i$ for particle species i , the BE reads

$$k^\mu \frac{\partial}{\partial x^\mu} f_{\mathbf{k}}^i = \mathcal{C}^{2 \rightarrow 2}[f] + \mathcal{C}^{2 \leftrightarrow 3}[f], \quad (4.17)$$

where $\mathcal{C}^{2 \rightarrow 2}[f]$ and $\mathcal{C}^{2 \leftrightarrow 3}[f]$ are the elastic and inelastic collision terms. BAMPS uses the test particle method: The physical particle number is increased by an integer factor N_{test} ; however, all cross sections σ are simultaneously scaled down, $\sigma \rightarrow \sigma/N_{\text{test}}$. This procedure increases the statistics but does not affect the physical results. Throughout this work, we include three flavors of light quarks, antiquarks, and gluons. All particles are on

shell and massless (corresponding to an ideal equation of state) and carry physical electric charges and degeneracies. We neglect heavy quarks (see Refs. [209,219,237]) because their presence is subdominant for photon observables. Space is discretized in small cells with volume ΔV and particles scatter and propagate within time steps Δt . Within each cell, the probability for binary scattering is

$$P_{22} = \frac{\sigma_{\text{tot},22}(s)}{N_{\text{test}}} v_{\text{rel}} \frac{\Delta t}{\Delta V}, \quad (4.18)$$

where $\sigma_{\text{tot},22}(s)$ is the (in general Mandelstam- s -dependent) binary total cross section. For $2 \rightarrow 3$ particle scattering the probability is equivalently

$$P_{23} = \frac{\sigma_{\text{tot},23}(s)}{N_{\text{test}}} v_{\text{rel}} \frac{\Delta t}{\Delta V}. \quad (4.19)$$

The inelastic $3 \rightarrow 2$ backreaction has a similar probability expression¹. For massless particles, the relative velocity of the two incoming particle with four-momenta $p_{1,2} = (E_{1,2}, \vec{p}_{1,2})$ is $v_{\text{rel}} = s/(2E_1 E_2)$. BAMPS allows binary and inelastic processes, which in all cases are based on perturbative QCD cross sections with effective, infrared safe propagators.

BAMPS features a running coupling $\alpha_s(Q^2)$, which is evaluated at the momentum transfer Q^2 of the respective scattering process [219]. Among the new features developed in this thesis, are dilepton and real photon production.

4.3.1. Elastic cross sections

The total isotropic cross section for binary collisions of two onshell partons is given by

$$\sigma_{2\leftrightarrow 2} = \frac{1}{2s} \frac{1}{\nu} \int \frac{d^3 p_3}{(2\pi)^3 2E_3} \int \frac{d^3 p_4}{(2\pi)^3 2E_4} |\mathcal{M}_{2\leftrightarrow 2}|^2 (2\pi)^4 \delta(p_1 + p_2 - p_3 - p_4), \quad (4.20)$$

with symmetry factor $\nu = 2$ (1) for identical (different) final state particles. It can be transformed in terms of the differential cross section in Mandelstam t , $d\sigma_{2\leftrightarrow 2}/dt = |\mathcal{M}_{2\leftrightarrow 2}(s, t, u)|^2 / (16\pi s^2)$,

$$\sigma_{2\leftrightarrow 2}(s) = \int_{-s}^0 \frac{|\mathcal{M}_{2\leftrightarrow 2}(s, t, u)|^2}{16\pi s^2} dt \quad (4.21)$$

For the binary scattering of quarks and gluons we use all possible tree-level pQCD matrix elements, which obtain hard-thermal loop effective propagators. This amounts in dressing gluon (quark) propagators with a Debye (thermal) mass $m_{D,g(q)} \sim gT$ (for binary photon production, see Sec. 6.2.1). There are 8 different cross sections possible, $gg \leftrightarrow gg$, $q\bar{q} \rightarrow gg$, $gg \rightarrow q\bar{q}, q(\bar{q})g \leftrightarrow q(\bar{q})g$, $q(\bar{q})q(\bar{q}) \leftrightarrow q(\bar{q})q(\bar{q})$, $q\bar{q} \leftrightarrow q\bar{q}$, $qq' \leftrightarrow qq'$, $q\bar{q}' \leftrightarrow q\bar{q}'$. The differential cross sections determine the angular distribution of the outgoing momenta, whereas the total cross section $\sigma_{2\leftrightarrow 2}(s)$, evaluated at the squared center of mass energy s , influences if the process happens or not along Eq. (4.18).

¹We do not include $3 \rightarrow 2$ processes involving photons, because these are subdominant processes. For gluon radiation it is implemented.

4.3.2. Radiative cross sections

For gluon radiation in $2 \rightarrow 3$ inelastic collisions we use the Gunion-Bertsch approximation for the matrix elements [238], which was further improved in Ref. [217], whereas for radiated photons we use the full QCD+QED matrix element, see Appendix B.

The bremsstrahlung process $q + q \rightarrow q + q + \gamma$ is an important ingredient to the LO photon rate (more details in Sec. 6.3), and processes radiating gluons $x + y \rightarrow x + y + g$ influence the QGP background dynamics considerably, thus in the following we give details regarding the evaluation of the total cross section.

Radiative processes (particles $1 + 2 \rightarrow 3 + 4 + 5$) are described by the momentum labels p_1, p_2, p_3, p_4 and $p_5 \equiv k$. The collision axis be the z -axis. All considered $2 \rightarrow 3$ processes have an internal gluon propagator with momentum q . We define the momentum components transverse to the z -axis by k_T and q_T , the longitudinal k component be k_z . The rapidity of the radiated particle in the center of momentum (CoM) frame is defined as $y = 1/2 \ln[(\omega + k_z)/(\omega - k_z)]$, where $\omega = k_\perp \cosh y$ is the CoM energy of the radiated particle. The energy of the outgoing particle 3 is $E_3 = q_\perp \cosh y_3$, with its rapidity being y_3 . The angle between \vec{q}_\perp and \vec{k}_\perp is ϕ . The total cross section for radiative processes is defined as

$$\begin{aligned} \sigma_{2 \rightarrow 3} &= \frac{1}{2\nu s} \int \frac{d^3 p_3}{(2\pi)^3 2E_3} \frac{d^3 p_4}{(2\pi)^3 2E_4} \frac{d^3 k}{(2\pi)^3 2E_k} \\ &\quad \times (2\pi)^4 \delta^{(4)}(p_1 + p_2 - (p_3 + p_4 + k)) |\mathcal{M}_{2 \rightarrow 3}|^2 \\ &= \frac{1}{256\pi^4} \frac{1}{\nu} \frac{1}{s} \int_0^{s/4} dq_\perp^2 \int_{k_{\perp,\min}^2}^{s/4} dk_T^2 \int_{y_{\min}}^{y_{\max}} dy \int_0^\pi d\phi \\ &\quad \times |\mathcal{M}_{2 \rightarrow 3}|^2 \mathcal{J}[s, q_\perp, k_\perp, \phi, y], \end{aligned} \quad (4.22)$$

with a symmetry factor $\nu = n!$ for n identical final-state particles, the radiative matrix element $|\mathcal{M}_{2 \rightarrow 3}|^2$ and the Jacobian

$$\mathcal{J}[s, q_\perp, k_\perp, \phi, y] = \sum \left\{ \left(\frac{\partial F}{\partial y_3} \right)^{-1} \right\}, \quad (4.23)$$

where the sum is over the roots of

$$\begin{aligned} F &= (p_1 + p_2 - p_3 - k)^2 \\ &= s - 2\sqrt{s}(q_\perp \cosh y_3 + k_\perp \cosh y) + 2q_\perp k_\perp \cos \phi \\ &\quad + 2q_\perp k_\perp (\cosh y_3 \cosh y - \sinh y_3 \sinh y). \end{aligned} \quad (4.24)$$

The lower integration limit $k_{\perp,\min}^2 > 0$ will be explained in Sec. 6.4 in the context of radiative photon production. For gluons, a similar effective description of the LPM effect is used, supplying the Gunion-Bertsch matrix element with a step function $\Theta(\lambda - X_{\text{LPM}}\tau_f)$, where τ_f is the formation time in the CoM frame, and λ the average mean free path.

The limits in the rapidity of the outgoing particle y_{\max}, y_{\min} are functions of $k_{\perp,\min}^2, k_\perp$ and s . For given coordinates $s, k_\perp, q_\perp, y, \phi$ we can unambiguously obtain four-momenta in the CoM frame p_1, p_2, p_3, p_4, k to get the value of the matrix element at this point without any approximation. In BAMPS, for quark and gluon bremsstrahlung the Gunion-Bertsch matrix element is used, which can be given in terms of $k_\perp, q_\perp, \phi, s, y$. The phenomenological factor X_{LPM} was set to 0.3 by comparison to experiment [218]. The bremsstrahlung matrix element for photons has no approximation and will be discussed in Sec. 6.4. More details regarding these kinematics can be found in Ref. [217].

4.3.3. Selected results from BAMPS

BAMPS had been developed to investigate the thermalization of gluons within a perturbative, kinetic framework. It was shown, e.g., that gluons thermalize fast and in the subsequent evolution local thermal equilibrium is maintained. In BAMPS, not only kinetic, but also chemical equilibration sets in, on timescales about three times longer than kinetic equilibration [40,214]. This picture was applied to color-glass condensate inspired initial conditions, where the thermalization timescale was extracted and it was found that soft and hard gluons thermalize around the same time [239]. The shear viscosity to entropy ratio η/s for the elastic and inelastic pQCD scattering processes was investigated in several studies and different methods. Using only gluons, and an approximative relation depending on the transport scattering rates was carried out in Ref. [240]. Using a second order² expression for the shear viscosity, it could be extracted from (1+1) dimensional boost invariant setup from BAMPS, including inelastic processes [241]. The shear viscosity could be extracted from BAMPS in two alternative ways using the Green-Kubo method in thermal equilibrium [64] and a gradient method [242].

The relativistic Riemann problem in viscous gluon matter was formulated within BAMPS such that the transition from ideal to viscous shock waves was investigated [243]. This could clarify the regime of validity of second-order fluid dynamics in relativistic shock phenomena [244]. BAMPS was widely acknowledged as an exact numerical solver for the relativistic Boltzmann equation. A novel formulation of relativistic dissipative fluid-dynamical theory (resummed transient relativistic fluid dynamics) up to second order in Knudsen number could be shown to handle strong gradients by comparing to BAMPS [245]. In a recent study, the applicability of dissipative fluid dynamics for small systems was explored by comparing to exact solutions in BAMPS [246]. BAMPS could be supplemented to handle Bose-Einstein distribution functions with condensation [236,247].

Concerning phenomenology, BAMPS explored elliptic flow of gluons at RHIC [65,240].

BAMPS could successfully describe the nuclear modification factor R_{AA} for RHIC and LHC for charged hadrons (using parton fragmentation functions), along with a significant buildup of elliptic flow [218]. With the same parameters, the shear-viscosity to entropy ratio could be shown to be in agreement with hydrodynamic model fits to experiment. In this reference, BAMPS could as a first model explain integrated elliptic flow and nuclear modification factor within the same framework.

The extraction of electromagnetic probes, mainly photons [4], is subject of this thesis in chapter 9. The medium response due to external magnetic fields was studied in Ref. [3], and is also part of this thesis, see chapter 3.

BAMPS has been used to study *hard probes* such as jets and/or heavy quarks. Jet quenching and energy loss of highly relativistic particles was studied, e.g., in Refs. [248,249]. The momentum imbalance of reconstructed jets was studied in a similar setup [250].

Heavy quark production during the dynamical evolution of heavy-ion collisions was examined in Ref. [251]. The elliptic flow and energyloss of heavy quarks with binary collisions was studied in [209], and an updated study in Ref. [219], where the need for radiative processes was realized. In Ref. [220] radiative heavy quark processes were presented and confronted to experiment. Also the momentum imbalance of D mesons at the LHC was studied within BAMPS [252]. Furthermore, the different energy loss mechanisms of inclusive and b-tagged reconstructed jets was investigated more differentially in Ref. [253].

Apart from the shear viscosity, other transport coefficients were studied within BAMPS. The heat flow of a gluonic gas could be compared to estimates from Chapman-Enskog theory [226]. The electric conductivity of a quark-gluon system with elastic and inelastic

²Including terms of second order in a momentum expansion of the deviation of the equilibrium.

processes including a running coupling was extracted in with two different methods in Ref. [150].

Recently, the initial state in BAMPS was extended to gluon distributions obtained from the color glass condensate in order to describe elliptic flow in small systems [5]. This is part of this thesis, and presented in chapter 11.

5. Theoretical foundations

In this chapter we introduce the fundamental theoretical principles of finite temperature field theory that are needed in the following chapter on photon production. Having this explicit application in mind, we focus the discussion strongly on a few topics: definitions of the partition sum and propagators, definition and examples of the self energy, thermal emission rate of photons and the zero temperature optical theorem and Cutkosky cutting rules. This chapter thus summarizes existing formalisms in literature, putting them in context and relating them to the production of photons and dileptons in heavy-ion collisions.

5.1. Basic definitions

We begin by recapitulating the fundamental definitions of finite temperature quantum field theory. This section is closely oriented on Ref. [254,255], and we restrict ourselves to the imaginary time formalism.

Central object in quantum statistics and thermodynamics is the partition sum \mathcal{Z} , which is defined as the sum of weighted energy states of the theory. It gives direct access to thermodynamic quantities, e.g., the isotropic pressure in thermal equilibrium is given by $p = (V\beta)^{-1} \ln \mathcal{Z}(\beta, V, \mu)$, where $\beta = T^{-1}$ is the inverse temperature, V the volume and μ the chemical potential of the conserved particle species under consideration.

The partition sum can be expressed as $Z(\beta) = \text{Tr} \left(e^{-\beta \hat{H}} \right)$, where \hat{H} is the Hamilton operator of the theory (neglect chemical potentials). Then the thermal average of an operator \hat{O} in finite temperature field theory is

$$\langle \hat{O} \rangle = \frac{1}{Z(\beta)} \text{Tr} \left(\hat{O} e^{-\beta \hat{H}} \right). \quad (5.1)$$

As customary in finite temperature field theory, we use imaginary times doing a Wick rotation from the ordinary time t ,

$$t \rightarrow -i\tau. \quad (5.2)$$

The partition sum Z of a quantum many body system at finite temperature can be written in path integral form,

$$Z(\beta) = \int_{\phi(0)=\phi(\beta)} \mathcal{D}\phi(\tau) e^{-S_E(\beta)}, \quad (5.3)$$

where $S_E(\beta)$ is the unitless Euklidean action with periodic boundary conditions,

$$S_E(\beta) = \int_0^\beta d\tau \int d^3\vec{x} \mathcal{L}_E, \quad (5.4)$$

and \mathcal{L}_E the Euklidean Lagrangian. In Eq. (5.3) one sums all paths of the fields $\phi(\tau)$ with the boundary condition $\phi(0) = \phi(\beta)$. From now on, this will be implied with the symbol $\int \mathcal{D}\phi$.

5.1.1. Propagators

Propagators constitute one of the most fundamental objects in quantum field theory. They are Green's functions, describing the probability of propagation of particles. More precise, the propagator $\Delta(X - Y)$ denotes the probability to find a particle located at spacetime point X at spacetime point Y .

Using the position operators $\hat{\phi} = e^{i\hat{H}t}\hat{\phi}e^{-i\hat{H}t}$ in the Heisenberg picture, the propagator can be given in terms of a time ordered product of the Heisenberg position operators, similar to zero temperature quantum field theory,

$$\Delta(\tau) = \left\langle \mathcal{T} \left(\hat{\phi}(-i\tau)\hat{\phi}(0) \right) \right\rangle, \quad (5.5)$$

where the time ordering operator \mathcal{T} is defined as $\mathcal{T}(a(\tau_1)b(\tau_2)) = a(\tau_1)b(\tau_2)\Theta(\tau_1 - \tau_2) + b(\tau_2)a(\tau_1)\Theta(\tau_2 - \tau_1)$. Due to the periodicity of the action in Eq. (5.4), Eq. (5.5) is periodic in β , $\Delta(\tau - \beta) = \Delta(\tau)$. As an example, the harmonic oscillator (HO) with frequency ω has the propagator $\Delta_{\text{HO}}(\tau) = [(1 + n(\omega)) \exp(-\omega\tau) + n(\omega) \exp(\omega\tau)]/(2\omega)$, where $n(\omega)$ is the Bose-Einstein distribution. We observe that the propagator has the unit of inverse energy. The Fourier transform of Eq. (5.5) is

$$\Delta(i\omega_n) = \int_0^\beta d\tau e^{i\omega_n\tau} \Delta(\tau), \quad \omega_n = 2\pi n/\beta, \quad (5.6)$$

which now has units of energy⁻². It is often useful to define the generating functional

$$Z(\beta; j) = \int \mathcal{D}\phi(\tau) \exp \left[-S_{\text{E}}(\beta) + \int_0^\beta j(\tau)\phi(\tau)d\tau \right]. \quad (5.7)$$

Functional differentiation gives

$$\left. \frac{\delta^2 Z(\beta; j)}{\delta j(\tau_1)\delta j(\tau_2)} \right|_{j=0} = \int \mathcal{D}\phi(\tau) \phi(\tau_1)\phi(\tau_2) e^{-S_{\text{E}}(\beta)}. \quad (5.8)$$

It can be shown, that this is exactly the propagator,

$$\left. \frac{1}{Z(\beta)} \frac{\delta^2 Z(\beta; j)}{\delta j(\tau_1)\delta j(\tau_2)} \right|_{j=0} = \langle \mathcal{T} (q(-i\tau_1)q(-i\tau_2)) \rangle. \quad (5.9)$$

5.1.2. Scalar field theory

For any further consideration, we have to specify the action S , corresponding to a specified Lagrangian \mathcal{L} . In order to explain basic principles without bloating the required formalism, we confine ourselves to neutral scalar field theory (without conserved charges). A real scalar field $\phi(x)$ (unit energy) of particles with mass m and interaction potential $V(\phi)$ has the Lagrangian $\mathcal{L} = (\partial_\mu\phi)(\partial^\mu\phi)/2 - m^2\phi^2/2 - V(\phi)$.

Fixing the interaction term to zero, $V(\phi) \equiv 0$, one can proceed with the free (F) theory and, e.g., obtain the free imaginary time propagator,

$$\Delta_{\text{F}}(i\omega_n, k) = \frac{1}{\omega_n^2 + k^2 + m^2}, \quad (5.10)$$

which can be Fourier transformed to obtain a dependence on imaginary time,

$$\Delta_{\text{F}}(\tau, k) = \frac{1}{2\omega_k} [(1 + n(\omega)) \exp(-\omega\tau) + n(\omega) \exp(\omega\tau)], \quad \omega_k \equiv k^2 + m^2. \quad (5.11)$$

Fourier transformation of k would lead to the propagator in 4-position X , $\Delta(x)_F$, which now has units of energy squared. A non-zero interaction term, like $V(\phi) = \lambda\phi^4/4!$ with unitless coupling λ , will induce a different propagator. It can be defined like in Eq. (5.8),

$$\Delta(X - Y) = \frac{1}{Z(\beta)} \int \mathcal{D}\phi \phi(X)\phi(Y) e^{-S_E(\beta)}. \quad (5.12)$$

The propagator in Eq. (5.12) is called a *full* propagator, because it contains all possible processes (within the theory) in the two-point amplitude of the particle. The most easy way how to deal with the propagator in Eq. (5.12) is the perturbative expansion of the exponential, under the condition that one has a small quantity in the action, e.g., the dimensionless coupling λ . Doing so, up to first order in λ , yields

$$\Delta(X - Y) = \Delta_F(X - Y) - \frac{\lambda}{2} \int_0^\beta d^4 Z \Delta_F(X - Z) \Delta(Z = 0) \Delta(Z - Y) + \mathcal{O}(\lambda^2). \quad (5.13)$$

We allow now real values of time t , and define a time-ordered propagator

$$D(t) \equiv \left\langle \mathcal{T} \left(\hat{\phi}(t) \hat{\phi}(0) \right) \right\rangle. \quad (5.14)$$

Immediately one can also define its two terms,

$$\begin{aligned} D^<(X) &\equiv \left\langle \hat{\phi}(0) \hat{\phi}(X) \right\rangle \\ D^>(X) &\equiv \left\langle \hat{\phi}(X) \hat{\phi}(0) \right\rangle. \end{aligned} \quad (5.15)$$

5.1.3. Spectral density

For later purposes, we introduce the spectral density, or spectral function ρ ,

$$\rho(k^0) = D^>(k^0) - D^<(k^0). \quad (5.16)$$

The spectral function (dimension energy⁻¹) is a real function, odd in its argument.

The Matsubara propagator in Eq. (5.6) is complex, but its domain of definition is the set of discrete Matsubara frequencies on the imaginary axis. One can analytically continue the domain uniquely, such that $\Delta(z)$, $z \in \mathbb{C}$ where z has the dimension of energy. The requirement is, that $|\Delta(z)| \rightarrow 0$ for $|z| \rightarrow \infty$ and the analyticity of $\Delta(z)$ in the complex z plane without the real axis. Then, using Eq. (5.16), we can write

$$\Delta(i\omega_n) = - \int_{-\infty}^{\infty} \frac{dk^0}{2\pi} \frac{\rho(k^0)}{i\omega_n - k^0} \rightarrow \Delta(z) = - \int_{-\infty}^{\infty} \frac{dk^0}{2\pi} \frac{\rho(k^0)}{z - k^0}. \quad (5.17)$$

We now introduce the retarded propagator, which is the most relevant function for linear response theory. It can be defined in various ways [254, 255]. The retarded (advanced) propagator $D_{\text{ret}}(D_{\text{adv}})$ with space-time dependence is

$$\begin{aligned} D_{\text{ret}}(X) &= \left\langle \theta(x^0) \left[\hat{\phi}(X) \hat{\phi}(0) \right] \right\rangle, \\ D_{\text{adv}}(X) &= - \left\langle \theta(-x^0) \left[\hat{\phi}(X) \hat{\phi}(0) \right] \right\rangle. \end{aligned} \quad (5.18)$$

The connection of the retarded propagator to the finite temperature imaginary time propagator in Eq. (5.6) is most easily given in momentum space by the analytic continuation $D_{\text{ret}}(k^0) = -i\Delta(k^0 + i\eta)$, where η is a small positive number.

5.1.4. Self energy

The full propagator $\Delta(X - Y)$ to first order in λ can be Fourier transformed

$$\Delta(i\omega_n, k) = \Delta_F(i\omega_n, k) - \frac{\lambda}{2} \Delta_F(i\omega_n, k) \left(T \sum_m \int \frac{d^3k}{(2\pi)^3} \Delta_F(i\omega_m, k) \right) \Delta_F(i\omega_n, k) \quad (5.19)$$

The self-energy Π is defined via

$$\Delta^{-1}(i\omega_n, k) = \Delta_F^{-1}(i\omega_n, k) + \Pi(i\omega_n, k) \quad (5.20)$$

or

$$\frac{\Delta(i\omega_n, k)}{\Delta_F(i\omega_n, k)} = (1 + \Pi(i\omega_n, k) \Delta_F(i\omega_n, k))^{-1} \quad (5.21)$$

To first order in λ , we have from Eq. (5.19)

$$\begin{aligned} \frac{\Delta(i\omega_n, k)}{\Delta(i\omega_n, k)_F} &= 1 - \left(\frac{\lambda T}{2} \sum_m \int \frac{d^3k}{(2\pi)^3} \Delta_F(i\omega_m, k) \right) \Delta_F(i\omega_n, k) \\ &= \frac{1}{1 + \left(\frac{\lambda T}{2} \sum_m \int \frac{d^3k}{(2\pi)^3} \Delta_F(i\omega_m, k) \right) \Delta_F(i\omega_n, k)} + \mathcal{O}(\lambda^2) \end{aligned} \quad (5.22)$$

By comparing with Eq. (5.21) we conclude the explicit expression for the self-energy to first order in λ ,

$$\Pi(i\omega_n, k) = \frac{\lambda T}{2} \sum_m \int \frac{d^3k}{(2\pi)^3} \Delta_F(i\omega_m, k) \quad (5.23)$$

Doing the integral, we find the self energy in scalar field theory to first order in λ , $\Pi = \lambda T^2/24$. We remark that the Schwinger-Dyson equation $\Delta = \Delta_F - \Delta_F \Pi \Delta$ is identical to Eq. (5.20).

The *retarded* self energy is accessible by analytic continuation from the imaginary time self energy, or can be derived from the retarded Dyson-Schwinger equation,

$$\Delta^R = \Delta_F^R - \Delta_F^R \Pi^R \Delta^R. \quad (5.24)$$

The self energy describes particle interactions within the propagation of a particle between two space-time points. Without interactions, the self energy vanishes. One can construct Feynman rules for the self energy, and subsequently impose it any any given order in perturbation theory by diagrammatic methods [255]. In simple cases, the self energy acts effectively as a thermal mass, $m_{\text{eff}} \sim \sqrt{\Pi}$. For applications in thermal field theory, it became very useful to use an effective field theory, where self energy insertions in propagators are resummed. This is known as hard thermal loop (HTL) effective theory, proposed by Braaten and Pisarski [256–258]. In later chapters, we will make use of effective propagators, known under the concept of Debye screening, which dates back to the HTL approximation.

5.2. Thermal emission rate of photons

In thermal equilibrium at temperature T the emission rate of photons with four momentum $K^\mu = (E_k, \vec{k})$ is proportional to the imaginary part of the trace of the retarded photon self energy $\text{Im} \Pi_\mu^{R, \mu}$ [255, 259],

$$E_k \frac{dR}{d\vec{k}} = \frac{-2}{(2\pi)^3} \text{Im} \Pi_\mu^{R, \mu} \frac{1}{e^{E_k/T} - 1}. \quad (5.25)$$

This is a valid description to all orders in the strong coupling g (for possible strongly interacting contributions in $\text{Im}\Pi_{\mu}^{R,\mu}$); however, only to order e^2 for electromagnetic interactions. This carries the assumption, that the medium is so dilute, that the photon does not scatter anymore once produced. More precise, the formula is valid for systems of spatial extends smaller than the mean free path of the photon (which is the case in any application of interest within this thesis).

5.3. Optical theorem and cutting rules

The optical theorem relates the imaginary part of a Feynman diagram to a sum of products of matrix elements of physical sub-processes. This can be refined to a set of so-called cutting rules, which give a prescription how to obtain sub-diagrams from a Feynman diagram from which its imaginary part is easier to compute. In the later chapters of this work, we will need the evaluation of the imaginary part of a self-energy diagram for a different reason: The sub-diagrams obtained by ‘‘cutting’’ a self-energy diagram are physical scattering processes which are suitable for dynamical modeling in transport approaches, whereas the imaginary part of the self energy itself would only give a rate by Eq. (5.25).

The optical theorem follows directly from the unitarity of the S -matrix. The S -matrix, as defined in, e.g., Ref. [7], relates asymptotically incoming and outgoing many particle states

$$\langle p_1 p_2 \cdots | k_1 k_2 \cdots \rangle_{\text{ingoing}} \equiv \langle p_1 p_2 \cdots | S | k_1 k_2 \cdots \rangle. \quad (5.26)$$

The following discussion follows mainly Refs. [7,260]. There is the probability that even in interacting theories there is no scattering among the incoming particles, such that $S = \mathbb{1}$. One thus conveniently separates the interesting from the non-interacting part,

$$S = \mathbb{1} + iT. \quad (5.27)$$

The usual matrix element \mathcal{M} is defined by

$$\langle p_1 p_2 \cdots | iT | k_1 k_2 \cdots \rangle = (2\pi)^4 \delta^{(4)} \left(\sum k_i - \sum p_f \right) i\mathcal{M}(k_1, k_2, \dots \rightarrow p_1, p_2, \dots). \quad (5.28)$$

From the unitarity of the S -matrix, $SS^\dagger = \mathbb{1}$, it follows,

$$\begin{aligned} \mathbb{1} &= S^\dagger S = (\mathbb{1} - iT^\dagger)(\mathbb{1} + iT) = \mathbb{1} - iT^\dagger + iT + T^\dagger T \\ &\Leftrightarrow i(T^\dagger - T) = T^\dagger T \end{aligned} \quad (5.29)$$

We sandwich the right hand side of this equation by initial $|i\rangle$ and final $\langle f|$ states. We can now insert a complete set of orthogonal states $|n\rangle\langle n| = |\{p_i\}\rangle\langle\{p_i\}|$,

$$\langle f | T^\dagger T | i \rangle = \sum_n \prod_{i=1}^n \int \frac{d^3 p_i}{(2\pi)^3} \frac{1}{2E_i} \langle f | T^\dagger | n \rangle \langle n | T | i \rangle. \quad (5.30)$$

We specialize now to the case, where the initial and final states are the same $|i\rangle = |f\rangle$, which is the case for self energy diagrams which shall be important in this work. The ingoing and outgoing momentum be k , the matrix element of the process $\mathcal{M}(k \rightarrow k)$. Using Eq. (5.28) we can write Eq. (5.29) in terms of matrix elements,

$$\begin{aligned} -i [\mathcal{M}(k \rightarrow k) - \mathcal{M}^*(k \rightarrow k)] &= \sum_n \prod_{i=1}^n \int \frac{d^3 p_i}{(2\pi)^3} \frac{1}{2E_i} \mathcal{M}^*(k \rightarrow n) \mathcal{M}(k \rightarrow n) (2\pi)^4 \delta^{(4)}(A) \\ \Leftrightarrow 2\text{Im}\mathcal{M}(k \rightarrow k) &= \sum_n \prod_{i=1}^n \int \frac{d^3 p_i}{(2\pi)^3} \frac{1}{2E_i} \delta^{(4)}(A) |\mathcal{M}(k \rightarrow n)|^2, \end{aligned} \quad (5.31)$$

where the function A within the delta function depends on k and all momenta in the outgoing state of the matrix elements,

$$A \equiv k - \sum_{j=1}^n p_j. \quad (5.32)$$

Equation (5.31) is the *Optical Theorem*. This equation says, that the imaginary part of a self energy diagram is given by the sum of all its sub-scattering diagrams, each of which contains on-shell incoming and outgoing states. The right hand side can be reformulated to a sum of total cross sections for scattering processes from the initial particles to all possible final states of these particles.

In his original work [261], Cutkosky has invented a set of cutting rules, which can be applied to the original scattering amplitude to obtain the sub-processes of Eq. (5.31). *Cutting* essentially means putting propagators on-shell, but we shall be more detailed in the following. The optical theorem was proven to all orders in perturbation theory by using the cutting rules.

Zero temperature and density cutting rules

In the following we recapitulate the zero temperature and density derivation of the cutting scheme by 't Hooft and Veltman in Ref. [262]. For simplicity we work with a simple scalar field theory (see Sec. 5.1.2). Consider a Feynman diagram with n vertices, from which we shall attempt to find the imaginary part. In the simplest case, this can be a one-loop self energy. We first ignore external lines, and write the corresponding amplitude in coordinate space as $F(x_1, x_2, \dots, x_n)$. We will first introduce a subset of diagrams obtained from F , and then sketch the derivation of the *largest time equation*. Then we attach external lines and transform F to be a physical amplitude. Subsequently we find rules for the non-vanishing set of sub-diagrams, obtained by graphically cutting the diagram. It then becomes apparent, that the imaginary part of the amplitude is given by the sum of the cut diagrams.

We begin with the Källén-Lehmann representation of the propagator from space time x_i to x_j ,

$$\Delta_{ij}^{\pm}(x_i - x_j) = \int \frac{d^4 p}{(2\pi)^3} e^{ip \cdot (x_i - x_j)} \Theta(\pm p_0) \rho(p^2), \quad (5.33)$$

where $\rho(p^2)$ is the a positive spectral density and we define the Feynman propagator for positive and negative energies,

$$\Delta_{ij}(x) = \Theta(x_0) \Delta_{ij}^+(x) + \Theta(-x_0) \Delta_{ij}^-(x), \quad (5.34)$$

with $x \equiv x_i - x_j$. Note that $(\Delta^{\pm})^* = \Delta^{\mp}$, and $\Delta_{ij}^{\pm} = \Delta_{ji}^{\mp}$, and

$$\Delta_{ij}^* = \Theta(x_i^0 - x_j^0) \Delta_{ij}^- + \Theta(x_j^0 - x_i^0) \Delta_{ij}^+. \quad (5.35)$$

Each vertex obtains a coupling constant ig . We now draw all possible copies of the original Feynman diagram $F(x_1, x_2, \dots, x_n)$ where we *circle* one or more vertices in all possible combinations. We define new functions F for each of these circled diagrams by the following rules,

1. Use the original amplitude as a starting point
2. Replace the propagator Δ_{ij} by Δ_{ij}^+ if vertex x_i is circled but not vertex x_j

3. Replace the propagator Δ_{ij} by Δ_{ij}^- if vertex x_j is circled but not vertex x_i
4. Replace the propagator Δ_{ij} by Δ_{ij}^* if vertices x_i and x_j are circled
5. Insert a factor (-1) for each circled vertex.

If vertex x_i is not circled, and the time component of x_i is larger than any other time component of any other vertex, the value of the diagram is minus the value of the same diagram with the vertex x_i circled. This is called *largest time equation*, and can be stated as follows,

$$F(x_1, \dots, x_i, \dots, \textcircled{x_j}, \dots, x_n) = -F(x_1, \dots, \textcircled{x_i}, \dots, \textcircled{x_j}, \dots, x_n). \quad (5.36)$$

This is easy to proof from the definitions Eq. (5.34) and Eq. (5.35), considering a vertex combination $\dots x_k \dots x_i \dots \textcircled{x_j} \dots$ and its counterpart $\dots x_k \dots \textcircled{x_i} \dots \textcircled{x_j} \dots$. What do these rules mean? Clearly, circling all vertices is nothing else than complex conjugating the diagram,

$$F(\textcircled{x_1}, \textcircled{x_2}, \dots, \textcircled{x_n}) = F^*(x_1, x_2, \dots, x_n). \quad (5.37)$$

Having a circled and an uncircled vertex controls the flow of energy inside the diagram; the energy flow points always from the uncircled to the circled vertex, which is a consequence from Eq. (5.33). Immediately from Eq. (5.36) follows

$$\sum_{\text{all possible circles}} F(\dots, \textcircled{x_i}, \dots) = 0. \quad (5.38)$$

Introducing now external lines to the diagrams, one must multiply the corresponding phase factor (e.g., external momentum k attaching to vertex x needs $\exp(ik \cdot x)$), and integrate over all internal vertices. The Fourier transform of the propagators is proportional to Θ -functions of the energy, $\Delta^\pm(k) \sim \Theta(\pm k^0)$, thus energy must flow into circled vertices. Due to energy conservation, some combinations of circlings in Eq. (5.38) vanishes. Working out the possible cases one can proof that only those diagrams survive which have two connected regions, each one connects to at least one external line: one circled region and one uncircled region. Thus one must be able to “cut” through the diagram with a continuous cut, thus separating the diagram in two parts, each containing at least one external line. What follows is the Cutkosky cutting rule, where \tilde{F} denotes the Fourier transform of F ,

$$\tilde{F}(\text{no circles}) + \tilde{F}(\text{all circled}) = - \sum_{\text{all possible cuts}} \tilde{F}(k_1, \dots, k_n). \quad (5.39)$$

The diagrams F , multiplied by the sources and integrated over space are a contribution of the S-matrix, Eq. (5.27). Multiplication of a factor $-i$ yields the T-matrix and Eq. (5.39) is of the form of Eq. (5.29) and as such equivalent to the optical theorem¹

Note that for fermions, special care has to be taken about the routing of the charge and the momenta. To be more precise to what has been said above, positive energy flows from uncircled to circled vertices, but negative energy flows from circled to uncircled vertices. One should therefore name all positive momenta in the original diagram, together with the flow of charge. Next, the cuts are applied. For each cut diagram, working on one side of the cut, one specifies if the cut propagator (which now represents an external line) is ingoing or outgoing. Hereby the momentum label must be kept [263]. Simple Feynman

¹More details can be found in Ref. [262].

rules for cut diagrams can be found, e.g., in Ref. [262]. The resulting contribution of each cut diagram in the sum of Eq. (5.39) is an integral over a product of the matrix element of the diagram at the left hand side of the cut times the complex conjugated of the right hand side. Specifically, axis-symmetric cuts generate squared matrix elements of the process left (or right) of the cut.

Specific examples of cut diagrams and their corresponding matrix elements can be found in Ref. [264]. Albeit for QED with a massive vector particle, the principles are universal. Ref. [264] focuses on finite temperature and density cutting rules, the worked out matrix elements of self energy cuts are valid at zero temperature, too. In Ref. [263] self energy diagrams for a scalar field theory are evaluated up to four-loop order using cutting rules. In Ref. [265], important examples for scattering amplitudes from, e.g., QED self energies are given, which are very similar to what we will need in Chap. 6.

Finite temperature cutting rules

One of the first worked out examples of an imaginary part of a self energy can be found in Ref. [266]. This was still done without a cutting scheme, however, Kobes and Semenoff generalized the Cutkosky cutting rules to finite temperature in Ref. [267], and used the results from Ref. [266] as reference. Later, Refs. [264, 265, 268] improved on this scheme. Especially the handling of internal loops was refined. In Ref. [268], physical amplitudes were extracted in the imaginary time formalism for the two loop vector boson self energy in QCD, whereas the authors of Ref. [267] work in the real time formalism. At finite temperature, Eq. (5.39) can not be written in this form. The notion of *cuts* can not be applied anymore without further constrains [267] as now thermal factors appear. Physically, the thermal medium can absorb and emit particles, and diagrams which would have impossible combinations of circlings at zero temperature can survive.

6. Microscopic photon production

Quantum electrodynamics is the most consistent and complete theory of light and its interaction with electric charges. The electromagnetic field is quantized, and the *photon* is its elementary excitation.

In this chapter we review perturbative photon production processes in ensembles of on-shell quarks and gluons, and explain different orders in perturbation theory. In this context we construct algorithms for what we call *microscopic* photon production, as opposed to thermal photon rates, which are used, e.g., in hydrodynamics.

We distinguish two types of microscopic photon production processes. One possibility is the use of algorithms based on vacuum scattering matrix elements with one outgoing photon, which are reasonably modified to yield correct rates in a thermal setup. Those photon production processes require the momenta of two individual scattering partners (quarks and gluons). It is the purpose of this chapter to construct the corresponding cross sections.

This is methodically different from photon production based on a radiation kernel, which requires the temperature of the medium and the momentum of a radiating quark. The latter method will be described in Chapter 7 in the context of jet emission, however, it is numerically also suitable for (thermal or nearly thermal) ensembles of quarks.

6.1. Construction of photon production processes

In this section we explain order by order the different production mechanism for photons. As detailed in Sec. 5.2, the imaginary part of the retarded photon self energy controls the rate of photon production, Eq. (5.25). In order to understand the underlying microscopic processes, our aim is to find out which incoming and outgoing states are relevant for the production of a real photon, and subsequently obtain the corresponding scattering amplitudes. The photon self energy can be expanded in loops up to some finite order in the strong coupling g . Then, by the optical theorem, Eq. (5.31), or the Cutkosky cutting rule from Eq. (5.39) the imaginary part of the self energy can be obtained as a set of squared matrix elements, and Eq. (5.25) is equivalent to a rate equation in relativistic kinetic theory. This is not only useful for the understanding of the microscopic origin of the interactions, but in many cases the only practical way how to deal with the self energy. In the following we will go loop by loop through the corresponding processes. The one-loop contribution turns out to vanish, whereas the two-loop diagram constitutes Compton scattering and quark-antiquark annihilation processes. Higher loops correspond to inelastic pair annihilation and bremsstrahlung.

In Sec. 5.3 we presented the cutting rules for zero and finite temperature. Finite temperature cutting rules are considerably more complicate and intricate, but we shall not need to evaluate them. The reason is, that for the microscopic implementation of photon production processes we will need solely the vacuum scattering matrix elements $\mathcal{M}(\{\text{initial}\} \rightarrow \gamma + X)$. The incoming momenta can be thermally distributed or not, this is only part of the evolution within the dynamical transport setup. Several approaches in literature seek an algorithmic and thus easier way how to deal with self energies, with the goal to compute exactly this quantity. In this case, naturally, thermal weights must be

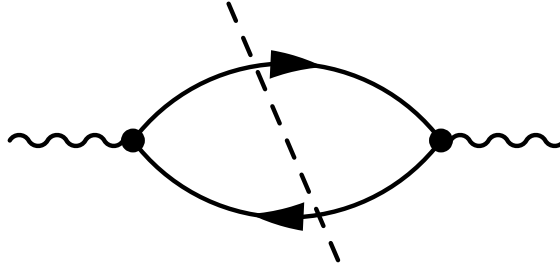


Figure 6.1.: The photon self energy at one loop order, and the only possible cut.

taken into account, and zero temperature cutting rules cannot be applied any more.

We repeat the zero temperature cutting prescription formally derived in Sec. 5.3: Draw the self-energy diagram with unique momentum labels on all internal propagators, respecting momentum conservation at the vertices. Draw all topologically different cuts (through propagators), that separate the diagram into two, where each of the two contains at least one external particle. Specify how momentum flows through the cuts on both sides of the cut. Cut lines become external lines (they are put on-shell). All external lines can represent either incoming or outgoing particles. In all following diagrams, the arrows on quark propagators or external lines denote the flow of negative electric charge. For each cut diagram, we may apply the zero-temperature Feynman rules to obtain the amplitudes. For the diagrams considered here, where we have a circularly connected quark line, the momentum routing can be clockwise or anticlockwise, and the same cut with both routings must be included.

It is useful to label cut propagators at the cut point and the external photon with either the label „in“ or „out“ in all possible ways, denoting whether the particle is incoming in the scattering amplitude or outgoing. Do this labeling on the left as well as on the right side of a single cut propagator with the same label. Having done this, use the usual zero temperature Feynman rules to write down the amplitude for the left hand side $\mathcal{M}_P^{(\text{left})}$ and the right hand side of the diagram $\mathcal{M}_P^{(\text{right})}$, understanding the external „in“ („out“) lines as incoming (outgoing) particles. By this procedure, an axis-symmetric cut generates now amplitudes that are the complex conjugate of each other, $\mathcal{M}_P^{(\text{left})} = \left(\mathcal{M}_P^{(\text{right})}\right)^*$. For axis-symmetric cuts, the contribution to the imaginary part of the self energy generates a squared matrix element, more precise, it includes the product of the left-hand side of the cut diagram with the right-hand side. Cuts which are not graphically axis-symmetric, generate interference diagrams. In general, every cut diagram has the interpretation as a product of the left and right scattering matrix elements, that it creates.

6.1.1. One-loop contribution

The simplest possible contribution to the photon self energy is shown on Fig. 6.1. It is of order e^2 , and corresponds to quark antiquark annihilation to a photon, quark antiquark production from a photon or photon absorption by a quark or antiquark. All processes are kinematically forbidden; thus it does not contribute to the rate.

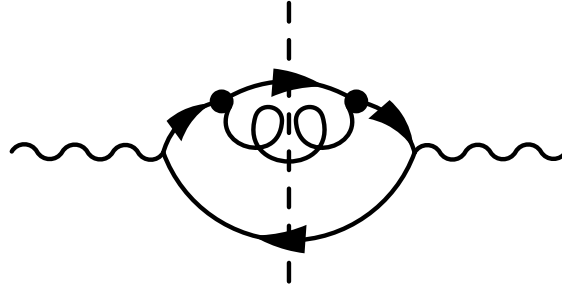


Figure 6.2.: One particular contribution to the photon self energy at two loop order, and one particular cut that is possible.

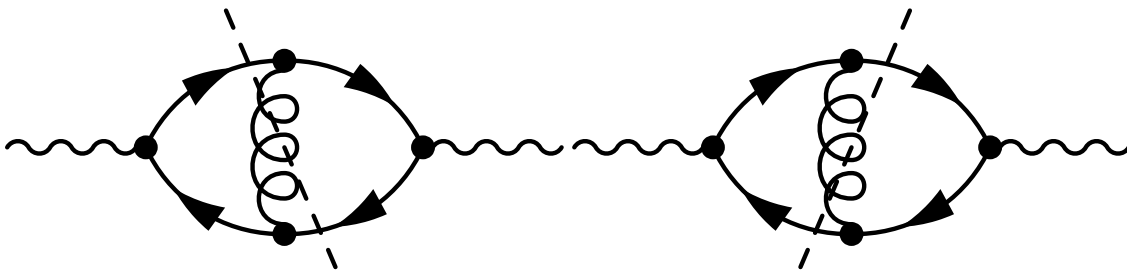


Figure 6.3.: One particular contribution to the photon self energy at two loop order, and the two cuts that are possible, but give equivalent contributions after changing the routing of the momenta.

6.1.2. Two-loop contribution and symmetric cuts

The next possible order of the self-energy is e^2g^2 , including one gluon propagator¹. The gluon propagator can be connected in two different ways. In Fig. 6.3 the diagram with one so-called *gluon rung* is shown. It can be seen as a vertex correction to the diagram from Fig. 6.1. The dashed lines indicate the possible symmetric cuts, that are equivalent upon reversing the momentum routing of the quark loop. In Fig. 6.2 the diagram with a gluon is shown, which can be seen as a propagator correction to the diagram from Fig. 6.1. The dashed line indicates the only possible symmetric cut. Of course the gluon can also attach to the lower quark line, which again is the same upon reversing the quark momentum direction. We will show now, how the well-known diagrams² of Fig. 6.4 are encoded in these cut diagrams. Let us consider Fig. 6.2 first. We define the photon to carry the label „out“, as we are exclusively interested in photon *production* and not decay. There are four possible ways to assign the labels to the external lines after the cuts:

1. The cut gluon propagator can be „out“, the cut (and now external) quarks are then „in“. It can be read off from Fig. 6.2, that in this case a quark with negative charge is incoming, and a quark with positive charge is incoming; the photon and a gluon

¹It will become clear later, why also diagrams with more than one gluon propagator contribute at the same order to the rate, even if the diagrams are formally of higher order. First we explain the diagrams arising from one gluon propagator, the calculation with two or more gluons is more involved

²These diagrams only have been used by Refs. [23,269,270] to obtain a photon production rate.

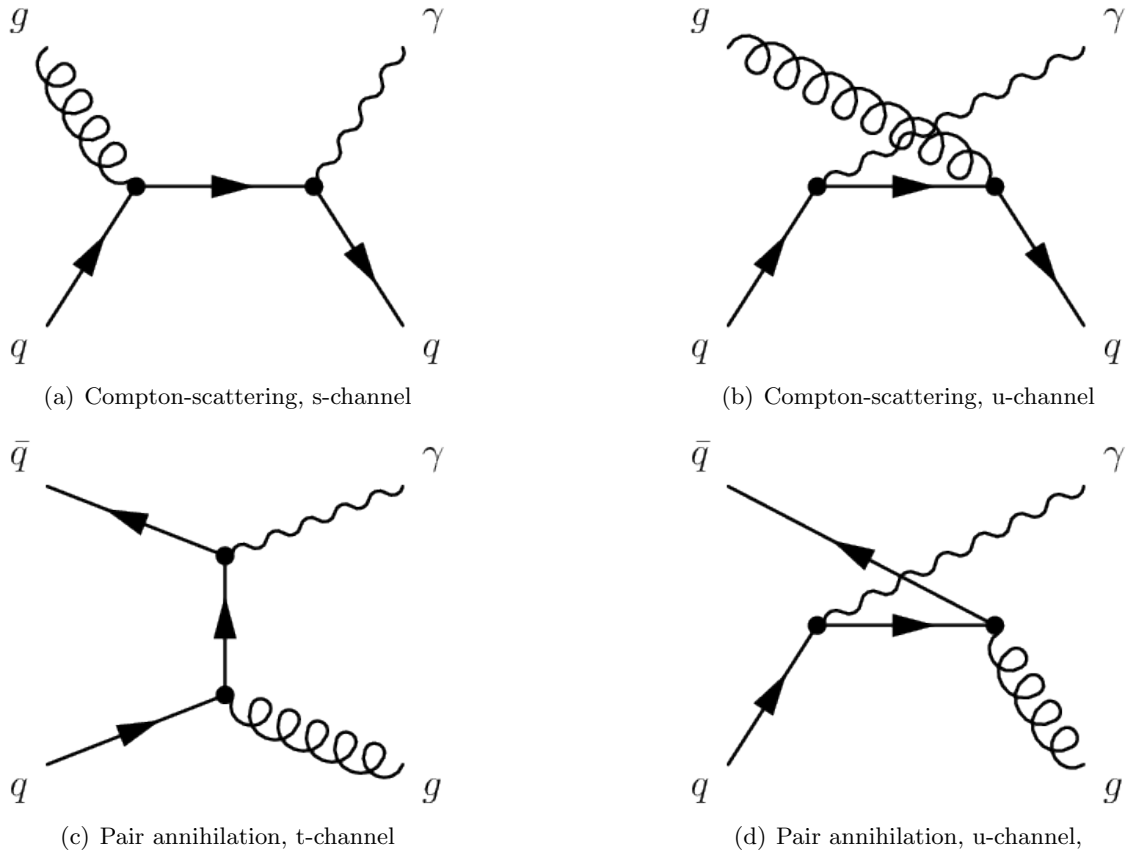


Figure 6.4.: The pictures/diagrams stemming from symmetric cuts of the photon self energy at order $e^2 g^2$. The diagram in Fig. 6.2 yields the square of each of the shown channels, the diagram in Fig. 6.3 yields the interference terms between s and u (t and u) channels for the Compton scattering process (pair annihilation process). There is no interference between Compton and annihilation pictures/diagrams.

are outgoing. This setting holds for the left- as well as the right-hand side of the cut diagram. This corresponds to the pair annihilation process of quarks to a photon and gluon.

With the routing of the quark loop³ from Fig. 6.2, we get the square of Fig. 6.4(d).

2. If we reverse only the routing of the quarks in Fig. 6.2, but keep everything else as in the previous case, we get the square of the diagram in Fig. 6.4(c).
3. The cut gluon propagator and the lower quark propagator be „in“, the photon and upper quark propagator be „out“. This gives on the left-hand side of the cut the diagram in Fig. 6.4(b), and on the right-hand side the same diagram, but quarks are replaced by antiquarks, so we obtain the square of the u-channel diagram of Fig. 6.4(b).
4. The cut gluon propagator and the upper quark propagator be „in“, the photon and lower quark propagator be „out“. The right-hand side of the cut corresponds to the diagram in Fig. 6.4(a), and on the left-hand side it corresponds to the same

³We define that the left hand side of the cuts in the self energy gives the scattering matrix element, and the right hand side its complex conjugate.

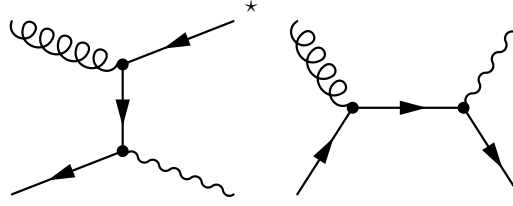


Figure 6.5.: One interference diagram resulting from the cut in Fig. 6.3. It is the interference contribution between s- and u-channel of the Compton scattering process.

diagram, but where quarks are replaced by antiquarks and we obtain the square of the s-channel diagram of Fig. 6.4(a).

Now we turn to Fig. 6.3. This cut diagram will generate interference terms between the channels. Again, we label the cut propagators systematically:

1. Consider the left diagram of Fig. 6.3. The gluon propagator and the lower right quark propagator be „in“, the upper left quark be „out“. The left and right-hand side of the cut produce in this case the interference diagram in Fig. 6.5.
2. Reversing the momentum routing of the quark loop results in the same interference term as before, just quarks and antiquarks in Fig. 6.5 must be swapped (arrows reversed).
3. We consider the left diagram of Fig. 6.3. The gluon propagator and the upper left quark propagator be „in“, the lower right quark be „out“. Reversing the depicted momentum routing, the left and right-hand side of the cut produce the interference diagram in Fig. 6.5.
4. The left diagram of Fig. 6.3 with the depicted momentum routing (keeping the same in- and out-states as before) yields the interference term from figure Fig. 6.5, where quarks and antiquarks must be swapped. Because of the crossing symmetry, this is the same contribution as before.
5. We consider the left diagram of Fig. 6.3, but now the gluon propagator be „out“ and both quark propagators be „in“. We assign a momentum label to the upper quark line, and define here to draw the resulting external incoming line beginning from the top left end in the tree diagram. This generates the interference diagram of the annihilation channels, as shown in Fig. 6.6.
6. We can equally well define the external incoming line, stemming from the upper cut quark line, to begin from the bottom left end in the tree diagram. This gives the complex conjugated of the diagram in Fig. 6.6.
7. Reversing the momentum routing generates exactly the interference term in Fig. 6.6, but with quarks and antiquarks swapped. This holds for both configurations in point 5 and 6 above.

Note that the right diagram of Fig. 6.3 produces exactly the same contributions as the above cases, thus we omit them. To conclude this section, we have proven that the imaginary part of the photon self energy to two-loop order involves the square of two matrix elements, which are the well known Compton scattering matrix element and quark-antiquark annihilation.

6.2. Binary photon rates

The binary rate⁴ for the production of hard photons with momentum $K = (E_k, \vec{k})$ from two particles with momenta $P = (E_p, \vec{p})$ and $P' = (E_{p'}, \vec{p}')$ can be written in kinetic theory as

$$R = \mathcal{N} \int \frac{d^3 p}{2E_p (2\pi)^3} \int \frac{d^3 p'}{2E_{p'} (2\pi)^3} \int \frac{d^3 k}{2E_k (2\pi)^3} \int \frac{d^3 k'}{2E_{k'} (2\pi)^3} (2\pi)^4 \delta^{(4)}(P + P' - K - K') \times |\mathcal{M}|^2 f_{B,F}(P) f_{B,F}(P') (1 \pm f_{B,F}(K')), \quad (6.1)$$

where $K' = (E_{k'}, \vec{k}')$ is the last outgoing momentum. The probability of finding particles with momentum P, P' is given by the thermal Bose (Fermi) distribution functions $f_B(f_F)$ for bosons (fermions). The last factor accounts for Bose enhancement (+) or Pauli blocking (−) for the outgoing particle with momentum K' being a boson or fermion. The prefactor \mathcal{N} is a symmetry factor respecting the electric charges q_i and degeneracies d_i of the incoming species,

$$\mathcal{N} = \sum_{\substack{\text{incoming} \\ \text{species } i,j}} d_i d_j \sum_{\substack{\text{incoming} \\ \text{species } k}} q_k^2. \quad (6.2)$$

In the case of Compton scattering, the symmetry factor for two flavors is $\mathcal{N} = 5/9 \times 12 \times 16 = 320/3$, for three flavors $\mathcal{N} = 128$. In the case of quark-antiquark annihilation, the symmetry factor for two flavors is $\mathcal{N} = 20$, for three flavors $\mathcal{N} = 24$. The scattering matrix element \mathcal{M} in this expression can be expressed in terms of the usual Mandelstam variables $s = (P + P')^2$, $t = (P - K')^2$ and $u = (P - K)^2$ [23, 271],

$$|\mathcal{M}|_{\text{Compton}}^2 = \frac{16}{3} \pi^2 \alpha_{EM} \alpha_s \left(\frac{s^2 + st}{s^2} + \frac{s^2 + st}{u^2} \right), \quad (6.3)$$

$$|\mathcal{M}|_{q\bar{q}\text{-ann.}}^2 = \frac{128}{9} \pi^2 \alpha_{EM} \alpha_s \left(\frac{-st - t^2}{t^2} + \frac{-st - t^2}{u^2} \right). \quad (6.4)$$

Using bare (quark) propagators in \mathcal{M} will not yield a finite rate due to an infrared divergence (as one integrates up to zero momentum transfer). There are two possibilities to account for this divergence: a) one can fix a lower integration limit greater than zero in the divergent integration over the transferred momentum⁵; b) one can introduce massive propagators, such that the integrands at the lower integration limits $s, t, u = 0$ still give finite results. The traditional calculations of binary photon production rates (Refs. [23, 269], later [272] and, with a similar method, just another purpose, Ref. [270]) use method a);

⁴The total rate is the total number of photons emitted per volume per time (0'th moment), $R = \int_0^\infty dE \frac{dR}{dE}$.

⁵In Ref. [23] this is written as $-k_c^2 \geq t$, whereas Ref. [270] and Ref. [272] use other integration variables, such that $q_{\text{cut}} \leq q$ or $q_* \leq q$.

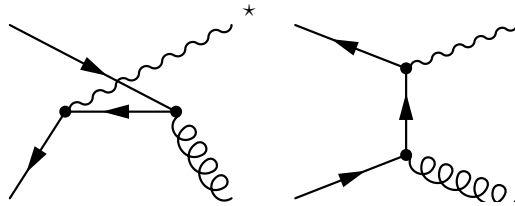


Figure 6.6.: One interference diagram resulting from the cut in Fig. 6.3. It is the interference contribution between u- and t-channel of the pair annihilation process.

however, they treat the low momentum transfer region separately, and add both contributions in the end. It turns out, that the sum of both contributions is independent of the cut in the momentum integral, and the final result is unambiguously defined.

Infrared contribution

We shall briefly summarize the calculations that lead to a finite contribution for the photon rate at the lowest momentum transfers, as carried out in Refs. [23,269,270,272]. Physically, a new effect becomes important in a thermal many-body system when the momentum transfer goes to zero. Charges are screened and propagators become effectively massive. This effect can be captured in the effective hard thermal loop theory (HTL) which has been introduced in Ref. [256–258]. To account for screening effects, propagators and vertices are replaced by effective HTL propagators and vertices. Those carry one-loop corrections evaluated at high temperatures. It was argued in Ref. [23] that at lowest order in g , only one quark propagator in the one-loop photon self energy must be dressed⁶. With four-momentum P of the dressed quark propagator, and $K - P$ the bare one, the one-loop photon self energy is [23],

$$\Pi^{\mu\nu}(K) = -3e^2 \sum_f q_f^2 T \sum_{\substack{j=-\infty \\ p^0=2\pi jT}}^{\infty} \int \frac{d^3\vec{p}}{(2\pi)^3} \text{Tr} [S_{\text{dressed}}(P)\gamma^\mu S(K-P)\gamma^\nu], \quad (6.5)$$

where $S_{\text{dressed}}(P)$ denotes the HTL effective quark propagator and $S(K-P)$ the bare propagator. The trace of the *retarded* self energy $\Pi_\mu^{R,\mu}(K)$ is accessible by contraction and analytic continuation from the imaginary time self energy (see Secs. 5.1.2 and 5.1.4). After some calculations, one can write the imaginary part of the retarded self energy as an integral over the quark energy ω and its absolute momentum $|\vec{p}|$, where one calculates only the soft part which satisfies $0 \geq \omega^2 - \vec{p}^2 \geq -p_c^2$. The cutoff momentum is on the order of $p_c \gtrsim gT$, and plays the role of a thermal mass of the dressed quark. It separates the infrared part of the phase space and the high momentum transfer part.

Hard momentum transfers

In order to find an analytic expression, the authors of Ref. [23] make the approximation that the photon energy E_k is large, $E_k \gg T$. This enables them to rewrite Eq. (6.1) with matrix elements Eqs. (6.3) and (6.4) in integrals over Mandelstam s and t . The diverging phase space is cut off by inserting the energy scale p_c as infrared cutoff, $-p_c^2 \geq t \geq -s + p_c^2$, $2p_c^2 \leq s \leq \infty$. The cutoff is much smaller than the hard scale T , $p_c^2 \ll T^2$, and one can evaluate the integrals and subsequently take the limit $p_c^2 \rightarrow 0$. In Ref. [269] this is done similarly.

Full rate

By summing the results of the infrared contribution of the rate and the hard contribution, the authors of Ref. [23] report for two flavor QCD,

$$E_k \frac{dR}{d^3k} = \frac{5}{9} \frac{\alpha_{EM}\alpha_s}{2\pi^2} T^2 e^{-E_k/T} \log \left(\frac{2.912 E_k}{g^2 T} \right). \quad (6.6)$$

This rate is independent from the cutoff scale p_c^2 , which would lie in the range $gT < p_c < T$. The rate calculated by essentially the same method in Ref. [269] is identical.

⁶“dressed” means replaced by the corresponding HTL effective propagator.

The authors of Refs. [272, 273] repeat the calculation from Refs. [23, 269], but relax the approximation of large photon energies, at the cost of two integrals which must be evaluated numerically in the end of the calculation. One of those integrals involves a cutoff scale $q^* \sim p_c$ which will also appear in a corresponding soft calculation (as in Ref. [23]). After numerical evaluation one sums both contributions and repeats this procedure for several $q^* \rightarrow 0$, until the result converges. This then constitutes the most precise result to date.

Note that Eq. (6.6) is an approximated rate for $E_k \gg T$, however, already for $E_k/T \gtrsim 3$ the approximation deviates only a few percent from the precise result [272],

$$E_k \frac{dR}{d^3k} = (2\pi)^3 8\pi T^2 \alpha_{EM} \alpha_s f_F(k) \left(\sum_{\text{flavor } f} q_f^2 \right) \left[\ln\left(\frac{3}{g}\right) + \frac{1}{2} \ln\left(\frac{2k}{T}\right) + C_{2\leftrightarrow 2}(k/T) \right] \quad (6.7)$$

where $C_{2\leftrightarrow 2}(k/T)$ involves the numerical evaluation of integrals. A parametrization of the precise numerical results for it is given by

$$C_{2\leftrightarrow 2}\left(\frac{k}{T}\right) = 0.041 \frac{T}{k} - 0.3615 + 1.01 \exp\left(-1.35 \frac{k}{T}\right). \quad (6.8)$$

Notice that Eq. (6.7) equals Eq. (6.6) when taking the limit $\lim_{k/T \rightarrow \infty} C_{2\leftrightarrow 2}(k/T) \simeq -0.3614902$ and replacing $f_F(k)$ by its Boltzmann limit, $\sim \exp(-k/T)$.

6.2.1. Semi-analytic evaluation of a screened photon rate

In this section we outline the evaluation of the kinetic photon rate from Eq. (6.1) with screened matrix elements. The low momentum region can be treated in two different ways, as explained below. It shall later be our strategy to compare the result from this section to Eq. (6.7), and tune two parameters to obtain a similar total rate.

To begin with, note that for thermally distributed particle momenta in the incoming states, the Mandelstam variables t and u are interchangeable in the sense that the total scattering rate for matrix elements $|\mathcal{M}|^2(u, t)$ equals the rate for matrix elements $|\mathcal{M}|^2(t, u)$. As we only compute total rates in this section, we define simplified matrix elements,

$$|\mathcal{M}|_{\text{Compton}}^2 = \frac{16}{3} \pi^2 \alpha_{EM} \alpha_s \left(-\frac{s}{t} - \frac{t}{s} \right) \quad (6.9)$$

$$|\mathcal{M}|_{q\bar{q}\text{-ann.}}^2 = \frac{128}{9} \pi^2 \alpha_{EM} \alpha_s \left(\frac{2u}{t} \right). \quad (6.10)$$

We now follow the procedure from Ref. [270] (Appendix A), which again follows Ref. [272]. The terms of the matrix elements in Eq. (6.9) and Eq. (6.10), which involve Mandelstam t channel propagators have to be treated differently to the s channel term in Eq. (6.9), when a minimal momentum transfer is imposed. This is because the integration over the exchanged momentum would diverge in the t channel without further changes, and the integration has to include an explicit cutoff in exchanged momentum. The integration over the s channel term requires no special treatment for soft momenta. This has been shown explicitly in Ref. [274]. However, without the use of a fixed minimal momentum transfer q_{min} , one can screen the propagators by hand to include a thermal mass $\sim gT$. Having the screened matrix elements at hand, we then carry out the integration to obtain the total cross section and finally the photon spectra. This integration requires no special treatment of the s channel. These rates will by construction not be equal to the HTL

improved rate Eq. (6.7), that is why we multiply the thermal masses by a real number κ . The propagators for the different channels read correspondingly,

$$\begin{aligned} \frac{1}{t^2} &\rightarrow \frac{1}{(t - \kappa m_{D,q}^2)^2}, & \frac{1}{u^2} &\rightarrow \frac{1}{(u - \kappa m_{D,q}^2)^2}, \\ \frac{1}{s^2} &\rightarrow \frac{1}{(s + \kappa m_{D,q}^2)^2}. \end{aligned} \quad (6.11)$$

The squared thermal mass for light quarks is defined as

$$m_{D,q}^2 = g^2 C_F \int \frac{d^3 p}{(2\pi)^3 E_p} (f_g + f_q). \quad (6.12)$$

Thermal quark masses $m_{D,q}$ (“quark Debye mass”) are very similar to thermal gluon masses, which are often dubbed (gluon) Debye masses (we will need gluon Debye masses later for screened propagators in inelastic matrix elements). Quark and gluon Debye masses are of order gT but have different prefactors depending on the type of statistics. The squared thermal gluon mass is defined as [254]

$$m_{D,g}^2 = 16\pi\alpha_s \int \frac{d^3 p}{(2\pi)^3 E_p} (N_c f_g + N_f f_q). \quad (6.13)$$

Using Boltzmann statistic distributions, it evaluates to

$$m_{D,g}^2 = \frac{8}{\pi} (N_c + N_f) \alpha_s T^2 \approx 15.28 \alpha_s T^2, \quad (6.14)$$

whereas the squared thermal quark mass is

$$m_{D,q}^2 = \frac{1}{9} m_D^2 = \frac{8\alpha_s T^2}{9\pi} (N_c + N_f) = \frac{16}{3\pi} \alpha_s T^2 \approx 1.7 \alpha_s T^2. \quad (6.15)$$

Using quantum statistic distributions, the squared gluon Debye mass is

$$m_{D,g}^2 = \frac{4\pi\alpha_s}{3} \left(N_c + \frac{N_f}{2} \right) T^2 = 6\pi\alpha_s T^2 \approx 18.85 \alpha_s T^2, \quad (6.16)$$

whereas the squared thermal quark mass is

$$m_{D,q}^2 = \frac{1}{2} m_\infty^2 = \frac{1}{2} \frac{C_F g_s^2 T^2}{4} = \frac{2\pi\alpha_s}{3} T^2 \approx 2.09 \alpha_s T^2. \quad (6.17)$$

We will explain below in more detail, how to choose the value of κ in Eq. (6.11) in order to reproduce Eq. (6.7).

Coming back to the integration as done in Ref. [270], we begin with a first choice of integration variables, which is suitable for t channel integrations with lower momentum cutoff. Defining the momenta in the scattering process, $p + p' \rightarrow k + k'$, one introduces the exchanged momentum $\vec{q} = \vec{p} - \vec{k}$, and $\omega = p - k$ (where we define $p = |\vec{p}|$, and so on), such that the Mandelstam variable $t = (P - K)^2 = \omega^2 - q^2$. In the full rate R , the authors of Ref. [270] replace the integration over \vec{p} with an integration over \vec{q} . Then one uses the spatial delta function $\delta^{(3)}(\vec{p} + \vec{p}' - \vec{k} - \vec{k}')$ to eliminate the integration over \vec{k}' . In spherical coordinates one trivially integrates out $d\phi_k d\phi_q$ with remainder,

$$\begin{aligned} R &= \int p'^2 dp' d\phi_{p'} q^2 dq k^2 dk d\cos\theta_{kq} d\cos\theta_{p'q} \delta(p + p' - k - k') \frac{2(2\pi)^2}{(2\pi)^8 2^4 p p' k k'} \\ &\quad \times |\mathcal{M}|^2 f(\omega + k) f(p') (1 \pm f(\omega + p') \theta(\omega + k) \theta(\omega + p')). \end{aligned} \quad (6.18)$$

It is useful to introduce also an integration over the transferred energy ω [275, 276],

$$\delta(p + p' - k - k') = \int_{-\infty}^{\infty} d\omega \delta(\omega + k - p) \delta(\omega + p' - k'), \quad (6.19)$$

where the new delta distributions can be transformed to be functions of the cosines,

$$\begin{aligned} \delta(\omega + k - p) &= \frac{p}{qk} \delta\left(\cos\theta_{qk} - \frac{\omega^2 - q^2 + 2\omega k}{2qk}\right) \theta(\omega + k) \\ \delta(\omega + p' - k') &= \frac{k'}{qp'} \delta\left(\cos\theta_{p'q} - \frac{\omega^2 - q^2 + 2\omega p'}{2p'q}\right) \theta(\omega + p'). \end{aligned} \quad (6.20)$$

As the momentum \vec{k} of the photon is isotropically distributed, one can transform

$$k \frac{dR}{d^3k} = \frac{dR}{4\pi k dk}, \quad (6.21)$$

and thus

$$E_k \frac{dR}{d^3k} = \frac{1}{16(2\pi)^7 E_k} \int dq dp' d\omega d\phi_{p'} |\mathcal{M}|^2 f(\omega + k) f(p') (1 \pm f(\omega + p')) \theta(\omega + k) \theta(\omega + p'). \quad (6.22)$$

The Mandelstam variable $u \equiv (P' - K)^2$ can be expressed as

$$u = -2p'k(1 - \cos\theta_{kq} \cos\theta_{p'q} + \sin\theta_{kq} \sin\theta_{p'q} \cos\phi_{p'}), \quad (6.23)$$

where $\cos\theta_{p'q}$ and $\cos\theta_{kq}$ can be determined by the delta distributions Eqs. (6.20). The final expression for the t -channel integration reads, after trivially integrating $d\phi_{p'}$,

$$E_k \frac{dR}{d^3k} = \frac{\mathcal{N}}{16(2\pi)^6 E_k} \int_{q_{\min}}^{\infty} dq \int_{\max\{q-2k, -q\}}^q d\omega \int_{(q-\omega)/2}^{\infty} dp' |\mathcal{M}|^2 f(\omega + k) f(p') (1 \pm f(\omega + p')). \quad (6.24)$$

Here we inserted the degeneracy factor from Eq. (6.2), which accounts for the degeneracies of the incoming species and their electric charges. Eq. (6.24) can readily be solved numerically, under the condition that one specifies the scale q_{\min} , or, uses well-behaved matrix elements (from Eqs. (6.11)) and sets $q_{\min} = 0$.

The s channel integration is most conveniently done using a different parameterization, where we shift the integration over \vec{p} to an integration over $\vec{q} = \vec{p} + \vec{p}'$ with $\omega = p + p'$, such that $s = \omega^2 - \vec{q}^2$. Again, using the spatial delta function one can perform the \vec{k}' integration. The temporal delta function can be split in delta functions over total energy ω ,

$$\delta(p + p' - k - k') = \int_0^{\infty} d\omega \delta(\omega - p - p') \delta(\omega - k - k'), \quad (6.25)$$

and

$$\begin{aligned} \delta(\omega - p - p') &= \frac{p}{p'q} \delta\left(\cos\theta_{p'q} - \frac{\omega}{q} + \frac{s}{2p'q}\right) \Theta(\omega - p') \\ \delta(\omega - k - k') &= \frac{k'}{kq} \delta\left(\cos\theta_{kq} - \frac{\omega}{q} + \frac{s}{2kq}\right) \Theta(\omega - k). \end{aligned} \quad (6.26)$$

Moment	AMY/Born
0'th	99.5 %
1st	112.5 %
2nd	121.9 %
3rd	128.1 %
4th	132.1 %

Table 6.1.: The comparison of AMY with Born-photon rates for higher moments of the photon rate, using the fixed value of $\kappa = 2.45$.

The final expression for integrating the s channel reads

$$E_k \frac{dR}{d^3k} = \frac{\mathcal{N}}{16(2\pi)^6 E_k} \int_k^\infty d\omega \int_{|2k-\omega|}^\omega dq \int_{(\omega-q)/2}^{(\omega+q)/2} dp' |\mathcal{M}|^2 f(\omega+k) f(p') (1 \pm f(\omega+p')). \quad (6.27)$$

Note that the Mandelstam variables which have to be inserted in the matrix element in Eq. (6.27) differ from the definition in the t -channel integration (e.g., in Eq. (6.23)), it can now be expressed as

$$u = -s - t$$

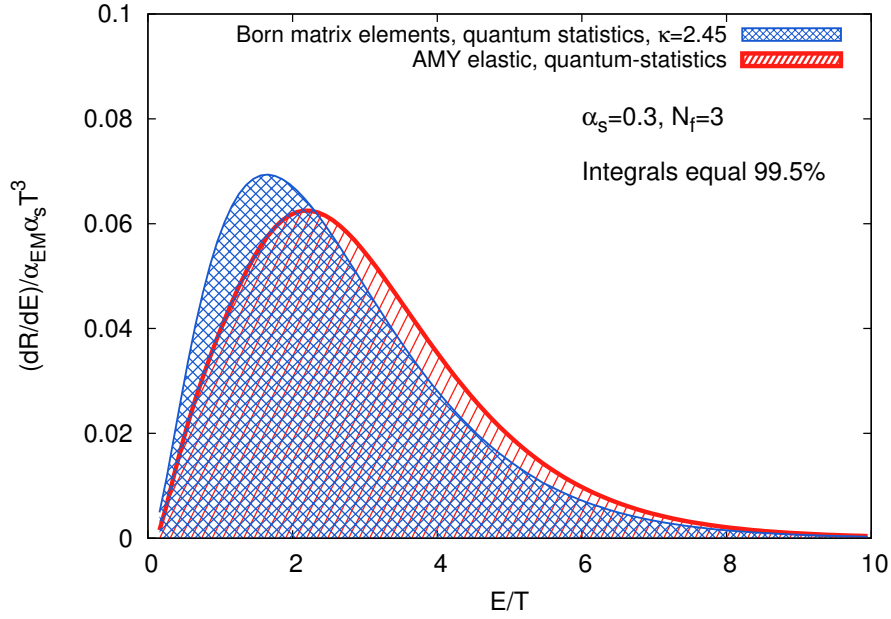
$$t = \frac{s}{2q^2} \left([(p' - p)(k - k') - q^2] + \cos \phi_k \sqrt{(4p'p - s)(4kk' - s)} \right), \quad (6.28)$$

6.2.2. Screening of soft momentum transfers

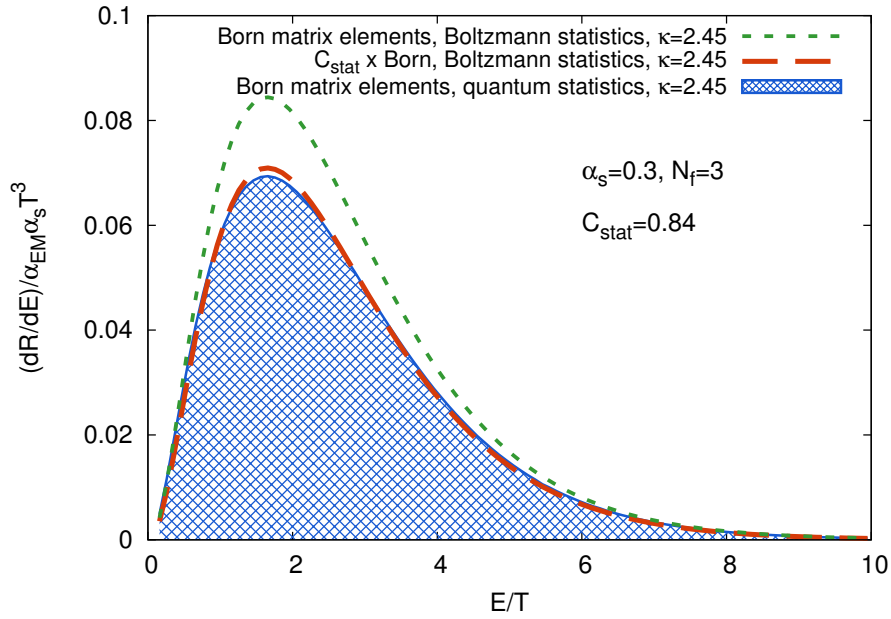
We will use the integrations from Eqs. (6.24) and (6.27), with matrix elements from Eqs. (6.9) and (6.10) where the propagators are screened as in Eqs. (6.11), to compute a thermal rate. It is now our strategy to choose the value of κ in such a way that our simplified procedure leads to a rate that resembles the HTL improved rate from Eq. (6.7) closely (a similar procedure was done for heavy quark energy loss, e.g., in Ref. [277]). We do this by comparing the moments of the rate (where the n 'th moment is defined as $\int_0^\infty dE E^n \frac{dR}{dE}$). To this end we solve Eq. (6.24) numerically first for quantum statistical distributions and screened matrix elements including the κ -factor (we call this ‘‘Born’’-rate), and compare the result to the HTL improved ($2 \leftrightarrow 2$) rate, Eq. (6.7), from Refs. [272, 273] (we call this ‘‘AMY’’-rate). We adjust κ (which is of order $\mathcal{O}(1)$) so that the total rates R are equal, with the result,

$$\kappa = 2.45 \quad (6.29)$$

The comparison is shown in Fig. 6.7(a), where we plot dR/dE in both schemes. One observes that the Born rate (blue cross shaded area) has a slightly shifted peak when compared to the HTL improved rate. The deviation in the energy spectrum of the Born rate to the AMY rate is mild, and maximal 20% for certain photon energies. To get a handle on the quality of the comparison, we compare higher moments of the rate, the results are shown in Tab. 6.1. The deviation increases for higher moments, but even the 4th moment of the Born rate deviates only about 32% to the AMY rate. This gives confidence, that the screening model is physical, and can be used in phenomenological situations in a well-controlled way. Note that the result for κ is rather insensitive to the numerical integration limits, as the integrand drops to zero for $E/T \rightarrow 0, \infty$.



(a) The parameter $\kappa = 2.45$ is tuned to make both integrated rates equal.



(b) The Born matrix element integrated with Boltzmann statistics (green dotted line). Reducing this rate by $C_{\text{stat}} = 0.84$ (orange dashed line), the total rate R equals the Born rate with quantum statistics (which equals approximately the elastic HTL improved rate, see panel (a)).

Figure 6.7.: The photon rate from Refs. [272,273] compared to the rate obtained from the numerical solution of Eq. (6.1) with matrix elements Eq. (6.4) and (6.3), using a Debye mass $\kappa m_{D,q}^2$. In the left panel the κ is fixed. In right panel we keep $\kappa = 2.45$ and fix the parameter C_{stat} by integrating the Born matrix element with Boltzmann statistics.

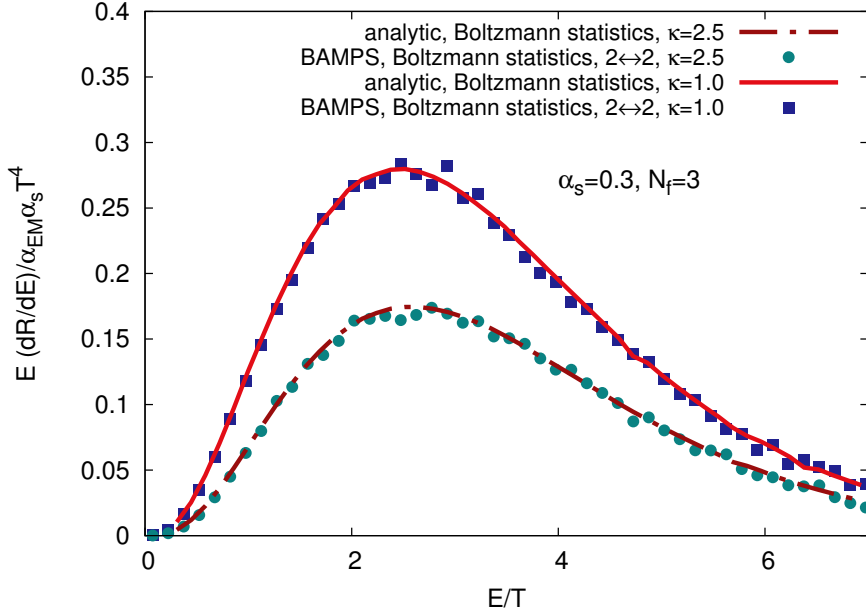


Figure 6.8.: For two values of κ we compare the numerically obtained $2 \leftrightarrow 2$ photon rate to the analytic expectation (obtained by using the method from Ref. [270]).

6.2.3. Correction of the distribution functions

Finally, we need to correct for the small effect of the distribution functions. In the numerical study which we aim at, we can only use Boltzmann (classical) statistics, in initial and final states. There is no Pauli blocking or Bose enhancement (for an exploratory study in this direction, see Ref. [236]). That is why we will multiply the cross sections (equivalent to the rate) with a factor C_{stat} to get the correct number of photons even without quantum statistics. This factor does not alter the differential cross section, as it is an overall prefactor. Note that also the Debye mass follows the Boltzmann distribution (later it is dynamically computed in simulations with Boltzmann statistics). To obtain C_{stat} , we solve Eq. (6.24) numerically with Boltzmann distributions and ignore Pauli blocking or Bose enhancement, but keep the fixed value of κ from the procedure above⁷. Then we compare again to the HTL resummed $2 \leftrightarrow 2$ rate from Refs. [272, 273], which uses quantum statistics. The difference of both total rates is

$$C_{\text{stat}} = 0.84 \quad (6.30)$$

The rates are shown in Fig. 6.7(b). The fact that C_{stat} is below unity implies that the Pauli-blocking effect of the outgoing quark in the Compton channel is more important than the Bose enhancement effect of the outgoing gluon in the annihilation channel. This is consistent, because the Compton process happens more often (due to the combinatorics of the incoming particles).

Sampling a thermal ensemble of partons in a homogeneous box simulation with BAMPS (see Sec. 11.4), we can use the $2 \leftrightarrow 2$ photon production rate including the above explained ingredients to produce emitted photons. As an important numerical check, we compare the numerical results with the analytic expectation by using the exact same matrix elements (using two arbitrary values of κ for illustration) in Fig. 6.8, and find excellent agreement.

⁷Here again, the Debye mass is in Boltzmann form.

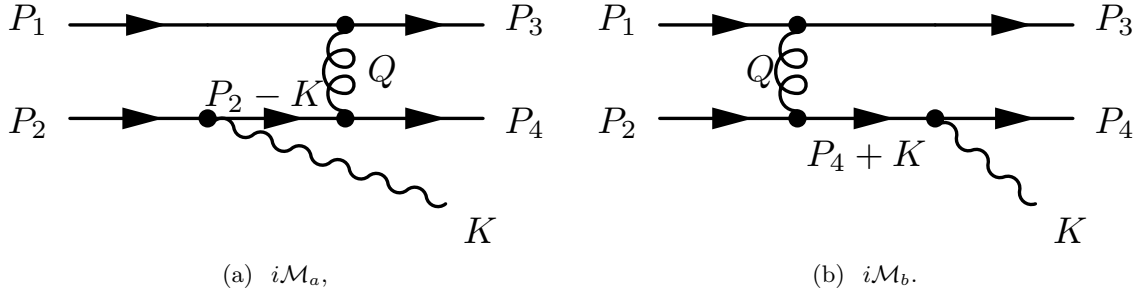


Figure 6.9.: The two contributing vacuum diagrams we use for the numerical evaluation of the radiative photon rate. All internal propagators are screened by hand, and an overall factor K_{inel} ensures the similarity to the AMY rate, as explained in Sec. 6.4.

6.3. Bremsstrahlung, LPM effect and inelastic photon production

The purely binary photon production rate from the previous section is of order $\mathcal{O}(e^2 g^2 T^4)$. In the beginning of the 1990s it was believed, that diagrams of higher order in the coupling, like bremsstrahlung of quarks, would also contribute to the rate at higher order in the rate, and was therefore neglected. However, in certain kinematic regions, higher order diagrams contribute at the same order $\mathcal{O}(e^2 g^2 T^4)$. This was rigorously proven by Arnold, Moore and Yaffe in Refs. [272,273]. Their main result is a rather complicated integral equation, whose numerical solution yields the thermal photon production rate (more details in Sec. 7.2). The parameterization of Refs. [272,273] reads

$$k \frac{dR_{\text{inel}}^\gamma}{d^3\vec{k}} = 2\alpha_{EM} \left(\sum_s q_s^2 \right) g_s^2 T^2 f_F(k) C_{\text{inel}} \left(\frac{k}{T} \right)$$

$$C_{\text{inel}}(x) = \sqrt{1 + \frac{N_f}{6}} \left[\frac{0.548 \log(12.28 + 1/x)}{x^{3/2}} + \frac{0.133x}{\sqrt{1 + x/16.27}} \right], \quad (6.31)$$

where q_s is the fractional charge of a quark species s (e.g., $2/3$ for up quark species), and $f_F(k)$ is the Fermi-Dirac distribution function.

We now outline briefly the arguments of Refs. [272,273] leading to the leading order photon rate, before coming explicitly to interference phenomena.

6.3.1. Parametric estimates of higher order photon production

The argument chain of Refs. [272,273] begins with the diagram Fig. 6.9(b). As it is important for the motivation of this study, we concisely report it here. If the momentum of the exchanged gluon is hard, $Q \sim T$, then the naive diagrammatic power counting is valid, and the process yields a rate of order $\mathcal{O}(e^2 g^4 T^4)$ which is subdominant compared to the binary rate of order $\mathcal{O}(e^2 g^2)$. However, one can show that for soft exchanged momenta of order gT the rate can be as strong as $\mathcal{O}(e^2 g^2)$. For simplicity, Ref. [273] uses scalar quarks to show the power counting, although the results are true also for fermionic quarks. We consider the squared amplitude for the process in Fig. 6.9. The gluon propagator, $\sim 1/Q^2$ contributes $1/Q^4 \sim 1/(g^4 T^4)$. We now make the restriction, that

$$Q \cdot P_2 \sim g^2 T^2. \quad (6.32)$$

This restriction constrains the angle between the momentum P_2 and Q to be small. In principle, all components of Q are of order gT , and $P_2 \sim T$, but by $g^2T^2 \equiv P_2 \cdot Q = gT^2(1 - \cos \alpha) \sim gT^2\alpha^2$ the angle α is restricted to be of order \sqrt{g} . In Ref. [273], it is argued, that in the regime, where $P_2 \cdot Q \sim gT^2$, there is a cancellation within the scattering matrix elements, which makes only the high collinear region contribute.

From Eq. (6.32), by energy-momentum conservation $Q + P_2 = P_4 + K$ and the fact that the incoming and outgoing momenta are almost onshell, $K^2 \approx P_2^2 \approx P_4^2 \approx 0$, it is implied that $P_4 \cdot K \sim g^2T^2$. From

$$Q^2 = -2K \cdot P_2 + 2P_4 \cdot Q \quad (6.33)$$

it follows that also $K \cdot P_2 \sim g^2T^2$ and $P_4 \cdot Q \sim g^2T^2$, given that all external particles are on-shell. The angle between \vec{p}_4 and \vec{k} be Θ . These conditions imply collinearity, as the following calculation shows,

$$\begin{aligned} g^2T^2 &\sim P_4 \cdot K = p_4^0 k^0 - \vec{p}_4 \cdot \vec{k} = p_4^0 k^0 - p_4 \cdot k \cos \Theta \\ &\sim T^2(1 - \cos \Theta) \approx T^2(\Theta^2/2) \\ &\Leftrightarrow \Theta \sim g. \end{aligned} \quad (6.34)$$

It follows directly, that the (scalar) quark propagator gives a large enhancement, $\frac{1}{(P_4+K)^2} \sim 1/(g^2T^2)$. The gluon vertices give a factor g^2 . The physical photon polarization ϵ is purely spatial ($\epsilon^0 = 0$) and orthogonal to \vec{k} . The photon-quark vertex in Fig. 6.9(b) (in scalar QCD) is $(P_2 + Q + P_4) \cdot \epsilon$ (or $(P_2 + P_4 - Q) \cdot \epsilon$ for Fig. 6.9(a)). For P_2 and P_4 the product is $\mathcal{O}(gT)$,

$$\vec{\epsilon} \cdot p_{2,4} = \cos\left(\frac{\pi}{2} - \Theta\right) p_{2,4} = p_{2,4} \sin \Theta \approx p_{2,4} \Theta \sim gT. \quad (6.35)$$

Note that this implies also that the component of \vec{k} orthogonal to \vec{p}_4 is also $\mathcal{O}(gT)$. For $Q \cdot \epsilon$ we have

$$\vec{\epsilon} \cdot \vec{q} = \cos(\beta) q \sim \cos(\beta) gT \lesssim gT, \quad (6.36)$$

such that the photon vertices contribute $(P_2 + P_4 \pm Q) \cdot \epsilon \sim egT$. The angle between $\vec{\epsilon}$ and \vec{q} is β . Now, in order to get the rate from the $2 \rightarrow 3$ diagrams, one must integrate out all incoming and outgoing on shell momenta (where the integration can be performed only over three momenta, as the energy is fixed by the on-shell condition). In general, all external momenta are $\mathcal{O}(T)$, so that the external lines contribute $\mathcal{O}(T^2)$. One can substitute some integration variables to integrate, among others, over \vec{q} and Θ . As we have seen before that the dominant contribution to the rate comes from soft \vec{q} and small angles, the integration must give a phase space suppression $g^3 \times g$. There will be two unrestricted integrations over three momenta left, contributing $\mathcal{O}(T^6)$. In the rate, the matrix elements are squared, and from all the above the total rate goes like

$$R \sim \underbrace{T^3 T^3}_{\text{int.measure}} \underbrace{e^2 g^4}_{\text{vertices}} \underbrace{T^4}_{\text{other momenta}} \underbrace{\frac{1}{g^4 T^4} \frac{1}{g^4 T^4}}_{\text{propagators}} \underbrace{g^4}_{\text{ph.sp.supp.}} \underbrace{g^2 T^2}_{\gamma\text{-quark-vertex}} \sim e^2 g^2 T^4. \quad (6.37)$$

This is a remarkable result, as the $2 \leftrightarrow 2$ rate has exactly the same order. This means that any sensible photon production rate must include radiative processes.

Note that the parametric estimate above does not specify any Landau-Pomeranchuk-Migdal effect. In fact, it turns out, that not only the diagram above contributes at leading $e^2 g^2 T^4$ order to the rate, but also diagrams with more gluon rungs, interfering with each other.

6.3.2. Landau-Pomeranchuk-Migdal effect

Apart from a rigorous calculation, there are multiple ways to show heuristically the existence and mechanism of multiple scattering and interference effects in bremsstrahlung processes. Our first explanation is based on the previous arguments and uses the dominant part of the phase space derived earlier [272, 273].

We have seen, that the momentum of the photon transverse to the emitting quark is $\mathcal{O}(gT)$, which implies that the spatial extent of the wave packets must be of order $\mathcal{O}(1/gT)$. The angle between the photon momentum and the quark momentum is $\mathcal{O}(g)$, so that by simple geometry the traveling time of the quark before it separates from the photon must be $\mathcal{O}(1/g^2T)$. Within this time, which is parametrically larger than the time the photon travels transversely to the quark, the quark may scatter again, which the following reasoning shows. The $2 \leftrightarrow 2$ cross section can be obtained from, e.g., pQCD scattering matrix elements by

$$\sigma_{\text{tot}} = \frac{1}{16\pi s^2} \int_{-s}^0 dt |\mathcal{M}_{22}|^2. \quad (6.38)$$

For soft scattering, the typical momentum transfer is $\sqrt{t} \sim gT$. The squared matrix elements typically behave as $|\mathcal{M}_{22}|^2 \sim g^4 s^2/t^2$, or similar combinations of Mandelstam variables, which do not change our parametric result qualitatively. This implies,

$$\sigma_{\text{tot}} \sim g^2 T^2 \frac{g^4}{g^4 T^4} \sim \frac{g^2}{T^2}, \quad (6.39)$$

such that the mean free path between individual soft scatterings is

$$\lambda_{\text{mfp}}^{\text{soft}} \sim \frac{1}{n\sigma_{\text{tot}}} \sim \frac{1}{g^2 T}. \quad (6.40)$$

This is of the same order as the time the quarks takes to separate from the photon, which indicates that sequential scatterings may interfere and can not be treated independently. This is the origin of the Landau-Pomeranchuk-Migdal (LPM) effect. Before the photon is completely formed, the quark can scatter again and those multiply radiated photons can interfere. For photons it turns out that the interference from successive bremsstrahlung acts destructively, such that corrections due to the LPM effect suppress the photon production rate. Note that a single soft collision of a quark with energy E and momentum transfer q_T has by geometry (and $\tan \Theta_{\text{single}} \approx \Theta_{\text{single}}$) typical angles of

$$\Theta_{\text{single}} = \frac{q_T}{E} \sim \frac{m_D}{E}, \quad (6.41)$$

with an effective mass m_D . Hard collisions, that is collisions with large momentum transfers, $\sqrt{t} \sim \sqrt{s} \sim T$ have typical cross sections of $\sigma_{\text{tot}} \sim g^4/T^2$ which implies a mean free path for large angle (LA) scatterings,

$$\lambda_{\text{mfp}}^{\text{LA}} \sim \frac{1}{g^4 T} \gg \lambda_{\text{mfp}}^{\text{soft}}. \quad (6.42)$$

If for certain processes the mean free path is parametrically larger than $\mathcal{O}(1/g^2T)$, such as large angle scatterings, these processes do not play a significant role for the LPM suppression, as the emission time is $\mathcal{O}(1/g^2T)$. Therefore only soft scattering is important, and the calculation of Refs. [272, 273] ignores processes with parametrically larger momentum transfer than gT . The authors of Refs. [272, 273] also argue, that much softer scatterings,

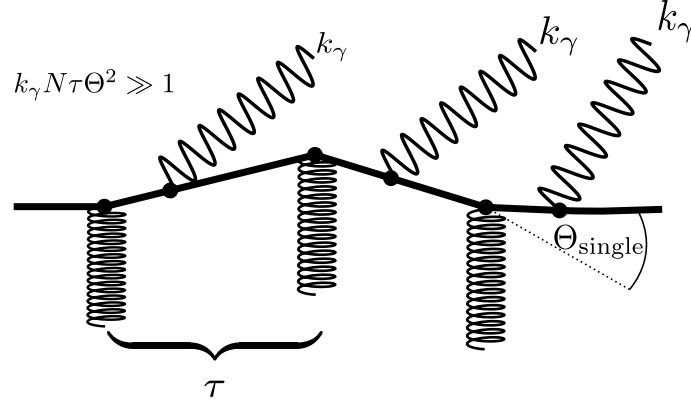


Figure 6.10.: Independent scattering of a quark (thick line) with gluons with subsequent photon emission.

with scattering angles $\Theta \ll g$ would be too ineffective to be important for interference effects, and can safely be neglected.

A second, more classical picture can be given in the following way, which also explains some important scales [278]. A quark moves with ultra-relativistic high energy E and scatters N times randomly with particles. Each collision deflects the particle by a small angle Θ_{single} , such that the total angle, which should still be small, is the result of a random walk of N steps, namely $\Theta = \sqrt{N\Theta_{\text{single}}}$. This is depicted schematically in Figs. 6.10 and 6.11. Classically, the soft photon field itself is peaked around the angle Θ around the quark (see the angle in Fig. 6.11). Now, classically, each scattering at point x_i generates a photon wave which contains a factor $\exp(K_\gamma \cdot x_i)$. If the first (at point x_1) and last (at point x_N) scatterings are independent, the phase factors are large, $K_\gamma \cdot (x_N - x_1) \gg 1$, whereas in the case of interferences $K_\gamma \cdot (x_N - x_1) \ll 1$. One computes

$$\begin{aligned} K_\gamma \cdot (x_N - x_1) &= k_\gamma^0(x_N^0 - x_1^0) - \vec{k}_\gamma \cdot (\vec{x}_N - \vec{x}_1) \\ &= k_\gamma(1 - \cos \Theta) |\vec{x}_N - \vec{x}_1| \sim k_\gamma N \tau (1 - \cos \Theta) \\ &\approx k_\gamma N \tau \Theta^2 \ll 1 \end{aligned} \quad (6.43)$$

where the photon is on-shell $|\vec{k}_\gamma| = k_\gamma^0$ as well as the massless particle, such that $\Delta t \equiv x_N^0 - x_1^0 = |\vec{x}_N - \vec{x}_1| = N\tau$. In the case of interference, there are typically $N \sim 1/\sqrt{k_\gamma \tau \Theta_{\text{single}}^2}$ scatterings, which can not be resolved by the radiated photon and thus act as one single scattering, as shown in Fig. 6.11. Equation (6.43) is valid for soft $k_\gamma \ll E$, but if $E - k_\gamma \sim \mathcal{O}(E)$, and $k_\gamma \sim E$, it is parametrically still correct. Using Eq. (6.41), the number of soft collisions for hard bremsstrahlung ($k_\gamma \sim E$) is $N \sim \max\left(1, \sqrt{E/(\tau m_D^2)}\right)$. Clearly, for mean free times $\tau \gg E/m_D^2$, there will be no interference between successive soft collisions, $N \sim 1$. Imagine two such scatterings at point x_A and x_B , each with typical angles Θ_{single} . One can define a classical formation time t_f by requiring that the two waves have different phase factors, $K_\gamma \cdot (x_A - x_B) \sim 1$, which by a similar calculation as in Eq. (6.43), and the definition $x_A^0 - x_B^0 \equiv t_f$ reduces to $k_\gamma t_f \Theta_{\text{single}}^2 \sim 1$. The angle can either be defined by the momentum transfer before the photon radiation, $\Theta_{\text{single}} \sim q_T/E$, so that the formation time for the $N = 1$ case is $t_f \sim E/q_T^2$. Defining a transverse momentum k_T of the photon with respect to the quark (see Fig. 6.12), one finds another parametric estimate for the scattering angle,

$$\Theta_{\text{single}}^2 \approx k_T^2/k_\gamma^2, \quad (6.44)$$

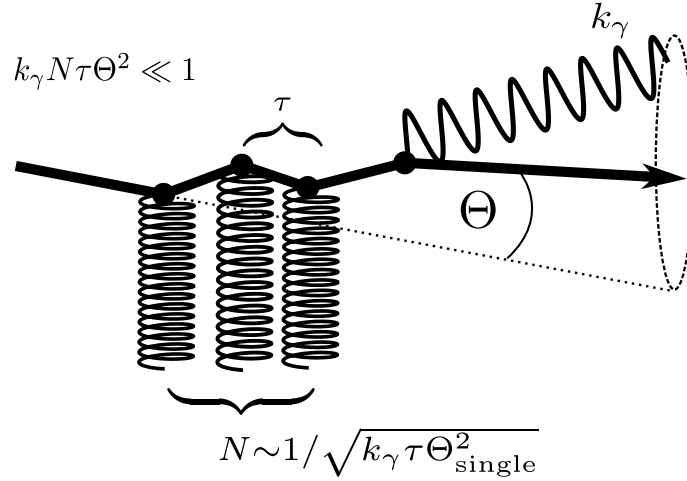


Figure 6.11.: Photon radiation of a quark (thick line) due to multiple soft scattering with gluons. The typical radiation cone is sketched.

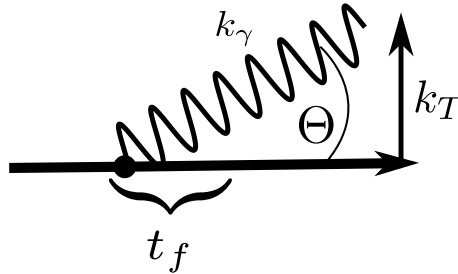


Figure 6.12.: Kinematics in a photon radiation process of a quark (thick line), with transverse momentum k_T and opening angle Θ .

and as such,

$$t_f = \frac{k_\gamma}{k_T^2}. \quad (6.45)$$

For $k_\gamma \sim E$ and $\Theta_{\text{single}} \sim q_T/E$ the formation time is simply $t_f \sim E/q_T^2$. For small τ , such that N successive scatterings strongly interfere, the formation time is $t_f \sim N\tau$. From the above we have

$$t_f \sim N\tau \sim \frac{1}{\Theta^2 k_\gamma} \sim \frac{1}{EN\Theta_{\text{single}}^2} \sim \frac{E}{Nq_T^2}. \quad (6.46)$$

This formula is valid in the single and in the multiple soft scattering case. We see that for softer photons, $k_\gamma \ll E$, the formation time is longer than for hard photons. Note that radiated gluons, due to their capability to scatter during formation, will typically lose their coherence faster than photons.

6.3.3. Interference effects in transport models

Many transport approaches, such as BAMPS, which we shall use extensively in this work, are based on the numerical solution of the Boltzmann equation. The validity of the Boltzmann equation requires that individual scatterings are sequential and the scattering duration is shorter than the mean free time between collisions. A priori it is therefore not

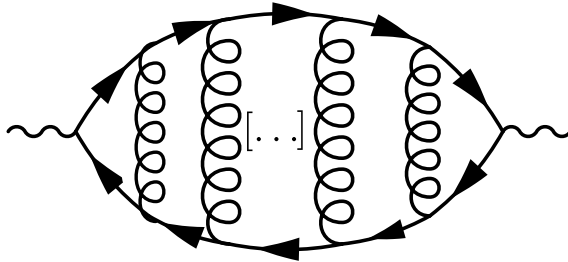


Figure 6.13.: The diagrams which contribute to the inelastic photon production rate at leading order. The dots [...] represent infinite possible gluon rungs, which must be resummed.

possible to include interference effects such as the LPM effect by using successive scattering processes from the Boltzmann collision kernel. The reason is, that all scattering processes are independent (this is immediately apparent in Monte-Carlo solutions of the Boltzmann equation). However, incorporating a local mean free path in the scattering matrix element allows for an effective description of the LPM effect. We have seen that a large mean free path will lead to the interference free regime,

$$\tau \gg E/m_D^2 \sim t_f, \quad (6.47)$$

whereas a short mean free path leads to formation times, which are N times longer than the mean free time between collisions, $t_f \sim N\tau$. It is natural to use the formation time of produced photons as a scale to compare to the mean free path. The simplest case of an implementation would be to discard any produced photon which has a formation time t_f larger than the mean free path of the radiating parent quark. As such, we allow only single independent scatterings.

6.4. Radiative photon production

We have seen in Sec. 6.3.1 that due to certain kinematic enhancements some diagrams contribute at the same order to the photon rate as the $2 \leftrightarrow 2$ photon production. In fact, the authors of Refs. [272, 273] have proven, that only diagrams of the type shown in Fig. 6.13 contribute. All other diagrams with crossed gluon rungs, or other more complicated combinations, do not show the kinematic enhancements and thus do not contribute at leading order.

We want to stick to this picture, and neglect diagrams which would not emerge by cuts of this self-energy, even though in our transport setup those could be substantial.

To this end, we again employ the cutting-rules of Sec. 5.3, and obtain scattering matrix elements. This is more intricate for diagrams like Fig. 6.13, and details concerning the cuts is outlined in appendix A. What emerges are exactly the diagrams of Fig. 6.9.

Note that a (possible) $2 \rightarrow 3$ process like $g + q \rightarrow q + g + \gamma$ (with a three gluon vertex), is not included in the set of diagrams resulting from the cuts. Ignoring the rigorous LO power counting of Refs. [272, 273], and just looking at the number of vacuum QCD vertices, this process could be included and would contribute significantly within BAMPS, because gluons are abundant, especially in the early phase of the QGP. This will be investigated in a future study. For now we use only one kind of matrix element, motivated by the leading-order picture. As we only have vacuum matrix elements, we will insert thermal screening masses by hand into the propagators, as done before in the case of $2 \leftrightarrow 2$ scattering. In Appendix B.1 we derive the full squared matrix element $|\overline{\mathcal{M}}|_{\text{rad}}^2$ starting from spinors

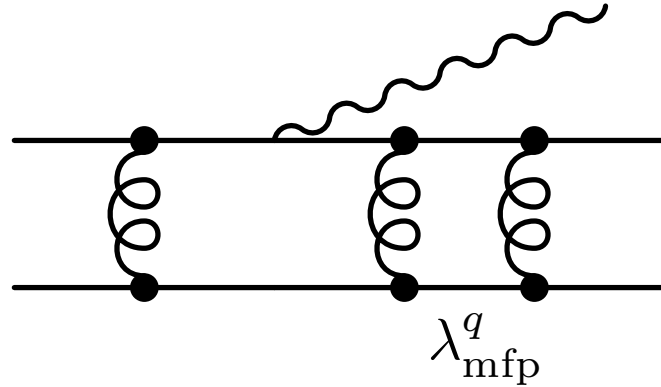


Figure 6.14.: Sketch of an LPM interference effect: Due to a short quark mean free path a subsequent radiation is suppressed. Note that this diagram is not used as shown here, we rather evaluate the quark-quark elastic mean free path dynamically in BAMPS and compare it to the formation time of the photon. The photon is produced by the pure bremsstrahlung subdiagram.

and propagators without any further approximation. This is the radiative matrix element for photons that we will use in BAMPS, using techniques from Ref. [217].

Interference effects

As outlined before, photon radiation from bremsstrahlung processes suffers from the Landau-Pomeranchuk-Migdal effect. The analytic calculation of the leading order radiative photon production rate in Refs. [272, 273] fully includes the interferences among subsequently radiated photons. Within a transport approach, using individual scatterings for photon production, such interferences are necessarily destroyed, and must be restored by hand. In our microscopic description which is based on individual scatterings, we use an effective method to simulate the LPM interference effect, based on the mean free path of the radiating quark. As the only relevant diagram is that of Fig. 6.13, we need an effective method which respects the processes from Fig. 6.13. This is the reason, why we need a *specific* mean free path, calculated only from the quark-quark scattering processes appearing in the diagram.

At first, we calculate the specific inverse rate $\lambda_{\text{mfp}}^{\text{spec}}$ of the quark species which appear in the inelastic matrix elements for photon production⁸. For the calculation of $\lambda_{\text{mfp}}^{\text{spec}}$ we take solely the specific $2 \leftrightarrow 2$ processes into account which appear as subdiagram before or after the photon is radiated (see Fig. 6.14). These specific processes are:

processes 1 $qq \rightarrow qq / \bar{q}\bar{q} \rightarrow \bar{q}\bar{q}$

processes 2 $q\bar{q} \rightarrow q\bar{q}$

Here q (\bar{q}) are quark (antiquark) species, for up, down and strange quarks. The corresponding numerical method is explained in Appendix B.1.4, and a typical process is schematically depicted in Fig. 6.14. In Fig. 6.15 we show numerical results for the inverse rate (mean free path) corresponding to these processes separately. It depends strongly on the (anti-)quark fugacity and temperature. We will come back to the fugacity dependence of the mean free path and the rate in Sec. 6.4.1.

⁸This can be seen as a mean free path (mfp), where only certain scattering processes are included.

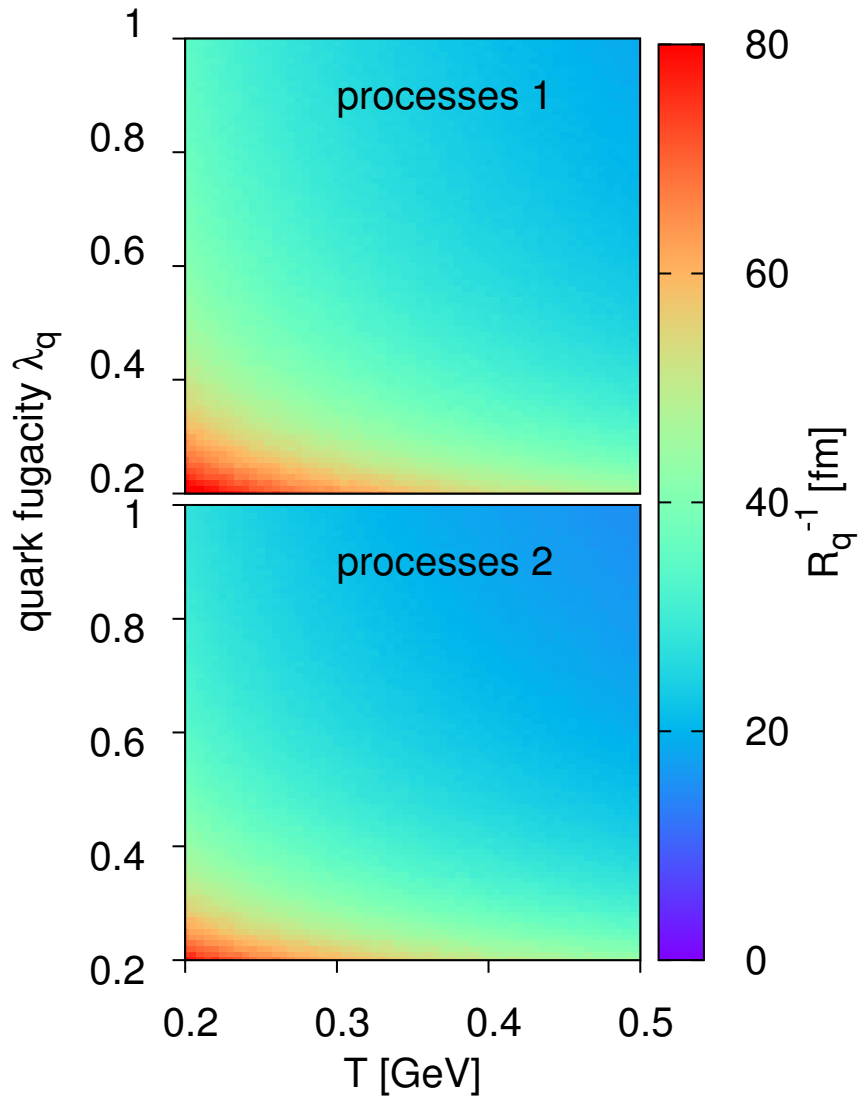


Figure 6.15.: Numerical results for the specific mean free path for a quark corresponding to different reactions (processes 1: $qq \rightarrow qq / \bar{q}\bar{q} \rightarrow \bar{q}\bar{q}$, processes 2: $q\bar{q} \rightarrow q\bar{q}$), depending on temperature and fugacity.

Next we multiply the amplitude for photon radiation by a Heaviside-function $\Theta\left(\lambda_{\text{mfp}}^{\text{spec}} - \tau_f\right)$ which ensures, that the formation time τ_f of the radiated photon is smaller than the mean free path of the radiating quark,

$$|\overline{\mathcal{M}}|_{\text{rad.}}^2 \rightarrow |\overline{\mathcal{M}}|_{\text{rad.}}^2 \Theta\left(\lambda_{\text{mfp}}^{\text{spec}} - \tau_f\right). \quad (6.48)$$

By doing this, we discard photons with such soft k_{\perp} (transverse momentum relative to the radiating quark), that the radiating quark could have scattered again within the formation time. The k_{\perp}^2 integration in Eq. (4.22) in this case is limited by $k_{\perp,\text{min}}^2 = \left(\lambda_{\text{mfp}}^{\text{spec}}\right)^{-2}$. As this procedure reflects the underlying interference effect only incomplete, we must insert a scale factor K_{inel} in front of the matrix element.

Recall that the current implementation of the LPM effect for radiated gluons in BAMPS is done in a similar way, the only difference is a factor X_{LPM} being multiplied to the formation time and a different determination of the mean free path. These differences are motivated by two physical effects: First, radiated gluons suffer from scatterings after the radiation process, which dynamically alter their formation time. That is why we allow more radiated gluons than would actually be radiated if we required them to be fully formed. Second, gluon radiation rates involve far more diagrams (see, e.g., Ref. [279]), such that the mean free path is the total mean free path $qX \rightarrow Y$ where X can be a quark or gluon.

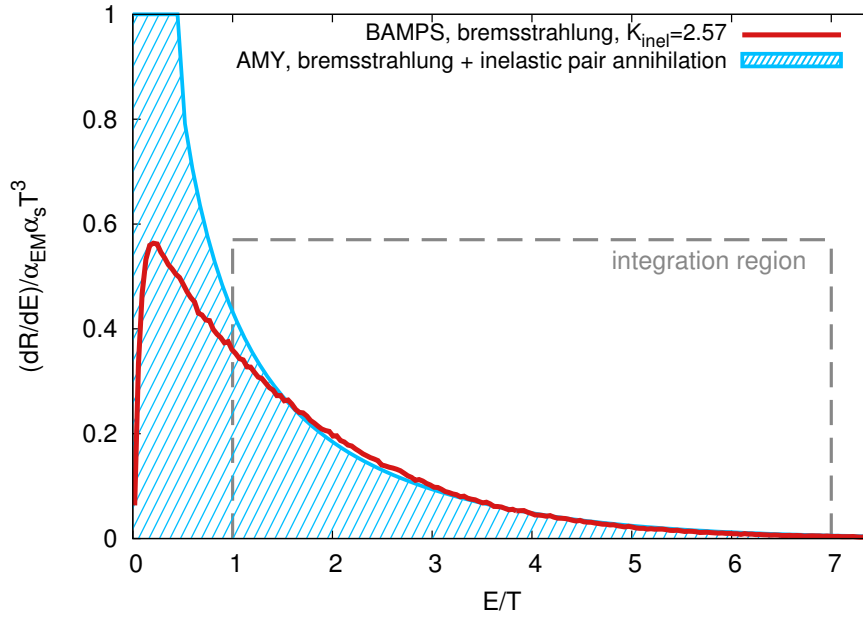
Fixing the scaling factor for bremsstrahlung

As mentioned in the previous section, the implementation of radiative photon production is incomplete. There are in fact several parts which deviate from the AMY description. First, as we include only vacuum matrix elements with Debye screened propagators, we miss the correct treatment of soft momentum transfers. In the matrix element there are two propagators (a quark- and a gluon propagator) where we insert Debye or thermal masses by hand and we could in principle tune these Debye masses by multiplying κ -factors as in the $2 \leftrightarrow 2$ case from Sec. 6.2.2. However, it is not clear how and if they should be tuned individually. The second simplification is the LPM effect described in the previous section. Third, we have the small effect of missing quantum statistics here, too. At last, the full AMY rate includes effectively not only the bremsstrahlung process, but also inelastic pair annihilation (a $3 \rightarrow 2$ process), which we do not include here in this study. In Refs. [272, 273] it is shown that this is a subdominant contribution. To cure all these problems, we scale the full matrix element $|\overline{\mathcal{M}}|_{\text{rad.}}^2$ with a factor K_{inel} . Such scaling is the simplest choice, and very common in transport approaches.

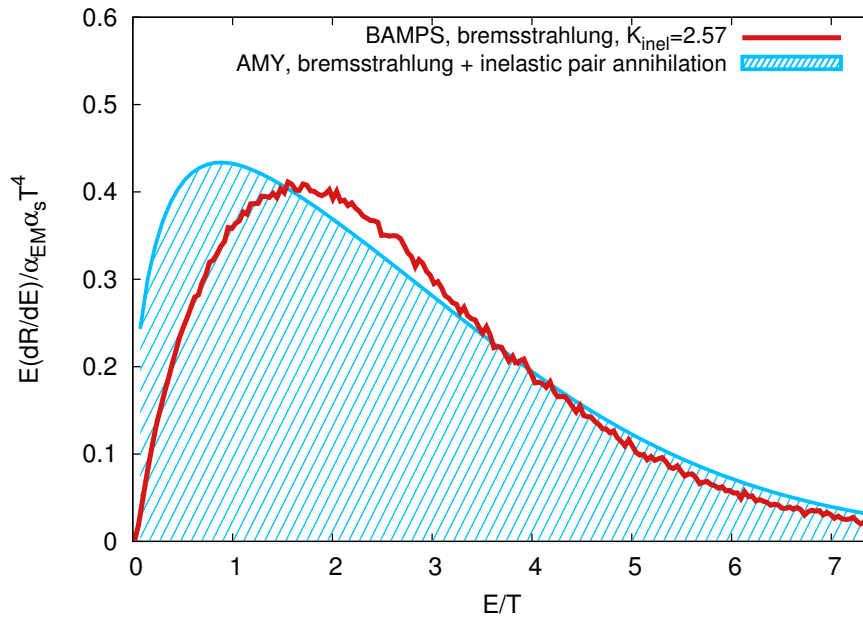
For inelastic processes, the total AMY rate dR/dE diverges for small E , and the integral is ill defined. However, for small energies (transverse momentum), experiments are not capable to measure anymore, and, the perturbative AMY description breaks down [159], so that we choose a suitable lower integration limit.

Having our application in mind, where we focus on transverse momenta in the range $0.5 < p_T/\text{GeV} < 3$, we translate this at $T \sim 0.4$ GeV to a sensible integration region of $1 < E/T < 7$, where the result is very insensitive to the upper integration limit. For the following, we use this integration region, and obtain $K_{\text{inel}} = 2.57$.

Using this factor, we make sure that we get (in an equilibrium case) the same number of photons and a similar spectrum in the energy region of interest. In Fig. 6.16 we show the numerical photon rate compared to the AMY rate, and also its first moment. The numerical rate from microscopic scatterings in Fig. 6.16(a) shows a similar slope as the AMY rate in the considered integration region, and the integrals of the curves in the plot are equal.



(a) The equilibrium radiative photon rate from $2 \rightarrow 3$ matrix elements compared to the AMY result.



(b) The equilibrium radiative photon rate from the two approaches weighted by photon energy.

Figure 6.16.: The photon rate for bremsstrahlung (a), and the rate weighted by the photon energy (b) from BAMPS (red solid line) compared to the full inelastic AMY result (blue shaded area). The integral of the rate dR/dE within $1 < E/T < 7$ is equal.

Using instead the first moment of the rate to fit K_{inel} would result in a less than 1 % different value, using the second moment less than a 4 % different value.

In Appendix B.1.5 we show the corresponding differential cross sections and cross-checks of the kinematics. As a note, the thermal photon elliptic flow, being a transfer of flow from a boosted thermal distribution to photons, is not sensitive to the differential photon rate (because photons are emitted isotropically in the local rest frame). In a non thermal case this is not true anymore, and differential cross sections matter.

6.4.1. Photon rate at nontrivial quark fugacities

The photon rate naturally depends on the quark and gluon content of the medium. For finite baryon chemical potentials (or quark chemical potential) the rate is modified by the (trivial) statistical factors ($q\bar{q}$ annihilation and Compton scattering behave differently), but also by other ingredients of the rate, such as the gluon self energies. These effects are studied thoroughly in Ref. [280]. The authors conclude, that the effect of the chemical potential to the photon spectra at RHIC or LHC is small, due to the small baryon chemical potential and the moderate sensitivity of the rates. Although we use a simplified diagrammatic setup, the effect of a quark-antiquark number asymmetry is included in the transport approach by default. For the present study at high energies, however, the effect is negligible.

The second, more important characterization of the parton content is the “absolute” fugacity. Assuming by the previous argument, that the number of quarks equals the number of antiquarks, we define the gluon (quark) fugacities $\lambda_g(\lambda_q)$ as

$$\begin{aligned} n_g &= \lambda_g n_g^{\text{equilibrium}} \\ n_q + n_{\bar{q}} &= \lambda_q \left(n_q^{\text{equilibrium}} + n_{\bar{q}}^{\text{equilibrium}} \right). \end{aligned}$$

Effectively, for the considerations in this section, there is no difference between quark and antiquark. Note that the fugacities in heavy-ion collisions are in general time dependent. The initial state is still uncertain, especially the quark and gluon content is under debate. It is commonly believed, that gluons are saturated or over-saturated [281], and quark-antiquark pairs are not very abundant in the very early phase after the collision [214]. In Ref. [282] an undersaturation of quark-antiquark pairs ($\lambda_q < 1$) seems to be favored by data within a rate equation approach. However, no precise answer about the fugacity dependence could be given up to now. Other studies [281, 283–286] give slightly different pictures, but we shall not elaborate on this topic here. Common ground is a quark fugacity λ_q which is lower than unity and may or may not approach it within the lifetime of the fireball. We investigate in the following, how the photon rate behaves for nontrivial quark/gluon fugacities. Our arguments are similar to those of Ref. [287].

Naively, the $2 \leftrightarrow 2$ Compton scattering (quark-antiquark annihilation) rates are proportional to $\lambda_q \lambda_g$ ($\lambda_q \lambda_g$) just by taking the incoming parton distribution functions into account. However, the Debye screening prescription from Eq. (6.11) lets the quark and gluon fugacities enter one more time into the rate. This will scale the rates differently as naively expected. In Fig. 6.17 we show the fugacity dependence of the $2 \leftrightarrow 2$ photon production (purple triangles) by comparing the total rate R to the rate at unity fugacity, $R[\lambda_q]/R[\lambda_q = 1]$. We have computed the Compton scattering and quark-antiquark annihilation rates for several quark fugacities (the gluon fugacity λ_g is unity here), and find a combined scaling as $\lambda_q^{1.07}$. We conclude that the $2 \leftrightarrow 2$ rates can be seen as being simply proportional to the quark fugacity.

The inelastic photon rate will scale naively with $\lambda_q \lambda_g$; however, our implementation of the LPM effect uses the numerically (i.e., dynamically) evaluated quark mean free path

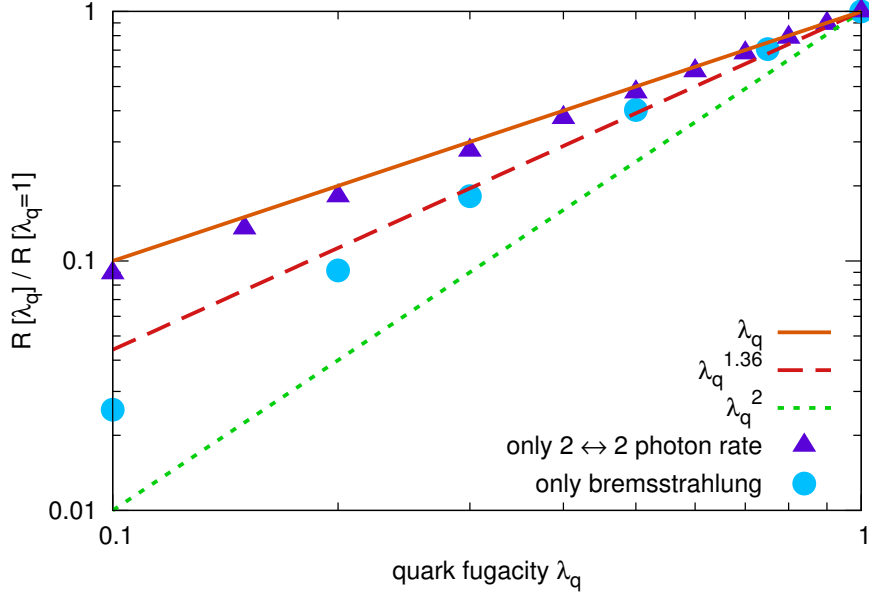


Figure 6.17.: Dependence of the photon rate R on the quark fugacity λ_q , and the comparison to the naive expectations $R \sim \lambda_q^{1,2}$ (solid, dotted line). The bremsstrahlung rate shows roughly a $R \sim \lambda_q^{1.36}$ dependence (dashed line, fit), whereas the $2 \leftrightarrow 2$ photon production processes show a behavior $R \sim \lambda_q^{1.07}$.

for specific processes (see Fig. 6.15), which depends on the average cross sections σ and particle densities n and thus on the (quark) fugacity λ_q as $\sim 1/(n\sigma) \sim 1/(\sigma\lambda_q T^3)$. The average cross sections are themselves Debye screened, and decrease for higher fugacities. These effects are summarized in Fig. 6.18, where we show the scaling of Debye mass, density, average cross section and mean free path, for the two processes considered.

Additionally, the fugacities enter also in the Debye screened gluon propagator. In Fig. 6.17 we show the scaling of the inelastic photon rate (normalized to the rate at $\lambda_q = 1$) with the fugacity and compare with a naive scaling (without the effect from the LPM procedure or Debye screening), $R[\lambda_q]/R[\lambda_q = 1] = \lambda_q^2$. By fitting a simple power law we find for bremsstrahlung roughly $R \sim \lambda_q^{1.36}$, for $\lambda_q \gtrsim 0.3$.

6.4.2. Running Coupling

It was pointed out in Ref. [288] that it is possible to define an infrared-finite running coupling. In two separate experiments the effective infrared behavior of the running coupling has been determined, including non-perturbative effects. The time-like part, $Q^2 > 0$ [288] can be extended also for space-like scales [289]. We use the following parametrization of the coupling constant,

$$\alpha_s(Q^2) = \frac{4\pi}{11 - 3n_f/3} \frac{1}{\ln(-Q^2/\Lambda_{\text{QCD}}^2)}, \quad \text{for } Q^2 < -\Lambda_{\text{QCD}}^2 \quad (6.49)$$

$$\alpha_s(Q^2) = \frac{4\pi}{11 - 3n_f/3} \left(\frac{1}{2} - \frac{1}{\pi} \arctan \left[\frac{\ln(Q^2/\Lambda_{\text{QCD}}^2)}{\pi} \right] \right), \quad \text{for } Q^2 > 0. \quad (6.50)$$

$$\alpha_s(Q^2) = \alpha_s^{\text{max}} \equiv 1, \quad \text{for } -\Lambda_{\text{QCD}}^2 < Q^2 < 0 \quad (6.51)$$

Space-like momentum transfers include most importantly the Mandelstam t variable. It has been checked, that observables are insensitive to the value of α_s^{max} [220]. Due to

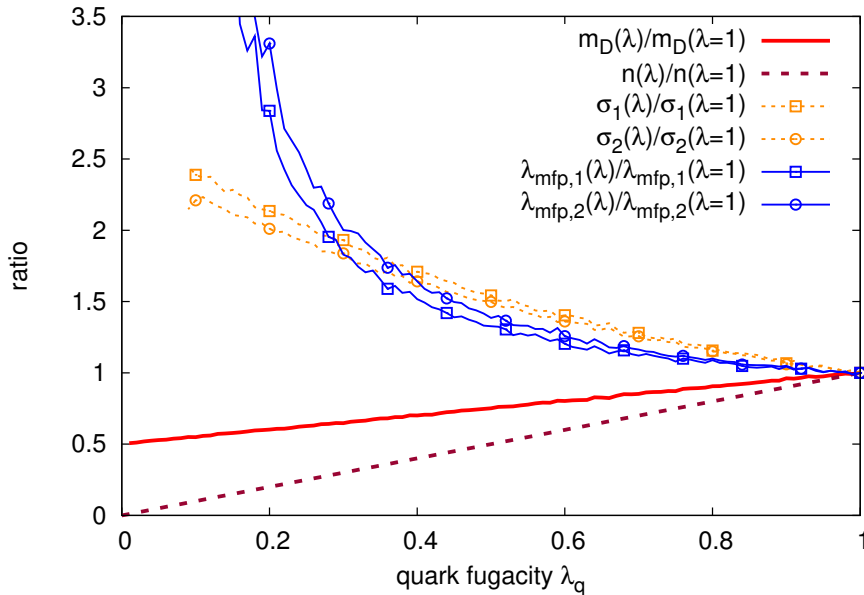


Figure 6.18.: Quark fugacity λ_q scaling of Debye mass m_D , quark density n , average cross section at $T = 0.4$ GeV, $\sigma_i \equiv \langle v_{\text{rel}} \sigma_{\text{tot},i}(s) \rangle$ (where $i = 1, 2, 3$ corresponds to the three different specific processes considered) and the specific inverse rate λ_{mfp} .

renormalization flow equations, the scale at which the running coupling is evaluated can not be set definitely, but should represent the typical scale of the problem.

Since we are using screened pQCD matrix elements (Eqs. (6.9), (6.10), (6.11) and (B.14)) the momentum scales at the vertices (Mandelstam variables) are in an individual scattering different from the background medium, whose energy scale is the temperature T . The hard-thermal loops thus operate at characteristic scale T .

In order to evaluate the running coupling $\alpha_s(Q^2)$, at the vertices one should use the Mandelstam variables of the respective channel, $Q^2 = s, t$ or u . The running coupling appears however also within the definition of the Debye mass, $m_{D,g} \sim \sqrt{\alpha_s(Q^2)}T$, see Eqs. (6.12)-(6.17). Here we have several possibilities what to use for Q^2 . In the past, it was customary within the BAMPS framework to also use the hard scale, the Mandelstam variables, however, following the above argument of hard thermal loop theory, the scale should rather be the squared temperature T^2 . More precise, it is common to use the squared first Matsubara frequency $(2\pi T)^2$ instead [254]. In literature, there was an argument to use the Debye-mass itself as a scale, see Ref. [290]. This leads to a self-consistent, recursive evaluation of the Debye mass,

$$m_{D,g}^2 = \frac{4\pi}{3} \alpha_s(m_{D,g}^2) (N_c + N_f/2) T^2. \quad (6.52)$$

This can be solved easily numerically, we will however not pursue this approach any further. In Fig. 6.19 we compare all these different descriptions for the Debye mass but the one at the Mandelstam scale, because m_D in this case depends on the scattering channel. We see that at the most relevant temperatures $T \sim 0.2 - 0.8$ GeV all descriptions are very close and the temperature dependence of $m_{D,g}/T$ is mild. Self-evidently this holds also for the thermal quark mass $m_{D,q}$.

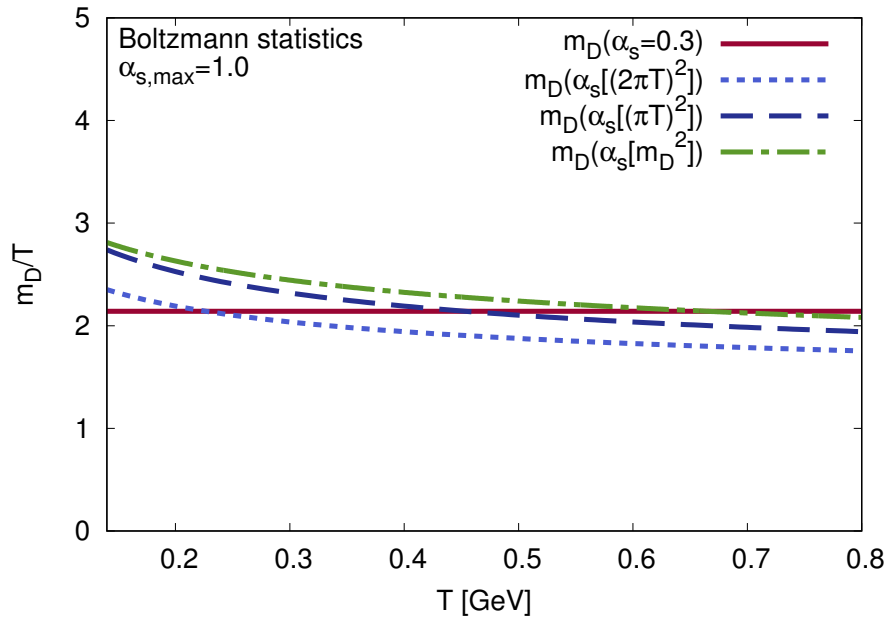


Figure 6.19.: Gluon Debye mass $m_D \equiv m_{D,g}$ for Boltzmann statistics ((6.13)) over temperature for different temperatures and four descriptions of the strong coupling: fixed coupling ($\alpha_s = 0.3$), running coupling at scale $Q^2 = \pi^2 T^2$, $4\pi^2 T^2$ and the recursive description $m_D^2 \sim \alpha_s(m_D^2)$.

7. Photon radiation using thermal resummed rates

In this chapter we first introduce a different photon production algorithm based on thermal radiation rates. Applied in a thermal or nearly thermal medium, only the temperature and the energy of an individual quark must be known to calculate the probability of radiating a photon from this quark per unit time as well as the photon’s energy distribution. This method is theoretically based on the perturbative calculation from Arnold, Moore and Yaffe [272,273], hence dubbed “AMY-formalism”. In contrast to the original works of AMY, which mostly concentrated on thermal emission rates, we evaluate the photon emission for single quarks, which in turn can easily be generalized to a thermal ensemble of the latter. We will compare the so obtained spectra of different systems (single quarks and thermal ensembles) to spectra obtained via microscopic photon production constructed in chapter 6. The stark physical differences lie in the angular emission structure (the AMY formalism has a simplifying assumption of exact collinearity) and the energy spectra. More important, the AMY formalism includes an exact resummation of the Landau-Pomeranchuk-Migdal effect. This microscopic photon radiation using a radiation kernel can be seen as an alternative method to that using the $2 \rightarrow 3$ matrix element.

7.1. Caveats in evaluating differential photon rates

One should divide the problem of jet-photon emission to the total rate of emitted photons from a jet, its rate differential in photon energy and the angular emission pattern of the photons. The term “jet” in this context only describes a single quark traversing a medium (in usual heavy-ion terminology it describes a shower of high energy particles). The first quantity is the number of photons per time, $\Gamma(p)$, emitted from a quark of momentum p . The differential rate is $d\Gamma(p)/dk$, where the photon energy is k . The angular spectrum is $d\Gamma(p)/d\theta$, where θ is the angle between the jet and the emitted photon.

As a reminder, at leading order in the rate, half of the photons in a thermal QGP bath are produced from binary processes (Compton scattering and quark-antiquark annihilation), the other half from bremsstrahlung processes $qq \rightarrow qq\gamma$ or inelastic pair annihilation $q\bar{q}q \rightarrow \gamma q$. In Secs. 6.2 and 6.3 we have shown in detail, how photon scattering matrix elements (of the above processes) can be constructed, which lead to the approximate leading order, thermal photon rates in a chemically and thermally equilibrated heat bath, $E_k dR^\gamma/d^3\vec{k}$. This was done by comparing to isotropic, local rest frame photon rates from leading order perturbation theory (AMY rate) and the subsequent fixing of the model parameters $\kappa, C_{\text{stat}}, K_{\text{inel}}$.

However, it stays somewhat questionable that also the microscopic photon emission rates $\Gamma(p)$, $d\Gamma(p)/dk$ or $d\Gamma/d\theta$ of *non-thermal systems* like “jet”-particles traversing a thermal medium are fully correct.

In the next section (Sec. 7.2) we will construct a numerical method within BAMPS using radiation kernels to guarantee that the rate $d\Gamma(p)/dk$ and $\Gamma(p)$ is nearly identical to the AMY result, as well as the thermal rate $E_k dR^\gamma/d^3\vec{k}$, without any fitting parameter. In this

method, however, the angle of a single emitted photon is assumed to be zero (consistent with AMY) and might not be fully physical.

7.2. Gluon and photon splitting in the AMY formalism

Based on the original (thermal heat bath) AMY formalism, we can describe the probability of radiating photons or gluons from single hard quarks. Based on the separation of scales $T \gg gT \gg g^2T$, radiation rates are calculated by solving a complicated integral equation, respecting the LPM effect and the Bethe-Heitler regime correctly, but assuming an infinite medium, such that no length dependence appears (as, e.g., in the Baier-Dokshitzer-Mueller-Peigne-Schiff (BDMPS) [291] scheme).

7.2.1. From thermal photon rates to jet transition rates

We now summarize systematically in detailed steps the differential photon production rates from quarks of fixed momentum p , beginning with the thermal equilibrium formulas (a numerical parametrization was given in Eq. (6.31)), based on Refs. [272,273,279,292–294].

Let the quark propagate in z -direction [294]. Then $p_z \sim T$, and $\vec{p}_\perp \sim gT$, and the quark is nearly on-shell, $p^0 = p = p^z + \mathcal{O}(g^2T)$. We denote the electric charge of a flavor f with q_f , e.g., an up-quark carries $q_{\text{up}} = (2/3)e$. The rate is [272,273,279],

$$k \frac{dR^\gamma}{d^3k} = \frac{3\alpha_{EM}}{4\pi^2} \left(\sum_f \frac{q_f^2}{e^2} \right) \int_{-\infty}^{\infty} \frac{dp_z}{(2\pi)} \int \frac{d^2\vec{p}_\perp}{(2\pi)^2} f_F(p_z + k) [1 - f_F(p_z)] \\ \times \frac{p_z^2 + (p_z + k)^2}{2p_z^2(p_z + k)^2} 2\vec{p}_\perp \cdot \text{Re}\vec{f}(\vec{p}_\perp, p_z, k). \quad (7.1)$$

Here, f_F denotes the Fermi distribution function and \vec{f} is a dimensionless function, obeying the integral equation (in this form explicitly and correctly¹ given in Refs. [296,297]),

$$2\vec{p}_\perp = i\delta E \vec{f}(\vec{p}_\perp, p_z, k) + g_s^2 T \int \frac{d^2\vec{q}_\perp}{(2\pi)^2} \mathcal{C}(\vec{q}_\perp) \left[\vec{f}(\vec{p}_\perp, p_z, k) - \vec{f}(\vec{p}_\perp - \vec{q}_\perp, p_z, k) \right]. \quad (7.2)$$

The collision kernel is [296,298]

$$\mathcal{C}(\vec{q}_\perp) = \frac{m_{D,g}^2}{\vec{q}_\perp^2 (\vec{q}_\perp^2 + m_{D,g}^2)}. \quad (7.3)$$

with squared gluon Debye mass

$$m_{D,g}^2 = \frac{g_s^2 T^2}{6} (6 + N_f). \quad (7.4)$$

The inverse formation time of the photon [297] is

$$\delta E = k \frac{\vec{p}_\perp^2 + m_\infty^2}{2p_z(p_z + k)} \quad (7.5)$$

and the asymptotic (quark) mass,

$$m_\infty^2 = g_s^2 C_R T^2 / 4 = m_q^2. \quad (7.6)$$

¹In Ref. [294] there is a 2 missing, and in Ref. [295] there is an unclear factor $\frac{2\pi}{3}$.

It is useful to show, that the last integral in Eq. (7.1) scales with g_s^2 . To this end, we define scaled variables,

$$\begin{aligned}\tilde{\vec{p}}_{\perp} &= \vec{p}_{\perp}/g_s, \\ \tilde{\vec{q}}_{\perp} &= \vec{q}_{\perp}/g_s, \\ \tilde{f}(\tilde{\vec{p}}_{\perp}, p_z, k) &= g_s \vec{f}(\vec{p}_{\perp}, p_z, k), \\ \tilde{m}_D^2 &= m_D^2/g_s^2, \\ \tilde{m}_{\infty}^2 &= m_{\infty}^2/g_s^2,\end{aligned}\tag{7.7}$$

such that Eq. (7.1) becomes

$$\begin{aligned}k \frac{dR^{\gamma}}{d^3k} &= \frac{3\alpha_{EM}}{4\pi^2} \left(\sum_f \frac{q_f^2}{e^2} \right) \int_{-\infty}^{\infty} \frac{dp_z}{(2\pi)} f_F(p_z + k) [1 - f_F(p_z)] \frac{p_z^2 + (p_z + k)^2}{2p_z^2(p_z + k)^2} \\ &\quad \times g_s^2 \int \frac{d^2\tilde{\vec{p}}_{\perp}}{(2\pi)^2} 2\tilde{\vec{p}}_{\perp} \cdot \text{Re}\tilde{f}(\tilde{\vec{p}}_{\perp}, p_z, k).\end{aligned}\tag{7.8}$$

In these scaled variables, Eq. (7.2) has no dependence on g_s^2 any more, such that it must only once be solved numerically to obtain the rate for arbitrary g_s^2 . We keep the original notation (without the scaled variables) from now on.

The dp_z integration can be interpreted physically as follows,

$$\begin{aligned}-\infty < p_z < -k &: && \text{Bremsstrahlung of antiquark of energy } -p_z \\ -k < p_z < 0 &: && \text{Inelastic pair annihilation with antiquark from medium, energy } p \\ 0 < p_z < \infty &: && \text{Bremsstrahlung of quark of energy } p + k\end{aligned}\tag{7.9}$$

We define the integrand of Eq. (7.1) as

$$G(p_z, k) \equiv f_F(p_z + k) [1 - f_F(p_z)] \frac{p_z^2 + (p_z + k)^2}{2p_z^2(p_z + k)^2} \int \frac{d^2\vec{p}_{\perp}}{(2\pi)^2} 2\vec{p}_{\perp} \cdot \text{Re}\vec{f}(p_z, \vec{p}_{\perp}, k),\tag{7.10}$$

and write the integral as

$$\begin{aligned}\int_{-\infty}^{\infty} \frac{dp_z}{(2\pi)} G(p_z, k) &= \int_{-\infty}^{-k} \frac{dp_z}{(2\pi)} G(p_z, k) + \int_{-k}^0 \frac{dp_z}{(2\pi)} G(p_z, k) + \int_0^{\infty} \frac{dp_z}{(2\pi)} G(p_z, k) \\ &= \int_{-\infty}^0 \frac{dp_z}{(2\pi)} G(p_z, k) \Theta(-k - p_z) + \int_{-\infty}^0 \frac{dp_z}{(2\pi)} G(p_z, k) \Theta(p_z + k) \\ &\quad + \int_0^{\infty} \frac{dp_z}{(2\pi)} G(p_z, k) \\ &= \int_0^{\infty} \frac{dp_z}{(2\pi)} [G(-p_z, k) \Theta(-k + p_z) + G(-p_z, k) \Theta(-p_z + k) + G(p_z, k)].\end{aligned}\tag{7.11}$$

Using $f_F(-p) = 1 - f_F(p)$, we remark that $G(p_z - k, k) = G(-p_z, k)$, namely,

$$G(-p_z, k) \equiv f_F(p_z) [1 - f_F(p_z - k)] \frac{p_z^2 + (p_z - k)^2}{2p_z^2(p_z - k)^2} \int \frac{d^2\vec{p}_{\perp}}{(2\pi)^2} 2\vec{p}_{\perp} \cdot \text{Re}\vec{f}(-p_z, \vec{p}_{\perp}, k).\tag{7.12}$$

Here, the inverse formation time δE from Eq. (7.5) with substitution $p_z \rightarrow -p_z$ is the same as with substitution $p_z \rightarrow p_z - k$, thus $\text{Re}\vec{f}(-p_z, \vec{p}_\perp, k) = \text{Re}\vec{f}(p_z - k, \vec{p}_\perp, k)$. In the last integral (only the $G(p_z, k)$ term) of Eq. (7.11), we substitute

$$p'_z = p_z + k, \quad dp'_z = dp_z, \quad (7.13)$$

shifting the integration region to $k < p'_z < \infty$ (and renaming afterwards $p'_z \rightarrow p_z$), such that Eq. (7.11) becomes

$$\begin{aligned} \int_{-\infty}^{\infty} \frac{dp_z}{(2\pi)} G(p_z, k) &= \int_0^{\infty} \frac{dp_z}{(2\pi)} [G(-p_z, k)\Theta(p_z - k) + G(-p_z, k)\Theta(-p_z + k) \\ &\quad + G(p_z - k, k)\Theta(p_z - k)]. \\ &= 2 \int_0^{\infty} \frac{dp_z}{(2\pi)} \left[G(-p_z, k)\Theta(p_z - k) + \frac{1}{2}G(-p_z, k)\Theta(-p_z + k) \right]. \end{aligned} \quad (7.14)$$

The region describing the inelastic pair annihilation $0 < p_z < k$ includes the contribution of quarks and antiquarks. We introduce a function

$$b(p_z, k) = \left[\frac{1}{2}\Theta(k - p_z) + \Theta(p_z - k) \right], \quad (7.15)$$

which guarantees that the inelastic pair annihilation is not doubly counted when we write the rate of photon emission of only quarks,

$$\begin{aligned} k \frac{dR_q^\gamma}{d^3k} &= \frac{3\alpha_{EM}}{4\pi^2} \left(\sum_f \frac{q_f^2}{e^2} \right) \int_0^{\infty} \frac{dp_z}{(2\pi)} b(p_z, k) \int \frac{d^2\vec{p}_\perp}{(2\pi)^2} f_F(p_z) [1 - f_F(p_z - k)] \\ &\quad \times \frac{p_z^2 + (p_z - k)^2}{2p_z^2(p_z - k)^2} 2\vec{p}_\perp \cdot \text{Re}\vec{f}(p_z, \vec{p}_\perp, k). \end{aligned} \quad (7.16)$$

where the inverse formation time in the integral equation Eq. (7.2) must (in this notation, calling the function \vec{f} with positive p_z argument) be changed to

$$\delta E = k \frac{\vec{p}_\perp^2 + m_\infty^2}{2p_z(p_z - k)}. \quad (7.17)$$

This concludes the calculation for photons. In analogy to the radiative gluon production rate (from literature [278]), we however want to introduce another notation, for the only purpose of enabling a direct comparison to literature. As customary, we define a vector $\vec{h} = \vec{p} \times \vec{k}$. This is only an internal variable, but can be imagined as a measure, how non-collinear the final state is, since in an exactly collinear case \vec{h} would vanish. We define a two-dimensional vector in the transverse plane of $\vec{p}_z \equiv \vec{p}_\parallel$, which is denoted by $\vec{p}_\perp = p_\perp \vec{e}_\perp$ and order gT . In this notation, we have [279]

$$\vec{h} = \vec{p}_\parallel \times \vec{k} = p_\perp k \vec{e}_\perp = \vec{p}_\perp k, \quad (7.18)$$

thus Eq. (7.16) becomes

$$\begin{aligned}
k \frac{dR_q^\gamma}{d^3k} &= \frac{3\alpha_{EM}}{4\pi^2} \left(\sum_f \frac{q_f^2}{e^2} \right) \int_0^\infty \frac{dp_z}{(2\pi)} b(p_z, k) \int \frac{d^2\vec{h}}{(2\pi)^2 k^2} f_F(p_z) [1 - f_F(p_z - k)] \\
&\quad \times \frac{p_z'^2 + (p_z - k)^2}{2p_z'^2 (p_z - k)^2} \frac{\vec{h}}{k} \cdot \text{Re} \frac{\vec{F}}{k} \\
&= \frac{2}{2} \frac{3\alpha_{EM}}{8\pi^2 k} \left(\sum_f \frac{q_f^2}{e^2} \right) \int_0^\infty \frac{dp}{(2\pi)} b(p, k) \int \frac{d^2\vec{h}}{(2\pi)^2} f_F(p) [1 - f_F(p - k)] \\
&\quad \times \frac{1}{p^5} \frac{1 + (1 - x)^2}{x^3 (1 - x)^2} 2\vec{h} \cdot \text{Re} \vec{F}, \tag{7.19}
\end{aligned}$$

where we renamed $p_z \equiv p$ and introduced $x \equiv k/p_z$ in the second step.

The function $\vec{F} \equiv \vec{f}k$ must now be determined from Eq. (7.2) but with an appropriate variable change (this will be done in Eq. (7.27) with $C_A \equiv 0$) and wherein Eq. (7.17) changes to

$$\delta E = \frac{\vec{h}^2 + k^2 m_q^2}{2pk(p - k)}. \tag{7.20}$$

Equation (7.19) is the form of the radiative scattering rate given, e.g., in Ref. [279]. We now make the connection to the transition rate $d\Gamma_f^\gamma(p, k)/dk$. With the quark+antiquark density

$$\frac{dN^{q+\bar{q}}}{d^3\vec{x}} = \sum_f 12 \int \frac{d^3\vec{p}}{(2\pi)^3} f_F(p), \tag{7.21}$$

we transform the thermal photon production rate

$$\begin{aligned}
k \frac{dR_q^\gamma}{d^3\vec{k}} &\equiv \sum_f 12 \int \frac{d^3\vec{p}}{(2\pi)^3} f_F(p) k \frac{d\Gamma_f^\gamma(p, k, T)}{d^3\vec{k}} b(p, k) \\
&= \sum_f 12 \int_0^\infty \frac{dp p^2 (4\pi)}{(2\pi)^3} f_F(p) k \frac{d\Gamma_f^\gamma(p, k, T)}{k^2 dk (4\pi)} b(p, k) \\
&= \sum_f 12 \int_0^\infty \frac{dp}{(2\pi)^3} f_F(p) \frac{p^2}{k} \frac{d\Gamma_f^\gamma(p, k, T)}{dk} b(p, k) \\
&= 2 \sum_f 6 \int_0^\infty \frac{dp}{(2\pi)^3} f_F(p) \frac{p^2}{k} \frac{d\Gamma_f^\gamma(p, k, T)}{dk} b(p, k) = 2k \frac{dR_q^\gamma}{d^3k} \tag{7.22}
\end{aligned}$$

By rewriting Eq. (7.19),

$$\begin{aligned}
k \frac{dR_q^\gamma}{d^3\vec{k}} &= \sum_f 6 \int_0^\infty \frac{dp}{(2\pi)^3} f_F(p) \frac{p^2}{k} b(p, k) \\
&\quad \times \left[\frac{k}{p^2} \frac{\alpha_{EM}}{4k} \frac{q_f^2}{e^2} \int \frac{d^2\vec{h}}{(2\pi)^2} [1 - f_F(p - k)] \frac{1}{p^5} \frac{1 + (1 - x)^2}{x^3 (1 - x)^2} 2\vec{h} \cdot \text{Re} \vec{F} \right], \tag{7.23}
\end{aligned}$$

we find the radiative photon production rate from a single quark with flavor f , momentum p at background temperature T

$$\frac{d\Gamma_f^\gamma(p, k, T)}{dk} = \frac{q_f^2}{e^2} \frac{\alpha_{EM}}{4p^7} [1 - f_F(p - k)] \frac{1 + (1 - x)^2}{x^3 (1 - x)^2} \int \frac{d^2\vec{h}}{(2\pi)^2} 2\vec{h} \cdot \text{Re} \vec{F}(\vec{h}, p, k). \tag{7.24}$$

Alternatively, we can use

$$\frac{d\Gamma_f^\gamma(p, k, T)}{dk} = \frac{q_f^2 \alpha_{EM} k^4}{e^2 4p^7} [1 - f_F(p - k)] \frac{1 + (1 - x)^2}{x^3(1 - x)^2} \int \frac{d^2\vec{p}_\perp}{(2\pi)^2} 2\vec{p}_\perp \cdot \text{Re}\vec{f}(\vec{p}_\perp, p, k). \quad (7.25)$$

The rate for emission of an antiquark naturally has the same expression. The solution of the integral equations is most conveniently done by the impact parameter method [297, 298], transforming the integral equation into an ordinary differential equation which can be numerically solved.

7.2.2. Numerical implementation of AMY emission rates in BAMPS

We evaluate Eq. (7.25) numerically for several values of p/T and k/T . The rate diverges for $k = p$ and $k = 0$, that is why we omit singular regions of width $\Delta p/T = \Delta k/T = 0.05$. The rate is tabulated, and numerically interpolated, and can then be integrated over k/T from $k/T = 0$ to $k/T = \infty$ to obtain $\Gamma^\gamma(p, T) = \Gamma^\gamma(p/T)T$. In the local rest frame of a microscopic ensemble of quarks such as in BAMPS, the number of emitted photons from a quark with flavor f in timestep Δt is thus $\Delta t \Gamma_f^\gamma(p, T)$. If this number is not integer, one must sample the number of photons, according to the emission probability. If a photon is created, the momentum k of the photon is sampled along $d\Gamma^\gamma(p, T)/dk$. The numerical steps are

1. Boost every numerical cell into a frame with zero collective velocity
2. Extract the temperature T in this cell
3. For each quark with LRF momentum p , generate a photon with probability $\Delta t \Gamma_f^\gamma(p, T)$
4. Sample the momentum k of the photon with probability distribution Eq. (7.25)
5. Boost all particles, including the photons back to the original frame

Very crucial numerical tests include the comparison of (a numerical evaluation of) Eq. (7.25) with the same quantity obtained by propagating a single quark with energy p through a medium with temperature T in BAMPS, emitting photons with the above algorithm. This is done in Fig. 7.1, for up-quark type jets of energy $p/T = 1, 5, 50$. Clearly, the method is reliable and precise².

The second test one should conduct is the comparison of the analytic thermal photon production rate from Eq. (6.31) with the rate obtained in BAMPS, where one generates a thermal ensemble of $N_f = 3$ massless quarks and gluons, letting the quarks emit photons by the above algorithm. This effectively folds the thermal parton distribution function with the emission rate Eq. (7.25). This is done in Fig. 7.2. The agreement is quite precise and suffers only from small discretization errors due to tabulated and interpolated rates.

²We furthermore obtain identical emission rates as used in the established MARTINI code [299].

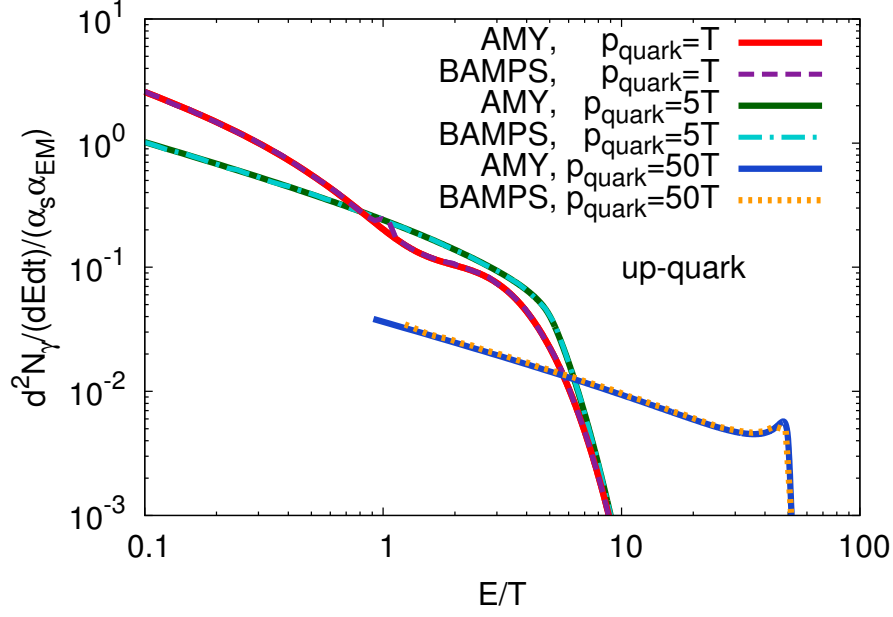


Figure 7.1.: Photon emission rate per up-quark of momentum p_{quark} versus photon energy E from Eq. (7.25) (“AMY”) and from BAMPS, using the tabulated “AMY” radiation kernel.

7.2.3. Gluon emission rates

The thermal invariant gluon production rate (for simplicity here only for processes $q \rightarrow q + g$ in a thermal bath) is [279]

$$\begin{aligned}
k \frac{dR^g}{d^3\vec{k}} &= \frac{g_s^2}{16(2\pi)^3 k^4} \sum_f 12C_R \int_{-\infty}^{\infty} \frac{dp}{2\pi} \int \frac{d^2\vec{h}}{(2\pi)^2} f_F(p+k) [1 - f_F(p)] [1 + f_B(k)] \\
&\quad \times \frac{p^2 + (p+k)^2}{p^2(p+k)^2} 2\vec{h} \cdot \text{Re}\vec{F}(\vec{h}, p+k, k) \\
&= \frac{g_s^2}{16(2\pi)^3 k^4} \sum_f 12C_R \int_{-\infty}^{\infty} \frac{dp}{2\pi} \int \frac{d^2\vec{h}}{(2\pi)^2} f_F(p) [1 - f_F(p-k)] [1 + f_B(k)] \\
&\quad \times \frac{(p-k)^2 + p^2}{(p-k)^2 p^2} 2\vec{h} \cdot \text{Re}\vec{F}(\vec{h}, p, k) \\
&= \frac{g_s^2}{16(2\pi)^3 k} \sum_f 12C_R \int_{-\infty}^{\infty} \frac{dp}{2\pi} f_F(p) \int \frac{d^2\vec{h}}{(2\pi)^2} [1 - f_F(p-k)] [1 + f_B(k)] \\
&\quad \times \frac{1}{p^5} \frac{1 + (1-x)^2}{x^3(1-x)^2} 2\vec{h} \cdot \text{Re}\vec{F}(\vec{h}, p, k),
\end{aligned} \tag{7.26}$$

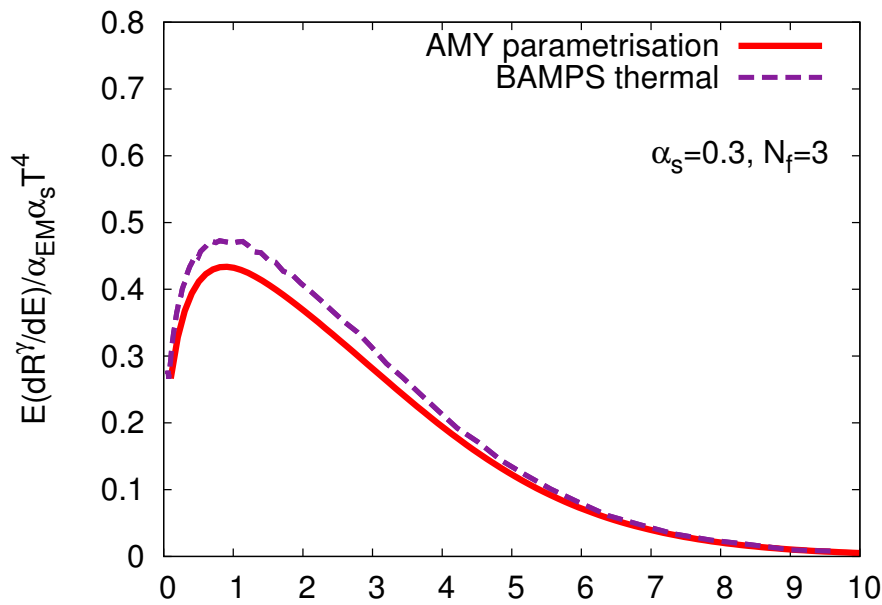
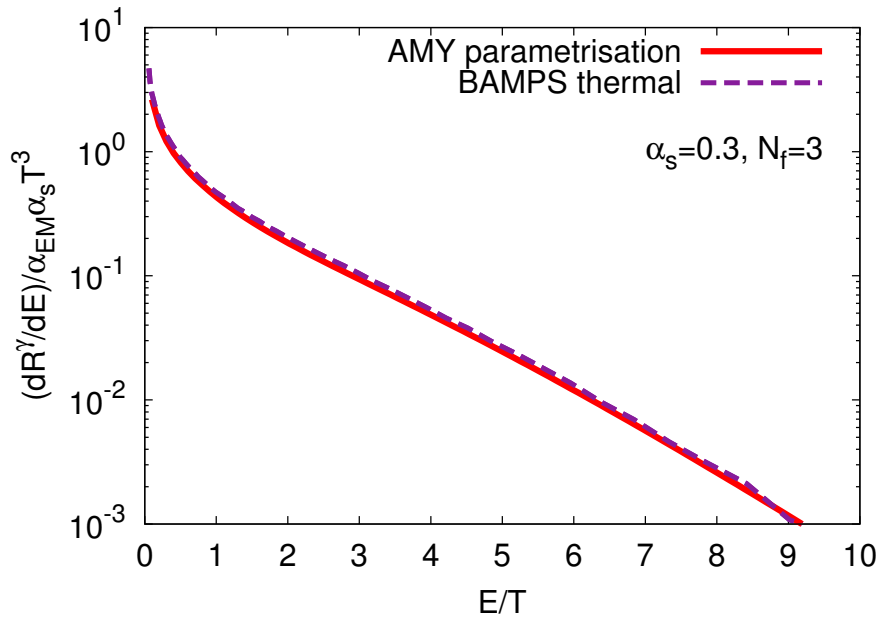


Figure 7.2.: Thermal equilibrium photon emission rate from the original parametrization (Eq. (6.31)) compared to the production of photons via AMY rates in a parton heat bath from BAMPS.

where $\vec{h} = \vec{p} \times \vec{k}$, the quadratic Casimir of the emitter, $C_R = 4/3$ and $x \equiv k/p$. The function $\vec{F}(\vec{h}, p, k)$ (unit energy) has to be determined by solving the following equation,

$$2\vec{h} = i\delta E(\vec{h}, p, k)\vec{F}(\vec{h}, p, k) + g_s^2 T \int \frac{d^2\vec{q}_\perp}{(2\pi)^2} \mathcal{C}(q_\perp) \left\{ (C_R - C_A/2) \left[\vec{F}(\vec{h}) - \vec{F}(\vec{h} - k\vec{q}_\perp) \right] \right. \\ \left. + (C_A/2) \left[\vec{F}(\vec{h}) - \vec{F}(\vec{h} + p\vec{q}_\perp) \right] \right. \\ \left. + (C_A/2) \left[\vec{F}(\vec{h}) - \vec{F}(\vec{h} - (p-k)\vec{q}_\perp) \right] \right\}, \quad (7.27)$$

with $C_A = 3$ and where

$$\delta E = \frac{\vec{h}^2}{2pk(p-k)} + \frac{m_k^2}{2k} + \frac{m_{p-k}^2}{2(p-k)} - \frac{m_p^2}{2p} \quad (7.28)$$

can be interpreted as the inverse formation time of the emitted particle. The masses of the particles, labeled by the momentum of the particle, are thermal masses $\sim gT$. For photons, $m_\gamma = 0$, for gluons, $m_g = m_{D,g}/\sqrt{2}$ (with squared Debye mass from Eq. (7.4)) and for quarks, $m_q = g_s T/\sqrt{3}$. For gluon emission from quark jets with momentum p , we get in a similar way as before for the photons,

$$\frac{d\Gamma^g}{dk}(p, k) = C_R \frac{g_s^2}{16\pi p^7} \frac{1}{1 - e^{-k/T}} \frac{1}{1 + e^{-(p-k)/T}} \frac{1 + (1-x)^2}{x^3(1-x)^2} \int \frac{d^2\vec{h}}{(2\pi)^2} 2\vec{h} \cdot \text{Re}\vec{F}(\vec{h}, p, k), \quad (7.29)$$

where the main difference is an additional Bose enhancement factor $1 + f_B(k) = (1 - \exp(-k/T))^{-1}$ for the outgoing gluon, and the overall g_s^2 dependence instead of e^2 as in the photon radiation case.

8. Differential kinematics of photon production

If the geometry of a heavy-ion collision is exactly known, one can define transverse symmetry axes, and evaluate momentum asymmetries with respect to these axes. The most important observable in this respect is the elliptic flow v_2 . If the geometry of an event is not known, in order to extract momentum asymmetries, one must compute multi-particle correlation functions and their Fourier decomposition [300, 301]. With the azimuthal angle ϕ and the event-plane angle ψ_n of the n 'th Fourier component, the n 'th order flow coefficient is $v_n = \langle \cos(n[\phi - \psi_n]) \rangle$, where the brackets denote the event average. If the geometry is fix, one can turn the coordinate system to set $\psi_n \equiv 0$. For the important case $n = 2$ we have $\cos \phi = p_x/p_T$ and $\sin \phi = p_y/p_T$ such that $\cos(2\phi) = (p_x^2 - p_y^2)/p_T^2$ and $v_2 = \langle (p_x^2 - p_y^2)/p_T^2 \rangle$. Note that the value of, e.g., the elliptic flow v_2 is not boost invariant, if the boost is in x or y direction. In the local rest frame of a thermal distribution function there is now elliptic flow, whereas a boosted distribution $dN/d^3\vec{p}'d^3\vec{x}'$ exhibits a nonzero $v_2 = \langle (p_x'^2 - p_y'^2)/p_T'^2 \rangle$ if the boost velocity has x or y components. In this chapter, we examine the relation of relativistic boosts and average momentum asymmetries, and focus on the question, how v_2 is translated from a particle distribution onto the distribution of produced particles such as photons. Additionally, we investigate the angular structure of photon emission of single quarks, for quark and gluon jets. In some cases one can speak of jet-photon conversion, and this can have consequences for the measured elliptic flow.

8.1. Boosted particle production rates

In general, a particle production rate of the following form is Lorentz invariant,

$$E \frac{dR}{d^3\vec{p}} = E' \frac{dR}{d^3\vec{p}'}. \quad (8.1)$$

For clarity, we first construct a simple production rate of particles with constant, isotropic cross section σ_{tot} , which is realized by the matrix element $|\mathcal{M}|^2 = 16\pi s\sigma_{22}$. This can be seen by the formula for massless particles,

$$\frac{d\sigma}{dt} = \frac{|\mathcal{M}|^2}{16\pi s^2}, \quad \int_{-s}^0 \frac{d\sigma}{dt} dt = \sigma_{\text{tot}}. \quad (8.2)$$

In this case, we are able to integrate the rate integral, Eq. (6.27), analytically, with the result

$$\mathcal{R}(E, T) \equiv E \frac{dR}{d^3\vec{p}} = \frac{1}{\nu} \frac{T^3}{2(2\pi)^6 E} (16\pi\sigma_{\text{tot}}) e^{-E/T} E^2. \quad (8.3)$$

Here, the symmetry factor $\nu = 2$ is due to the indistinguishable two incoming particles. For different particles in the initial state, one has $\nu = 1$. For a general velocity u^μ , this generalizes because of Eq. (8.1) to

$$E \frac{dR}{d^3\vec{p}} = \frac{1}{\nu} \frac{4T}{(2\pi)^5 p^\mu u_\mu} (T^2 \sigma_{\text{tot}}) e^{-p^\mu u_\mu/T} (p^\mu u_\mu)^2. \quad (8.4)$$

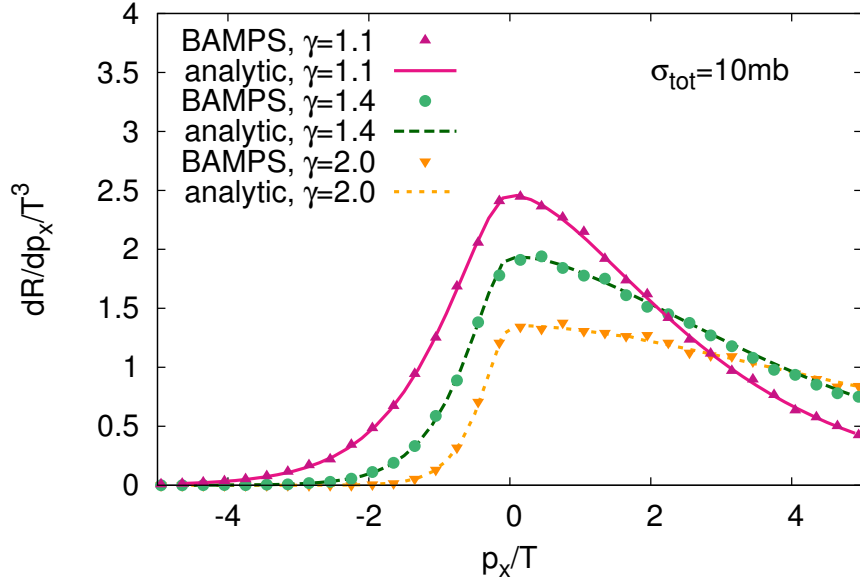


Figure 8.1.: A differential particle production rate in p_x for an in x direction boosted system. The production of the particles is governed by a constant isotropic cross section $\sigma_{\text{tot}} = 10$ mb.

For a boosted system, say, with boost velocity in x -direction, $u^\mu = (\gamma, \gamma\beta_x, 0, 0)$, the interesting differential rate is $dR/dp_x/T^3$, which is expected to show a tilt around $p_x/T = 0$, as particle momenta are boosted. One calculates the rate via,

$$\frac{dR}{dp_x} = \frac{dN}{dt d^3\vec{x} dp_x} = \int dp_y \int dp_z \frac{P \cdot U}{E} \frac{1}{P \cdot U} \mathcal{R}(P \cdot U, T), \quad (8.5)$$

where $E = \sqrt{p_x^2 + p_y^2 + p_z^2}$ and $P \cdot U = \gamma(E - \beta p_x)$. Using BAMPS, we initialize a boosted thermal distribution of particles (of single species), applying a fixed particle production cross section σ_{tot} . In Fig. 8.1 we compare Eq. (8.5) with the numerical results. We show the scaled production rate versus momentum component p_x for three different boosts, $\gamma = 1.1, 1.4, 2.0$. The rate becomes asymmetric, since the background distribution is already asymmetric around p_x . The perfect agreement validates the numerical extraction of the rate, as well as its implementation. The asymmetry in the p_x -component of the produced particles immediately implies a nonzero v_2 (with respect to p_x, p_y).

8.2. Analytically computed thermal average

Next we want to study, how momentum anisotropies of background particle distributions $f(p)$ translate into anisotropies of particles, which are radiated by the background medium. This is a fundamental question, because the elliptic flow v_2 , being a measure for momentum anisotropy, is experimentally measured for identified or inclusive hadrons, as well as for direct photons. The inclusive hadron spectra emerge from a nearly thermal, but anisotropically flowing QGP medium, which itself produces photons. The photons do not interact anymore until they reach the detector, and naturally one must ask how the momentum distributions of the quarks and gluons differ from that of the photons.

Thermal averages of momentum dependent observables like the momentum anisotropy

$$v_2(p_x, p_y) = \frac{p_x^2 - p_y^2}{p_x^2 + p_y^2} \quad (8.6)$$

can be computed analytically for systems of background (bg) particles belonging to a distribution $f = dN/d^3\vec{p}$:

$$\langle v_2^{\text{bg}} \rangle = \frac{\int d^3\vec{p} f(\vec{p}) v_2(p_x, p_y)}{\int d^3\vec{p} f(\vec{p})}. \quad (8.7)$$

For particles that are created with a certain rate R from a background distribution f , the average is given by a weighting with the differential rate,

$$\langle v_2^{\text{produced particles}} \rangle = \frac{\int d^3\vec{p} \frac{dR}{d^3\vec{p}} v_2}{\int d^3\vec{p} \frac{dR}{d^3\vec{p}}}, \quad (8.8)$$

where the rate is computed from a system where f is the underlying distribution. In Fig. 8.2 we show the comparison between the thermal averages Eq. (8.7) and Eq. (8.8) with the numerical results from BAMPS. To this end we sample a collection of particles from a boosted thermal distribution with $u^\mu = (\gamma, \gamma v_x, 0, 0)$. We then use three different cross sections to produce noninteracting particles. We plot γ on the horizontal axis and the average

$$v_2 = \langle v_2(p_x, p_y) \rangle \quad (8.9)$$

on the vertical axis in Fig. 8.2. The red spheres are values extracted by averaging $v_2(p_x, p_y)$ over the sampled background particles, and the red dotted line is the result from Eq. (8.7). The precise agreement shows that the sampling works satisfactorily. The green squares are obtained by using a constant, isotropic cross section σ_{tot} to produce particles, whereas the green line is obtained by using Eq. (8.8) with the distribution Eq. (8.4). The yellow upward triangles are the results from a $2 \leftrightarrow 2$ pQCD photon production (see Chap. 6), which is Compton scattering and quark-antiquark annihilation. Here we use Eq. (8.8) with a simplified analytic photon rate from Ref. [23]. The numerical results agree in both cases very well with the analytic estimate. We observe that the behavior of the momentum anisotropy is extremely similar to that obtained from constant isotropic cross sections. We expect, that also more complicated rates, such as bremsstrahlung, follows this trend. We therefore plot also the result for photon bremsstrahlung (see Chap. 6) with blue downward triangles, and see that this is true. In fact, this is the expected behavior since particle production rates must be evaluated in the local rest frame of an underlying particle system. This is common practice in hydrodynamics, and here, we merely show the corresponding formalism in a microscopic picture. Denoting the rate by $\mathcal{R}(E, T) = E \frac{dN}{d^3\vec{p} d^4x}$, the rate of photons of a flowing (hydrodynamic) medium is given by

$$E \frac{dR}{d^3\vec{p}} = \int_{\text{flow field}} d^4x \mathcal{R}(u^\mu(x) p_\mu, T(x)), \quad (8.10)$$

where it is made explicit that the rate is evaluated in the local rest frame.

The most important lesson to learn from this exercise however is the difference between the background v_2 and the v_2 of produced particles. For infinite boosts, $\gamma \rightarrow \infty$, as well as in the rest frame, they are equal ($v_2(\gamma = \infty) = 1$ or $v_2(\gamma = \infty) = 0$, respectively), in all other cases the v_2 of produced particles is smaller than the background v_2 . The reduction

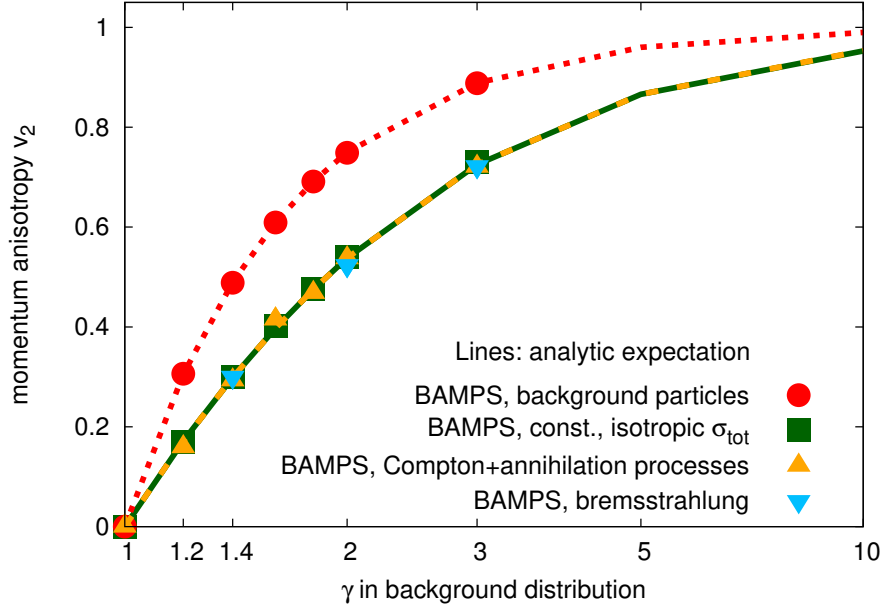


Figure 8.2.: Momentum anisotropy of background particles (red dots) and produced particles (squares and triangles) in a thermal system (vertical axis) versus boost parameter of the background distribution γ . The lines are the analytic expectation from Eq. (8.7) and Eq. (8.8).

depends on the strength of the boost, where the ratio $\langle v_2^{\text{produced particles}} \rangle / \langle v_2^{\text{bg}} \rangle$ is smallest for small boosts. In heavy-ion experiments, momentum anisotropies of charged hadrons are of the order of a few percent. Assuming a nearly thermal quark and gluon distribution to have a momentum anisotropy of the same order, one expects the photon anisotropy to be somewhat smaller.

8.3. Photonic elliptic flow from multiple sources

In relativistic heavy-ion collisions, photons are produced by very different mechanisms, each contributing a part to the photon spectrum, whereby the photons all show different strength of the momentum asymmetry observable v_2 . The final, observable photon v_2 is weighted average over all sources (prompt, preequilibrium, QGP, hadronic), the spectrum being the weight of each contribution:

$$v_2(p_T) = \frac{1}{\sum_{\text{source } i} \frac{dN^i}{dp_T}} \left(\frac{dN^{\text{prompt}}}{dp_T} v_2^{\text{prompt}}(p_T) + \frac{dN^{\text{preequilibrium}}}{dp_T} v_2^{\text{preequilibrium}}(p_T) + \frac{dN^{\text{QGP}}}{dp_T} v_2^{\text{QGP}}(p_T) + \frac{dN^{\text{hadronic}}}{dp_T} v_2^{\text{hadronic}}(p_T) \right). \quad (8.11)$$

At present, one mostly assumes vanishing v_2 for the prompt contribution, and in this thesis, we show that also the preequilibrium and QGP value of v_2 is small. It is however never enough to investigate only the flow patterns, the yield is just as important.

8.4. Elliptic flow of photons originating from parton jets

In BAMPS, photon production shows a small, positive v_2 , coming from a hydro-like flowing background, “carried over” from quarks to photons. At higher transverse momenta, we will partly see negative v_2 , which we explain by leaking particles; An asymmetric collision region, combined with collinear emission of photons or jet-photon conversion, has more photons emitted in the long direction of the almond-shaped collision region which can make the v_2 negative¹.

Here we investigate in some more detail this leakage effect. We remark that this observation would not be possible in hydrodynamic calculations.

8.4.1. Box calculation of photon leakage effect

To understand the kinetics of photons originating from hard partons qualitatively we use a fixed box with volume $V = L_x \cdot L_y \cdot L_z$, and populate it homogeneously with a thermal distribution of quarks and gluons (temperature T). This distribution can either be at rest with a four-velocity $u^\mu = (1, 0, 0, 0)$, or boosted in the x direction, $u^\mu = (\gamma, \gamma v_x, 0, 0)$, such that there is a strong collective flow in the x direction (as seen from the laboratory frame). We change the box size to be either very thin, $L_x/L_y \ll 1$ or cubic, $L_x = L_y = L_z$. Furthermore, we initialize at the geometric center of the box a large amount of “jet”-like particles isotropically with a fixed energy $E_j \sim 5T - 10T$. All particles are allowed to scatter and produce photons, however, when any particle hits the wall, it is deleted. We define a transverse momentum, $p_T = \sqrt{p_x^2 + p_y^2}$. Our observable resembles an elliptic flow v_2 , but here it is merely a momentum anisotropy,

$$v_2 = \left\langle \frac{p_x^2 - p_y^2}{p_T^2} \right\rangle_{\text{average all photons}}. \quad (8.12)$$

To this end, we consider five scenarios:

- A** Cubic box at rest, including jets
- B** Cubic box with flow, without jets
- C** Cubic box with flow, including jets (jet $p_T = 10T$)
- D** Thin box, $L_x/L_y \ll 1$ at rest, including jets (jet $p_T = 5T, 10T$)
- E** Thin box, $L_x/L_y \ll 1$ with flow, including jets (jet $p_T = 10T$)

Evaluating the momentum anisotropy from these scenarios, we plot the results in Fig. 8.3. As expected, no flow is visible in the symmetric scenario A. In scenario B a thermal, flowing background generates a momentum anisotropy which increases for higher p_T . Undisturbed flow from the background is carried over to photons. Here we note that, by a simple relativistic effect, the (Lorentz variant) result of Eq. (8.12) for produced particles is lower in magnitude than that for the background distribution. This effect depends on the boost. Including jets, which are isotropically emitted from the center, the flow reduces to zero at exactly the jet energy. For Compton scattering and quark-antiquark annihilation a large amount of photons inherit nearly the full momentum from the jets (jet-photon conversion). Because the jet momentum is dominant, the momentum anisotropy of these photons is

¹The results from Chap. 9 and Ref. [4] use a smooth Glauber initial state. An event-by-event calculation would probably be more realistic and also a leakage or escape effect reflecting the geometry could be possible.

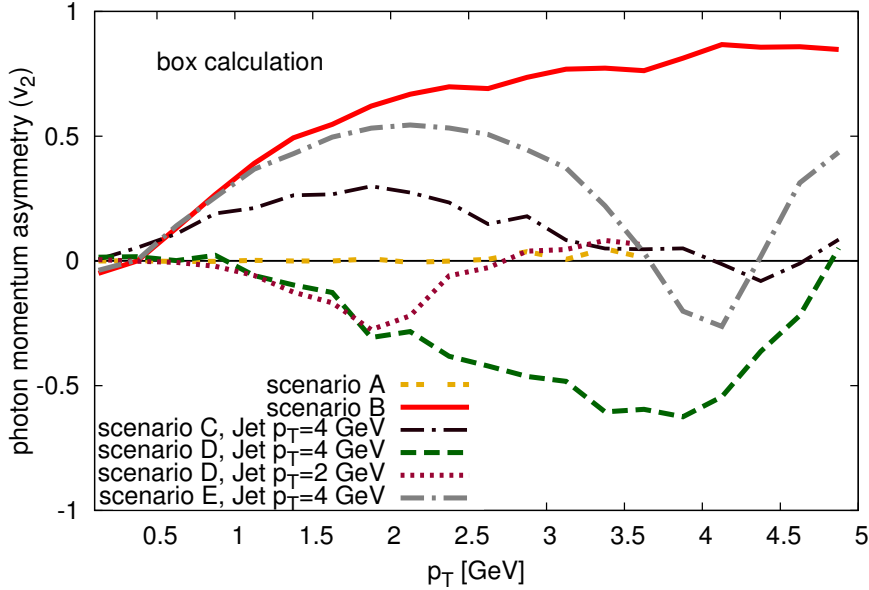


Figure 8.3.: Results for the qualitative understanding of elliptic flow of photons originating from flowing thermal background and non thermal "jet"-like partons for the 5 scenarios explained in Sec. 8.4.1. The thermal medium has a temperature of 0.4 GeV, and for simplicity photons originate from $2 \leftrightarrow 2$ processes only.

zero, hence the curve of scenario C drops at the jet energy. The flow at lower p_T stems from the background flow. In scenario D there is no background flow, and no positive v_2 contribution. The jets, initialized in the middle of the box, traverse it until whichever wall comes first until they are deleted. During their traveling path, they can hit a thermal particle and produce a (conversion) photon, with a momentum close to that of the parent jet. This is more likely to happen in the (long) y or z direction, than in x , as the box has a small L_x size. Most of the photons have larger p_y momenta than p_x , thus the v_2 becomes negative (see, e.g., Ref [302] for similar findings). We show this effect for two different jet p_T and, clearly, the minimal v_2 is reached at exactly the jet p_T . This effect can be termed the geometric leakage effect. Finally, the combined effect of thermal background flow and jet conversion photons is shown in scenario E: For low p_T there is substantial momentum anisotropy, whereas around the jet p_T the conversion effect dominates and pushes the v_2 into the negative region. This toy example shows what we can expect in a heavy-ion collision when both, jet particles and thermal flowing particles are present. The relative strengths of both effects have to be investigated in a full simulation.

8.5. Angular structure

To date, only insufficient knowledge exists about the correct angular emission pattern of photons. In the AMY formalism (explained in Sec. 6.3), the emission angle of radiated photons or gluons with respect to the momentum direction of the radiating parton is parametrically of order $\mathcal{O}(g)$. This is why it can be taken to be zero² (in the local rest frame of the background fluid cell in which the radiating parton is located). We however remind at this point, that in realistic scenarios, the coupling is large, $g \sim \mathcal{O}(g)$.

²This is done, for instance, in the microscopic event generator MARTINI [299].

The BAMPS framework (see Chap. 4) employing microscopic photon production by matrix elements is ideally suited to study the angular emission patterns, which are nontrivial due to the exact $2 \leftrightarrow 2$ and $2 \rightarrow 3$ matrix elements and their rich functional structure of the in- and outgoing momenta.

At this point we repeat, that the algorithm employing the matrix elements for photon production was constructed to generate the correct, total leading order rate (integrated over all angles) only in chemical and thermal equilibrium, and the angular structure of single emissions employing microscopic matrix elements may contain uncontrolled uncertainties.

In this section we look more closely to photons emitted from highly relativistic quarks scattering off the QGP background. This emission from “jet-like” particles is rather little understood and can give important contributions to experimentally measured direct photon spectra. To this end we point out when one can speak of jet-photon conversion, and look differentially in energy and angle how photon production behaves for quark and gluon induced photon radiation.

8.5.1. Jet photon conversion and angular structure with microscopic $2 \rightarrow 3$ matrix elements

To explicitly see how partons with fixed energy (called “jets” for higher energies) interact with thermal particles and create a photon, we carry out a simple box calculation, where quarks with fixed energy E_{quark} hit particles from a thermal bath ($N_f = 3$). All the following results are carried out in a *static* thermal QGP medium. A flowing medium would affect the results. In Fig. 8.4 we show the resulting photon spectra (N_γ =number of photons), normalized by the number of jets N_{jet} for a certain time t . Quark jets can interact via $2 \leftrightarrow 2$ (Compton scattering and quark-antiquark annihilation) and $2 \rightarrow 3$ processes (bremsstrahlung)

The specific mean free path, necessary for the bremsstrahlung processes (see Sec. 6.4) is set to the equilibrium value at unit fugacity, $R_q^{-1} = 21.4$ fm (processes 1) and $R_q^{-1} = 17.6$ fm (processes 2).

In the following we separate results for “only $2 \leftrightarrow 2$ ”, “only $2 \rightarrow 3$ ” and both processes. The shape of the spectrum depends on the ratio E_{quark}/T . In the top (bottom) panel of Fig. 8.4 we show results for $E_{\text{quark}}/T = 1$ ($E_{\text{quark}}/T = 10$). For higher jet energies (bottom panel), the total spectrum is dominated by the $2 \rightarrow 3$ processes at all energies, whereas at lower jet energies (top panel) $2 \leftrightarrow 3$ scattering dominates only below photon energies of 0.5 GeV, and above $2 \leftrightarrow 2$ and $2 \rightarrow 3$ contribute about equally. We make the following observations.

- Quark jets, interacting only in $2 \leftrightarrow 2$ processes, have a peak at the jet energy E_{quark} (barely visible in the bottom panel of Fig. 8.4).
- Quark jets, interacting only in $2 \rightarrow 3$ processes, show a peak at low photon energies, irrespective of the quark energy. Only the strength of the peak grows with the quark energy.
- The full spectrum ($2 \leftrightarrow 2 + 2 \rightarrow 3$) shows always a peak at low energies.

In Fig. 8.5 we show the angular spectrum of emitted photons with respect to the incident quark, again for two different ratios $E_{\text{quark}}/T = 1$ (top panel) and $E_{\text{quark}}/T = 10$ (bottom panel), normalized to the total rate R_γ . Clearly, at quark energies comparable to the background medium temperature, the total photon emission is almost isotropic; at least one cannot speak of a clear favorite direction. This is true individually for binary and

radiative photon production. At quark energies larger than the typical thermal energy of the background partons (bottom panel), there is a clear collinear peak, photons are emitted closely to the quark, for binary and radiative scattering. The $2 \leftrightarrow 2$ contribution shows a even more collinear shape, but the bremsstrahlung contribution is much more important, thus the total rate has a similar shape as the bremsstrahlung spectrum. To further disentangle the kinematics, we show in Fig. 8.6 more differentially how the angular distribution looks like for different photon energies. For low quark energies (top panel) all energy-bins have a similar angular distribution. For high quark energies (bottom panel) one observes that the large photon energies are more collinear than the low photon energies, which can have all angles and show only a small forward enhancement (low angles).

For a gluon jet, the only possible process is Compton scattering. In Fig. 8.7 we show the photon spectra by energetic gluons and quarks ($E_{\text{jet}} = T$ and $E_{\text{jet}} = 10T$), normalized as before. At low energy, $E_{\text{jet}} = T$, quark and gluon jets do not generate much different photon spectra. The comparison of the two radiative processes shows the strong low energy enhancement of the AMY kernel emission compared to the inelastic matrix element. At these low energies, one cannot speak of jet-photon conversion any more, as the “jet” particles have thermal energies. At high energies, $E_{\text{jet}} = 10T$, it can be seen, that for photon emission from gluons the photon spectrum is weakly peaked at values $E \sim \mathcal{O}(T)$ due to the present channel (Compton scattering). It is apparent that for gluons we cannot speak of jet-photon conversion. A quark jet interacting by only binary scattering exhibits a strong peak in the photon spectrum at the quark energy, which is a jet-photon conversion. The radiative emission patterns however have a broader energy distribution.

8.5.2. Phenomenological consequences

Having determined the kinematics of the single photon emission mechanisms, it remains to see how they behave in dynamical heavy-ion collisions. It became clear, that energetic quark jets are probable to almost collinearly translate to photons. Here, the higher the energy of the produced photon, the more collinear it will be to the originating quark. Gluon jets do not show this translation, photons (by the Compton mechanism) have a broad angular distribution.

The application of the AMY collision kernel guarantees much softer photons than the matrix element method, or binary scattering. We will see that this will show up in larger low- p_T spectra in heavy-ion collisions.

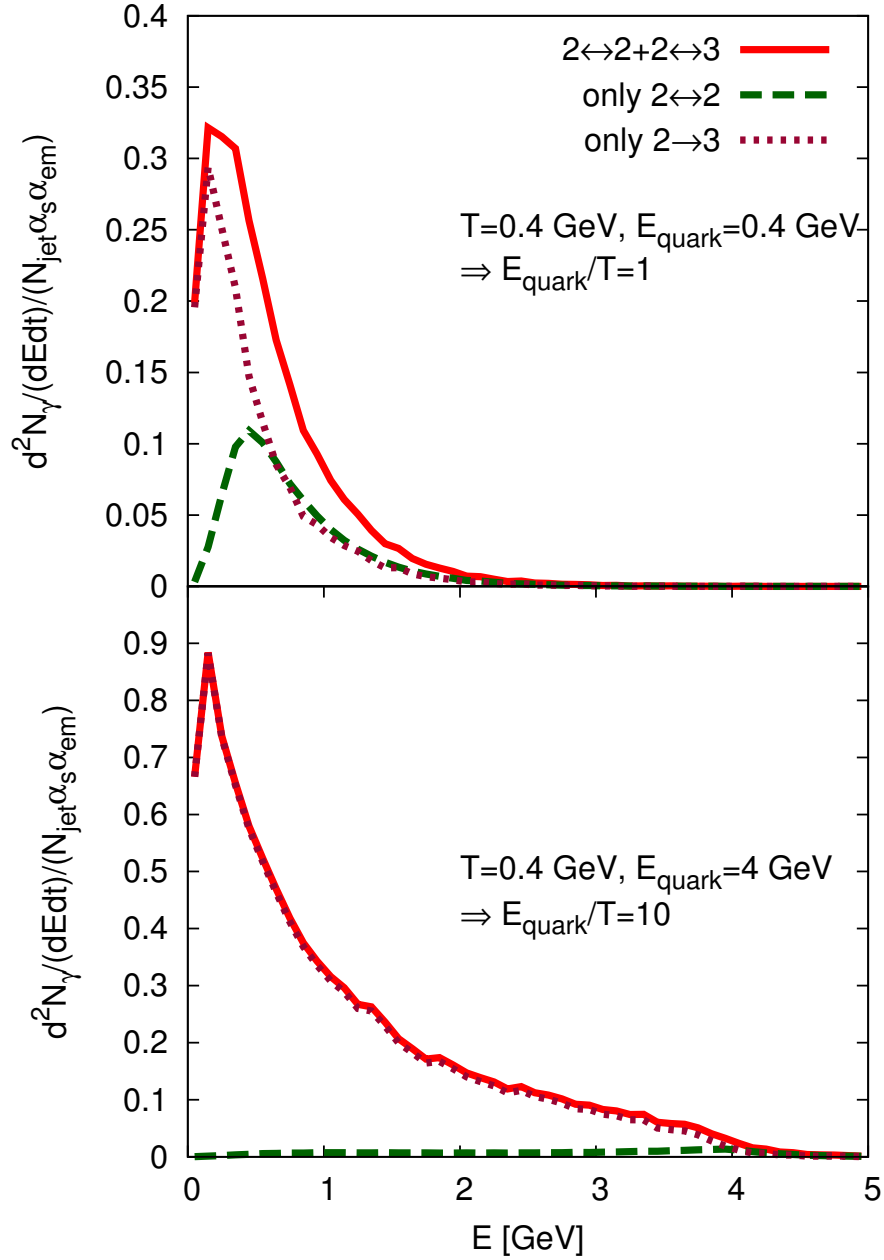


Figure 8.4.: Spectra of photons which are produced by an incident up-quark with fixed energy $E_{\text{quark}} = 0.4$ GeV (top panel) and $E_{\text{quark}} = 4$ GeV (bottom panel) hitting a thermal bath of temperature $T = 0.4$ GeV. We separate the $2 \leftrightarrow 2$ and $2 \rightarrow 3$ contributions and show the full result.

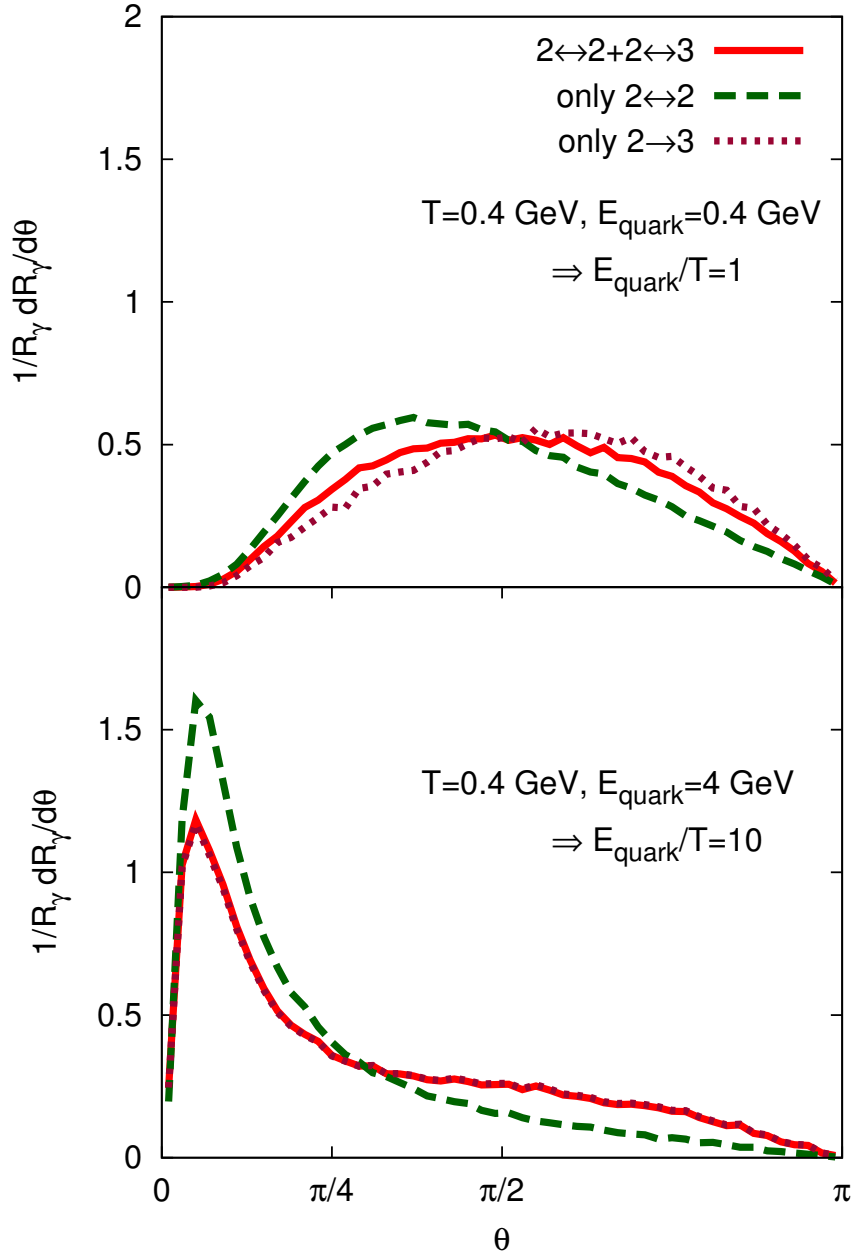


Figure 8.5.: Differential rate in scattering angle of photons which are produced by an incident particle with fixed energy $E_{\text{quark}} = 0.4 \text{ GeV}$ (top panel) and $E_{\text{quark}} = 4 \text{ GeV}$ (bottom panel) hitting a thermal bath of temperature $T = 0.4 \text{ GeV}$. For $2 \rightarrow 3$ scattering, $\lambda_{\text{mfp}} = 0.5 \text{ GeV}$. We show the results for only $2 \leftrightarrow 2$, only $2 \rightarrow 3$ scattering and both allowed processes. For each curve, the differential rate is individually normalized to the corresponding total rate R_γ .

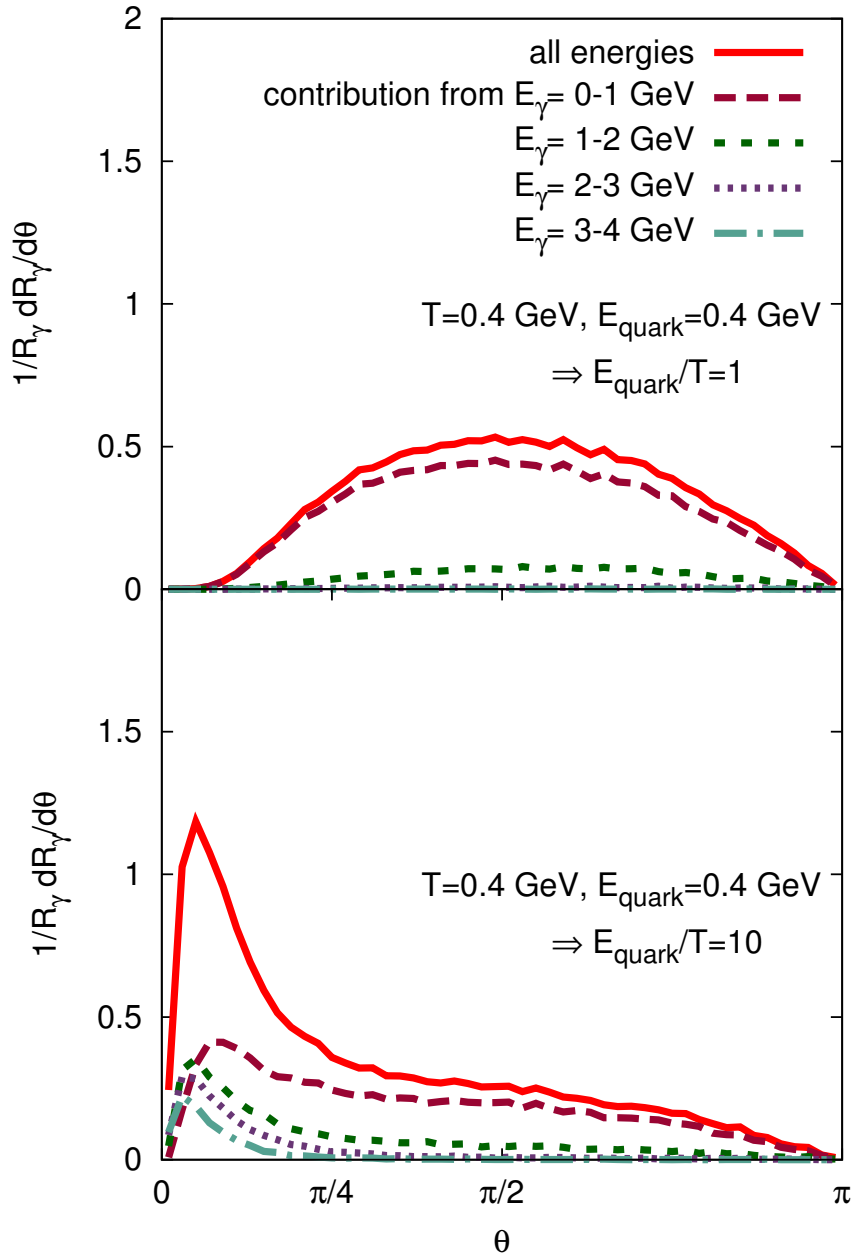


Figure 8.6.: Differential rate in scattering angle of photons which are produced by an incident particle with fixed energy $E_{\text{quark}} = 0.4$ GeV (top panel) and $E_{\text{quark}} = 4$ GeV (bottom panel) hitting a thermal bath of temperature $T = 0.4$ GeV. We use the full $2 \leftrightarrow 2 + 2 \rightarrow 3$ photon production. The differential rate is normalized to the total rate R_γ . Here we show the contributions of different energies.

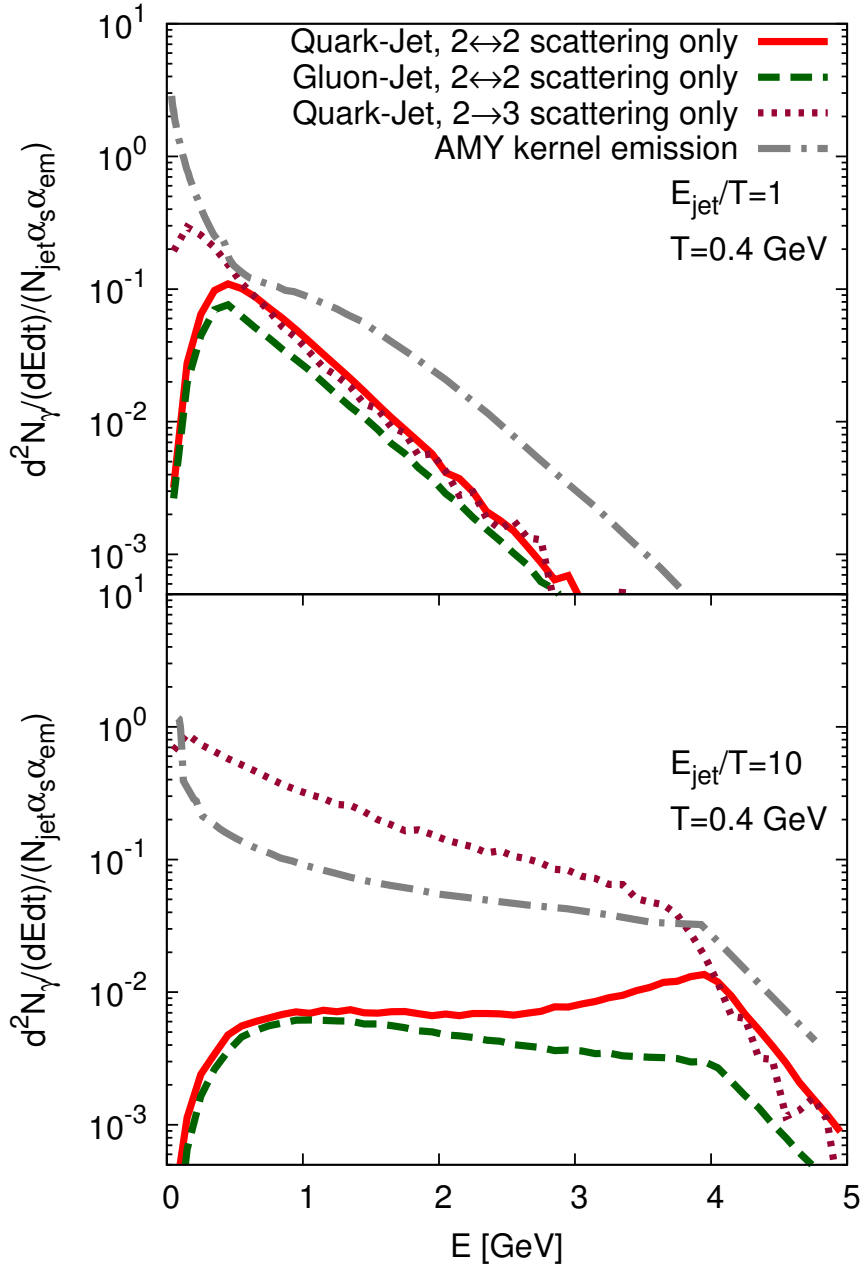


Figure 8.7.: Spectra of photons which are produced by an incident quark or gluon jet particle with $E_{\text{jet}} = T$ (top panel) and $E_{\text{jet}} = 10T$ (bottom panel) hitting a thermal bath of temperature $T = 0.4$ GeV. We show $2 \leftrightarrow 2$ and $2 \rightarrow 3$ contributions separately, and also the result of the microscopic AMY kernel emission.

9. Photons from heavy-ion collisions

In the following we show results from realistic simulations of heavy-ion collisions by using the photon production methods explained in Chap. 6 and Chap. 7 within the framework of BAMPS. To date, experimental data is rather limited, thus we must often compare to preliminary or very uncertain data.

The model BAMPS currently simulates only the QGP phase, beginning with formed partons. For the initial parton distribution we use PYTHIA 6.4 [303], a $p+p$ event generator. We compute the number of binary nucleon collisions N_{coll} depending on the centrality, and run N_{coll} individual $p+p$ events from PYTHIA to generate momenta of quarks and gluons (details about the implementation can be found in Ref. [237]).

The transverse positions are computed by a Glauber-type initial condition [40, 237]. Each particle obtains a formation time $\tau_f = p_T^{-1} \cosh(y)$. Before this formation time, it is not allowed to interact, but merely travels on a straight line while it is being formed. Further details concerning the BAMPS setup for heavy-ion collisions, as well as numerous previous studies can be found in [40, 218, 248, 249].

At RHIC, the PHENIX collaboration, working with $\sqrt{s_{NN}} = 0.2$ TeV Au+Au collisions, published midrapidity ($|y| < 0.35$) photon spectra at 0% – 20%, 20% – 40%, 40% – 60% and 60% – 92% most central events [80].

A centrality selection of an event ensemble as done in experiment would require a fluctuating impact parameter, but since we use individual $p+p$ collisions, we must estimate an average impact parameter b for which the theoretical N_{coll} coincides rather precise with the experimental average within a centrality class, $\langle N_{\text{coll}} \rangle$. The calculated number of participating nucleons N_{part} should also match the values quoted by experiment. We estimate N_{coll} from a standard Glauber model tuned by a factor of 80% due to shadowing effects. We so obtain the effective impact parameter $b = 4.4$ fm for 0% – 20% central collisions, $b = 7.9$ fm for 20% – 40% most central collisions, $b = 10.3$ fm for 40% – 60% most central collisions, and $b = 12.7$ fm for 60% – 92% most central collisions.

The ALICE collaboration, working at $\sqrt{s_{NN}} = 2.76$ TeV, uses 3 centrality classes of Pb+Pb collisions (0% – 20%, 20% – 40%, 40% – 80%) for spectra [76] as well as 0% – 40% in a first study [304] on v_2 . Recently, the ALICE collaboration published more precise data for the elliptic flow, using the 0% – 20% and 20% – 40% centrality class within 0.8 units of rapidity. In order to allocate an impact parameter b to those centralities we use the values from the ALICE collaboration [76, 305] for N_{part} and N_{coll} , and compare to the Glauber results, obtaining $b = 5$ fm for 0% – 20% most central collisions, $b = 8.4$ fm for 20% – 40% most central collisions and $b = 11.6$ fm for 40% – 80% most central collisions.

Because photons are very rare probes, they do not alter the collision dynamics. For this reason we use recorded BAMPS events, and sample photons by collisions among the recorded particles. This method allows us to reduce numerical noise by enhancing the photon cross section by a nearly arbitrary factor and scale the resulting spectra down by this factor. We have checked that all our results are independent of these factors. The background collision includes the latest improvements from BAMPS, such as the improved Gunion-Bertsch matrix elements for gluon radiation and a pQCD running coupling¹ [217,

¹Note that photon production is numerically separated from the background events, and we chose the coupling of the photon production processes to be fixed, see also Fig. 9.14.

218, 220]. The evolution of BAMPS runs until the energy density drops locally below $\epsilon_c = 0.6 \text{ GeV}/\text{fm}^3$. We have checked that the photon spectra are insensitive to this choice, because the rather cool medium in the later stages no longer produces many photons.

In this chapter we first take a closer look to effective thermodynamic properties of the medium in order to characterize the background medium, which radiates thermal photons. This means, we investigate temperature, collective velocity, energy and particle density and fugacity at different positions within the fireball. Subsequently, we compare available prompt photon spectra from literature, since they are essential for comparisons to experiment. We then present photon spectra and elliptic flow from BAMPS for RHIC and LHC, and compare, where possible to the experiments. Next, we compute photon spectra using different running coupling prescriptions. Since chemical equilibration plays a major role, we study the sensitivity of the photonic observables to the quark and gluon fugacities. Finally we show a global comparison to other models computing direct photons.

9.1. Background chemistry in BAMPS

BAMPS was built as a genuine tool for studying the non-equilibrium evolution of the quark-gluon plasma. As such, it is not unambiguous to characterize its properties with macroscopic quantities like temperature or chemical potential, which require an underlying equilibrium distribution function. It is however possible, and instructive, to do so approximately. In the case of temperature, one has in principle infinite possibilities of using different moments of the non-equilibrium distribution function, or combinations thereof, to obtain an effective temperature. In equilibrium, the energy density for massless particles is $\epsilon = 3nT$, and energy and particle density n are given by moments of the distribution function $f(p)$,

$$\epsilon = \int \frac{d^3\vec{p}}{(2\pi)^3 E_p} E_p^2 f(p) \quad (9.1)$$

$$n = \int \frac{d^3\vec{p}}{(2\pi)^3 E_p} E_p f(p) \quad (9.2)$$

which are in this form not Lorentz invariant. A boost of the momenta yields the respective local rest frame quantities ϵ_{LRF} and n_{LRF} , such that we can define an effective temperature by the second over the first moment, $T_\star^{2\text{nd}} = \epsilon_{\text{LRF}}/(3n_{\text{LRF}})$. Alternatively we can use the first moment over the zero'th moment, defined by Ref. [278],

$$\begin{aligned} \mathcal{J} &= \int \frac{d^3\vec{p}}{(2\pi)^3 E_p} f \\ \mathcal{I} &= \frac{1}{2} \int \frac{d^3\vec{p}}{(2\pi)^3 E_p} E_p f \\ T_\star^{1\text{st}} &= \sum_{\text{species } i} \nu_i \frac{g^2 C_i}{d_A} \mathcal{I}_i \bigg/ \sum_{\text{species } i} \nu_i \frac{g^2 C_i}{d_A} \mathcal{J}_i, \end{aligned} \quad (9.3)$$

where the dimension of the adjoint representation of SU(3) is $d_A = 8$, the degeneracy for gluons is $\nu_g = 16$, and for every quark and antiquark species $\nu_u = 6, \nu_{\bar{u}} = 6, \nu_d = 6, \nu_{\bar{d}} = 6, \dots$. The quadratic Casimir C_i for quarks in the fundamental representation is $C_F = 4/3$ and for gluons in the adjoint representation $C_A = 3$. Here we note, that \mathcal{J} is Lorentz invariant (proportional to the Debye mass), and can easily be evaluated in the lab frame, however, \mathcal{I} (proportional to the density) is not Lorentz invariant. In order to obtain the temperature (defined in the LRF) $T_\star^{1\text{st}}$, it is necessary to evaluate \mathcal{I} in the LRF, which

requires merely a factor of γ . Explicitly, within BAMPS, we sum up lab momenta of the particles within a cell of volume V , where the testparticle number is N_{test} , the number of gluons N_g , the number of quarks+antiquarks N_q and the boostfactor of the cell γ ,

$$\begin{aligned}\mathcal{I}_g &= \frac{1}{2} \frac{N_g}{\nu_g N_{\text{test}} V \gamma}, \\ \mathcal{I}_q &= \frac{1}{2} \frac{N_q}{12 N_f N_{\text{test}} V \gamma}, \\ \mathcal{J}_i &= \frac{1}{d_i} \frac{1}{V N_{\text{test}}} \sum_{\text{particles } j} \frac{1}{p_j}.\end{aligned}\quad (9.4)$$

The boost velocity $\vec{\beta}$ is cellwise computed by

$$\vec{\beta} = \frac{\sum \vec{p}}{\sum E}.\quad (9.5)$$

The boostfactor $\gamma = (1 - \beta^2)^{-1/2}$ is quite sensitive to the number of testparticles used for the average, since $\langle (1 - \beta^2)^{-1/2} \rangle \neq (1 - \langle \beta^2 \rangle)^{-1/2}$. Numerical studies showed, that at rest, at least 30 particles are necessary to obtain $\gamma \approx 1$ with good accuracy. To this end, we cluster all nine grid cells around each respective cell at the same space-time rapidity for the calculation of $\gamma, \mathcal{I}_q, \mathcal{I}_g, \mathcal{J}_i, \epsilon_{\text{LRF}}, n_{\text{LRF}}$, and also the Debye masses. Another temperature definition uses only the zero'th moment \mathcal{J} , by inversion of Eq. (6.14),

$$T_{\star}^{\text{0th}} = \sqrt{\frac{\pi}{8(N_c + N_f)\alpha_s}} m_{D,g}^2.\quad (9.6)$$

We use this form only for the evaluation of the running coupling, due to numerical reasons². Towards equilibrium, all temperature definitions coincide more and more closely. The energy density in the rest frame of the cell is only needed for the freeze-out criterion $\epsilon_{\text{LRF}} < \epsilon_c \equiv 0.6$ GeV/fm. The energy momentum tensor in the lab frame $T^{\mu\nu}$ is transformed to that in the rest frame of the cell \hat{T} ,

$$\hat{T}^{\mu\nu} = \Lambda_{\mu'}^{\mu} \Lambda_{\nu'}^{\nu} T^{\mu'\nu'},\quad (9.7)$$

The energy density is defined as the 00-component in the rest frame, $\epsilon_{\text{LRF}} = \hat{T}^{00}$. Thus we have

$$\begin{aligned}\epsilon_{\text{LRF}} &= (\Lambda_0^0)^2 T^{00} + (\Lambda_1^0)^2 T^{11} + (\Lambda_2^0)^2 T^{22} + (\Lambda_3^0)^2 T^{33} \\ &\quad + 2\Lambda_1^0 \Lambda_0^0 T^{10} + 2\Lambda_2^0 \Lambda_0^0 T^{20} + 2\Lambda_3^0 \Lambda_1^0 T^{30} + 2\Lambda_2^0 \Lambda_1^0 T^{21} \\ &\quad + 2\Lambda_3^0 \Lambda_1^0 T^{31} + 2\Lambda_3^0 \Lambda_2^0 T^{32} \\ &= \gamma^2 T^{00} + \gamma^2 v_x^2 T^{11} + \gamma^2 v_y^2 T^{22} + \gamma^2 v_z^2 T^{33} \\ &\quad - 2\gamma^2 v_x T^{10} - 2\gamma^2 v_y T^{20} - 2\gamma^2 v_z T^{30} \\ &\quad + 2\gamma^2 v_x v_y T^{21} + 2\gamma^2 v_x v_z T^{31} + 2\gamma^2 v_y v_z T^{32}\end{aligned}\quad (9.8)$$

which we calculate using all particles in each 3x3 cell cluster, corresponding to 0.9 fm \times 0.9 fm.

9.1.1. Temperature

The (effective) temperature within the fireball is strongly dependent on the transverse position as well as the time in the evolution. Generally, for times earlier than $t \sim 1$ fm/c

²It is unfeasible to tabulate cross sections differential in temperature and Debye mass.

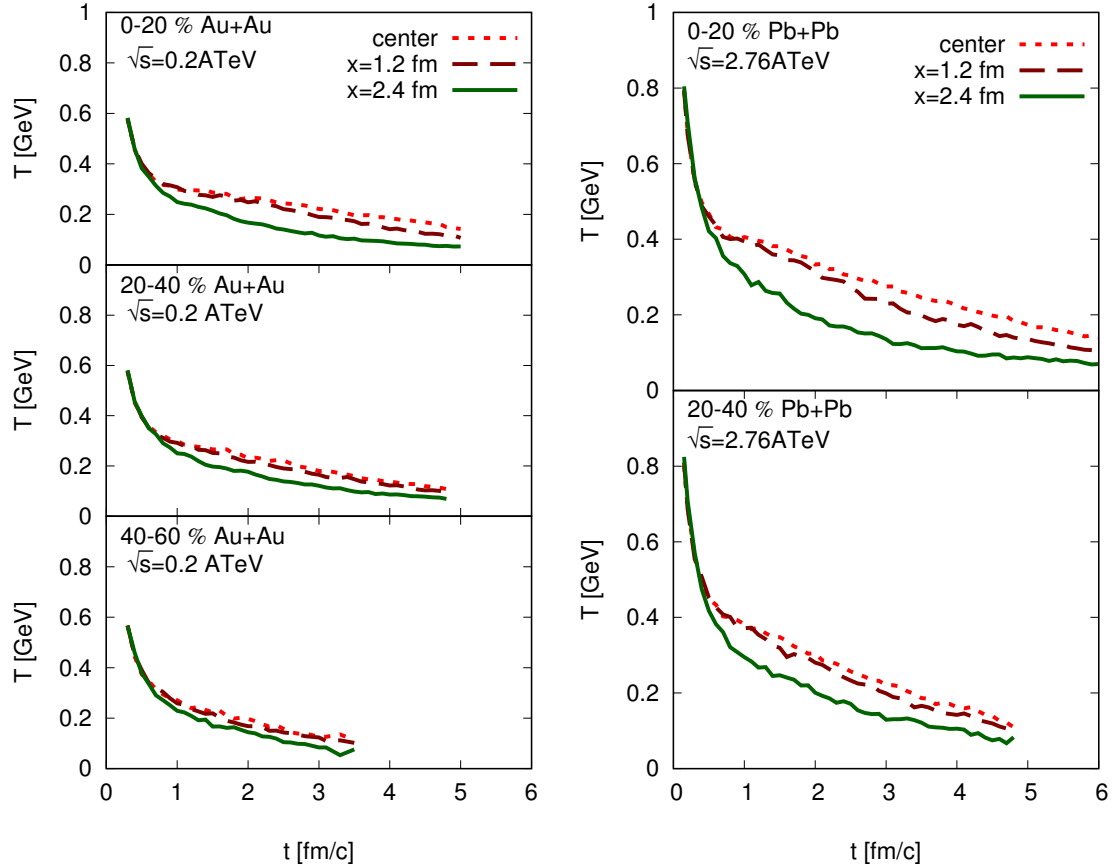


Figure 9.1.: The time evolution at midrapidity of the effective temperature $T \equiv T_{\star}^{1\text{st}}$ (calculated using Eq. 9.3) for RHIC (left) and LHC (right) at three different positions along the short axis (x -axis) in peripheral heavy-ion collisions.

the notion of temperature is questionable as the medium is not equilibrated. In this preequilibrium phase, using the above mentioned $T_{\star}^{1\text{st}/2\text{nd}}$ results in effective temperatures of around 600 – 800 MeV at the LHC and 400 – 600 MeV at RHIC. In Fig. 9.1 we show the time evolution of the effective temperature $T_{\star}^{1\text{st}}$ at three different locations across the almond-shaped fireball ($x = 0, 1.2, 2.4$ fm). Clearly, the medium is cooler in the outer region, but the difference in temperature between the center at the edge of the fireball is largest at around $t = 2$ fm/c for both RHIC and LHC.

In Fig. 9.2 we compare the temperature evolution of BAMPS (as an example for central RHIC collisions) with a simple Bjorken solution of hydrodynamic equations, Eq. (4.15), using as parameters $T_0 = 0.4$ GeV, $\tau_0 = 0.6$ fm. Clearly, the temperature falls of much steeper in BAMPS, but the lat-time behavior, due to the local equilibration, behaves comparable to Bjorken hydrodynamics. We also compare to the result of viscous hydrodynamics from Ref. [306] and a much simpler fireball model from Ref. [85]. Both are comparable, but start with different initial temperatures. BAMPS exhibits initially much higher temperatures than all other approaches. Since photon spectra are sensitive to the temperature profile (spacetime integrated) we can expect harder photon spectra from BAMPS than, e.g., hydrodynamics, assuming comparable flow velocities (collective flow can red or blueshift spectra).

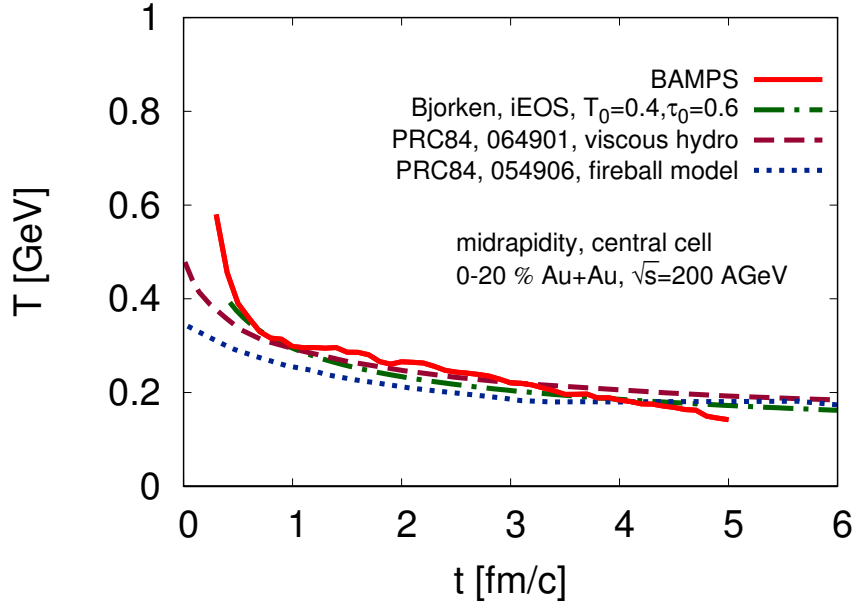


Figure 9.2.: Temperature profile from BAMPS for 0% – 20% most central collisions at RHIC compared to a simple Bjorken solution with $T_0 = 0.4$ GeV initial temperature, and two results from literature.

9.1.2. Velocity

In Fig. 9.3 we show the time evolution of the local boostfactor γ at the same positions as before for the temperature in Fig. 9.1. The boostfactor γ characterizes the collective flow of the cell, and it is quite interesting to observe, that the flow increases dramatically as one moves outwards from the center. At position $x = 2.4$ fm from the center of the fireball the boost is highly relativistic, up to $\gamma = 3$ at the LHC and $\gamma = 2.5$ at RHIC. The flowing medium produces photons; the relativistic translation of flow from the medium to photons is discussed in detail in Chap. 8, Sec. 8.2.

Elliptic flow of photons is a convolution of the rate (being proportional to the temperature squared $kdR^\gamma/d^3k \sim T^2$) with the flow velocity. The combination of large temperatures only at early times, where flow is still small, disfavors large final elliptic flow. The distribution in space shows the same pattern, in the peripheral areas, where the flow velocity is large, the temperature is lowest, whereas in the hot center the flow is zero. Many photons are thus emitted isotropically from the center, reducing the final elliptic flow.

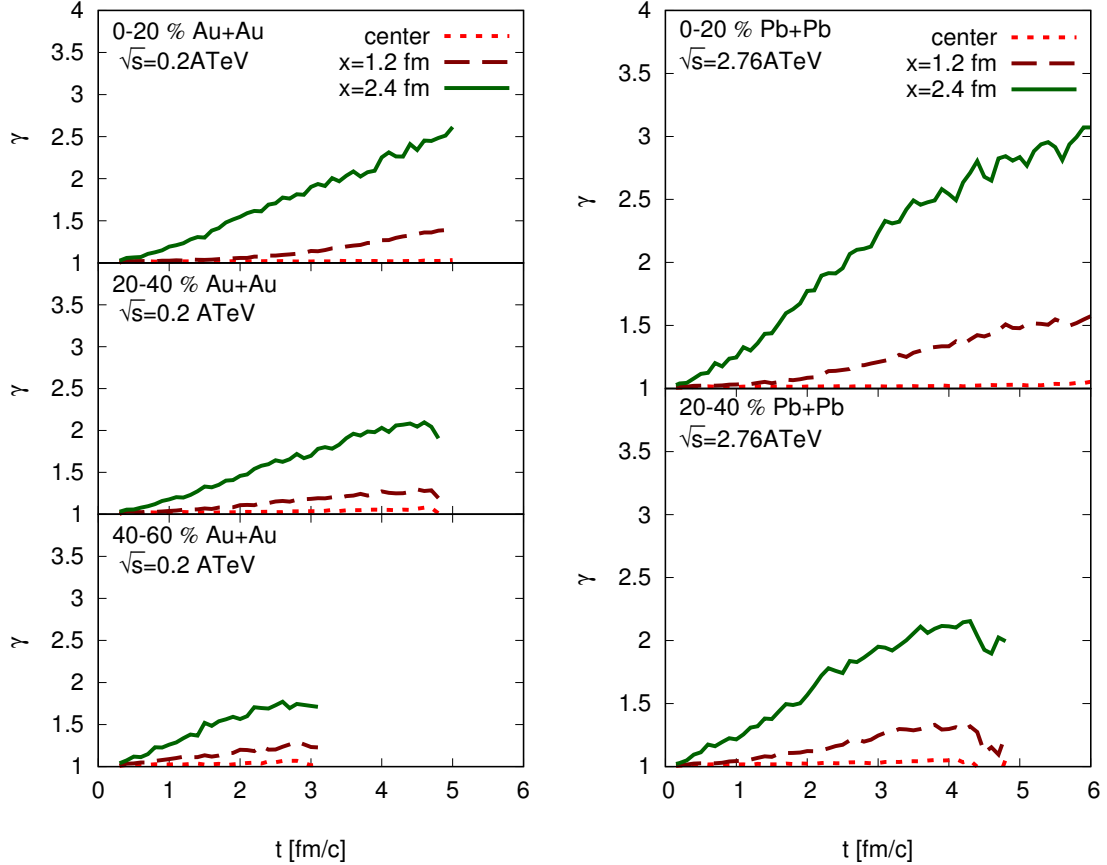


Figure 9.3.: The time evolution at midrapidity of the collective boostfactor for RHIC (left) and LHC (right) at three different positions along the short axis (x -axis) in peripheral heavy-ion collisions.

9.1.3. Energy density

The energy density of the medium ϵ , calculated from Eq. (9.8), is shown in Fig. 9.4 again averaged over squares of 0.81 fm^2 in the center, and 1.2 fm and 2.4 fm away on the short axis of the almond-shaped fireball. Here we observe, that the functional form of ϵ in the center is very different to the one at the edge, which falls off much steeper initially and levels off in a more shallow way at late times. This feature is seen in all five collision systems. Generally, the initial energy density decreases from the center to the edge, especially at early times. Since we keep the outer observation point at $x = 2.4 \text{ fm}$ fix, the flow of the medium increases the energy density at this point with respect to the center. Due to this radial flow, and also the slow equilibration, the functional form is different to the Bjorken assumption, Eq. (4.15).

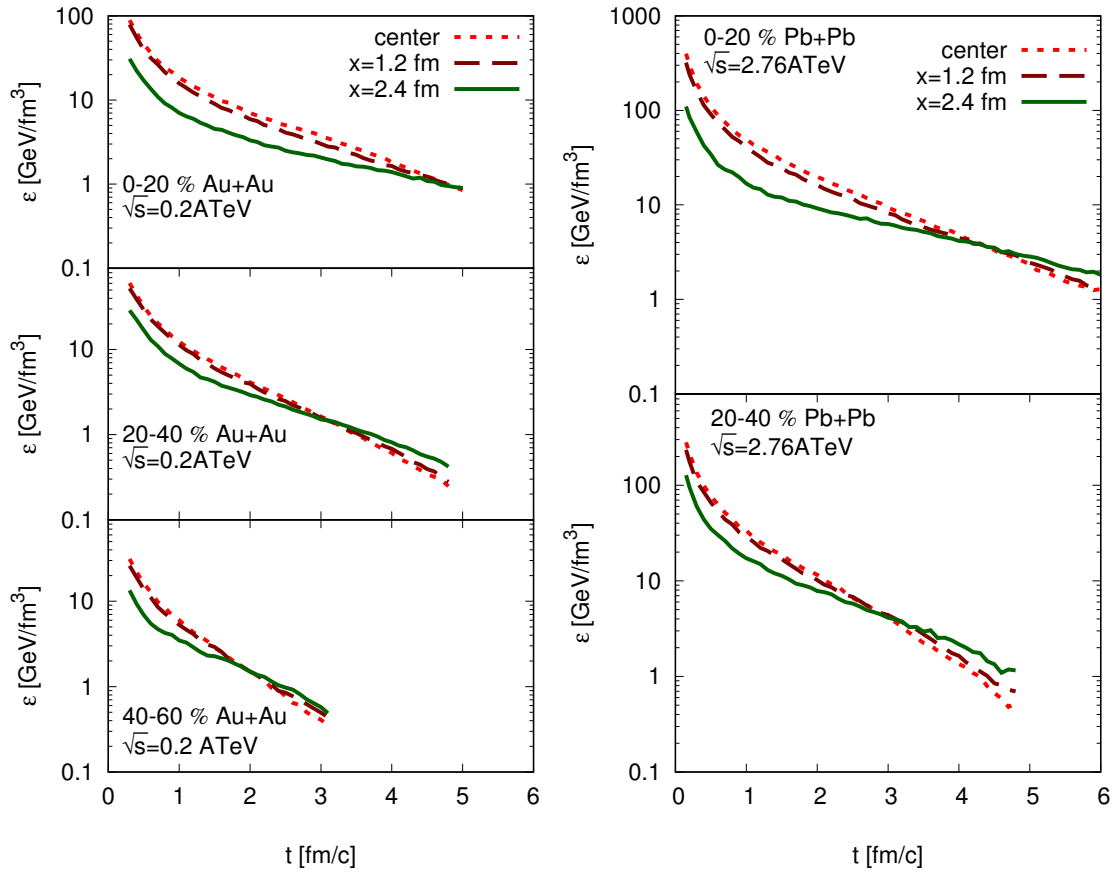


Figure 9.4.: The time evolution at midrapidity of the local rest frame energy density $\epsilon \equiv \epsilon_{\text{LRF}}$ for RHIC (left) and LHC (right) at three different positions along the short axis (x -axis) in peripheral heavy-ion collisions.

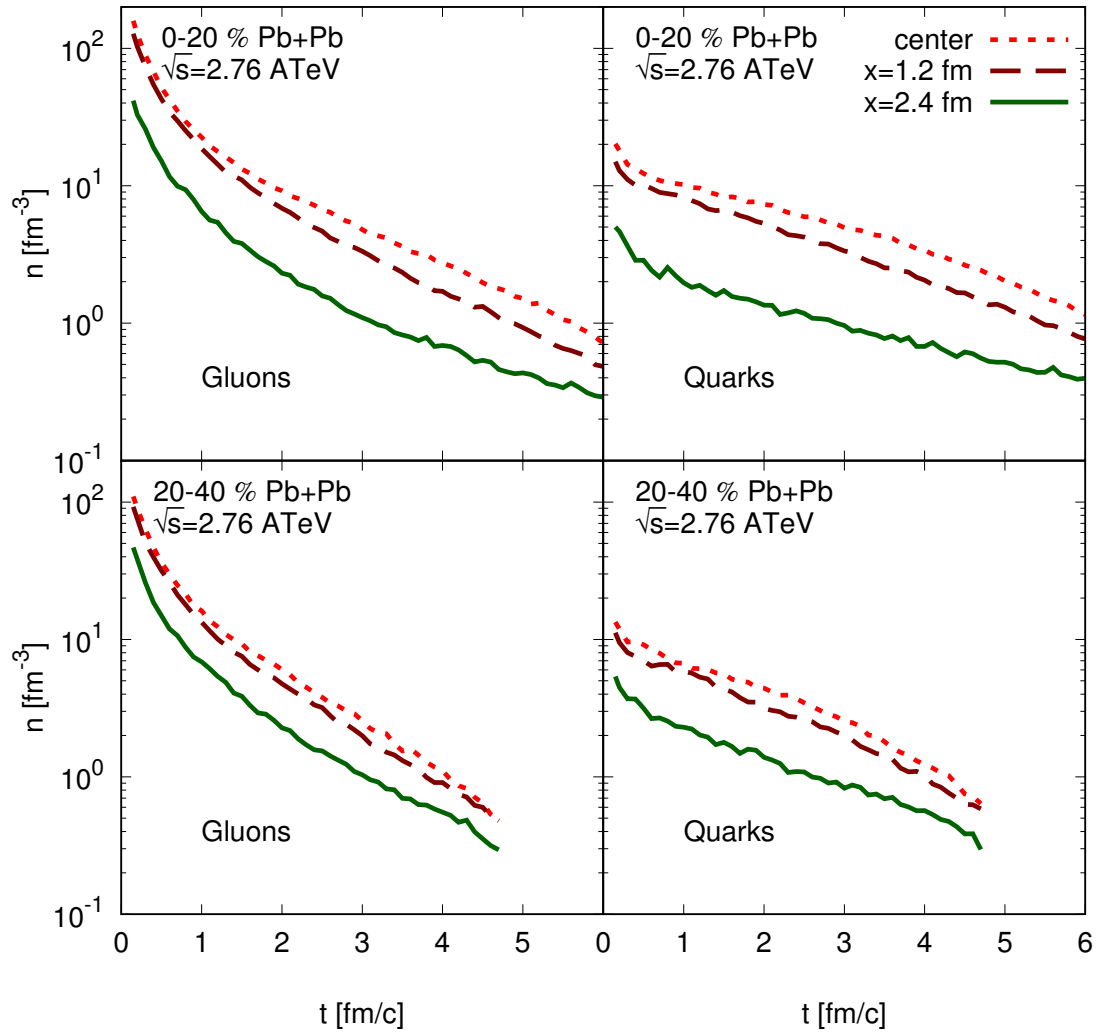


Figure 9.5.: The time evolution at midrapidity of the local rest frame quark and gluon densities $n \equiv n_{\text{LRF}}$ for the LHC at three different positions along the short axis (x -axis) in peripheral heavy-ion collisions.

9.1.4. Particle density and fugacity

The chemical composition of the background medium is seen in Fig. 9.5 for LHC and Fig. 9.6 for RHIC in terms of local rest frame density evolutions at $x = 0, 1.2, 2.4$ fm from the center. In absolute numbers, the quark densities begin about an order of magnitude lower than the gluon densities, but due to $gg \rightarrow q\bar{q}$ quark production processes, the densities become comparable or even larger at late times. Similar to the energy density, the particle densities fall off at the edges about a factor of 2 – 5, compared to the center.

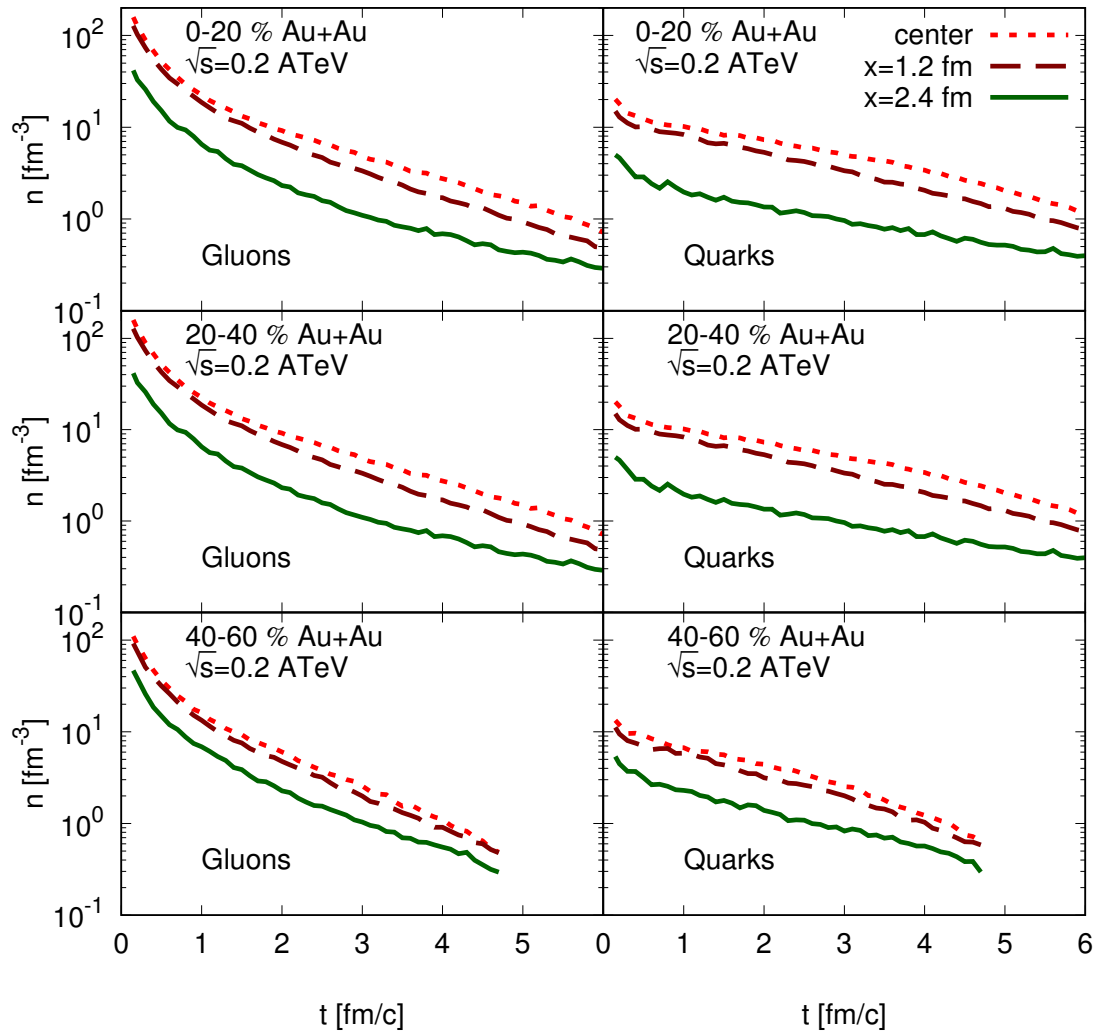


Figure 9.6.: The time evolution at midrapidity of the local rest frame quark and gluon densities $n \equiv n_{\text{LRF}}$ for the RHIC at three different positions along the short axis (x -axis) in peripheral heavy-ion collisions.

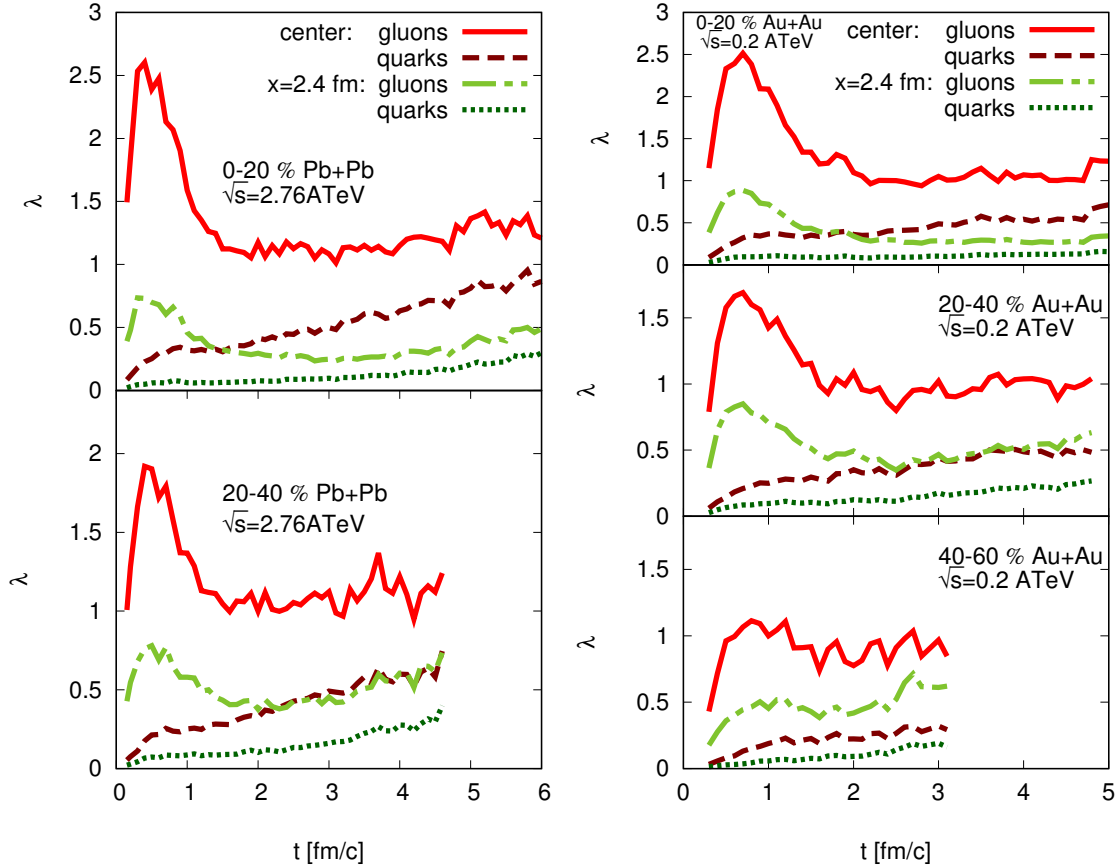


Figure 9.7.: Quark and gluon fugacity λ at midrapidity for LHC (left) and RHIC (right) computed in the center and a peripheral cell 2.4 fm from the center. For these fugacities the temperature prescription from Fig. 9.1 was used.

In order to characterize the parton composition of the medium even further, the fugacity, $\lambda = n/n_{eq}$ is the relevant quantity. In Fig. 9.7 we show the midrapidity fugacities for RHIC and LHC, corresponding to the densities and temperatures from Figs. 9.5, 9.6 and 9.1. We show the fugacity averaged in the center of the fireball and $x = 2.4$ fm away from the center. The gluon fugacity starts at a much higher value than the quark fugacity. Its prominent peak at early times should not be taken too serious, as the medium is not yet equilibrated and the concept of temperature still doubtful. The density is however large, and the formation of a Bose-Einstein condensate might be possible [236]. In all cases, the gluons saturate to around unity, whereas quarks only in the center of most central LHC collisions reach unity at late times. We see in addition, that the difference of chemical equilibration for quarks and gluons in the center and at the edge of the fireball is quite strong. The quark fugacities in the central cell are about double as large as at the edge. This difference decreases slightly for peripheral collisions. The gluon fugacities show the same tendency, albeit with very different shape, and gluons are strongly under saturated away from the center.

9.2. Photon yield from heavy-ion collisions

At present, BAMPS simulates only the QGP phase of heavy-ion collisions. This complicates studies and comparisons with direct photon data from experiment as for other observables (such as, e.g., heavy quarks, jets, or bulk medium elliptic flow). We however at this stage compare to data whenever possible and use additional contributions of prompt and hadronic photons when available.

Photons from $2 \leftrightarrow 2$ collisions are produced along the method described in Chap. 6. In the previous chapters we presented two alternative methods for radiative photon production: in Chap. 6 we described the use of microscopic $2 \rightarrow 3$ matrix elements. In equilibrium, and at unit quark and gluon fugacities, the $2 \rightarrow 3$ matrix elements were tuned to obtain spectra which are similar in shape and magnitude to the (parametrized) AMY resummed pQCD photon spectra. This method, added to photons from $2 \leftrightarrow 2$ collisions, is henceforth labeled as “22+23”.

The second method is described in Chap. 7, using radiation from individual quarks (numerically $1 \rightarrow 2$ processes), added to photons from $2 \leftrightarrow 2$ collisions, is henceforth labeled as “22+AMY”. It uses the emission kernel directly, and, in thermal and chemical equilibrium reproduces even more precise the analytic AMY rates. The fugacity dependence of photon radiation with this method is precisely $\sim \lambda_q$. The kernel utilizes the effective temperature T_\star^{1st} , defined in Eq. (9.3), which is, in practice, averaged within the computational cell (or including neighboring cells) in the transverse plane of the collision. This averaging geometry is also used to obtain the effective Debye masses which are used by the $2 \leftrightarrow 2$ and $2 \leftrightarrow 3$ matrix elements for the background as well as the photon production processes.

When looking at photon production within the BAMPS framework, one should bear in mind the following subtleties concerning the background evolution of the model.

- Within the BAMPS scheme, using N_{coll} -scaled $p + p$ collisions as initial state, the parton multiplicity is no free parameter. As a cross-check, the transverse energy distribution has been checked to be in the experimental ballpark. However, due to the unsolved hadronization problem of parton cascades such as BAMPS, a careful comparison of hadron multiplicities remains for the future.
- The initial state from BAMPS is harder than, e.g., in hydrodynamic simulations, as we concluded from Fig. 9.2.
- Since there are no physical fluctuations in the initial state, we do not perform an event-by-event analysis. A fluctuating initial state, which has a broad eccentricity distribution, analyzed event-by-event, will typically result in larger values for observables sensitive to momentum asymmetry, such as two particle correlation elliptic flow of partons, hence also for photons.

This being said, we emphasize the caveats within the BAMPS framework concerning the three production mechanisms for photons

- The radiative matrix elements for photons (“ $2 \rightarrow 3$ ”) suffer from the simplified LPM suppression, and simple Debye screened propagators, see Sec. 6.4. The corresponding rate in equilibrium was investigated in detail in Sec. 6.4, however, the extrapolation to the non-equilibrium situation in heavy-ion collision simulations in BAMPS might contain uncontrolled systematic uncertainties.
- The $2 \leftrightarrow 2$ matrix elements for photon production, screened by Debye masses, are under control in the equilibrium situation, see Sec. 6.2. In a non-equilibrium medium however, the screening algorithm is an assumption.

- The microscopic “AMY” formalism used within BAMPS is based on the full equilibrium calculation³ in Ref. [272,273]. We therefore assume thermal equilibrium, using an effective temperature, see Sec. 9.1.1. This might lead to uncertain radiative photon production rates, e.g., the effective temperatures appear generally quite large at early times. The overall fugacity dependence $\sim \lambda_q$ is maintained.
- The microscopic “AMY” formalism used within BAMPS assumes chemical equilibrium, thus the fugacities from BAMPS are ignored. This is in line with hydrodynamic calculations, but not in strict consistency with BAMPS. See also Sec. 9.3.
- The microscopic “AMY” formalism used within BAMPS assumes collinear emission. This is consistent with the analytic derivation, where the angle is order g , however, in realistic scenarios, where $\alpha_s \sim 0.3$, one would expect a broader distribution in the emission angle with respect to the emitting quark. The “22+23” method does not assume collinear emission, see also Sec. 8.5.1.

Furthermore, when comparing photon spectra in realistic scenarios of heavy-ion collisions, in general, one is sensitive to the following points.

- Direct photons, as measured in heavy-ion collisions, are emitted from initial nucleon-nucleon contacts (prompt photons), and the subsequent QGP and hadronic phase, whether thermal or not. The prompt contribution is mostly treated independently, and may contain serious uncertainty, see also Sec. 9.2.1. Most calculations add the prompt contribution on top, instead of a dynamic transfer of prompt collisions and the subsequent thermalization.
- The hadronization process, from the quark-gluon to the hadronic phase, is microscopically unknown. Hydrodynamic calculations claim to have a good description of the thermodynamic behavior across the phase transition (four-volume, temperature profile, velocity profile) using some equation of state including a cross-over phase transition, however, they assume chemical equilibrium and local thermal equilibrium across the phase transition. A more realistic description might yield different behavior, and thus a different photon yield. The spacetime profile of velocity and energy-momentum $T^{\mu\nu}$ of the quark-gluon and hadronic phase determine a large fraction of the low- p_T direct photons, and the spacetime borders are therefore crucial.
- The quark and gluon content is very important, since every photon production process must contain quarks. Most hydrodynamic calculations assume complete chemical equilibration, defined by local equilibrium quark and gluon densities, $n_q = n_{0,q}$, $n_g = n_{0,g}$. Stemming from the initial condition as computed by PYTHIA 6.4, the medium is in our case far from chemical equilibrium, as can be seen, e.g., from Fig. 9.7. Especially the quark and antiquark fugacities are important, as photon rates scale by powers of 1 – 2 of the quark fugacities, see also Sec. 9.3.

Despite those caveats, in the following we compare spectra and elliptic flow as much as possible with experimental data and other theoretical calculations.

9.2.1. Prompt photons in literature

In proton-proton collisions, photons are produced by Compton scattering or quark-antiquark annihilation among quarks and gluons within the colliding protons. They are then final

³In Ref. [294] this was generalized to include viscous corrections. In Ref. [280] the formalism was investigated for finite baryon chemical potential.

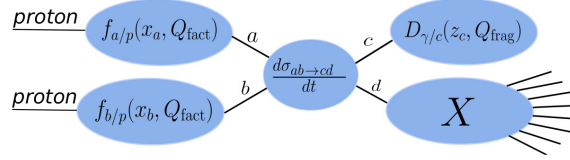


Figure 9.8.: Schematic diagram of prompt photon production by factorized proton parton distribution functions $f_{a,b/p}(x_{a,b}, Q_{\text{fact}})$, the photon fragmentation function $D_{\gamma/c}(z_c, Q_{\text{frag}})$ and the reaction cross section $d\sigma/dt$.

state particles from hard processes and may be separable from hadronic showers. Parton jets generated by hard initial parton interactions can also fragment into photons. Fragmentation photons are the result of higher order corrections in the strong coupling to the hard Compton or annihilation processes [307], and likely to be surrounded by hadrons, if not too energetic. The collisions are characterized by large momentum transfers and small coupling, the reason for which calculations in perturbative QCD are in good agreement with experimental measurements of direct photons in p-p collisions. See Ref. [307] for a detailed comparison to world-data.

It is customary to compute total invariant cross sections $\sigma_{pp \rightarrow \gamma X} = N_\gamma S_p$ instead of invariant yields $E_\gamma dN_\gamma/d^3k_\gamma$, where $\sigma_{pp \rightarrow \gamma X} = N_\gamma S_p$, with the plain transverse surface of the proton, S_p . In Fig. 9.8 we show the schematic diagram of the factorized process. The invariant photon production cross section then is (from Ref. [308]),

$$\begin{aligned}
 E_\gamma \frac{d\sigma}{d^3p_\gamma} &= \sum_{abcd} \int dx_a \int dx_b dz_c f_{a/p}(x_a, Q_{\text{fact}}) f_{b/p}(x_b, Q_{\text{fact}}) D_{\gamma/c}(z_c, Q_{\text{frag}}) \\
 &\quad \times \frac{s}{\pi z_c} \frac{d\sigma_{ab \rightarrow cd}}{dt} \delta(s+t+u) \\
 &= \sum_{abcd} \int_{x_{a,\min}}^1 dx_a \int_{x_{b,\min}}^1 dx_b f_{a/p}(x_a, Q_{\text{fact}}) f_{b/p}(x_b, Q_{\text{fact}}) D_{\gamma/c}(z_c, Q_{\text{frag}}) \frac{1}{\pi z_c} \frac{d\sigma_{ab \rightarrow cd}}{dt} \\
 \text{with } z_c &= \frac{x_T}{2x_b} e^{-y} + \frac{x_T}{2x_a} e^y, \\
 x_{a,\min} &= \frac{x_T e^y}{2 - x_T e^{-y}}, \quad x_{b,\min} = \frac{x_a x_T e^{-y}}{2x_a - x_T e^y}, \quad x_T = 2p_T/\sqrt{s_{pp}}
 \end{aligned} \tag{9.9}$$

Here, s, t, u are Mandelstam variables in partonic processes, s_{pp} is the squared center of mass energy of the p-p collision, p_T is the transverse photon momentum and y its rapidity. The protons are labeled A and B, and the fraction of longitudinal momentum carried by a parton a, b is x_a, x_b . Taken the positive z-axis as the axis of the incoming proton a , and the rapidity with respect to this axis, the Mandelstam variables in the differential cross section is given by [308]

$$s = x_a x_b s_{pp}, \quad t = -x_a p_T \sqrt{s_{pp}} e^{-y}, \quad u = -x_b p_T \sqrt{s_{pp}} e^y. \tag{9.10}$$

$d\sigma_{ab \rightarrow cd}/dt$ is the partonic differential cross section from Compton scattering or pair annihilation, which can be evaluated, e.g., at NLO in the strong coupling constant $\alpha_s(Q_{\text{ren}})$, evaluated at a typical scale Q_{ren} (transverse momentum) [309, 310].

The functions $f_{a(b)/p}(x_{a(b)}, Q_{\text{fact}})$ are parton distribution functions (PDFs) of the proton a (b). In Ref. [94], the authors use CTEQ61m [311] for the proton, and in case of prompt photons from AA collisions, the nuclear PDFs EPS09 are used [312]. For the parton-to-photon fragmentation function $D_{\gamma/c}(z_c, Q_{\text{frag}})$ the set BFG-2 [313] is commonly used. In

the calculation from Ref. [94] (within MUSIC) the scales are set equal, $Q_{\text{fact}} = Q_{\text{ren}} = Q_{\text{frag}} = Q = p_T/2$. In order to estimate the prompt rate in heavy-ion collisions, the yield in pp, evaluated with the above algorithm, is then scaled by the number of binary collisions N_{coll} . MUSIC computes prompt photons also for very low p_T , even though pQCD at these scales should not be applicable. However, the exact value of the scale of breakdown is not clear, and experimental p-p direct photon data can be described by the algorithm of Ref. [94] down to $p_T = 1$ GeV.

In Fig. 9.9 we show spectra of direct photons in AA collisions from the PHENIX experiment at RHIC, measured at midrapidity ($|y| < 0.35$), compared to the theoretical results for only prompt photons from MUSIC [94] and PHSD [314] (PHSD uses experimental values), as well as N_{coll} -scaled pp-results from experiment, see Refs. [78, 80].

First we observe, that above $p_T \geq 3$ GeV the prompt photon yield reaches the experimental data within their uncertainty, in all three cases. In general, the three calculations agree well (compared to the experimental uncertainty) with each other for $p_T \geq 1$ GeV. Below, the NLO calculation shoots significantly above the scaled experimental pp yield. This is due to the fact, that below $p_T = 1$ GeV there is no direct photon data available, and the curves were extrapolated to low p_T with functional form $a(1+p_T^2/b)^c$, which might be doubtful at low p_T .

In the following, we use the MUSIC estimate of prompt photon sources for comparisons of BAMPS to experiment.

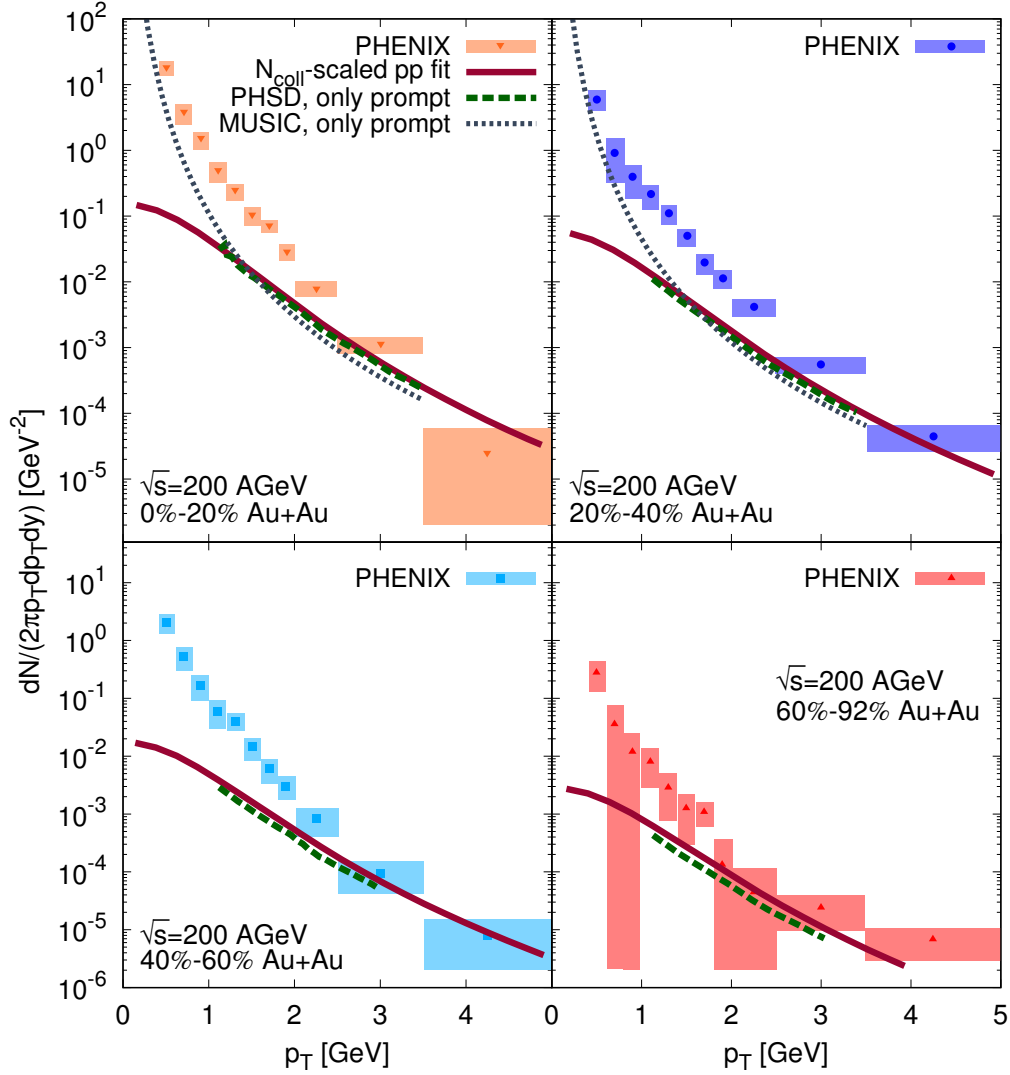


Figure 9.9.: Comparison of an N_{coll} -scaled fit to pp direct photon data from Ref. [80] (red solid line), the prompt contribution adopted within the PHSD framework [314] as well as the approach from MUSIC [94], which relies on the formalism presented in Eqs. (9.9),(9.10).

9.2.2. Spectra and elliptic flow at LHC from BAMPS

In Fig. 9.10 we show the currently available experimental data for direct photon spectra from the ALICE collaboration, along with selected results from BAMPS, in four centrality classes. These results are for center-of-mass energies of $\sqrt{s_{NN}} = 2.76$ TeV for Pb+Pb collisions, measured at midrapidity ($|y| < 0.8$). It is clear that here we compare a model for the photon production in the QGP phase with direct photon data, which includes hadronic and prompt photons, however, it is instructive since in an intermediate p_T -window ($\sim 2 - 4$ GeV), photons from the QGP are expected to dominate the spectra.

The red solid line shows photons obtained by binary processes and radiative photons from the “22+AMY” method. The green dashed line shows photons obtained by the “22+23” method.

At the highest p_T , the spectra of “22+AMY” are a factor 2 larger than with photons obtained by “22+23”. The very peripheral calculation (40% – 80%) is an exception, here the “22+AMY” results diverge from the “22+23” matrix element results at higher p_T . The most pronounced difference however is seen at very low p_T . Here, the correct treatment of the LPM effect in the “AMY” scattering kernel leads to enhanced emission of low p_T photons, up to a factor of 10 above the matrix element results. This could be expected from Fig. 6.16(a), where photons from the $2 \rightarrow 3$ matrix element are seen to be much suppressed compared to the analytic AMY result for small energies, $E/T \leq 1$. The way how this is realized dynamically in low- p_T regions is in fact quite interesting.

As mentioned above, the “AMY” algorithm within BAMPS has a trivial, linear λ_q dependence. Since every quark has its (temperature and momentum dependent) emission probability, the rate scales linearly with fugacity $R \sim \lambda_q$. However, the algorithm elsewhere assumes a chemically equilibrated medium, such that the screening masses are the equilibrium ones. As investigated in Fig. 6.17, the $2 \rightarrow 3$ matrix element has a much more complicated fugacity dependence, scaling approximately with $\lambda_q^{1.36}$ for $\lambda_q \geq 0.3$. As an example, assuming $\lambda_q = 0.2$, the ratio $\lambda_q/\lambda_q^{1.36} \approx 1.8$ explains approximately the higher rates. We remark, that photons produced by the “AMY” method, obey the rule, that production stops, when the energy density drops below $\epsilon \leq 0.6$ GeV/fm³. We however checked, that an additional temperature cut (production stops, when the effective temperature drops below $T_c \leq 160$ MeV) does not make a visible difference.

We added the prompt contribution from Ref. [94] to our photon spectra in the two most central multiplicity classes (dotted lines). These results miss only thermal hadronic data, but at the highest available p_T , the hadronic photon spectrum should not contribute any more. Comparing the dotted lines with data, the theoretical calculations undershoot the data about a factor of 2 – 3, however, the slope of the resulting spectra comes very close to the data.

Arguing from the slope, we conclude, that the thermodynamic properties, like the flow field $u^\mu(t, \vec{x})$ and temperature field $T(t, \vec{x})$ are realistic. The too little overall factor hints to a possibly large hadronic contribution, a medium which is even denser, or equilibrates chemically much faster.

In Fig. 9.11 we show the elliptic flow of direct photons from the LHC for 0% – 20% and 20% – 40% most central collisions. Under the assumption of full correlation of the systematic uncertainties in p_T , the experimental collaboration reports a significance of the deviation from the hypothesis of vanishing elliptic flow with 1.0σ (0% – 20%) and 1.4σ (20% – 40%). We compare the data points to the results from BAMPS, which constitute only the QGP contribution. The above mentioned leakage effect affects the elliptic flow negatively, but the final result is a combined effect of leakage and the weighted average of the sources. All BAMPS results show elliptic flow of only up to a few percent. The result using the “22+AMY” method shows a significant elliptic flow of up to 5 %, whereas in the

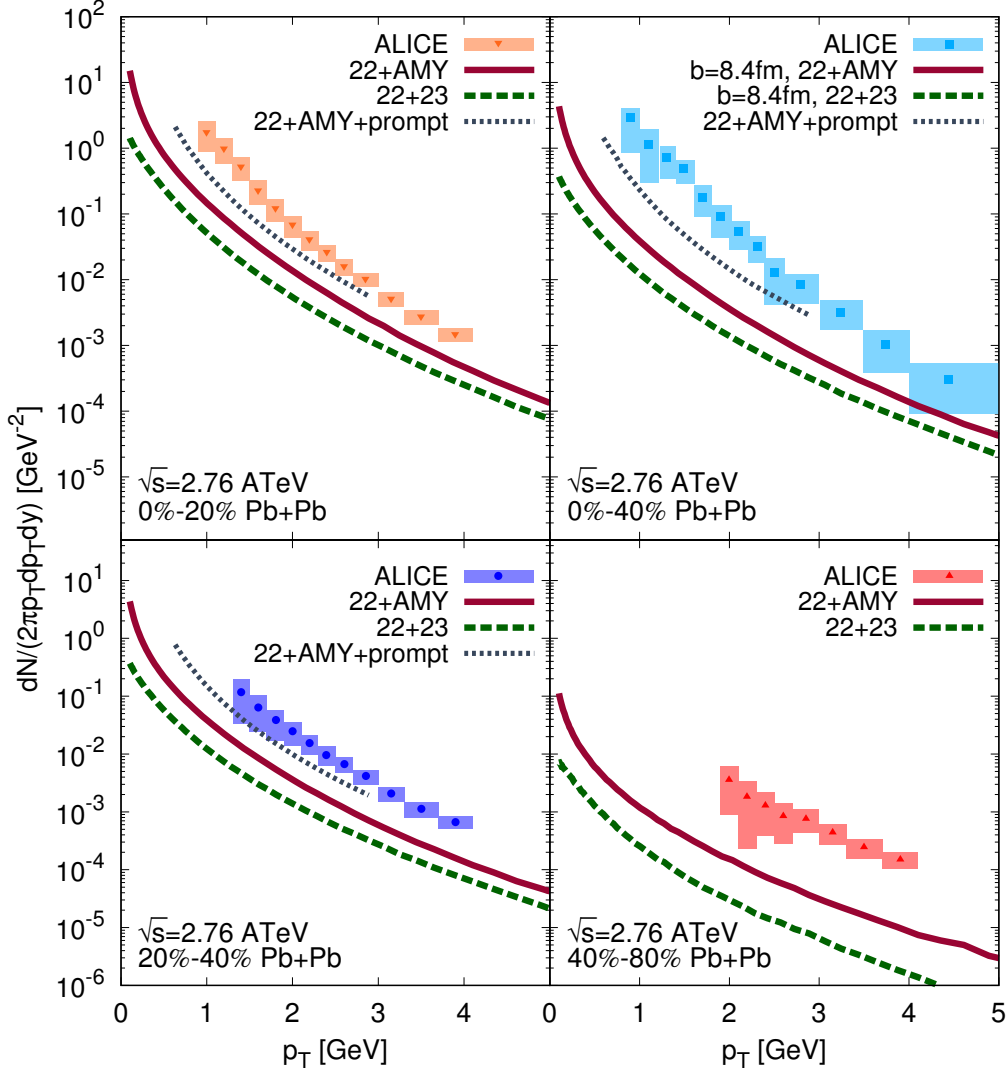


Figure 9.10.: Experimental direct photon spectra from the ALICE collaboration [76, 304] compared to photons from the QGP computed within BAMPS with two different methods (22+23: microscopic matrix elements, 22+AMY: microscopic $2 \leftrightarrow 2$ matrix elements and AMY emission kernel emission.)

matrix element calculation “22 + 23” the flow is consistent with zero. The reason for this is twofold. First, photon elliptic flow is the result of a weighted average of flow, weighted by yield, across the entire emission lifetime. The “AMY” radiation yield scales with effective temperature, thus the weighting is different from the “22+23” method. Second, the photons radiated by quarks from the AMY method are emitted exactly collinearly, which can have a difference in the azimuthal distribution for a non-equilibrium situation. The results suggest, that the radiative part of the photons in the “22+AMY” scheme is responsible for all the flow, since the “22+23” method does not show visible flow.

9.2.3. Spectra and elliptic flow at RHIC from BAMPS

In Fig. 9.12 we show spectra of direct photons at from the PHENIX experiment at RHIC, measured at midrapidity ($|y| < 0.35$), compared to theoretical results from BAMPS, using

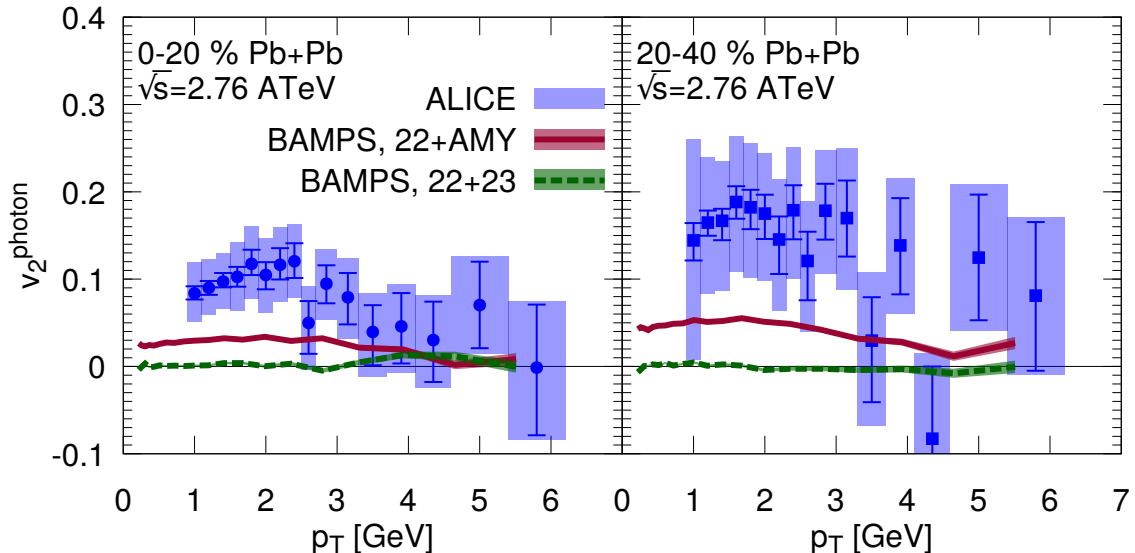


Figure 9.11.: Elliptic flow of direct photons as measured from the ALICE collaboration within $|y| < 0.8$ in rapidity for 0% – 20% (left panel) and 20% – 40% (right panel) most central collisions at $\sqrt{s_{NN}} = 2.76$ TeV. We only compare here to theoretical calculations of photons emitted from the QGP using BAMPS. The red solid line shows results from the “AMY” method, whereas the green dashed line shows results from the binary and inelastic matrix elements.

the two methods described above, “22+AMY” (red solid) and “22+23” (green dashed). The blue dotted lines in the two top panels show theoretical direct photon calculations, obtained by summing prompt photons (from Ref. [94]), the BAMPS results “22+AMY” and the thermal hadronic contribution from hydro (as well from Ref. [94]).

For the two more central event classes, the difference between the two production methods is not as large as for the LHC calculations in Fig. 9.10. Interestingly, the experimental spectra are much steeper than the BAMPS QGP photon spectra, opposed to the LHC case, where the slope of the QGP spectra from BAMPS are very similar to the experimental data. The two methods, “22+AMY” and “22+23” show similar shapes of the spectra, where the “22+AMY” results are about a factor of 2 larger in magnitude than the “22+23” for central collisions, the difference increasing with decreasing centrality.

We observe, that in all but the 60% – 92% centrality bin, the QGP results from BAMPS (using the “22+AMY”) method crosses or touches the highest p_T bin of the experimental data. For the “22+23” method, only in the most central case (top left panel), the experimental data at the $3.5 < p_T < 5$ GeV bin is reached by the QGP contribution. Comparing the simulated direct photon spectrum (dotted line) with the experimental data, we see an underestimation of the spectrum for the 0% – 20% centrality bin in all but the bin at $p_T \sim 3$ GeV. In the 20% – 40% centrality bin the theoretical direct spectrum touches the error bars of the experimental data for the lowest p_T bins, $p_T \leq 1$ GeV, indicating that the hadronic calculation from Ref. [94], dominating at the lowest momenta, is reasonable. At intermediate p_T , we undershoot the data, whereas above $p_T \geq 2.5$ GeV the error bars are crossed.

In Fig. 9.13 we show the elliptic flow of direct photons from RHIC for 0% – 20%, 20% – 40% and 40% – 60% most central collisions. Here again, the flow is small, and the result of leakage and the weighted average of the moving sources.

We compare the data points to the results from BAMPS with “22+AMY” (red solid)

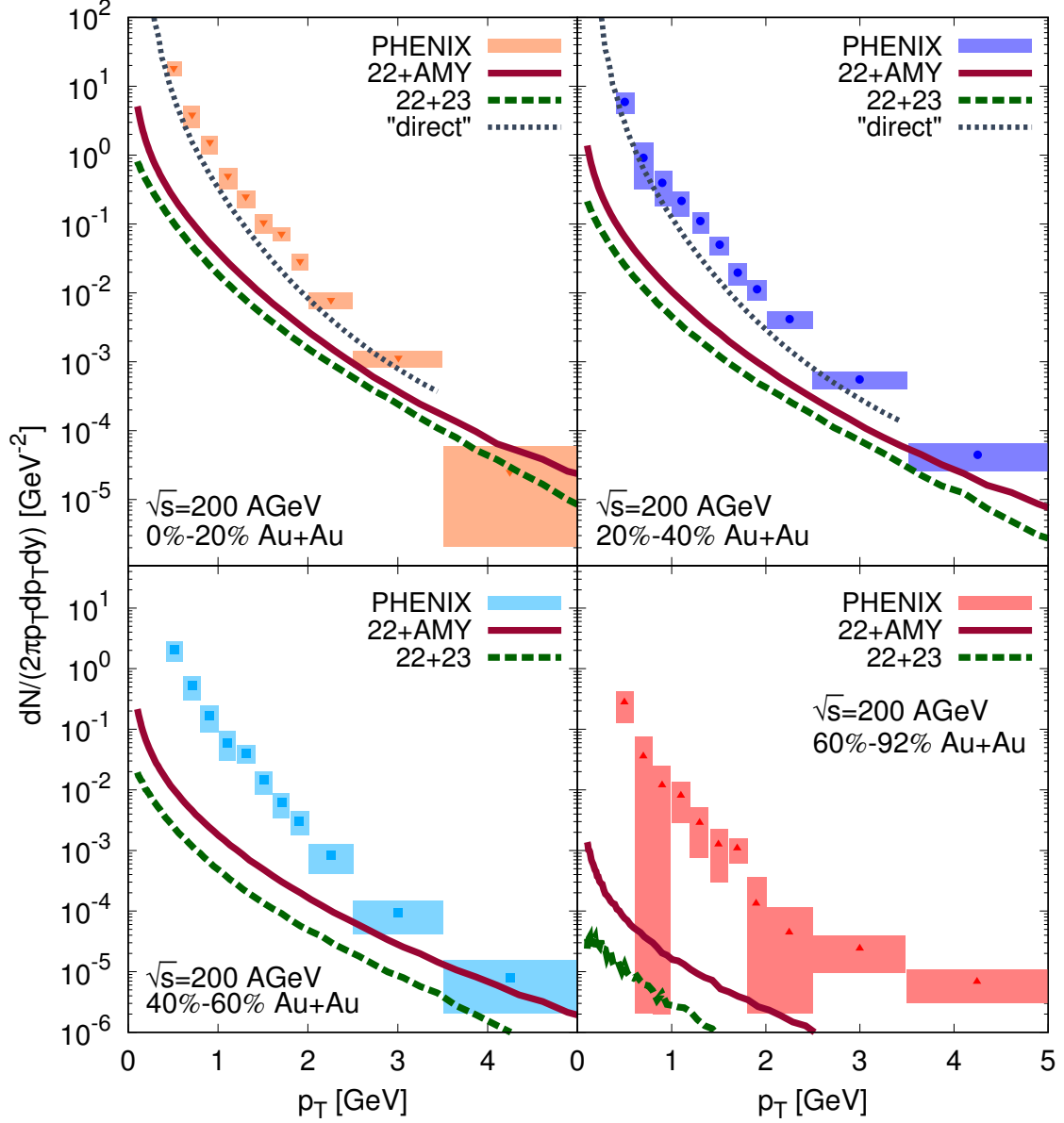


Figure 9.12.: Compilation of direct photon spectra at midrapidity ($|y| < 0.35$) from RHIC (PHENIX experiment, Ref. [80]) in four centrality classes, compared to thermal QGP photons from BAMPS. Here we compare photons obtained from the $2 \leftrightarrow 2 + 2 \leftrightarrow 3$ matrix elements (dubbed 22 + 23) with the spectra obtained using the $2 \leftrightarrow 2$ matrix elements and the microscopic AMY radiation (dubbed 22 + AMY). For the two more central multiplicity classes 0% – 20% and 20% – 40% we add prompt photons and thermal hadronic photons from Ref. [94] to the 22 + AMY QGP spectra from BAMPS (the sum is dubbed “direct”).

and “22+23” method (green dashed), which constitute only the QGP contribution. Additionally, the blue dash-dotted line shows the weighted average of all components of direct photons, where we use Eq. (8.11). Again, the prompt and thermal hadronic data come from Ref. [94].

The “22+23” QGP result shows no significant flow, whereas the “22+AMY” method

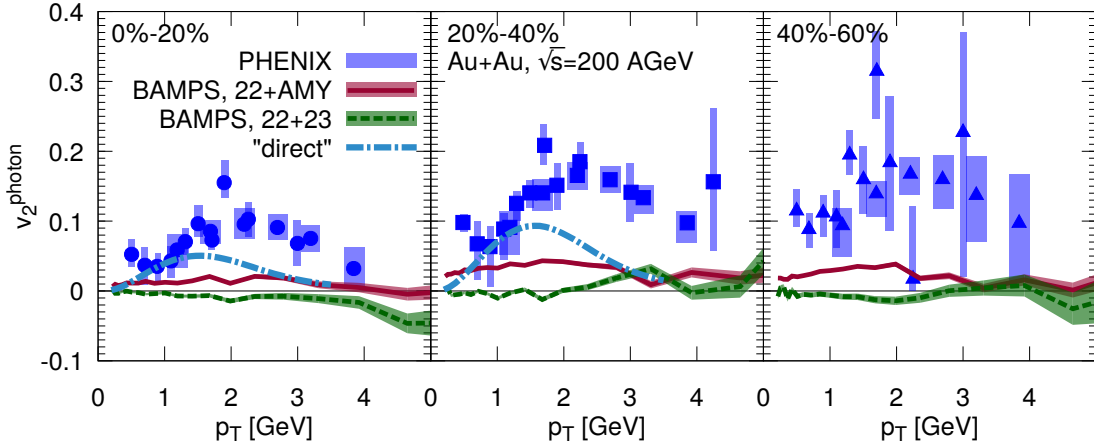


Figure 9.13.: Elliptic flow of direct photons at midrapidity ($|y| < 0.35$) from RHIC (PHENIX experiment) in three centrality classes as function of transverse momentum p_T (blue symbols). We compare to the thermal QGP radiation from BAMPs, using the $2 \leftrightarrow 2$ matrix elements and the microscopic AMY radiation (“22+AMY”, red solid line) and the “22+23” method (green dashed line). For the two more central multiplicity classes 0% – 20% and 20% – 40% we use additional prompt photons and thermal hadronic photons from Ref. [94], weighted by their corresponding spectra together with the “22+AMY” QGP spectra from BAMPs (in total dubbed “direct”).

shows flow with a maximum at $p_T \sim 2$ GeV of 3% at 0% – 20% and 5% at 20% – 40%. The weighted average of direct photons (blue dashed-dotted) line hits the experimental data points below $p_T \leq 1.5$ GeV. This is due to quite large hadronic flow and non-vanishing QGP results which count positive in the weighting. The large experimental values on the order of 10% – 20% remain a puzzle.

9.2.4. Running coupling

In Sec. 6.4.2 we differentiated different prescriptions of how to implement a running strong coupling in thermal photon production processes.

Here we show in Fig. 9.14 selected results from BAMPs on how this affects final photon spectra of the QGP, using as an example 0% – 20% most central Au+Au collisions at RHIC. Using a fixed coupling $\alpha_s = 0.3$ at the vertices and in the Debye and thermal masses we show spectra for only binary photon production (red solid line) and “22+23” binary and inelastic photon production (blue solid line). This we compare to photons computed with running coupling evaluated at the Mandelstam scale at the vertices, $\alpha_s(s, t, u)$, and the scale $(2\pi T)^2$ in the Debye and thermal masses (red dashed line for binary photon production and blue dotted line for binary and inelastic photon production). For binary photon production we show the resulting spectrum using the Mandelstam variables of each channel as the scale within the Debye and thermal masses $m_{D,g/q}^2 \sim \alpha_s(s, t, u)$. It is apparent, that in all cases, running strong coupling increases the photon rates compared to the standard choice $\alpha_s = 0.3$. We observe, that the running coupling ($m_{D,g/q}^2 \sim \alpha_s[(2\pi T)^2]$) increases the spectra by about a factor of 1.5 within $2 < p_T/\text{GeV} < 5$, and 1.7 within $0 < p_T/\text{GeV} < 2$. The spectrum is thus softened slightly (larger slope). In Fig. 9.15 we show the elliptic flow from BAMPs for fixed (solid lines) and running coupling (dashed and dotted lines). Here we do not see any significant change, the v_2 is nearly zero in all

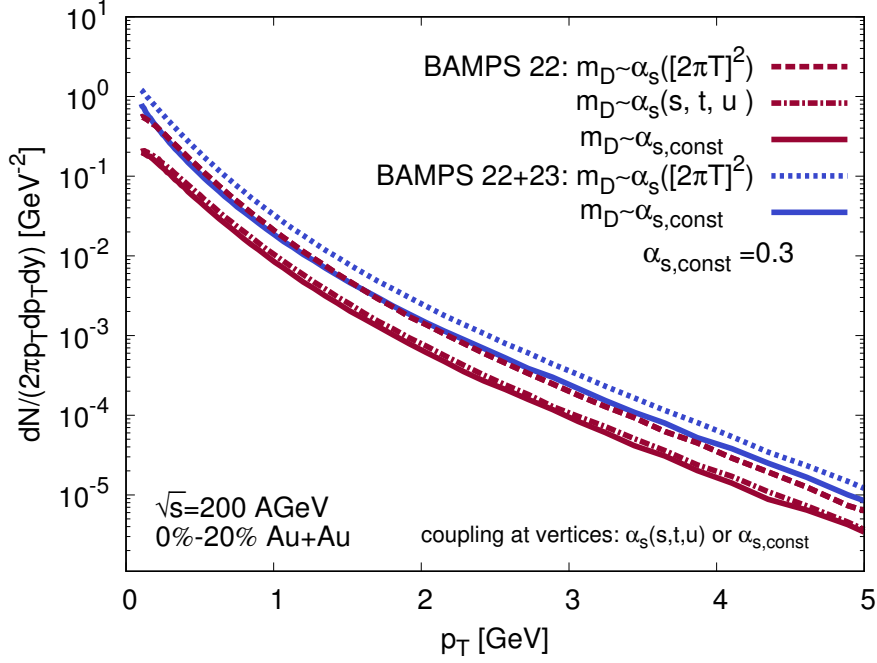


Figure 9.14.: Photon spectra from BAMPS for RHIC 0% – 20% most central collisions, where we compare photons obtained through the “22+23” matrix element method (blue) and only $2 \leftrightarrow 2$ photon production (red) with fixed coupling (solid lines) and running coupling. At the vertices, the scale of the running coupling is the momentum transfer (Mandelstam variables s, t, u). The strong coupling in the Debye mass is evaluated both at $Q^2 = (2\pi T)^2$ (dashed and dotted lines) or as well the Mandelstam variables (dash-dotted line).

cases. The running coupling does neither change the weighting of the v_2 contributions from different times, nor the non-equilibrium emission characteristics to gain significant v_2 .

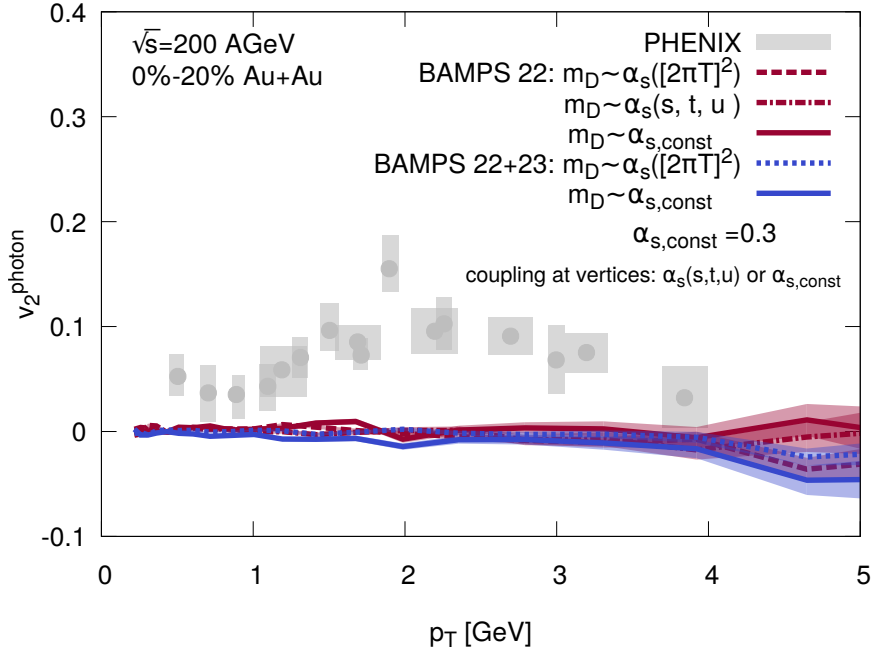


Figure 9.15.: Elliptic flow of photons from BAMPS for RHIC 0% – 20% most central collisions. Here we compare photons obtained through the “22+23” matrix element method (blue) and only $2 \leftrightarrow 2$ photon production (red) with fixed coupling (solid lines) and running coupling. At the vertices, the scale of the running coupling is the momentum transfer (Mandelstam variables s, t, u). The strong coupling in the Debye mass is evaluated both at $Q^2 = (2\pi T)^2$ (dashed and dotted lines) or as well the Mandelstam variables (dash-dotted line).

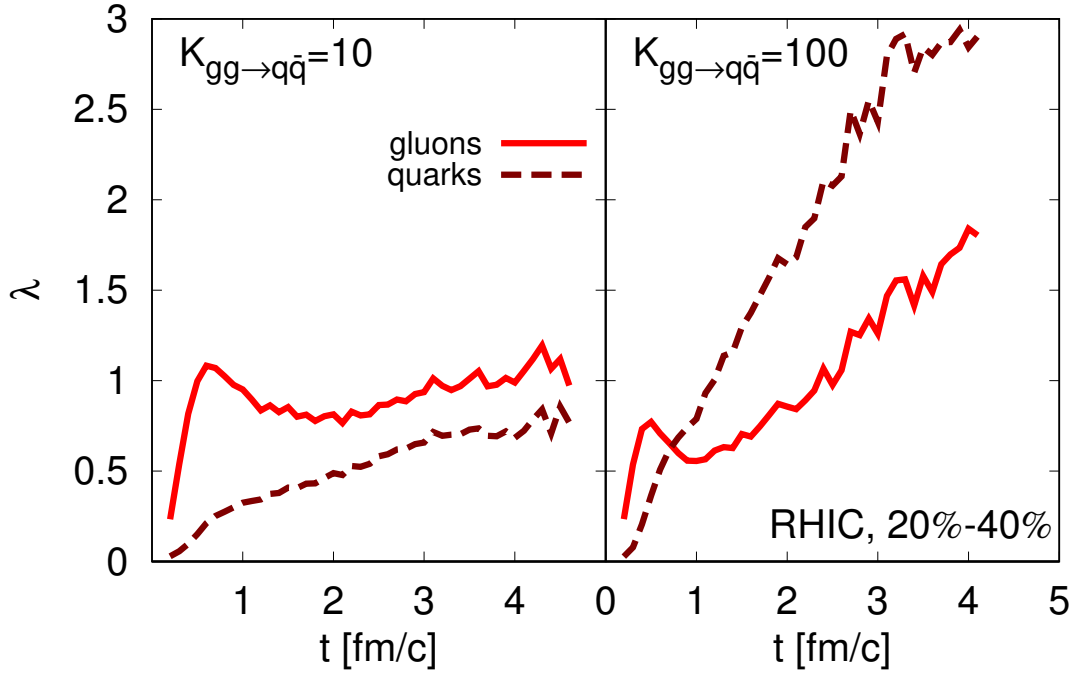


Figure 9.16.: Quark and gluon fugacity evolution in the central cell for Au+Au collisions at $\sqrt{s_{NN}} = 200$ GeV, where the $g + g \rightarrow q + \bar{q}$ cross section was increased by a factor $K_{gg \rightarrow q\bar{q}} = 10$ (left panel) and $K_{gg \rightarrow q\bar{q}} = 100$ (right panel).

9.3. Artificial equilibration scenario

As shown in Fig. 6.17 the $2 \leftrightarrow 2$ photon rates scale nearly linearly with the quark fugacity, so that they are strongly affected by the quark fugacities $\lambda_q \lesssim 0.2$ at early times in BAMPS. The inelastic ($2 \rightarrow 3$) rate has a more complicated fugacity dependence, such that the photon rate at $\lambda_q = 0.2$ is less than 10% of the equilibrium rate at $\lambda_q = 1$. Photon rates employing the AMY formalism in the form we presented above depend linearly on the quark density (emitters). In principle, the AMY emission rates for single quarks would have to adopt background fugacities, within the screening masses, Eqs. (7.4) and (7.6) which appear in the collision kernel and the inverse formation time in the integral Eq. (7.2). We omit this improvement at this point and just note, that in an under-saturated case, scattering rates would increase due to less effective screening. The distribution functions in Eq. (7.1) are represented by the BAMPS background medium itself and contain the fugacities already. The combined effects of the above said are apparent in the photon spectra.

To see which role is played by the chemically equilibrating medium, we alter the fugacity evolution of the quarks (and thus also the gluons) by tuning arbitrarily the quark-antiquark production cross section⁴ by a factor of 10 and 100. The resulting fugacity evolution is shown in Fig. 9.16. It can be seen, that at around $t = 2$ fm/c the quark fugacity increases from $\lambda_q(t = 2 \text{ fm/c}) \approx 0.3$ to $\lambda_q(t = 2 \text{ fm/c}) \approx 0.5$ (for $K_{gg \rightarrow q\bar{q}} = 10$) and $\lambda_q(t = 2 \text{ fm/c}) \approx 1.5$ (for $K_{gg \rightarrow q\bar{q}} = 100$). This can be compared to the original case from the middle right panel in Fig. 9.7.

In Fig. 9.17 the resulting photon spectra are shown. The difference between the three

⁴We ignore the tuning of the backreaction $q\bar{q} \rightarrow gg$ because the purpose of this test is to drive the chemical equilibration faster. In the central cell, the quark fugacity even increases above unity for late times and $K_{gg \rightarrow q\bar{q}} = 100$.

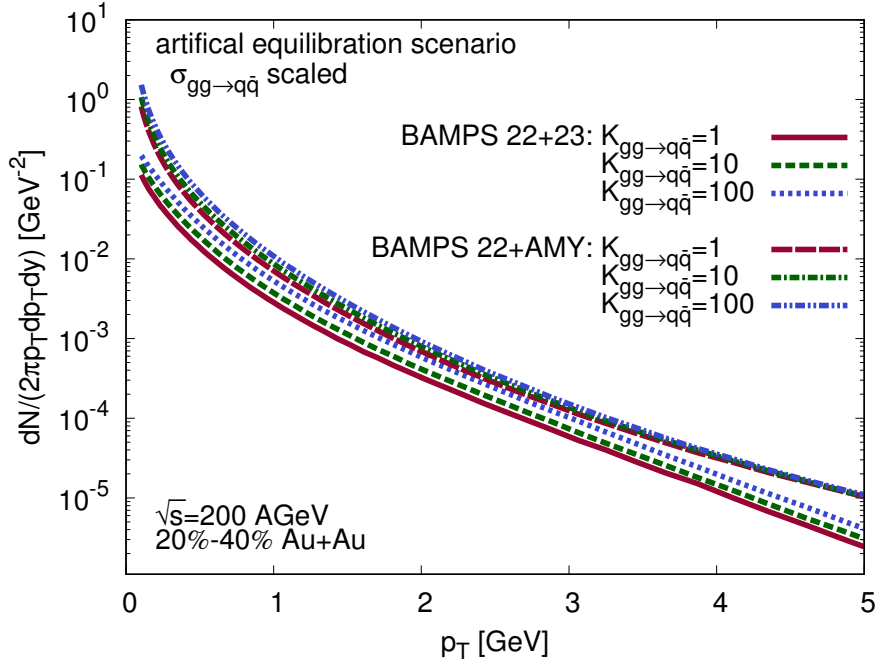


Figure 9.17.: The thermal photon spectrum from the QGP for RHIC collisions at $|y| < 0.35$, where we change the chemical equilibration of the medium during the evolution by artificially increasing the $gg \rightarrow q\bar{q}$ cross section by a factor of 10 (green dashed line) and 100 (blue dotted line).

scenarios is moderate, because most of the photons are produced within the first 2 fm/c.

The difference in the fugacity is however, much stronger at later times (for $K_{gg \rightarrow q\bar{q}} = 100$ at $t = 4$ fm/c about a factor of six), where not many photons are produced due to the thinner and colder medium. This shows, that the quark content at the very initial phase is crucial for photon spectra. In the case of “22+AMY” photon production, at high $p_T \geq 4$ GeV, there is almost no difference visible between the different background evolutions. This indicates, that those high- p_T photons are produced at the earliest times of the evolution, $t \ll 1$ fm/c, where the strong artificial equilibration has not yet set in, but temperatures are very high. The “22+23” photon spectra do not show this effect very strongly, since these rates are sensitive to the full distribution, and not single moments in terms of an effective temperature.

9.4. Comparison to other models

In Fig. 9.18 we show a compilation of direct photon contributions from BAMPS, MUSIC [94] and PHSD [314] for the two most central centrality classes along with PHENIX data. We emphasize here that at 0% – 20% centrality the direct photon sum of MUSIC and PHSD agree well (especially around $p_T \sim 2$ GeV), whereas at 20% – 40% centrality the agreement is not as precise.

The prompt contribution was compared already in Sec. 9.2.1, and is comparable. The QGP contribution is however very different in all three models: BAMPS shows the hardest spectrum (most shallow slope), and its magnitude is for $p_T < 2$ GeV below PHSD and MUSIC. PHSD again is about a factor of two below MUSIC, and harder at high p_T . The hadron gas contribution dominates the spectrum in MUSIC below $p_T \leq 1$ GeV, in PHSD

hadrons dominate the spectrum below $p_T \leq 2$ GeV for the 0% – 20% centrality class, increasing in importance as one goes to more peripheral collisions, such that at 60% – 92% centrality the photon spectrum below $p_T \leq 3.5$ GeV is hadron dominated. It becomes apparent that the suppressed QGP contribution in PHSD is compensated by an enlarged hadronic yield. At this point it remains an open question which approach is closer to nature.

9.5. Conclusion

In this chapter we have presented a detailed comparison of photon spectra and elliptic flow from BAMPS to other models and experiment, using two separate methods for photon production introduced in previous chapters. BAMPS has in general harder but lower photon spectra, and less elliptic flow than hydrodynamic models. In some cases comparisons with experiment are reasonably successful, even though flow and yield is mostly underestimated. Our very low absolute yield in the QGP hints to a possibly important hadronic contribution. We have set the resulting spectra in connection to the background chemistry of the model, and we have shown their sensitivity to it. The emerging physical picture bears a list of caveats, mainly due to the many different photon production stages across the spacetime evolution of the heavy-ion collision. Collected photons in the detector are a sum (for spectra) or weighted average (for elliptic flow) of all emission locations in spacetime, making it hard to distinguish and separate theoretical uncertainties of the models. However, it is very interesting to observe the dynamical realization of photon production influenced by the different processes, by running coupling, quark and gluon chemical equilibration and the temperature evolution. We have pointed out, why large elliptic flow of photons is strongly disfavored by the combination of parton flow and background thermodynamics. This is consistent with other studies in literature, however, in BAMPS we are dealing with a kinetic and chemical non-equilibrium. We conclude, that the chemical evolution in the QGP is extremely important. Compared to hydrodynamic models, the main differences lie in the non-equilibrium nature of BAMPS, the initial state, the equation of state and the viscosities. The transport model PHSD again has a different background dynamics, and also the photon production mechanisms differ.

It remains to say, that to date, no model explains experimental direct photon data neither from PHENIX nor ALICE for yield and flow satisfactorily. In future, additional, yet unexplored photon production mechanisms, or new insights in the initial state might lead to an improved picture. It is possible, that initial state photon radiation, possibly non-isotropic, leads to an additional positive contribution for both elliptic flow and total yield. Other ideas in literature deal with the connection to initially strong magnetic fields. In hydrodynamic studies, researchers explore the precise dependence of photon production rates to shear and bulk viscosities. Furthermore, hadronic rates are under debate.

It appears highly probable, that the solution of the “photon puzzle” is a delicate collection of improvements of model building, yet to come. In this work, we have evened the path and pointed out sensitivities which have not gained attention before or were plainly neglected.

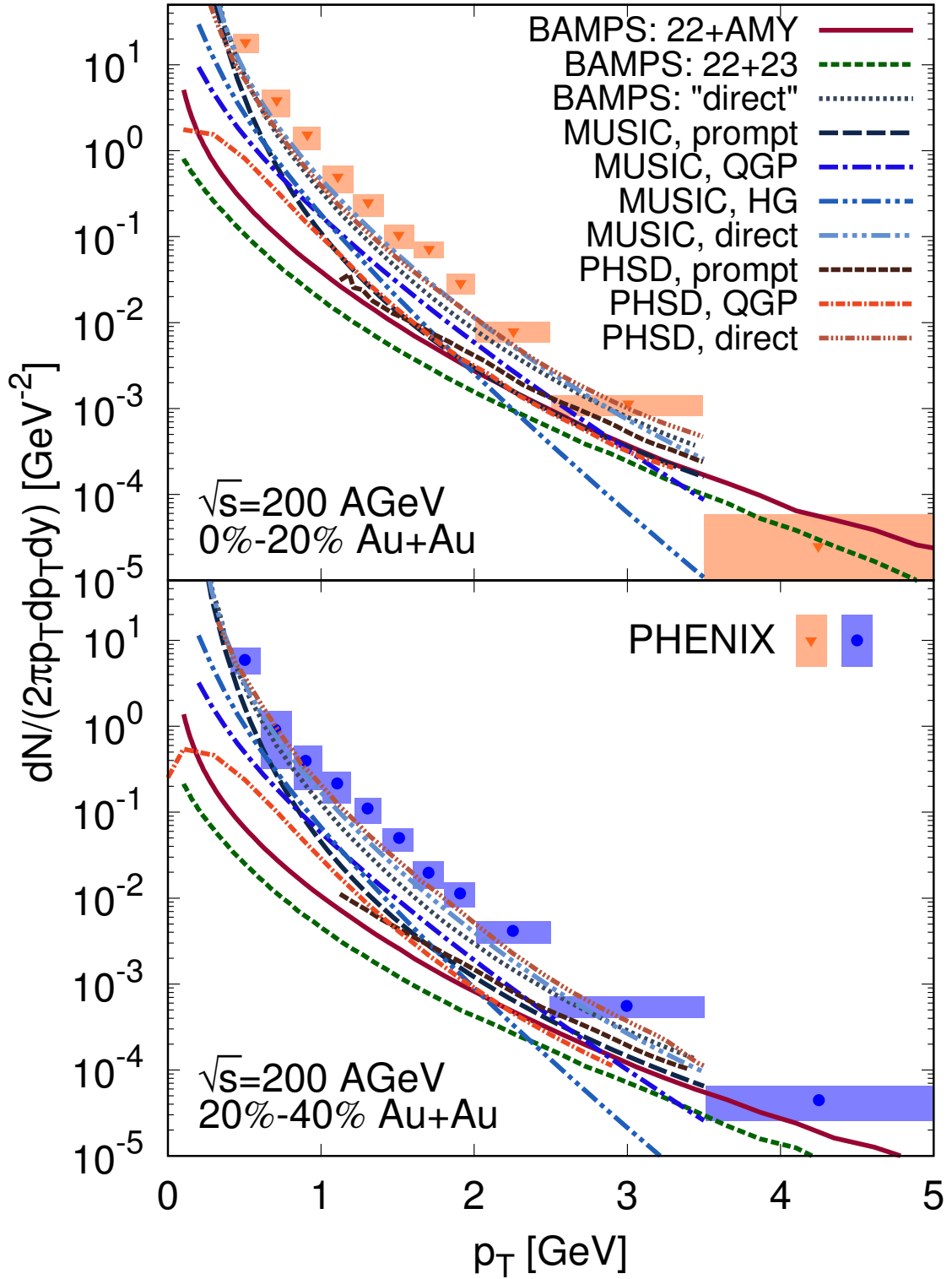


Figure 9.18.: Nearly complete comparison of the direct photon contributions from BAMPS, MUSIC and PHSD. The BAMPS results show the QGP results with the two different methods, along with a sum of prompt and thermal hadronic photons from MUSIC, Ref. [94] (see Fig. 9.12 and its description). The MUSIC prompt, QGP, hadron gas and direct photons are from Ref. [94]. The PHSD results are from Ref. [81].

10. Dileptons in heavy-ion collisions

Dileptons, such as e^+e^- , $\mu^+\mu^-$ or $\tau^+\tau^-$ pairs, are very important probes in heavy-ion experiments. They are virtual photons, and due to their finite mass have a different kinematics and different open questions in phenomenological studies. Dileptons are studied extensively in low energy experiments, and even in high-energy experiments the contribution from the hadron gas is much more important than from the QGP. This is the reason why we will be rather short in this chapter, merely elucidating the possibility of dilepton production within BAMPS. As a possible application, we extract an effective, averaged temperature from simulations of heavy-ion collisions.

10.1. Perturbative dilepton rates

Dilepton rates in the QGP do not suffer from the enhancement property of photons which, e.g., augments bremsstrahlung to leading order (see Chap. 6). The leading order diagram $q + \bar{q} \rightarrow l^+ + l^-$ is the only one contributing to the rate at leading order. The matrix element, spin averaged in the initial state and spin summed in the final state, reads [7,315],

$$|\mathcal{M}|^2 = \frac{(4\pi\alpha_{\text{EM}})^2}{N_c} \sum_{\text{species } i} q_i^2 \left(2 + 4\frac{t}{s} + 4\left(\frac{t}{s}\right)^2 \right). \quad (10.1)$$

Note that the color factor ($N_c = 3$) is due to the various color states in the initial state. The fractional quark charge q_i is in units of the elementary charge e , and the sum runs over all flavors, such that for $N_f = 3$, $\sum_i q_i^2 = 2/3$. The total cross section is

$$\begin{aligned} \sigma_{q\bar{q} \rightarrow l^+l^-} &= \sum_{\text{species } i} q_i^2 \frac{4\pi\alpha_{\text{EM}}^2}{9M^2} \left(1 + 2\frac{m^2}{M^2} \right) \sqrt{1 - 4\frac{m^2}{M^2}} \\ &\approx \sum_{\text{species } i} q_i^2 \frac{4\pi\alpha_{\text{EM}}^2}{9M^2}, \end{aligned} \quad (10.2)$$

where we assumed vanishing bare lepton mass in the second line, $m \equiv 0$. As a note, this cross section can be obtained by the pure QED cross section

$$\sigma_{e^-e^+ \rightarrow l^+l^-} = \frac{4\pi\alpha_{\text{EM}}^2}{3M^2}, \quad (10.3)$$

and its generalization to quark-antiquark production,

$$\sigma_{l^+l^- \rightarrow q\bar{q}} = N_c \sum_{\text{species } i} q_i^2 \frac{4\pi\alpha_{\text{EM}}^2}{3M^2}, \quad (10.4)$$

which must then be color averaged (factor 1/9) in order to obtain Eq. (10.2). This is correctly done in Refs. [7,315], whereas in Ref. [316] the cross section is wrong by a factor of 2 and in Ref. [317] by a factor 1/3.

The differential dilepton production rate (for massless leptons) is

$$\frac{dR}{d^4p} = \frac{dN}{d^4x d^4p} = \sum_{\text{species } i} q_i^2 \frac{\alpha^2}{4\pi^4} e^{-E/T} K_f(p, T, \mu), \quad (10.5)$$

where the function K_f for Boltzmann statistics is equal to unity, and for quantum statistics reads [316]

$$K_f = \frac{T}{p} \frac{1}{1 - e^{-E/T}} \ln \frac{\left(\exp \left\{ -\frac{E-p}{2T} \right\} + \exp \left\{ -\frac{E+\mu}{T} \right\} \right) \left(\exp \left\{ -\frac{E+p}{2T} \right\} + \exp \left\{ -\frac{\mu}{T} \right\} \right)}{\left(\exp \left\{ -\frac{E+p}{2T} \right\} + \exp \left\{ -\frac{E+\mu}{T} \right\} \right) \left(\exp \left\{ -\frac{E-p}{2T} \right\} + \exp \left\{ -\frac{\mu}{T} \right\} \right)}. \quad (10.6)$$

With the transformation $dP = dE d^3p = M/E dM d^3p$, and for isotropic systems $d^3\vec{p} = 4\pi p^2 dp$, the rate can be given as

$$\frac{dR}{dM dp} = \frac{M}{E} 4\pi p^2 \frac{dR}{d^4p}. \quad (10.7)$$

By integrating Eq. (10.7) over a certain range in p or M , one can plot and compare the rate easily. Implementing the total and differential cross section in the transport model BAMPS is straight forward. Since the only diagram is an s -channel, no screening is necessary, and Eqs. (10.1) and (10.2) can readily be implemented. In Fig. 10.1 the normalized equilibrium rates from BAMPS are compared to the analytic rates from Eq. (10.5) with perfect agreement.

10.1.1. Higher order rates

Dilepton rates at higher order were not implemented within this thesis. When the dilepton energy is on the order of gT one must include HTL corrections which are as large as the Born rate. In [318] this was done (for zero momentum) by resummation, to obtain an HTL improved annihilation rate. The authors of Ref. [318] conclude, that at low energies (order of thermal quark mass) the HTL resummed rate is larger by orders of magnitude compared to the Born rate. In Refs. [319] the dilepton rate for hard invariant masses ($M \geq \pi T$) at NLO was presented including extrapolation to finite three-momentum. At very soft invariant masses, $M \ll \pi T$, the dilepton rate must include an LPM resummation. This has been done at LO in Ref. [297] and been connected to the hard ($M \geq \pi T$, [319]) NLO computation in Ref. [320]. In Ref. [321] the dilepton rate at soft invariant masses was computed at NLO, with an increase of 30% – 40% with respect to the LO calculation. In lattice QCD, dilepton rates can only be computed at discrete temperatures. In quenched QCD, no significant temperature dependence was found [149]. An overview about the existing rates and also effective hadronic models can be found in Ref. [86].

10.2. Temperature fits

In Ref. [116] it was proposed to use the invariant mass spectrum as a *thermometer* of the medium. It does not suffer from Lorentz boost distortion (since the mass is the same in all frames) thus will give an average local rest frame temperature. In the intermediate mass range ($1 < M/\text{GeV} < 3$), medium effects on the spectral function are small ($\mathcal{O}(T^2/M^2)$), and a suitable fit function (fit parameters x_1, x_2) is given as

$$\frac{dR}{dM} = x_1 (M x_2)^{3/2} e^{-M/x_2}, \quad (10.8)$$

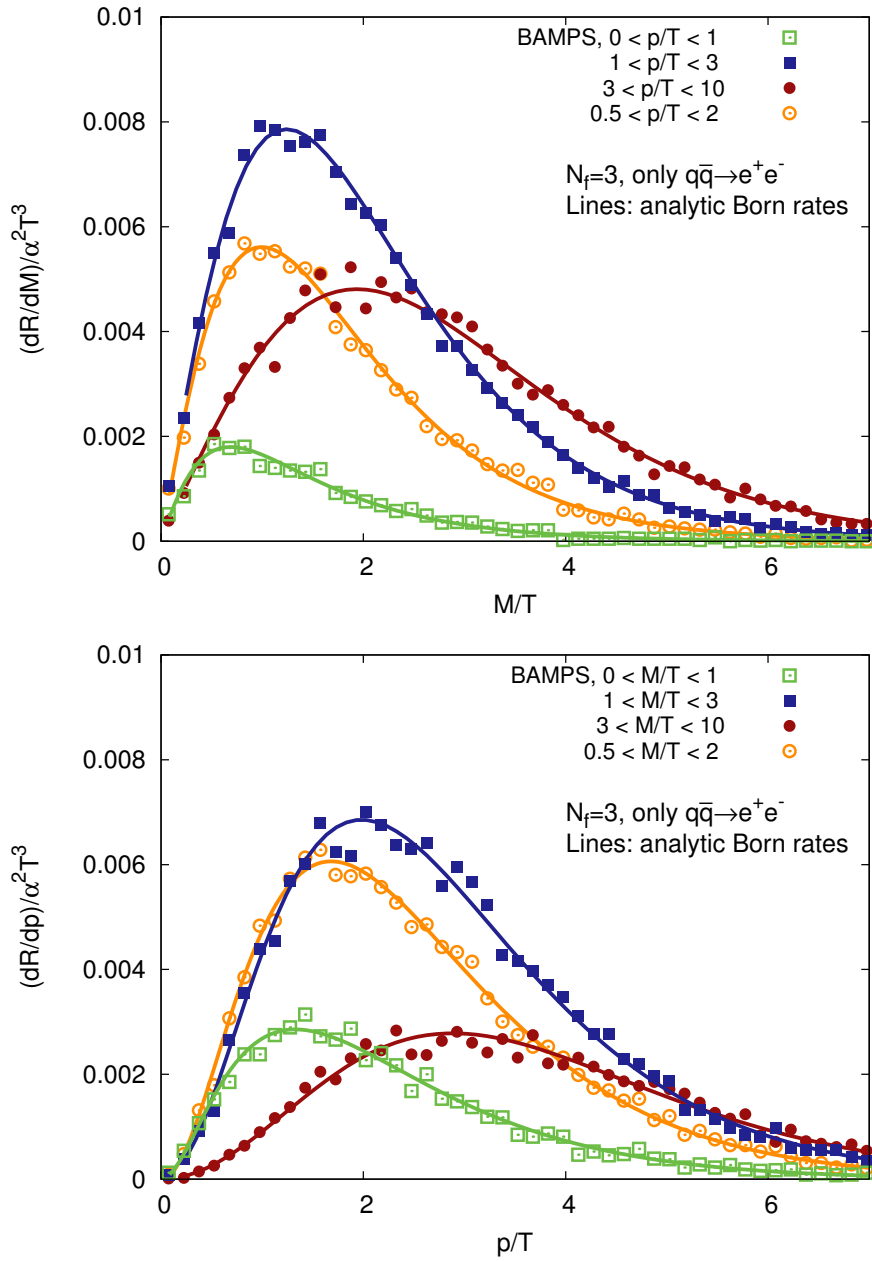


Figure 10.1.: Dilepton production rate differential in momentum p and invariant mass M from BAMPS compared to the analytic rate from Eq. (10.5).

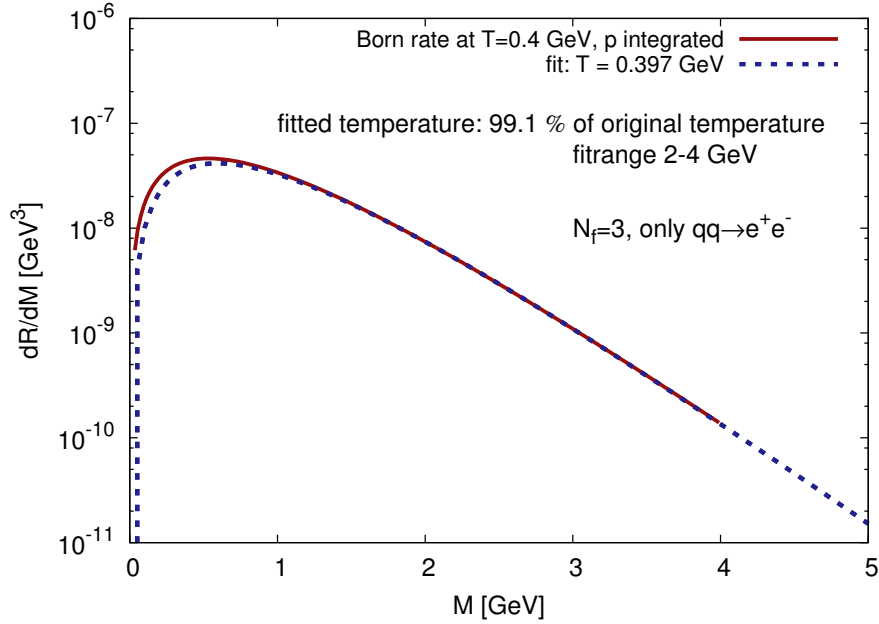


Figure 10.2.: Fit of an equilibrium invariant mass spectrum by using the fit function from Eq. (10.8). In the fitrange $5 < M/T < 10$, the temperature is reproduced by more than 99 %.

where the temperature is identified as $T \equiv x_2$ and x_1 is a unitless fit parameter without important relevance. We test this scheme with the analytic rate from Eq. (10.5) at $T = 0.4$ GeV in Fig. 10.2, where the fitrange is chosen from 2 – 4 GeV. Especially at low invariant mass, the fit deviates from the analytic rate, but in the intermediate mass fit range, it is acceptable. Using BAMPS, we calculate invariant mass spectra of dileptons in heavy-ion collisions. The result for Au+Au collisions at RHIC energies $\sqrt{s} = 200$ GeV is shown in Fig. 10.3 for six different times within the QGP evolution. We also show fits of those spectra, using Eq. (10.8) and their corresponding temperatures. The temperatures are higher than the temperatures extracted at certain space-time points of the collision, e.g., in Fig. 9.1. The comparison is however not entirely meaningful, since the dilepton fits give space-time averaged temperatures, and not a local temperature. We stress that this average is weighted by the local emission rates. The method using dilepton fits constitutes an independent check of an averaged temperature, weighted by the effective dilepton emission rates, and can serve as an (experimental) thermometer of the fireball.

10.3. Conclusion

We have shown how to correctly implement leading order dilepton production within the transport model BAMPS. We use the simple Born approximation, which includes the tree-level annihilation diagram. In an equilibrium setup, the invariant mass spectrum can be fitted with a simple parameterization, where one fitparameter yields the background temperature with great accuracy. As an example of application, we compute dilepton emission in a heavy-ion setup, where we are also able to extract temperatures by fitting. Dilepton phenomenology however focuses in most studies on the hadronic emission rates and their medium modifications. It would be certainly interesting in future to differentially compute azimuthal dilepton correlation functions, and more precise spectra. Especially at the highest energies of LHC the QGP should contribute much to those observables, and

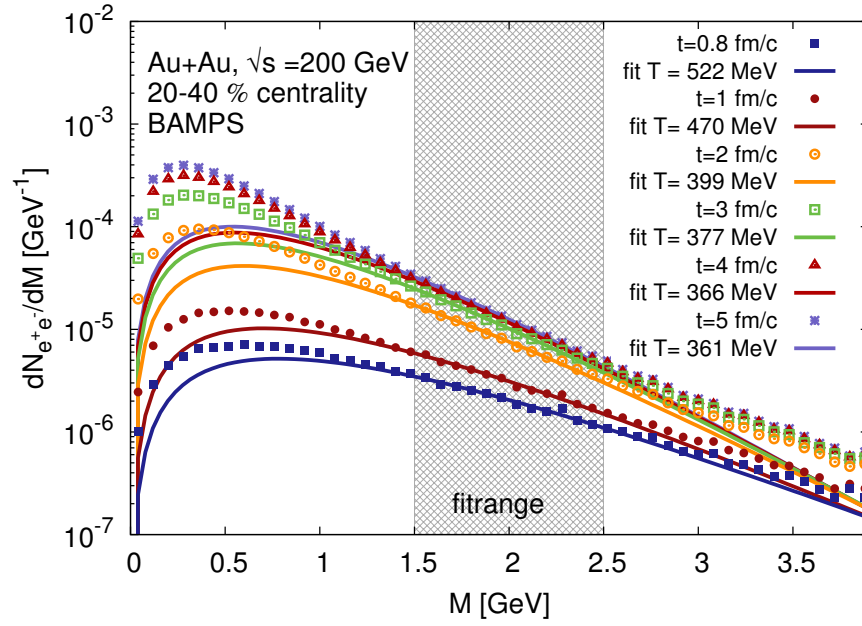


Figure 10.3.: Invariant mass spectra of dileptons at $\sqrt{s} = 200$ GeV Au+Au collisions from BAMPS for different lab times. Each spectrum is fitted by Eq. (10.8), giving averaged temperatures from 522 MeV to 361 MeV.

the use of BAMPS could give important supplementary information to coarse-graining, hydrodynamics, or other transport approaches.

11. Initial and final state effects in p+Pb collisions

In this chapter we introduce several new concepts and improvements in the modeling of high energy hadronic collisions, using proton-lead collisions as one important application.

We are pursuing a number of goals. First, we are developing the partonic cascade BAMPS (presented earlier in this thesis) further by including new analysis methods, a new initial state and novel event-by-event processing. We use this model to simulate proton-lead collisions at $\sqrt{s_{NN}} = 5$ TeV (LHC energies), touching the rich phenomenological questions behind these small systems. The presented results aim at understanding its dynamic nature, which has gained enormous interest in the community in the past years.

The Discovery of pronounced azimuthal two-particle correlations at large rapidity distances in small systems (p+p and p+Pb collisions) raised the question whether those can be attributed to a collective, multiparticle effect. In small systems, the measured long-range correlations are at first glance reminiscent to those observed in central and mid-central heavy-ion collisions, however, the size of the heavy-ion collision region is much larger. In heavy-ion collisions, the collective, hydrodynamic behavior is considered certain. It may also be, that initial state gluon saturation is mostly responsible for the momentum asymmetries.

Our novel methodology includes for the first time initial and final state interactions and should also be seen as a baseline for future projects and other applications not only for electromagnetic probes. We are now able to carry out a systematic multiplicity scan, probing the dynamics on the border of initial state dominated to final state dominated - but not yet fully developed hydrodynamic regime. The goal is to predict at which multiplicity and transverse momentum many-body QCD effects in the initial state can be experimentally unveiled.

Large parts of this chapter are published and reproduced from Ref. [5]. It is organized as follows. First, we give a concise overview of experimental efforts at the LHC. We then highlight in more detail the purpose of the present study before explaining the implementation of initial and final state interactions. After presenting the analysis method (which resembles that used in experiment), we show our results for p_T dependent and integrated two-particle correlation elliptic flow. After that, we show fragmented results and give an outlook of what can be done now, having set the stage with this model, and conclude the chapter.

11.1. Overview of experimental results

Beginning in 2013, the experimental collaborations ALICE, ATLAS and CMS published their measurements on correlations in small systems. In this section we summarize experimental results at the LHC mainly focusing on two particle $\Delta\eta - \Delta\phi$ correlation functions in p+Pb collisions at nucleon-nucleon center-of-mass energy of 5.02 TeV, however, also up to eight particle correlations can be measured. Often, the correlation functions are expanded in Fourier harmonics, v_n , which have a direct connection in hydrodynamics. The elliptic flow v_2 in hydrodynamics reflects directly the initial geometry of nuclear collisions and

the triangular flow v_3 the initial fluctuations. Experimental analyses thrive to subtract non-flow effects, such as back-to-back jets, by working with multi-particle cumulants or alternative methods such as Lee-Yang zeros method [322].

Two-particle correlations are measured usually as function of the difference in azimuthal angle ϕ of the momenta of charged particles, $\Delta\phi$, as well as their difference in pseudorapidity¹ $\Delta\eta$. It is very important to also differentiate between different multiplicities in small systems, to smoothly sweep over from (high-multiplicity) heavy-ion collision picture to low-multiplicity events (a p+p picture).

11.1.1. Multiplicity classes

In proton-lead collisions, the traditional event selection based on the geometrical impact parameter b is not practical any more. Instead, events are categorized in event classes corresponding to their average number of particles, or transverse energy, within certain kinematic ranges. In Tab. 11.1.1 we list common methods in classifying the multiplicity along with the most important publications of three collaborations at the LHC.

Experiment	Selection Observable	Event classes	Publication
ALICE	mid-rapidity multiplicity $\langle dN_{\text{ch}}/d\eta \rangle$, $ \eta < 0.5$	4	[323]
ATLAS	transverse energy Σ_T^{Pb}	12	[324]
ATLAS	transverse energy Σ_T^{Pb}	6	[325]
ATLAS	transverse energy Σ_T^{Pb} , particles $N_{\text{ch}}^{\text{rec}}$	23	[326]
CMS	reconstructed track multiplicity $N_{\text{trk}}^{\text{offline}}$	5	[327]
CMS	reconstructed track multiplicity $N_{\text{trk}}^{\text{offline}}$	15	[328]

Table 11.1.: Summary of important experimental publications on p+Pb collisions with their event selection observable and the used number of classes.

11.1.2. Experimental results

The three collaborations make use of a similar methodology, but due to the different hardware setups, they have different capabilities in extracting multi-particle correlation functions. Here we outline their individual results.

ALICE

The two particle correlation is computed as associated measured yield per trigger particle for $\sqrt{s_{NN}} = 5.02$ GeV by ALICE [323, 329]. In the kinematic range $0.5 < p_T/\text{GeV} < 4$, $|\eta| < 1.2$ for trigger and associated particles, ALICE sees a strong correlation around $\Delta\eta \approx 0$, $\Delta\phi \approx 0$ stemming from particles in the same jet. At $\Delta\phi \approx \pi$ an enhanced correlation for all $\Delta\eta$ is observed, interpreted as coming from particles with momenta back-to-back in azimuth. It is found that low-multiplicity p+Pb events have similar correlation results as p+p events and the correlation strength increases with multiplicity. Once the results of low-multiplicity events are subtracted from those at high-multiplicity, two “ridges” (enhanced correlation in a range of $\Delta\eta$, “long-range”) appear which are nearly identical at the “near-side” (around $\Delta\phi \approx 0$) and the “away-side” ($\Delta\phi \approx \pi$). The average transverse momentum $\langle p_T \rangle$ increases stronger with the total number of charged particles in p+Pb and p+p collisions than in Pb+Pb collisions.

¹The pseudorapidity is defined as $\eta = -\ln(\tan[\theta/2])$, with polar angle θ between the beam direction and the particle momentum.

CMS

The two-particle correlation function in $-4.8 < \Delta\eta < 4.8$ and full azimuth was measured by CMS for p+Pb collisions in different p_T ranges and for different track multiplicities [327]. The measurable absolute pseudorapidity range is $|\eta| < 2.5$. At low track multiplicity, $N_{\text{trk}}^{\text{offline}} < 35$, a narrow jet peak is seen at $\Delta\eta \approx 0$, $\Delta\phi \approx 0$ as well as a broader peak (extended in $\Delta\eta$) from back-to-back particles at the away-side, $\Delta\phi \approx \pi$, similar as in the ALICE experiment. These phenomena are well understood and also appear at higher multiplicities. At $N_{\text{trk}}^{\text{offline}} > 115$, a near-side ($\Delta\eta \approx 0$) long-range ($\Delta\eta > 4$) ridge is very pronounced. This structure is not as well understood². In very high-multiplicity p+p collisions this was observed by CMS [330]. Averaging over $\Delta\eta$, the correlation in $\Delta\phi$ was investigated for several p_T ranges and multiplicities. The long-range near-side correlation increases for higher multiplicities, and can only be seen above $N_{\text{trk}}^{\text{offline}} > 35$, being largest for $1 < p_T/\text{GeV} < 2$. In p+Pb collisions it is always higher than in p+p. In Ref. [328], the measurement of CMS was extended to study a larger sample of high-multiplicity events. The integrated yield of the long-range near-side ridge³ was studied as function of transverse momentum up to $p_T \sim 11$ GeV and multiplicity up to $N_{\text{trk}}^{\text{offline}} \sim 350$, which corresponds to mid-central Pb+Pb collisions. It is found, that in p+p, p+Pb and Pb+Pb collisions the long-range near-side ridge builds up above $N_{\text{trk}}^{\text{offline}} \gtrsim 40 - 50$. In Pb+Pb collisions it is about two times higher than in p+Pb, but in both systems it rises with multiplicity, and the maximum is seen in a bin around trigger particle transverse momentum of $2 < p_T^{\text{trig}}/\text{GeV} < 3$. A Fourier decomposition of the $\Delta\phi$ correlation function gives the elliptic and triangular flow coefficients, which were also measured by a four-particle cumulant analysis. Several methods are used to reduce jet-like correlations and other non-flow components. This was done for p_T differential v_2 and v_3 as well as for p_T integrated flow coefficients as function of multiplicity. The main findings are, that at low p_T , the elliptic flow coefficient is about 30% higher in Pb+Pb than in p+Pb. The v_3 is consistently smaller than v_2 , but in all cases the maximum is at $p_T \sim 2 - 3$ GeV. As function of increasing multiplicity, the p_T integrated v_2 increases slowly in Pb+Pb collisions whereas in p+Pb it is almost constant (above $N_{\text{trk}}^{\text{offline}} \gtrsim 120$). The collective origin of the strong v_2 signal was further supported by using a 6 and 8-particle cumulant method by CMS in Ref. [331]. A very detailed and recent study was presented in Ref. [332].

ATLAS

ATLAS has done an independent study of the $\Delta\eta - \Delta\phi$ correlation at a slightly higher range in pseudorapidity than ALICE or CMS, $|\Delta\eta| < 5$. ATLAS characterizes the event activity by the sum of the transverse energy in the calorimeter at the lead-going side, $\sum E_T^{\text{Pb}}$. In Ref. [324], results for 12 multiplicity classes were presented. Some of them were combined to two effective multiplicity classes: central events with $\sum E_T^{\text{Pb}} > 80$ GeV, corresponding to $\langle dN_{\text{ch}}/d\eta \rangle \sim 30$ and $\sum E_T^{\text{Pb}} < 20$ GeV, corresponding to $\langle dN_{\text{ch}}/d\eta \rangle \sim 5$. ATLAS sees the near-side jet peak as CMS and ALICE, and explicitly a broadening of the away-side ridge from low to high-multiplicity. With higher multiplicity, the near-side peak (ridge) appears, consistent with the CMS results, and the away-side peak grows in a similar shape with increasing $\sum E_T^{\text{Pb}}$. This was concluded by integrating the 2D-correlation in $2 < |\Delta\eta| < 5$ as a function of multiplicity. By doing a Fourier-type decomposition, it was found that the long-range component contains a back-to-back (recoil) component and a $\Delta\phi$ component symmetric around $\pi/2$. The difference between central to peripheral events

²In Pb+Pb collisions, it is also seen, and attributed to hydrodynamic flow patterns.

³The two-particle correlation function integrated over $-1.2 < \Delta\phi < 1.2$, $|\Delta\eta| > 2$ or $|\Delta\eta| < 1$ (the latter selects the jet-structure).

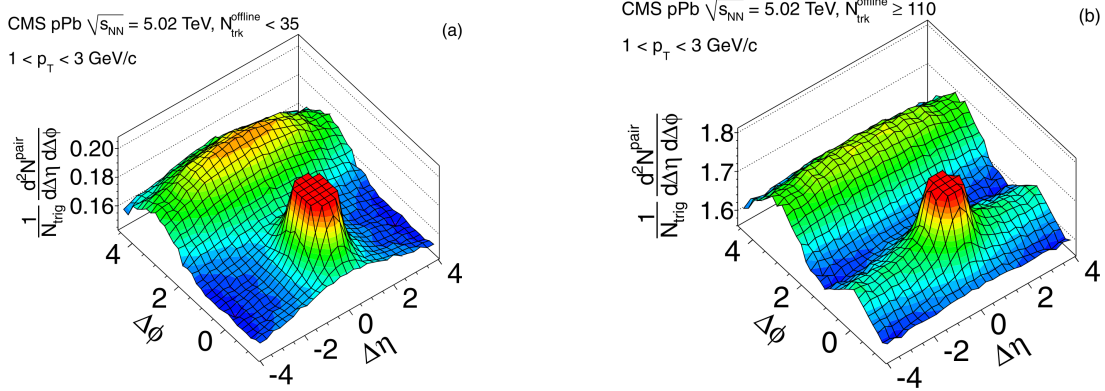


Figure 11.1.: Two-particle correlation function $1/N_{\text{trig}} dN^{\text{pair}}/d\Delta\eta d\Delta\phi$ for charged particles, normalized to the number of trigger particles, N_{trig} , from the CMS experiment [327]. Left: low-multiplicity event, $N_{\text{trk}}^{\text{offline}} < 35$, the near-side long-range correlation is absent. Right: the near-side long-range correlation is very pronounced.

in the near-side and away-side correlation has a similar p_T dependence, and a maximum at $p_T \approx 3 - 4$ GeV. The near-side ridge has a maximum around $p_T \approx 2 - 4$ GeV. ATLAS concludes in Ref. [324] that their results are consistent with final-state effects exhibiting collective features. In Ref. [325] the measurement was extended to two and four particle cumulants, $c_2\{2\}$ and $c_2\{4\}$, and p_T differential and integrated elliptic flow v_2 .

11.2. Purpose of the present study

A fluctuating initial geometry in peripheral A+A collisions, to first order elliptic (but dominated by fluctuating nucleon positions in the incoming nuclei) is known to be converted due to hydrodynamic pressure gradients into anisotropic momentum space distributions. Hydrodynamic simulations agree well with a wide range of experimental observables at RHIC and LHC [56–59].

As summarized in the previous section, measurements in smaller collision systems such as p+p and p+A, in particular those of multi-particle correlation functions, have shown very similar features as in heavy-ion collisions (see also Ref. [333] for a review). While calculations within the hydrodynamic framework have also been quite successful in describing observables in p+p and p+A collision systems [98, 334, 335], alternative explanations relying entirely on intrinsic momentum correlations of the produced particles can also reproduce many features of the experimental data. This includes two and more particle azimuthal correlations and their p_T dependence [333, 336, 337] and mass splitting of identified particle v_n [338]. Apart from the existence of alternative explanations, the applicability of hydrodynamics becomes increasingly doubtful as the system size decreases and gradients increase. Some recent studies argue that hydrodynamics should be applicable in systems of sizes down to ~ 0.15 fm [339], but off-equilibrium corrections to particle distribution functions for momenta $p_T \gtrsim 0.5$ GeV can be significant [335], which limits at least the quantitative reliability of the framework.

So far all calculations of multi-particle correlations in small collision systems have studied either only intrinsic momentum correlations or purely final state driven effects. Here we present the first study where both effects are combined into a single framework to assess their relative importance.

In ultrarelativistic heavy-ion collisions, the initial state is defined as the immediate reactions once the nucleons of both nuclei have merged. One speaks of initial state physics within the first $\tau \approx 0.2 - 0.6$ fm/c after the first nucleon-nucleon contact. After the initialization of the collision event, a non-equilibrium phase leads the system to local thermal equilibrium, given that the system is dense enough and its lifetime long enough. Thermalization is intimately connected to the nature of the initial state.

In this chapter we show results obtained by using a color glass condensate initial model combined with a partonic cascade for the evolution of the QGP. The latter is then evolved until fragmentation, which leads to hadronic observables that can be measured in experiment.

To this end we compute initial state gluon Wigner-distributions from the Impact Parameter dependent Glasma model (IP-Glasma) [340, 341] and via sampling of individual gluons feed them into the partonic transport simulation 'Boltzmann approach to multiparton scatterings' (BAMPS) [40]. The initial gluon distributions [342, 343] from the IP-Glasma model are anisotropic in momentum space [338, 344, 345], thus contain the intrinsic momentum space correlations of the color glass condensate (CGC) picture [346, 347]. Final state interactions mediated by perturbative quantum chromo dynamic (pQCD) cross sections are then simulated microscopically in BAMPS. We analyze the time evolution of the momentum space anisotropy of the partonic plasma by simulating events in two different multiplicity classes to understand how final state interactions modify initial state momentum correlations and whether signals of the latter can survive to affect final observables.

11.3. Initial state & phase-space distribution

Based on the IP-Glasma model, including event-by-event fluctuations of the proton's geometrical structure [348], we calculate the solution to the classical Yang-Mills equations of motion up to $\tau_0 = 0.2$ fm/c following the standard procedures described in [340, 341]. Event-by-event we extract the Wigner distribution $\frac{dN_g}{dyd^2\mathbf{x}_T d^2\mathbf{p}_T}$ in hyperbolic phase-space coordinates $x^\mu = (\tau \cosh \eta_s, \mathbf{x}_T, \tau \sinh \eta_s)$, $p^\mu = (|\mathbf{p}_T| \cosh y, \mathbf{p}_T, |\mathbf{p}_T| \sinh y)$, by evaluating equal time correlation functions in Coulomb gauge and projecting them onto the transversely polarized mode functions $\xi_{\mathbf{p}_T}^{(\lambda)}(\tau)$ of the free theory according to (details and notation can be found in Ref. [349])

$$\begin{aligned} \frac{dN_g}{dyd^2\mathbf{x}_T d^2\mathbf{p}_T} &= \frac{1}{(2\pi)^2} \sum_{\lambda=1,2} \sum_{a=1}^{N_c^2-1} \tau^2 g^{\mu\mu'} g^{\nu\nu'} \\ &\times \int d^2\mathbf{s} \left(\xi_{\mathbf{p}_T, \mu}^{(\lambda)*}(\tau) i \overleftrightarrow{\partial}_\tau A_{\mu'}^a(\mathbf{x}_T + \mathbf{s}/2) \right) \\ &\quad \left(A_{\nu'}^a(\mathbf{x}_T - \mathbf{s}/2) i \overleftrightarrow{\partial}_\tau \xi_{\mathbf{p}_T, \nu}^{(\lambda)}(\tau) \right) e^{-i\mathbf{p}_T \cdot \mathbf{s}}. \end{aligned} \quad (11.1)$$

Even though the position and momentum dependent Wigner distribution includes all relevant information about the initial state coordinate space eccentricity as well as the initial state momentum space anisotropies, it suffers from the deficiency that it is not necessarily positive semi-definite. To warrant a probabilistic interpretation of a quasi-particle distribution entering the subsequent Boltzmann transport simulation, it is necessary to perform a smearing of the Wigner distribution over phase space volumes $\sigma_x \sigma_p \geq \hbar/2$. Accounting for the boost-invariant nature of the classical Yang-Mills fields the single particle distribution function f_0^g , which will enter the subsequent parton cascade, is obtained by

performing the Gaussian smearing

$$f_0^g(\mathbf{x}_T, \eta_s, \mathbf{p}_\perp, y) = \frac{(2\pi)^3}{2(N_c^2 - 1)} \frac{\delta(y - \eta_s)}{|\mathbf{p}_T| \tau} \quad (11.2)$$

$$\times \int \frac{d^2 \mathbf{x}'_T d^2 \mathbf{p}'_T}{(2\pi)^2} e^{-\frac{(\mathbf{x}_T - \mathbf{x}'_T)^2}{2\sigma_x^2}} e^{-\frac{(\mathbf{p}_T - \mathbf{p}'_T)^2}{2\sigma_p^2}} \frac{dN_g}{dy d^2 \mathbf{x}'_T d^2 \mathbf{p}'_T},$$

with $\sigma_x = 0.197$ fm and $\sigma_p = 1$ GeV chosen to achieve a reasonable compromise between spatial and momentum resolution.

11.4. Final state interactions

Even though the classical Yang-Mills evolution includes re-scattering effects at early times, the semi-classical description of the dynamics becomes inapplicable after a relatively short time when quantum effects become important and the subsequent dynamics is more appropriately described in terms of weakly interacting quasi-particles [349–351]. We simulate the dynamics within $0.2 \text{ fm}/c < \tau < 2.0 \text{ fm}/c$, with a 3+1-dimensional Boltzmann approach to multi-parton scatterings (BAMPS), which, starting from the initial phase-space density of gluons in Eq. (11.2), solves the relativistic Boltzmann equation

$$p^\mu \frac{\partial}{\partial x^\mu} f^i(x, p) = \sum_{j=g,q,\bar{q}} C_{ij}(x, p), \quad (11.3)$$

for the phase-space distribution function $f^i(x, p)$ of massless on-shell quarks, anti-quarks and gluons by Monte-Carlo techniques [40, 214, 236]⁴. The collision integrals C_{ij} include $2 \leftrightarrow 2$ and $2 \leftrightarrow 3$ interactions, based on perturbative QCD matrix elements (using a fixed strong coupling constant $\alpha_s = 0.3$) where internal propagators are regulated by a dynamically computed screening mass $m_D^2 \sim \alpha_s \int d^3 p f^i(x, p)/p$ (see, e.g., Refs. [217, 218]). Inelastic $2 \leftrightarrow 3$ interactions are simulated based on the improved Gunion-Bertsch matrix elements [217], and the Landau-Pomeranchuk-Migdal (LPM) effect is treated effectively, based on a dynamically determined mean free path [218].

Since in practice the Monte-Carlo implementation is based on individual particles, propagating along straight lines between scattering events, one needs to supply a list of particle positions x_{Init}^μ and momenta p_{Init}^μ as initial condition for BAMPS. For every event we sample a collection of individual gluons from the momentum distribution $f_0^g(\mathbf{x}_T, \eta_s, \mathbf{p}_T, y)$ of the IP-Glasma model, such that the overall number of gluons is given by the integral of the distribution. Since according to Eq. (11.2) the initial momentum rapidity y is equal to the coordinate space rapidity η_s , which we sample uniformly between $-2 < \eta_s < 2$ from the boost invariant distribution, the initial position and momentum vectors of each particle are given by $x_{Init}^\mu = (\tau_0 \cosh(\eta_s), \mathbf{x}_T, \tau_0 \sinh(\eta_s))$ and $p_{Init}^\mu = (|\mathbf{p}_T| \cosh(\eta_s), \mathbf{p}_T, |\mathbf{p}_T| \sinh(\eta_s))$.

We have checked explicitly, that the energy density ($T^{\tau\tau}$) and flow coefficients (v_2) extracted from the sampled particle ensemble agree well with the corresponding quantities extracted directly from the IP-Glasma distribution. Even though the IP-Glasma initial condition is boost invariant, the BAMPS calculation is performed in 3+1 dimensional Minkowski space. We will therefore extract all observables at $|y| < 0.5$ for different lab times t , where $y = \log[(E + p_z)/(E - p_z)]/2$, noting that at midrapidity $|y| \approx |\eta_s| \approx 0$ such that the lab time $t \approx \tau$.

⁴Even though the IP-Glasma initial state only contains gluons, quarks and anti-quarks are produced during the kinetic evolution of the fireball.

11.5. Evolution of azimuthal anisotropies

We investigate the evolution of the azimuthal momentum space anisotropy characterized by the Fourier harmonics $v_n\{2PC\}$ of the two-particle correlation function. We follow the experimental analysis [328] in decomposing the (normalized) two-particle correlation function for N_{trig} trigger particles in a momentum range given by p_T^{ref} and N_{assoc} particles in a momentum bin around p_T , in Fourier harmonics w.r.t. the relative azimuthal angle $\Delta\varphi_{p_T}$:

$$\frac{2\pi}{N_{\text{trig}}N_{\text{assoc}}}\frac{dN^{\text{pair}}}{d\Delta\varphi_{p_T}}(p_T, p_T^{\text{ref}}) = 1 + \sum_n 2V_{n\Delta}(p_T, p_T^{\text{ref}})\cos(n\Delta\varphi_{p_T}). \quad (11.4)$$

The two particle $v_2\{2PC\}$ is obtained as [328]

$$v_n\{2PC\}(p_T) = \frac{V_{n\Delta}(p_T, p_T^{\text{ref}})}{\sqrt{V_{n\Delta}(p_T^{\text{ref}}, p_T^{\text{ref}})}}, \quad (11.5)$$

with the reference momentum range chosen as $0 \text{ GeV} < p_T^{\text{ref}} < 8 \text{ GeV}$ by default⁵. Since in our model the double-inclusive spectrum in each event is given by the product of single inclusive spectra, we follow [345, 352] and directly compute

$$V_{n\Delta}(p_T, p_T^{\text{ref}}) = \left\langle \text{Re} \frac{b_n(p_T)b_n^*(p_T^{\text{ref}})}{b_0(p_T)b_0^*(p_T^{\text{ref}})} \right\rangle_{\text{events}} \quad (11.6)$$

where in each event $b_n(p_T) = \int \frac{d\phi_{p_T}}{2\pi} \frac{dN_g}{d^2\mathbf{p}_T} e^{in\phi_{p_T}}$ is the azimuthal Fourier coefficient of the single-inclusive spectrum. Since our model does not include correlations from back-to-back di-jet pairs, we also note that – contrary to the experimental analysis – no additional subtractions are required to eliminate such correlations.

Including both initial state effects and final state evolution, we analyze the time evolution of the momentum space anisotropy $v_2\{2PC\}(p_T)$ for $\sqrt{s_{pA}} = 5.02 \text{ TeV}$ p+Pb collisions in Fig. 11.2. We show $v_2\{2PC\}(p_T)$ at different times, $t = 0.2$ (initial), 0.4, 0.6, 1, 2 fm/c for the following event classes:

low-multiplicity: $0.5 < (dN_g/dy) / \langle dN_g/dy \rangle < 1$

high-multiplicity: $(dN_g/dy) / \langle dN_g/dy \rangle > 2.5$.

While in both cases momentum correlations lead to a sizeable initial state v_2 [345], the subsequent dynamics is quite different: In high-multiplicity events, we observe a pronounced effect of the final state interactions such that the high initial anisotropy at intermediate momenta ($p_T \sim 2 - 5 \text{ GeV}$) is significantly reduced within the first 0.2 fm/c evolution in the parton cascade, while at the same time the correlation strength at higher and lower momenta begins to increase. Subsequently, the azimuthal anisotropy increases for all p_T up to maximally 5%. As a result, the pronounced peak at around $p_T \sim 3 \text{ GeV}$, present after the IP-Glasma stage, is washed out by the final state interactions. In contrast, for low-multiplicity events modifications due to final state effects appear to be less significant,

⁵Because we are studying the momentum anisotropy of gluons, we choose the reference momentum to extend to larger values than the range used in the experimental analysis.

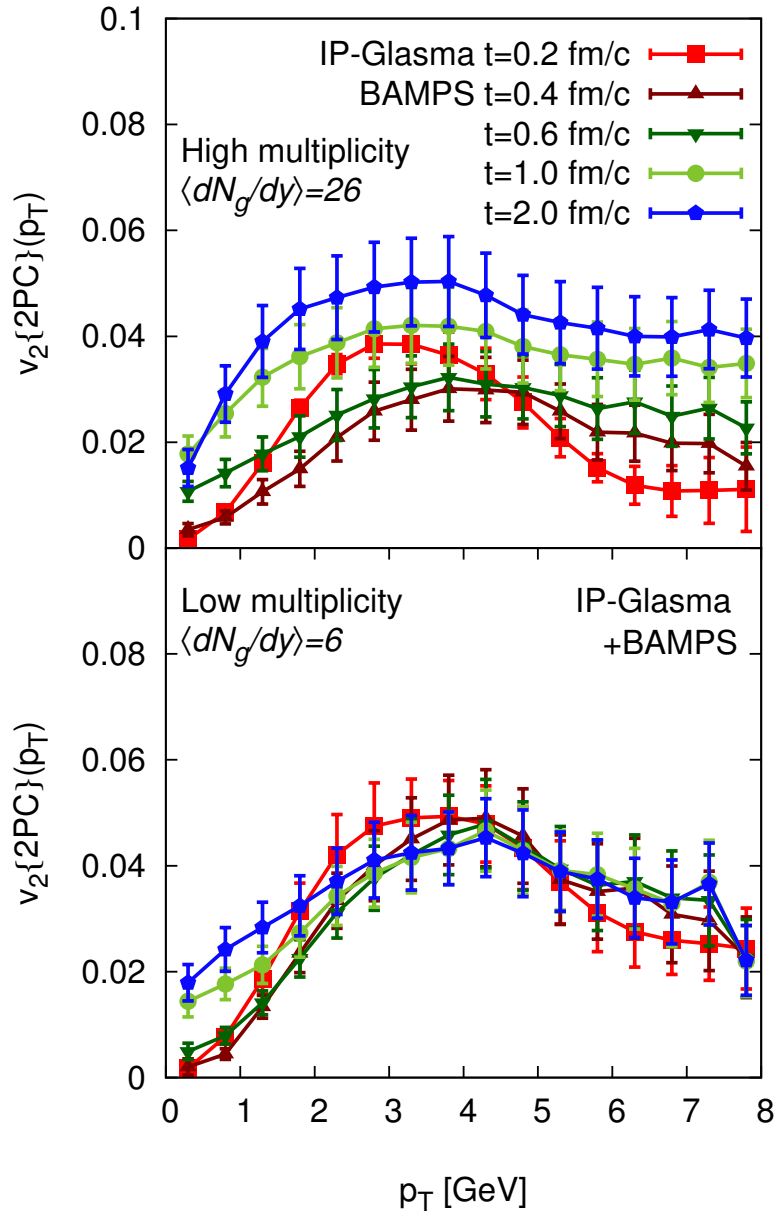


Figure 11.2.: Gluon $v_2\{2PC\}(p_T)$ at mid-rapidity ($|y| < 0.5$) for different times in high-multiplicity ($\langle dN_g/dy \rangle = 26$, upper panel) and low-multiplicity ($\langle dN_g/dy \rangle = 6$, lower panel) p+Pb collisions.

as the final curve $v_2(p_T)$ closely resembles that of the IP-Glasma initial state. Only at low transverse momenta, $p_T \lesssim 2$ GeV the azimuthal anisotropy is increased to 2 – 3 %.

While our results confirm the basic expectation that final state effects gain significance as the density of the medium increases in high-multiplicity events [336, 353], the way this is realized dynamically is in fact very interesting. We find that the average number of interactions in low-multiplicity events ($N_{\text{scat}} = 4.5 \pm 1.1$) is indeed almost the same as in high-multiplicity events ($N_{\text{scat}} = 5.6 \pm 1.1$). Because of the nature of the QCD cross sections, most interactions however correspond to small momentum transfers $\sim m_D$ which itself depends on the density of the medium [278], such that the average momentum transfer is larger in high-multiplicity events. Hence, the average number of *large angle scatterings*, estimated according to $N_{\text{scat}}^{\text{large angle}} = \frac{1}{N_{\text{particles}}} \sum_{\text{coll}} \frac{3}{2} \sin^2 \theta_{\text{c.o.m.}}^{\text{coll}}$ where $\theta_{\text{c.o.m.}}^{\text{coll}}$ is the scattering angle in the c.o.m. frame of the partonic interaction⁶, is in fact significantly larger in high-multiplicity events ($N_{\text{scat}}^{\text{large angle}} = 1 \pm 0.18$) as compared to low-multiplicity events ($N_{\text{scat}}^{\text{large angle}} = 0.53 \pm 0.14$).

Initial state vs. final state effects. In order to further disentangle the effects of initial state momentum correlations and final state response to geometry, we performed an additional set of simulations (henceforth labeled rand. azimuth) where the azimuthal angle of the transverse momentum \mathbf{p}_T of each gluon is randomized ($0 < \varphi_{p_T} < 2\pi$) before the evolution in the parton cascade. Our results are compactly summarized in Fig. 11.3, where we compare the azimuthal anisotropy $v_2\{2PC\}(p_T)$ in the different scenarios. By construction no initial state momentum correlations are present in the rand. azimuth case – shown as open gray symbols – and the initial state v_2 vanishes identically at $t = 0.2$ fm/c. However, over the course of the kinetic evolution a $v_2(p_T)$ of $\sim 4\%$ at $p_T \sim 2$ GeV in high-multiplicity events and $\lesssim 3\%$ at $p_T \sim 1$ GeV in low-multiplicity events is built up by $t = 2.0$ fm/c. Nevertheless, for momenta above $p_T \sim 2.0$ GeV (low-multiplicity) and $p_T \sim 4.0$ GeV (high-multiplicity), the purely final state v_2 in the rand. azimuth scenario remains significantly below the initial state + final state v_2 of the full calculation, indicating the importance of initial state momentum correlations.

Despite the fact that initial state correlations have a significant impact on $v_2\{2PC\}$, we find that the additional $v_2\{2PC\}$ built up in the parton cascade can be attributed to the response to the initial geometry. In order to demonstrate this feature more clearly, we have also computed the azimuthal anisotropy $v_2\{\text{ecc. plane}\}$ w.r.t to the coordinate eccentricity plane – obtained by replacing the reference momentum vector $b_n(p_T^{\text{ref}})$ in Eq. (11.6) with the coordinate eccentricity vector $e_n = \int d^2\mathbf{x}_T T^{\tau\tau}(\mathbf{x}_T) |\mathbf{x}_T|^n e^{in\phi_{x_T}}$, where ϕ_{x_T} is the azimuthal angle in space. Our results in Fig. 11.4 show that the initial anisotropy with respect to the geometric eccentricity plane vanishes, as the initial momentum space anisotropy is uncorrelated with the event geometry [345].

In contrast, during the kinetic evolution a clear correlation with the initial state geometry is built up. The magnitude of this final state generated $v_2\{\text{ecc. plane}\}$ depends only weakly on the presence or absence of initial state momentum correlations. While the comparison of the results for $v_2\{\text{ecc. plane}\}$ (Fig. 11.4) with $v_2\{2PC\}$ (Fig. 11.3) indicates that in the rand. azimuth case, the observed $v_2\{2PC\}$ can almost entirely be attributed to a geometric response, this is clearly not the case for the more realistic scenario including initial state correlations.

Even though the effects of initial state momentum correlations are more apparent in low-multiplicity events, quantitative differences remain also in high-multiplicity events, as

⁶Note that the pre-factor 3/2 is chosen such that for constant isotropic cross sections $N_{\text{scat}}^{\text{large angle}} = N_{\text{scat}}$.

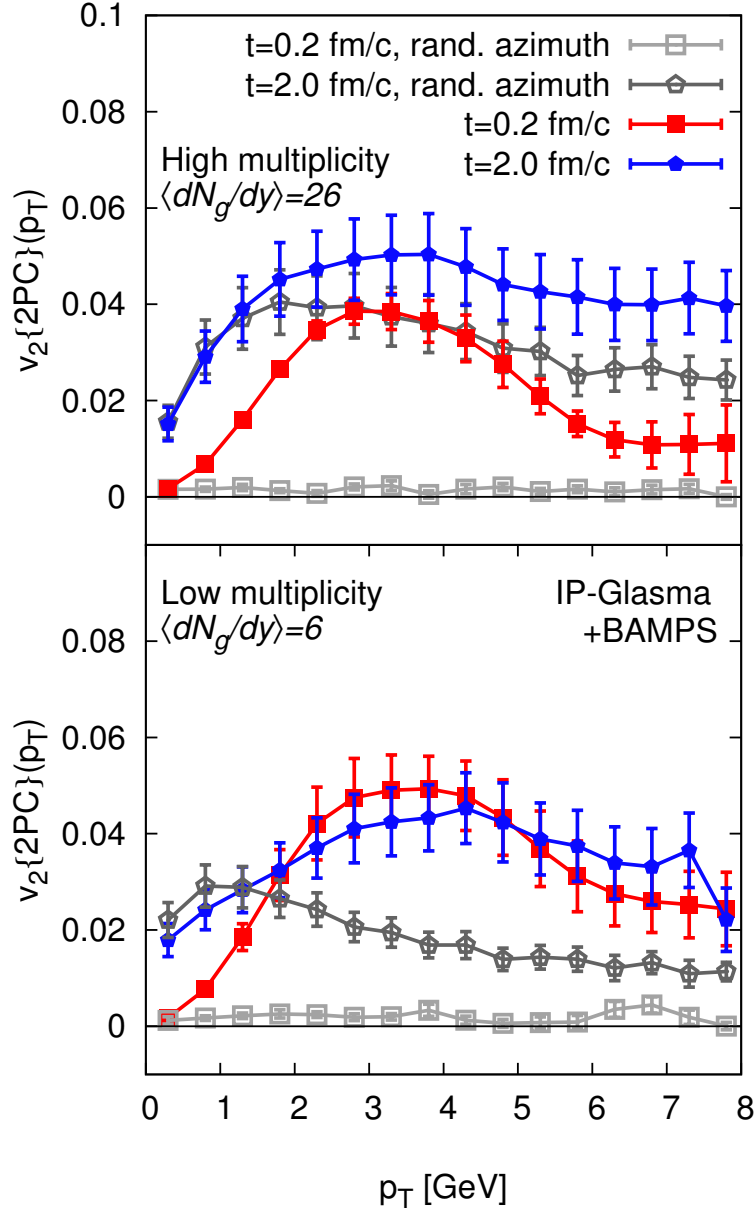


Figure 11.3.: Comparison of initial and final two-particle $v_2(p_T)$ for high (upper panel) and low (lower panel) multiplicity $\sqrt{s_{pA}} = 5.02$ TeV p+Pb events. Events including initial state momentum correlations (filled symbols) are compared to the same events where the initial momenta were randomized in azimuth (rand. azimuth, open symbols).

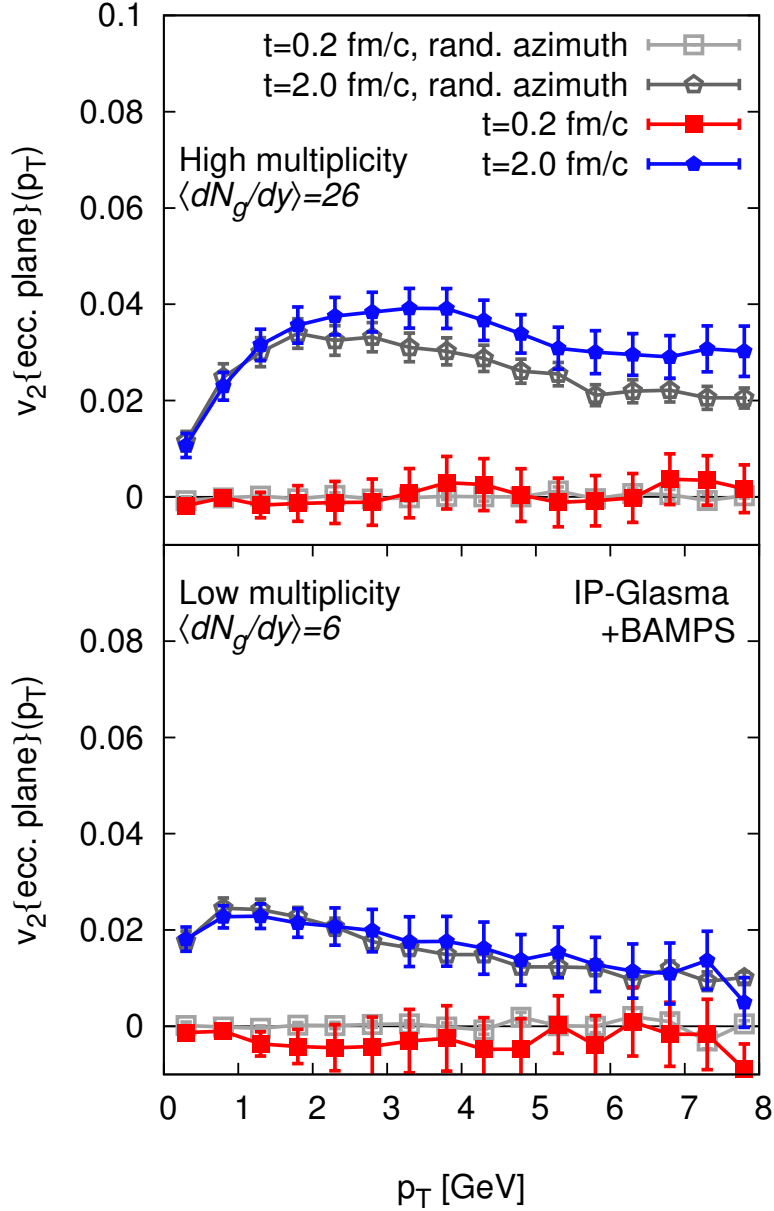


Figure 11.4.: Comparison of initial and final $v_2(p_T)$ with respect to the eccentricity plane for high (upper panel) and low (lower panel) multiplicity $\sqrt{s_{pA}} = 5.02$ TeV p+Pb events. Events including initial state momentum correlations (filled symbols) are compared to the same events where the initial momenta were randomized in azimuth (rand. azimuth, open symbols).

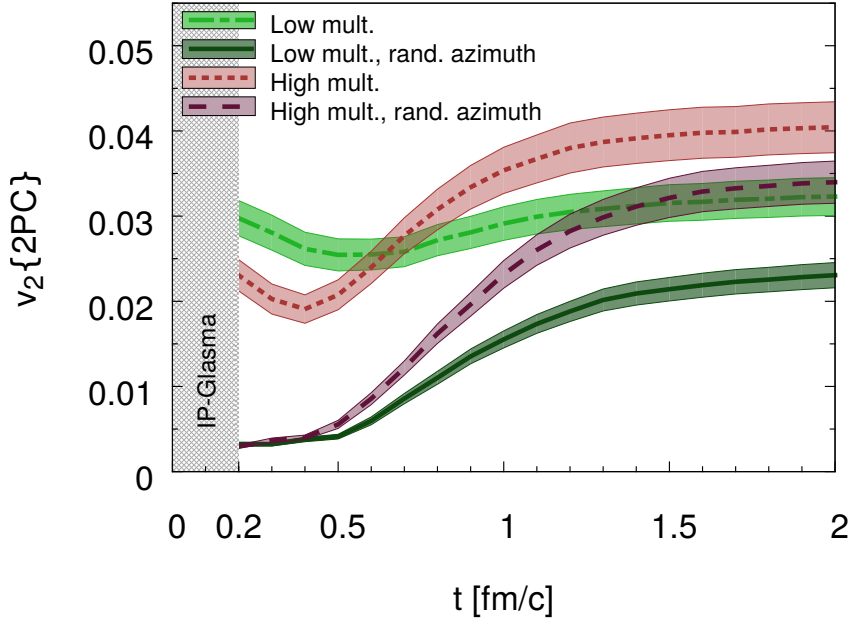


Figure 11.5.: Evolution of the p_T integrated azimuthal anisotropy $v_2\{2PC\}$ for high and low-multiplicity p+Pb events.

can also be observed from Fig. 11.5, where we study the time-evolution of the p_T integrated $v_2\{2PC\}$. While in the rand. azimuth case, the $v_2\{2PC\}$ is built up slowly as a function of time in response to the initial state geometry, a qualitatively different behavior emerges in the more realistic case including initial state correlations. In this case, large angle scatterings at early times begin to destroy initial state momentum correlations leading to an initial decrease of $v_2\{2PC\}$ as a function of time. This happens because the directions of the initial state anisotropy and the eccentricity responsible for generating the final state v_2 are generally uncorrelated. Subsequently, between $t \sim 0.5 - 1$ fm/c the response to the initial state geometry sets in, leading again to an increase of $v_2\{2PC\}$. Overall, we find that the relative effect of initial state correlations on the final $v_2\{2PC\}$ is on the order of 25 – 50%, being larger for low-multiplicity events.

11.6. Multiplicity selection and fragmentation

We now work more differentially on several multiplicity classes, defined by gluon multiplicity of $N_g = 0.5 - 3.45 \times \text{min.bias.}$, where “min.bias.” denotes the minimal bias gluon multiplicity (e.g., at CMS $dN_{\text{trk}}/dy = 8.46$).

We use a strong coupling in the Yang-Mills evolution (acting as normalization) of $g^2 = 6.25$ and (as an arbitrary choice) the parameter $X_{\text{LPM}} = 0.05$ in BAMPS, as well as a running coupling $\alpha_s(Q^2)$ evaluated at the Mandelstam scale of microscopic scatterings within BAMPS. (This small value of $X_{\text{LPM}} = 0.05$ might lead to an unphysically small value of η/s , but here we merely want to see the possibilities of strong final state interactions.) In Fig. 11.6 we show gluon $v_2\{2PC\}$ for $n = 0.5, 1.5$ and 3.45 compared to data from the CMS experiment at the LHC [328], where the $3.45 \times \text{min.bias.}$ multiplicity calculation would correspond to the lowest multiplicity from CMS⁷, $120 < N_{\text{trk}} < 150$,

⁷The mean multiplicity at CMS is $\langle N_{\text{trk}}^{\text{min.bias.}} \rangle = 40$, such that $3.45 \langle N_{\text{trk}}^{\text{min.bias.}} \rangle = 138$ within an acceptance of $\Delta\eta = 4.8$.

even though CMS data is very mildly dependent on multiplicity only, as can be seen by the $220 < N_{\text{trk}} < 260$ class (gray triangles). We observe that the multiplicity dependence from BAMPS is also mild, but visible, and increases for increasing p_T .

The choice of $X_{\text{LPM}} = 0.05$ enhances the inelastic transport rate considerably compared to the previously used value of $X_{\text{LPM}} = 0.3$, and thus increases the elliptic flow variable, however, the experimental data is about a factor of 1.5 larger. In Fig. 11.7 we show the

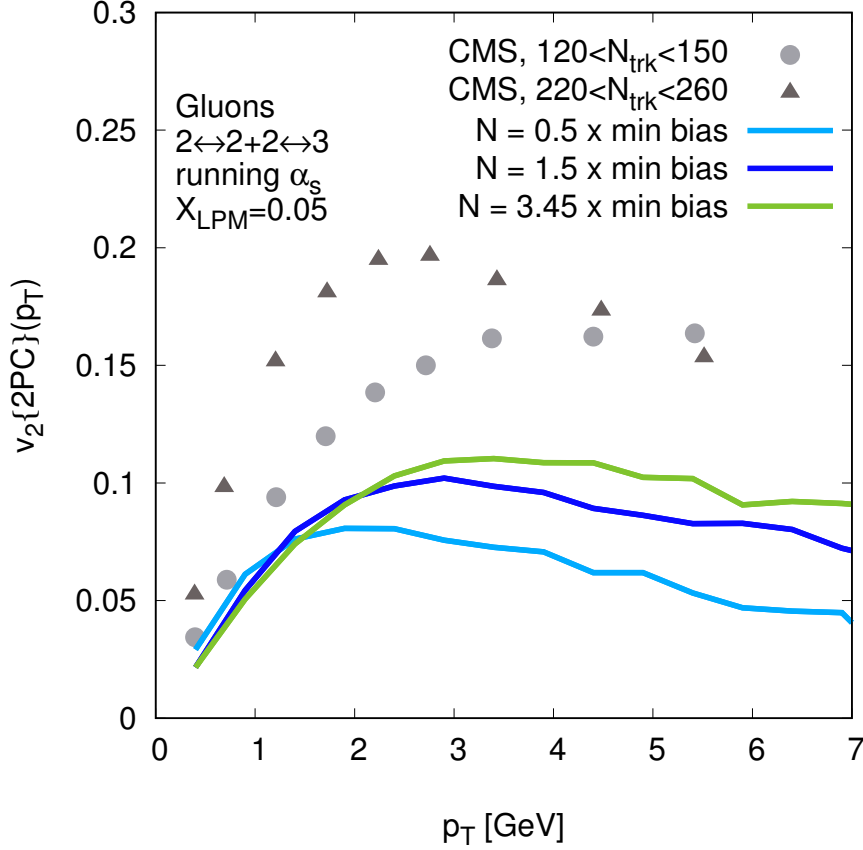


Figure 11.6.: Final $v_2 \{2PC\} (p_T)$ from CMS at two multiplicity classes [328] compared to the corresponding class from BAMPS, $3.45 \times \text{min.bias.}$ (green solid line) as well as two lower multiplicity classes. Here we use running strong coupling, α_s and $X_{\text{LPM}} = 0.05$.

time evolution of gluon $v_2 \{2PC\}$ from time $t = 0.2$ fm to $t = 2$ fm for two multiplicity classes, $N = 0.5, 3.45 \text{ min.bias.}$. Here we confirm the previously drawn conclusions, that at $N = 3.45 \text{ min.bias.}$ elliptic flow builds up strongly in BAMPS up to $p_T = 7$ GeV, whereas at $N = 0.5 \text{ min.bias.}$ only below $p_T = 3$ GeV elliptic flow is built up. So far we used only gluons as dynamical particles, however, in experiments, (charged) hadrons are measured. At high p_T , a very common hadronization model is the concept of “fragmentation”. It describes hadrons, propagating collinearly to the parton, carrying away a fraction z of the parton momentum. The probability of a contribution from parton i to a hadron h at momentum scale Q^2 is the so-called fragmentation function $D_i^h(z, Q^2)$. It is extracted from global fits to experimental data. We will use the set of fragmentation functions from

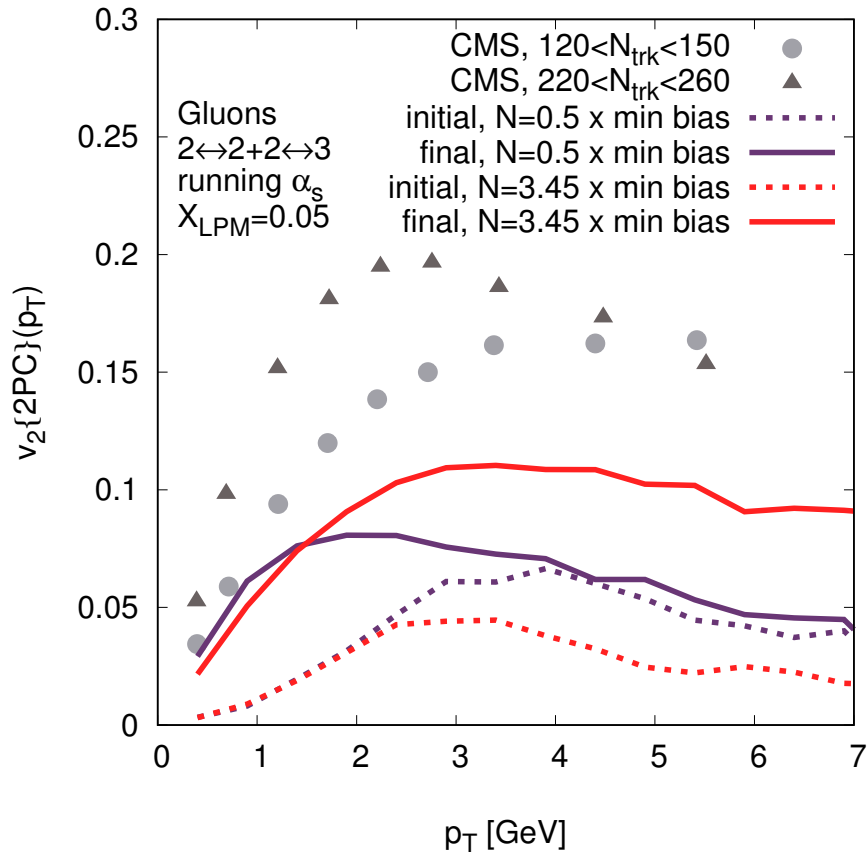


Figure 11.7.: Same experimental data as before from CMS [328], but now we show also the initial (at $t = 0.2$ fm/c) values in BAMPS for low and high-multiplicity events.

Kniehl, Kramer and Potter (KKP) [354]. Using

$$\begin{aligned} \frac{dN_h}{d^2p_T^h dy} (p_T^h) &= \sum_{\text{species } i} \int_{z_{\min}}^1 \frac{dz}{z^2} D_i^h(z, Q^2) \frac{dN_i}{d^2p_T^i dy} \\ &= \sum_{\text{species } i} \int_{z_{\min}}^1 \frac{dz}{z^2} \int d^2p_T^i \delta^{(2)} \left(p_T^i - \frac{p_T^h}{z} \right) D_i^h(z, Q^2) \frac{dN_i}{d^2p_T^i dy} \end{aligned} \quad (11.7)$$

in the formula for any hadronic observable

$$O^h(p_T^h) = \int d^2p_T^h O(p_T^h) \frac{dN_h}{d^2p_T^h dy} \quad (11.8)$$

gives

$$O^h(p_T^h) = \sum_{\text{species } i} \int d^2p_T^i \frac{dN_i}{d^2p_T^i dy} \int_{z_{\min}}^1 dz O(zp_T^i) D_i^h(z, Q^2) \quad (11.9)$$

where $z_{\min} = 0.05$. In Fig. 11.8 we show gluon $v_2(2PC)(p_T)$ and its corresponding hadronic

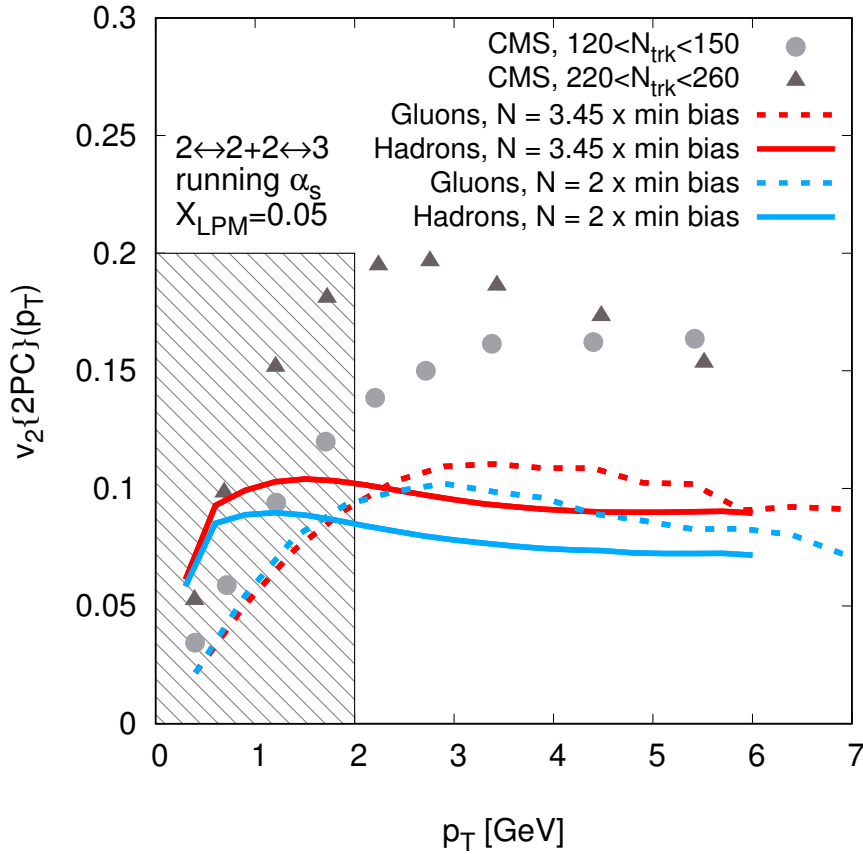


Figure 11.8.: Two-particle elliptic flow versus transverse momentum at two different multiplicities for gluons and, after fragmentation, hadrons, compared to CMS data. The shaded are denotes the region where fragmentation functions are not expected to be any more reliable.

result, for two different multiplicity classes. The fragmentation mechanism of Eq. (11.9)

shifts the partonic curves further left towards lower p_T , whereby a certain mixing of the partonic values at different p_T takes place. This mechanism can however not easily increase the value of $v_2(2PC)(p_T)$ since it is an averaging and folding procedure. The shaded area in Fig. 11.8 indicates the region $p_T < 2$ GeV wherein the fragmentation functions are not reliable any more, but only there the value increase due to the shift of the values from the right. The multiplicity dependence is small, but it is visible that (above $p_T \gtrsim 2$ GeV) our model lies one third below the data. It may very well be, that a more realistic hadronization process, such as microscopic hadronization (e.g., by using an event generator) could explain the missing ingredient.

11.7. Conclusions

The observation of long range rapidity correlations with characteristic structures in azimuthal angle in small systems has challenged our understanding of the space-time evolution of high-energy nuclear collisions. Despite the fact that several phenomenological works have attempted to explain various aspects of the experimental data, it remained unclear to what extent observed correlations should be attributed to initial state or final state effects. Based on a weak-coupling picture of the space-time dynamics, we developed a new framework including both initial state momentum correlations and final state interactions. By matching classical Yang-Mills dynamics (IP-GLASMA) to an effective kinetic description (BAMPS) on an event-by-event basis, we showed that the relative importance of initial and final state effects in p+Pb collisions at LHC energies depends on the event multiplicity as well as the transverse momenta under consideration. Especially at low-multiplicity, the initial state correlations are very important for integrated as well as differential v_2 , and need to be taken into account in a quantitative theoretical description.

We also note that multi-particle correlations of more than two particles can provide additional insight into the nature of the observed correlations. Since final state induced correlations emerge in response to the global event-geometry, these naturally produce m -particle correlations (with $m > 2$) of similar strength. Conversely, for initial state correlations the existence of pronounced multi-particle correlations is not a priori obvious. However, it was shown recently in an Abelian model that initial state effects can generate similar 4-, 6-, and 8- particle correlations [355]. Explicit studies of multi-particle correlations beyond $m = 2$ within our framework are numerically very intensive and will be left for future work. Our results indicate that a differential study of azimuthal correlations across a large range of multiplicities and transverse momenta, can provide new insights into properties of the initial state and the early time non-equilibrium dynamics of high-energy collisions. In this context, it would also be interesting to include jet-like correlations at higher momenta, to achieve a fully comprehensive framework of multi-particle correlations. It is furthermore desirable to construct a microscopic hadronization method in order to consistently compare our results to experimental data. It then becomes feasible to carry out a systematic multiplicity scan, and predict kinematic windows revealing initial and final state correlations.

12. Summary, conclusion and outlook

We now briefly summarize the main aspects of this thesis, conclude and explain possible next steps. We then highlight important future extensions and interesting follow-up projects. In Fig. 12.1 we show a word cloud highlighting the most frequent words used in this thesis.

12.1. Summary

In this work we study different aspects of high energy physics, focusing on heavy-ion and p+A collision phenomenology.

In order to better characterize the hot Quark-Gluon Plasma (QGP) medium as well as the hot hadron gas (HG) we compute their electric conductivity and the conserved charge diffusion matrix. These transport coefficients have gained less interest in literature compared to, e.g., the shear viscosity to entropy ratio η/s or the bulk viscosity to entropy ratio ζ/s . Based on the Chapman-Enskog formalism, and related linear response theory from literature, we develop an algorithm to compute diffusion coefficients and electric conductivity from the linearized Boltzmann equation. In the HG, we use binary, isotropic scattering of up to 19 hadronic species and wherever available the collision cross sections are Mandelstam- s dependent resonance cross sections. In the QGP, we here use a simple toy-model, keeping all partons massless with an isotropic cross section which guarantees $4\pi\eta/s = 1$.

For the electric conductivity, we present the -to our knowledge- most extensive result available in the HG, and compare to several other works in literature. Around the phase transition temperature, we match results from lattice QCD (lQCD) and our temperature dependence is close to that of chiral perturbation theory.

We investigate diffusion currents due to gradients in the thermal potentials (chemical potential over temperature) and find, that gradients of each charge couple to currents of all charges, thus a whole matrix must be considered. Relevant charges in heavy-ion collisions are baryon, electric and strangeness charge. The diagonal coefficients are what is known as the baryon diffusion coefficient (κ_{BB}), the electric diffusion coefficient (κ_{QQ}) and the

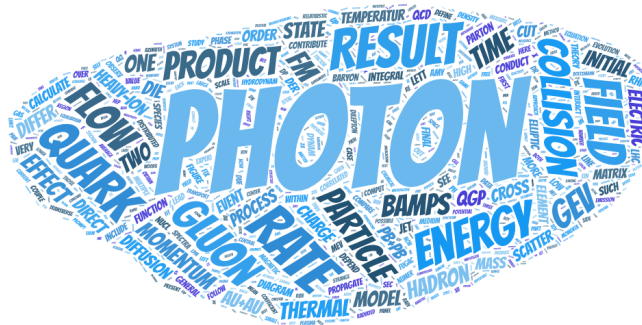


Figure 12.1.: Word cloud of the most frequent words of this thesis. Small common english words are not counted. Created with <https://wordart.com/>.

strangeness diffusion coefficient (κ_{SS}). The off-diagonal coefficients ($\kappa_{QB}, \kappa_{SQ}, \kappa_{SB}$) of the (by Onsager's theorem diagonal) matrix describe the coupling of gradients and currents of the three charges, and have never been computed before. By presenting the complete diffusion matrix relevant for heavy-ion collisions, we can draw important conclusions for the evolution of high-density experiments. We find, that the temperature and chemical potential dependence in the QGP is mild, but strong in the HG. In most cases the simple assumptions of the QGP are sufficient to surprisingly well match the coefficients quite closely at the phase boundary, the off-diagonal coefficient κ_{BQ} being the exception. The strangeness diffusion coefficient κ_{SS} is the largest, such that possible diffusion effects for strange baryons might be observable. The cross coefficient κ_{SB} is negative, which means that a gradient in baryon thermal potential initiates a negative strangeness current.

The rest of the thesis uses the model Boltzmann Approach to Multi-Parton Scatterings (BAMPS) as the main tool. BAMPS models the QGP phase of heavy-ion (or proton-ion) collisions as a non-equilibrium ensemble of partons governed by the Boltzmann equation. This numerical framework solves the relativistic Boltzmann equation numerically exact in $3 + 1$ dimensions, by using Monte-Carlo methods. Hereby BAMPS employs elastic and radiative pQCD cross sections, running coupling, as well as a simple approximation of the LPM effect for subsequent radiative scattering.

It is known, that in the center of peripheral heavy-ion collisions extremely large magnetic fields appear in vertical direction. Those are generated by the passing spectator nucleons which have relativistic speeds. The Lorentz force pushes charged partons on circular trajectories. We use BAMPS, supplied with a simple power-law initial state and constant cross sections, to investigate the influence of external magnetic fields on the dynamics of the fireball. After investigating the appearing Liénard-Wiechert Potentials and the resulting fields for several configurations we find out which kinematic regions in momentum space are affected by the Lorentz force. We then compare spectra and elliptic flow with and without magnetic fields. We find, that even for optimistic estimates of the field configuration, a change of the spectra and an enhancement of the elliptic flow in most measurable regions of transverse momentum p_T is small.

We then turn to the theoretical description of photon production processes. To this end we first construct matrix elements for photon production, and modify them in a reasonable way, such that they are infrared safe and do not diverge. We furthermore specify parameters, which modify the matrix elements in a way, that in thermal and chemical equilibrium the corresponding photon rates are very close to leading order rate calculations in thermal field theory. We do this separately for binary and radiative matrix elements. We furthermore investigate the fugacity dependence of the rates within the microscopic algorithms, and show that they scale like λ_q^{1-2} . We show how photon production rates change under boosts, and proof the correct generation of boosted rates in BAMPS. The translation of the elliptic flow variable from a boosted background onto produced particles suffers from a relativistic reduction effect, which we elucidate. We have constructed a second, alternative way to microscopically generate photons, based on the ‘‘AMY’’ scattering kernel. We clarify its formalism and test the resulting rates. This photon production requires an effective background temperature and the momentum of the radiating quark. In thermal and chemical equilibrium the method reproduces very precisely the analytic rates, however, the angle of the outgoing photon is always approximated to be zero.

We investigate the collinearity and the energy spectra of the photon production mechanisms for single radiating quarks and show the effect of leakage of collinear photons. For some of the photon production cross sections the photon momentum is very probable to be close to the parton momentum, which we call parton-photon conversion. We highlight which kinematic regions exhibit a clear quark-photon conversion.

We compute direct photons from the QGP phase for RHIC and LHC collisions at several multiplicities, using the two alternative mechanisms. In order to understand their behavior we calculate the background thermodynamics and chemistry for the collision systems in BAMPS and set the photon rates in connection to it. Collected photons in the detector are a sum (spectra) or weighted average (elliptic flow) of all emission locations in spacetime, making it hard to distinguish and separate theoretical uncertainties of the models. However, it is very interesting to observe the dynamical realization of photon production influenced by the different processes, by running coupling, quark and gluon chemical equilibration and the temperature evolution.

Comparisons to direct photons from experiment are attempted by using the missing contributions (hadronic and prompt) from literature. The general picture is an underestimation of the yield and also the elliptic flow in all centrality classes. At RHIC, for high and low transverse momenta the agreement of the spectra to data is acceptable and within errors, at LHC we can only compare the high-momentum parts, also with reasonable agreement. Our calculation of the elliptic flow at RHIC describes the data well for transverse momenta $p_T \leq 1.5$ GeV. At LHC we are missing hadronic literature values. We realize, that the strict collinear “AMY” emission in all cases yields significantly stronger elliptic flow. We show that running coupling enhances the spectra by up to a factor of 1.7, but does not alter the elliptic flow. We systematically investigate the fugacity effect by generating artificial background events with a much faster quark generation. In these scenarios the photon yield increases, but the effect is rather mild, since photon production is dominated in the hot early phase where, in all scenarios, quark production is still at the onset. These results however proof and quantify the effect of the fugacities.

We compare to a different transport model (PHSD) and a hydrodynamic model (MUSIC). To date, no model explains experimental direct photon data neither from PHENIX nor ALICE for yield and flow satisfactorily. It is apparent that the QGP contribution differs significantly among the different models, so do the hadronic photon spectra. BAMPS shows harder spectra than both of them, and an overall lower magnitude. It is probable, that direct photon spectra and flow are dominated by hadronic sources in a wide kinematic range. Our model underlines further the importance of the chemical non-equilibrium and kinetic non-equilibrium effects such as collinear jet-photon conversion. The solution of the “photon-puzzle” certainly includes a number of subtle improvements and a collection of modifications to the current models. It seems probable, that only a combination of different models will give the desired success.

In a separate project, we study the influence and interplay of initial state and final state effects in the dynamics of small systems, focusing on azimuthal correlations at different multiplicities. Measurements in small collision systems such as p+p and p+A, in particular those of anisotropies in multi-particle correlation functions, have shown very similar features as those in heavy-ion collisions, and calculations within the hydrodynamic framework have been quite successful in describing observables even though the applicability of hydrodynamics becomes increasingly doubtful as the system size decreases and gradients increase. Calculations using only intrinsic momentum correlations of the initial state can also reproduce many features of the experimental data. We present a first study where both initial and final state effects are combined into a single framework to assess their relative importance for azimuthal correlation functions. We introduce a new model, matching the classical Yang-Mills dynamics of pre-equilibrium gluon fields (IP-GLASMA) to BAMPS (for the final state interactions) on an event-by-event basis.

In summary, depending on multiplicity of the event, we see transverse momentum dependent signatures of the initial, but also the final state in azimuthal correlation observables, such as $v_2\{2PC\}(p_T)$. For instance, we see in low-multiplicity events, that initial state

correlations dominate for transverse momenta $p_T > 2$ GeV, whereas in high-multiplicity events and at low momenta final state interactions dominate and initial state correlations strongly affect $v_2\{2PC\}(p_T)$ for $p_T > 2$ GeV as well as the p_T integrated $v_2\{2PC\}$. Nearly half of the final p_T integrated $v_2\{2PC\}$ is contributed by the initial state in low-multiplicity events, whereas in high-multiplicity the share is much less. We investigate furthermore the dynamic behavior of the integrated flow.

We have now set the stage to carry out a systematic multiplicity scan, which, supplemented with a hadronization scheme, allows the comparison to experimental data, probing the dynamics on the border of initial state dominated to final state dominated - but not yet hydrodynamic - regime.

12.2. Conclusion and outlook

All the presented projects are prone to multiple improvements, some of which are currently undergoing.

We have calculated a variety of transport coefficients such as conserved charge diffusion and electric conductivity, and it remains to show first and foremost how relevant their effect is for phenomenology, i.e. measurable observables. So far, hydrodynamics with diffusion currents is in its beginning, but efforts are underway to include all (also higher order) diffusion terms for multiple charges, and their couplings. In low-energy collisions, the rapidity distributions of baryons and strange baryons are still not fully understood, and it seems promising, that diffusive hydrodynamic simulations can give some answers. Due to the large parameter space from the cross sections, resonances and hadronic species it is certainly possible and desirable to improve the values of the transport coefficients even further. However, the presented (semi) analytic formalism is less suitable for significant extensions, such as inelastic scattering, as, e.g., dynamical hadronic transport models. In frameworks such as UrQMD, GiBUU or SMASH the diffusion matrix and the electric conductivity can be analyzed for instance via the Green-Kubo method, and resonance propagation, a nearly complete hadronic zoo, extensive scattering potentials, correct differential cross sections (s - and p -wave scattering) are no principle problem. The present results in this thesis can however benchmark those codes. Besides, it is unlikely that the results will change largely upon the inclusion of more species and more precise scattering, since the mass hierarchy determines the abundances in thermal equilibrium, and we include the 19 lightest species. Another, further unexplored possibility is the inclusion of Hagedorn states. Furthermore, it will be extremely interesting to compare the present results for the diffusion matrix with lattice QCD results. To date, they are not available. Results from other theories like holography are likewise welcome.

Currently, magneto-hydrodynamics is an acclaimed field of study. First magneto-hydro codes are working and being improved both numerically and theoretically, however a viscous hydrodynamic code with finite conductivity is not developed yet. We have found that in one of the most prominent observables, v_2 , magnetic fields are almost irrelevant. It will be interesting to verify our conclusion with a full magneto-hydrodynamical solution. At this point, our calculation of the electric conductivity comes into play - since a full magneto-hydrodynamical code requires a temperature and chemical potential dependent electric conductivity, which we provide in this thesis. Another immediate step is the simultaneous microscopic solution of the Boltzmann and Maxwell equation. We have carried out first tests in this direction in this thesis. Even if those algorithms might be unnecessary in the context of heavy-ion physics, there are many astrophysical applications.

Direct photons are a delicate probe in heavy-ion collisions, and to date no model explains the experimental data satisfactorily. The implementation of direct photon production in

BAMPS constitutes an important supplement to existing models. We have calculated direct photon spectra and elliptic flow for various collision systems. Photons are sensitive to rates and background, and it is probably necessary to improve on both. The leading order rates in the QGP are relatively well esteemed, and even known to NLO (also first lattice results show no significant differences to NLO rates). Hadronic rates are under more debate, and in near future important improvements are anticipated. Even prompt photon calculations are not parameter free, nor do all models coincide on them. Theoretical prompt photon spectra should thus be improved. Our results anticipate a possible large hadronic contribution to direct photon data. Improvements of the background will concern mostly its composition. One should focus some research effort to the question, whether the initial state is gluon dominated, and, if so, how fast quarks are produced. This is closely connected to the question of thermalization. We conclude based on our results that the importance of quark and gluon fugacities must not be underestimated. We cannot find an outshining importance of the preequilibrium phase, since our model of the initial state has a sparse quark population. The possibility exists, that non-isotropic initial state photon radiation leads to an additional positive contribution for both elliptic flow and total yield. It seems crucial to know the initial state very precisely, and the last project of this thesis is an important step in this direction.

Based on our development of a new framework for p+A systems including both initial state momentum correlations and final state interactions, it will be possible to construct a realistic hadronization framework, as follow up of the BAMPS evolution. Then, systematic comparisons with data in several multiplicity classes will quantify and reveal signatures of the initial state. If our framework proves to be able to explain a wide range of data, we would be able to predict which kinematic regions within azimuthal correlation observables are purely determined by the initial color glass condensate correlations. Going further into multiplicities where final state interactions begin to be visible, the early non-equilibrium phase can be investigated. In this stage, the quark and gluon content governs also early photon production rates. If experimental data become available, it will in fact be very interesting to learn about photon spectra of small systems. This in turn might hint to the missing ingredient of the “photon puzzle” in heavy-ion collisions.

Appendices

A. Cutting rules for bremsstrahlung

Here we want to elaborate more on the cutting schemes which are used within this thesis. First we look at non-symmetric cuts that appear at two-loop level, then we turn to three loop diagrams and their cuts to obtain bremsstrahlung matrix elements.

A.1. Two-loop contribution and non-symmetric cuts

At two loop order, there are possible cuts, which produce two fundamentally different diagrams at the left- and right-hand side of the cut. They are shown in Fig. A.1. The rules that were discussed in Sec. 6.1.2 apply essentially here in the same way. The difference is obvious: there are no squared amplitudes to be expected, as we are dealing only with non-symmetric cuts, that will generate only interference diagrams. The interference involves a diagram with a closed loop, and a photon-quark-antiquark pair diagram from Sec. 6.1.1. The method to deal with closed loops will be explained in the next section. In the present case the product of the left- and right-hand side of the cuts from Fig. A.1 involves so-called spectator particles from the heat bath, as explained in Refs. [264, 265]. We omit detailed calculations at this point, as the tree-level quark-antiquark annihilation part of the amplitude (which appears in all cases in the diagrams) has no phase space for on-shell particles.

A.1.1. Three-loop contribution and symmetric cuts

Including three loops results in diagrams and cuts as in Fig. A.2. Here we investigate the cuts which are denoted by the dashed lines and the dotted lines (Other possible cuts are not shown). The dashed lines each generate 4 cut propagators, that must be labelled “in” or “out” in all $\binom{4}{0} + \binom{4}{1} + \binom{4}{2} + \binom{4}{3} + \binom{4}{4} = 16$ possible ways. This cut generates squares and interference diagrams of various $1(2, 3, 4) \rightarrow 4(3, 2, 1)$ processes.

The dashed cuts of Fig. A.2 produce two on-shell gluons, and one quark line radiating a photon. This, and corresponding diagrams with more gluon rungs, represent a sequential scattering with gluons, which is included by default in BAMPS (see Chap. 4), because the dominating subprocess $q + g \rightarrow q + g$ was included from the beginning, and the rare radiation of the photon is Compton scattering in this case.

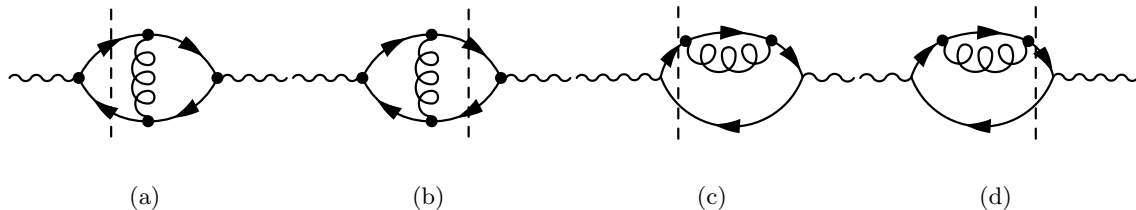


Figure A.1.: The two possible non-symmetric cuts for each of the possible diagrams of the photon self energy at (two-loop) order $e^2 g^2$. The first and last two are of course topologically the same.

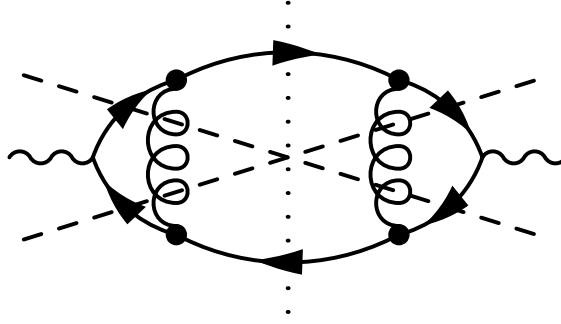


Figure A.2.: A possible three loop diagram with two gluon rungs. The dashed and dotted lines are possible, topologically different cuts.

The dotted line creates two diagrams with a single closed loop. Here we have to label the cut propagators that become on-shell by the label “in” or “out” in all possible ways, as shown in Fig. A.3, corresponding to incoming or outgoing quarks/antiquarks. The cutting rules prescribe in cases, where the cut diagrams show closed loops, that the loops has to be opened in all possible ways [264, 265, 268]. In Ref. [265] these openings are called tics, using the notation of marking opened propagators with a tic. This comes from the loop integration, which is the reason for putting all internal propagators in turn on-shell [264].

There are rules for allowed tics: 1) All loops must be opened 2) The total number of opened loops plus cut propagator lines must equal the number of loops in the original diagram plus one 3) From both external legs one can move continuously to the cut line along propagators without crossing tics or cuts (see Ref. [265]). All these rules are fulfilled by either ticing ①, ② or ③. In our case of Fig. A.3, the evaluation of the contribution to the imaginary part of the self energy by defining both cut lines as incoming, results in several $3 \rightarrow 2$ processes, like $q\bar{q}\bar{q} \rightarrow \bar{q}\gamma$, $qq\bar{q} \rightarrow q\gamma$ or $q\bar{q}g \rightarrow g\gamma$. Likewise, defining both cut lines as outgoing will end up in matrix elements of $1 \rightarrow 4$ processes (which are kinematically not allowed but this is not important at this point).

We want to compute the $2 \rightarrow 3$ contribution, which is generated by defining one of the cut quark propagators as incoming, the other as outgoing, as shown in the middle panel of Fig. A.3.

We have to tic the marked propagators one by one, which has the same effect as cutting it, with the difference, that one end of the ticed propagator is incoming, the other outgoing [264]. Doing this in turn for tic ①, ②, ③ generates six different diagrams. Of course, these diagrams have to be complex conjugated and multiplied with the six diagrams from the left-hand side of the cut.

In Fig. 6.9 the two topologically different bremsstrahlungs-diagrams are shown, that arise from the tic ③ in the diagram of Fig. A.3(b). The other four possible diagrams (arising from tics ① and ②) are for the processes $gq \rightarrow gq\gamma$ (s+t channel), $q \rightarrow q\bar{q}q\gamma$ and $q\bar{q} \rightarrow q\bar{q}q\gamma$ (s-channel).

For every possible in/out-configuration of the cut, the left- and right-hand side have to be multiplied. This will in principle generate interference diagrams among the six aforementioned diagrams. As we are interested in S-matrix elements with a specific in/out state, we consider only the states with the same in/out state, that is for example the two diagrams $qq \rightarrow qq\gamma$ as shown in Fig. 6.9. They have to be summed and multiplied with its complex conjugate.

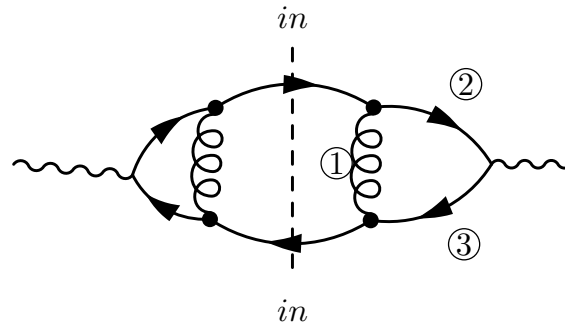
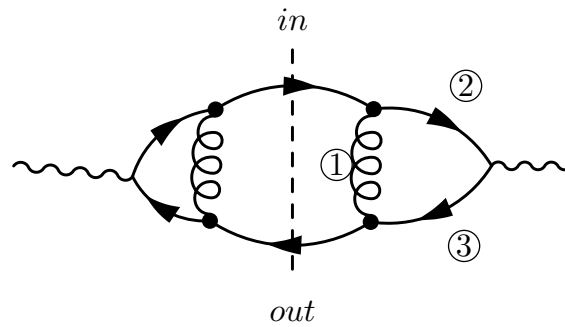
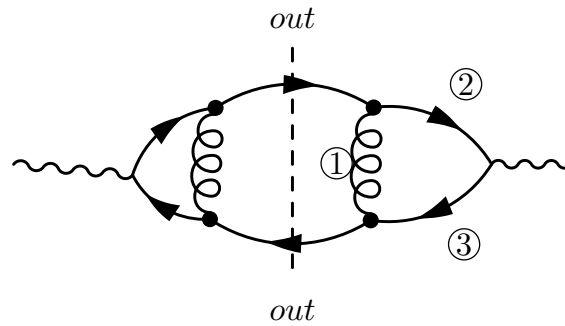
(a) This configuration generates $3 \rightarrow 2$ processes.(b) This configuration generates $2 \rightarrow 3$ processes.(c) This configuration generates $1 \rightarrow 4$ processes.

Figure A.3.: One of the two different symmetric cuts to the three-loop photon self energy. The cut propagators can be incoming or outgoing. The photon is defined to be outgoing. The loop on each side must be opened once, the three possibilities are given by circled numbers. There are 9 possibilities for the whole diagram, as left- and right-hand side must be multiplied.

B. Matrix elements for bremsstrahlung

B.1. Bremsstrahlung diagrams for quark-quark scattering

In this section we compute the squared matrix element for the $qq \rightarrow qq\gamma$ process, shown in Fig. 6.3. For this purpose, we label the amplitude of Fig. 6.9(a) with \mathcal{M}_a , and the one from Fig. 6.9(b) with \mathcal{M}_b . We have to compute $(\mathcal{M}_a + \mathcal{M}_b)^* \cdot (\mathcal{M}_a + \mathcal{M}_b)$. As customary in scattering theory, the matrix element is given by an average over initial spin, polarization and color states, and a sum over final states.

B.1.1. Matrix elements

With the momentum assignment $p_3 = p_1 + q$, $p_4 = p_2 - q - k$ we write down the first matrix element [Fig. 6.9(a)] by using momentum space Feynman rules:

$$\begin{aligned} i\mathcal{M}_a &= \bar{u}^w(p_3)(ig)\gamma^\mu\lambda_{ij}^a u^s(p_1) \frac{-ig_{\mu\nu}\delta_{ab}}{q^2} \bar{u}^r(p_4) \\ &\times (ig)\gamma^\nu\lambda_{mj}^b \frac{i(m + \not{p}_2 - \not{k})}{(p_2 - k)^2 - m^2} \\ &\times (iQ_{EM})\gamma^\alpha\epsilon_\alpha^*(k)u^t(p_2). \end{aligned} \quad (\text{B.1})$$

The second matrix element [Fig. 6.9(b)] is

$$\begin{aligned} i\mathcal{M}_b &= \bar{u}^w(p_3)(ig)\gamma^\mu\lambda_{ij}^a u^s(p_1) \frac{-ig_{\mu\nu}\delta_{ab}}{q^2} \bar{u}^r(p_4) \\ &\times (iQ_{EM})\gamma^\alpha\epsilon_\alpha^*(k) \\ &\times \frac{i(m + \not{p}_4 + \not{k})}{(p_4 + k)^2 - m^2} (ig)\gamma^\nu\lambda_{mj}^b u^t(p_2). \end{aligned} \quad (\text{B.2})$$

By using the Dirac equation we transform the numerators of the quark propagators in the following way:

$$\begin{aligned} (\not{p}_2 + m)\gamma^\alpha u(p_2) &= 2p_2^\alpha u(p_2) \\ (\not{p}_4 + m)\gamma^\nu u(p_2) &= 2p_4^\nu u(p_2), \end{aligned}$$

and we simplify the denominators,

$$(p_2 - k)^2 = -2p_2 \cdot k, \quad (p_4 + k)^2 = 2p_4 \cdot k. \quad (\text{B.3})$$

Note that, later on, we screen the t -channel quark-propagator in \mathcal{M}_a by using a Debye mass $m_{D,q}^2$,

$$\frac{1}{-2p_2 \cdot k} \rightarrow \frac{1}{-2p_2 \cdot k - m_{D,q}^2}, \quad (\text{B.4})$$

and the s -channel propagator in \mathcal{M}_b ,

$$\frac{1}{2p_4 \cdot k} \rightarrow \frac{1}{2p_4 \cdot k + m_{D,q}^2}. \quad (\text{B.5})$$

Only at this step we set the masses to zero, $m \equiv 0$. The gluon propagator will be screened with the Debye mass $m_{D,g}^2$,

$$\frac{1}{q^2} \rightarrow \frac{1}{q^2 - m_{D,g}^2}. \quad (\text{B.6})$$

B.1.2. Amplitude

Next we simplify the summed matrix elements,

$$\begin{aligned} i\mathcal{M}_a + i\mathcal{M}_b &= \bar{u}^w(p_3)(ig)^2\gamma^\mu\lambda_{il}^a\lambda_{mj}^b u^s(p_1)\frac{-ig_{\mu\nu}}{q^2}(iQ_{EM})\bar{u}^r(p_4) \\ &\times \left[\frac{i(\gamma^\nu p_2^\alpha - \gamma^\nu \not{k}\gamma^\alpha)}{-2p_2 \cdot k} + \frac{i(2\gamma^\alpha p_4^\nu + \gamma^\alpha \not{k}\gamma^\nu)}{2p_4 \cdot k} \right] u^t(p_2)\epsilon_\alpha^*(k) \\ &= -ig^2 Q_{EM}\bar{u}^w(p_3)\gamma_\nu u^s(p_1)\frac{\lambda_{il}^a\lambda_{mj}^a}{q^2}\bar{u}^r(p_4) \\ &\times \left[\frac{\gamma^\nu \not{k}\gamma^\alpha - \gamma^\nu p_2^\alpha}{2p_2 \cdot k} + \frac{\gamma^\alpha \not{k}\gamma^\nu + 2\gamma^\alpha p_4^\nu}{2p_4 \cdot k} \right] u^t(p_2)\epsilon_\alpha^*(k). \end{aligned} \quad (\text{B.7})$$

This amplitude needs to be squared in the next step, $(i\mathcal{M}_a + i\mathcal{M}_b) \cdot (i\mathcal{M}_a + i\mathcal{M}_b)^*$, and then summed over final states and averaged over initial states. We define the resulting summed and averaged squared matrix element as $|\overline{\mathcal{M}}|^2$. The sum over final photon polarizations reduces to [7]

$$\sum_\epsilon \epsilon_\alpha^*(k)\epsilon_\beta(k) \rightarrow -g^{\alpha\beta}. \quad (\text{B.8})$$

The sum of the color matrices is (see Ref. [7], Eq. (17.63))

$$\frac{1}{N_c^2} \sum_{\text{colors}} \lambda^a \lambda^a \lambda^b \lambda^b = \frac{2}{9}. \quad (\text{B.9})$$

The average over initial quark spins and sum over final spins gives a factor 1/4, and, by using

$$\sum_{\text{spin } t} u^t(p)\bar{u}^t(p) = \not{p}, \quad (\text{B.10})$$

we can transform the matrix element into traces,

$$\begin{aligned} |\overline{\mathcal{M}}|_{\text{rad.}}^2 &= \frac{1}{4} \frac{2}{9} \frac{Q_{EM}^2 g^4}{q^4} \text{Tr} \left\{ \not{p}_4 \left[\frac{-\gamma^\nu \not{k}\gamma_\beta + 2\gamma^\nu p_{2,\beta}}{2p_2 \cdot k} + \frac{-\gamma_\beta \not{k}\gamma^\nu - 2\gamma_\beta p_4^\nu}{2p_4 \cdot k} \right] \right. \\ &\times \left. \not{p}_2 \left[\frac{\gamma^\beta \not{k}\gamma^\mu - 2\gamma^\mu p_2^\beta}{2p_2 \cdot k} + \frac{\gamma^\mu \not{k}\gamma^\beta + 2\gamma^\beta p_4^\mu}{2p_4 \cdot k} \right] \right\}. \end{aligned} \quad (\text{B.11})$$

The gluon momentum squared is $q^2 = (p_4 - p_2 + k)^2$ and the gluon propagator reads,

$$\frac{1}{q^4} = \frac{1}{(2p_4 \cdot k - 2k \cdot p_2 - 2p_4 \cdot p_2)^2}, \quad (\text{B.12})$$

and after screening,

$$\frac{1}{q^4} \rightarrow \frac{1}{\left(2p_4 \cdot k - 2k \cdot p_2 - 2p_4 \cdot p_2 - m_{D,g}^2\right)^2}. \quad (\text{B.13})$$

The trace in Eq. (B.11) can be done using the MATHEMATICA package FeynCalc 8.2.0 [356], with the result (where we defined the scalar product of four-vectors $(ij) \equiv p_i \cdot p_j$),

$$\begin{aligned}
A &\equiv 2(25) + m_{D,q}^2 \\
B &\equiv 2(45) + m_{D,q}^2 \\
C &\equiv 4(45) + m_{D,q}^2 \\
D &\equiv (35)B^2 - 2(34)A(2(25) - B - m_{D,q}^2) \\
E &\equiv (23)A((25)C + (45)(-B - m_{D,q}^2)) + (24)A(2(34)A + (35)(A + B)) + (25)D \\
F &\equiv (24)A(A + B) + (25)B^2 \\
G &\equiv (23)A((24)B + (45)A) + (34)F \\
H &\equiv -2(23)B + (34)(-B - m_{D,q}^2) + (35)m_{D,q}^2 \\
J &\equiv (45)H + (24)(35)B + (25)((34)C + 2(35)(45)) \\
\overline{|\mathcal{M}|}_{\text{rad.}}^2 &= \frac{1}{4} \frac{2}{9} Q_{EM}^2 g^4 128 \frac{A((12)J - 2(13)(24)(45)A) + (14)E + (15)G}{A^2 B^2 (2(24) + 2(25) - 2(45) + m_{D,g}^2)^2} \quad (\text{B.14})
\end{aligned}$$

We have checked that the Ward identity is fulfilled.

B.1.3. Symmetry-factor

The self energy in Fig. A.3(b) with the given cut generates the $qq \rightarrow qq\gamma$ -process. We discuss its multiplicity factor here. The photon legs of the self energy can be crossed, which is why the self energy carries a factor of two. The four gluon vertices are completely identical. Every gluon can be reversed. This contributes a factor of four. The loop can be opened by tic-ing the upper or lower quark line, which introduces a factor of two. In total the symmetry factor is 16.

B.1.4. Algorithm to determine specific mean free paths

The mean free path is the inverse of the scattering rate per particle $\lambda_{\text{mfp}} = R^{-1}$. The inverse rate for scattering of a single particle q within a medium of particle density n_q is

$$\lambda_{\text{mfp},qq \rightarrow qq}^q = (n_q \langle \sigma(s) v_{\text{rel}} \rangle_{\text{therm}})^{-1}, \quad (\text{B.15})$$

where the average is over the thermal ensemble and $v_{\text{rel}} \equiv s/(2E_1 E_2)$, where E_1, E_2 are the energies of two incoming particles and the Mandelstam variable $s = (P_1 + P_2)^2$ is the squared sum over their four-momenta. A thermal ensemble allows for the direct calculation of the mean free path from the thermal ensemble, just given the cross section $\sigma(s)$ and the equilibrium density n_q . However, we explicitly want to extract the mean free paths in a chemical and/or kinetically nonequilibrated system. For this purpose, we choose all possible scattering partners i in each computational cell and compute their collision probability P_{22}^i from Eq. (4.18), such that

$$\begin{aligned}
\lambda_{\text{mfp},qq \rightarrow qq}^q &= (n_q \langle \sigma(s) v_{\text{rel}} \rangle_{\text{therm}})^{-1} \\
&= N_q \frac{1}{M} \sum_{i=1}^M \frac{P_{22}^i}{\Delta t}, \\
&= \frac{1}{\Delta V} \frac{2}{(N_q - 1)} \sum_{i=1}^M \frac{\sigma_i v_{\text{rel},i}}{\Delta t}, \\
M &\equiv \frac{1}{2} N_q (N_q - 1). \quad (\text{B.16})
\end{aligned}$$

Note, that here N_q is the total number of quarks in the cell with volume ΔV , which is the physical number times the number of test particles, N_{test} . The cross section in Eq. (4.18) is divided by N_{test} , such that the mean free path is the physical mean free path and independent of N_{test} . For processes $qq \rightarrow qq$ there are $\binom{N_q}{2} = 1/2 N_q(N_q - 1)$ possible scattering processes for N_q quarks in the system, and we take numerically the average to get the mean free path of a quark when considering only scatterings with another quark of the same flavor. In a similar way we can compute the mean free paths for $qq' \rightarrow qq'$, $\bar{q}\bar{q}' \rightarrow \bar{q}\bar{q}'$, $q\bar{q} \rightarrow q\bar{q}$.

B.1.5. Verification of the bremsstrahlung process and kinematics

To cross-check the inelastic photon production and verify the kinematic integration limits and the limit stemming from the LPM constraint, we show in Fig. B.1 a typical set of sampled photon momenta according to the full bremsstrahlung matrix element. Each of the red dots represents one sampled photon for a fixed (but arbitrary) configuration of incoming quark momenta. For illustrational purposes (to see the intrinsic asymmetry in y) we fix the quark line where the photon is emitted, and discard the radiation from the other quark line. However, in any real simulation of BAMPS the incoming quarks are randomly taken to be either quark one or two - thus the momentum spectrum will be symmetric in y . Omitting the integration over y in Eq. (4.22), we compute numerically the differential cross section $d\sigma_{23}/dy$ normalized by the total cross section σ_{tot} in Fig. B.2. Here the symmetry in y can clearly be seen. Omitting the integration over k_{\perp}^2 in Eq. (4.22), we compute also the differential cross section with respect to k_{\perp}^2 , as shown in Fig. B.3. Both figures are done for an arbitrary momentum setup of the incoming quarks, namely $p_1 = (2T, 0, 2T, 0)$, $p_2 = (2T, 0, 0, -2T)$ and $T = 0.4$ GeV. It is clearly visible, that the mean free path changes the kinematics of the outgoing photon momenta, a larger mean free path allows more collinear radiation.

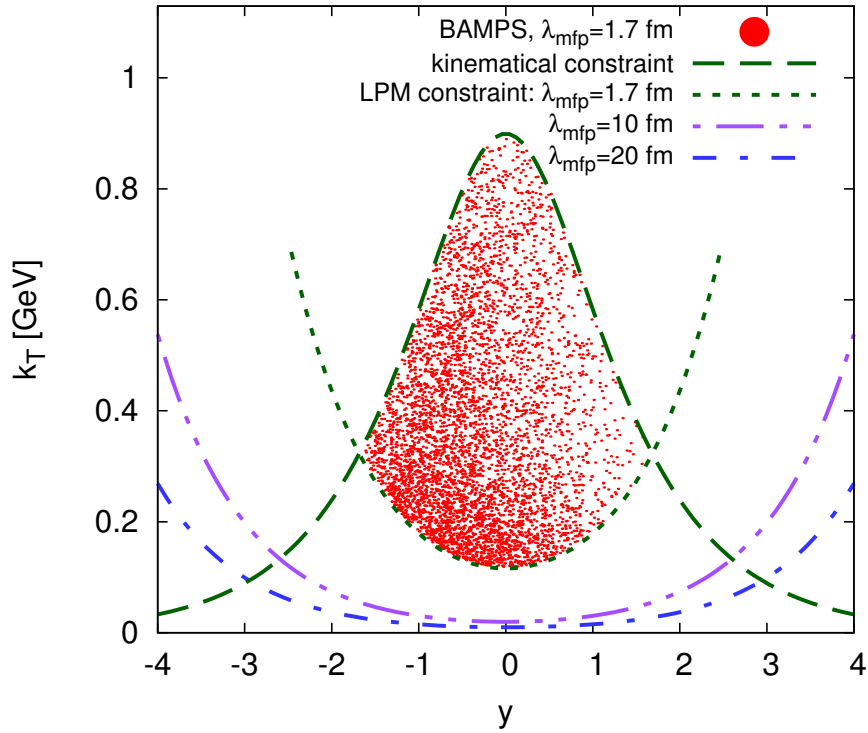


Figure B.1.: The exact photon bremsstrahlung matrix element is used to sample photons. Their momentum is given in $k_{\perp}, q_{\perp}, y, \phi$ -space; here we show several realizations (red dots) as an example, for a fixed configuration of the incoming momenta (see text). The green dashed curve represent the kinematic limit, the green dotted curve the LPM limit. The purple and blue dash-dotted lines show the limit from the LPM constraint for larger mean free paths. The asymmetry in y is forced by using only one fixed quark as the radiating one.

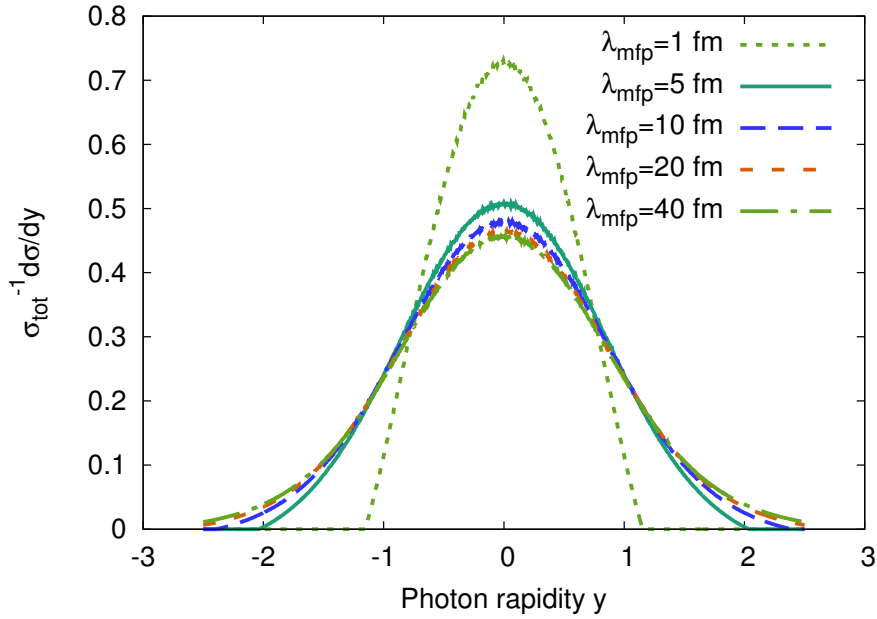


Figure B.2.: The differential cross section in the rapidity of the radiated photon for various mean free paths and a fixed configuration of the incoming momenta (see text).

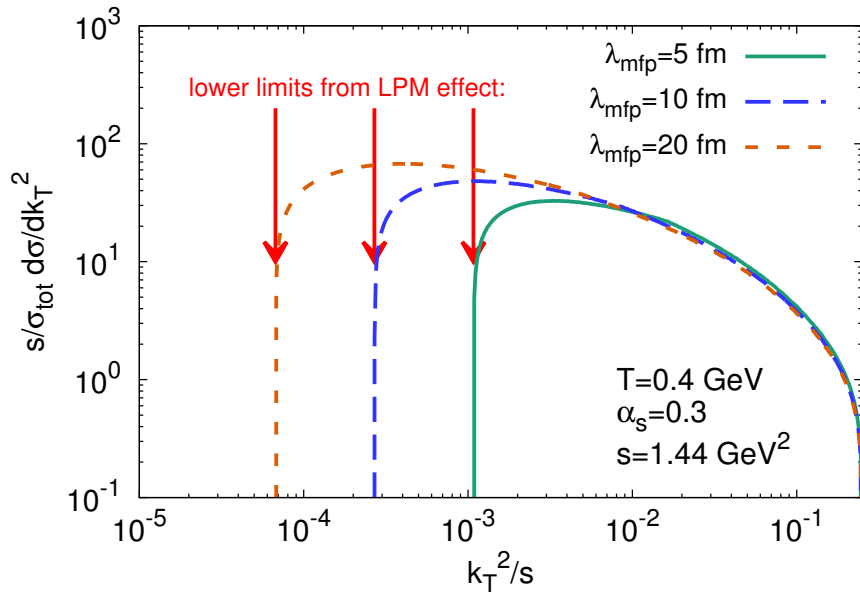


Figure B.3.: The differential cross section in the transverse momentum squared of the radiated photon for various mean free paths and a fixed configuration of the incoming momenta (see text).

C. Calculations for hadronic conductivity

C.1. Calculations of the collision integrals

In the calculations of the matrix elements, the following integrals have to be solved. We will show only some examples, all other integrals can be worked out in a similar fashion. Consider the following integral,

$$\int dP dP' (2\pi)^6 s \sigma_{ij}(s, \Theta) \delta^{(4)}(k^\mu + k'^\mu - p^\mu - p'^\mu) p^\alpha \equiv \Gamma^\alpha. \quad (\text{C.1})$$

We define a unitless vector (normalized total momentum of the collision) $\tilde{P}_T^\mu = (k^\mu + k'^\mu)/\sqrt{s}$, and the projection orthogonal to it, $\Delta_P^{\mu\nu} = g^{\mu\nu} - \tilde{P}_T^\mu \tilde{P}_T^\nu$. The tensor Γ^α can only depend on \tilde{P}_T^μ , so we can decompose,

$$\Gamma^\alpha = a(s) \tilde{P}_T^\alpha, \quad a(s) = \tilde{P}_T^\alpha \Gamma_\alpha \quad (\text{C.2})$$

where

$$a_{ij}(s) = \gamma_{ij} \int dP dP' (2\pi)^6 s \sigma_{ij}(s, \Theta) \delta^{(4)}(k_i^\mu + k_j'^\mu - p_i^\mu - p_j'^\mu) (p_i^\alpha \tilde{P}_{T,\alpha}). \quad (\text{C.3})$$

We can always evaluate a scalar integral in the center of momentum/center of mass frame, where $p_i^\alpha \tilde{P}_{T,\alpha} = p_i^0$. In the massless case, $a = \sigma_{ij}(s, \Theta) s \sqrt{s}/4$, in the massive case,

$$\begin{aligned} a_{ij}(s) &= \gamma_{ij} \int \frac{d^3 p}{p_i^0} \frac{d^3 p'}{p_j^0} s \sigma_{ij}(s, \Theta) \delta(p_i^0 + p_j'^0 - \sqrt{s}) \delta^{(3)}(\mathbf{p}_i + \mathbf{p}'_j) p_i^0 \\ &= \gamma_{ij} \int \frac{|\mathbf{r}|^2 d|\mathbf{r}|}{p_i^0 p_j'^0} s \sigma_{ij}(s, \Theta) \delta(p_i^0 + p_j'^0 - \sqrt{s}) \delta^{(3)}(\mathbf{p}_i + \mathbf{p}'_j) p_i^0 \\ &= \frac{1}{2} \left(\gamma_{ij} \int d\Omega \sigma_{ij}(s, \Theta) \right) \sqrt{(s - s_a^{ij})(s - s_b^{ij})} \sqrt{\frac{1}{4s} (s - s_a^{ij})(s - s_b^{ij}) + m_i^2} \end{aligned} \quad (\text{C.4})$$

where we defined

$$\begin{aligned} |\mathbf{r}| &= \frac{1}{2x} \sqrt{(x^2 - (m_i + m_j)^2)(x^2 - (m_i - m_j)^2)}, \quad s_a^{ij} = (m_i + m_j)^2, \\ s_b^{ij} &= (m_i - m_j)^2, \quad x = p_i^0 + p_j^0, \end{aligned} \quad (\text{C.5})$$

and use

$$\frac{dx}{x} = \frac{|\mathbf{r}| d|\mathbf{r}|}{p_i^0 p_j^0}. \quad (\text{C.6})$$

The $dK dK'$ -integrals of Eq. (2.26) are easily done in the massless case, but require numerical integration in the massive case.

C.2. Cross sections for pion-isotriplett elastic scattering via ρ resonances

As an example for the resonance cross sections, the total cross section for the reaction

$$\pi^\pm + \pi^\mp \rightarrow \rho^0 \rightarrow \pi^\pm + \pi^\mp \quad (\text{C.7})$$

is given by (we use the parametrization given e.g. in [111, 112])

$$\sigma_{\text{tot}}(\sqrt{s}) = \frac{\langle j_{\pi^\mp}, m_{\pi^\mp}, j_{\pi^\pm}, m_{\pi^\pm} || J_{\rho^0}, M_{\rho^0} \rangle (2S_{\rho^0} + 1)}{(2S_{\pi^\mp} + 1)(2S_{\pi^\pm} + 1)} \frac{\pi}{p_{\text{CMS}}^2} \frac{\Gamma_{\rho^0 \rightarrow \pi^\pm + \pi^\mp} \Gamma_{\text{tot}}}{(M_{\rho^0} - \sqrt{s})^2 + \frac{\Gamma_{\text{tot}}^2}{4}} \quad (\text{C.8})$$

Here, j, J is the isospin of the particle or resonance, S_{particle} its spin and m, M the z -component of it. The Clebsch-Gordon coefficients can be looked up:

$\langle j_{\pi^\mp}, m_{\pi^\mp}, j_{\pi^\pm}, m_{\pi^\pm} J_{\rho^0}, M_{\rho^0} \rangle$	$\mp \sqrt{\frac{1}{2}}$
$\langle j_{\pi^-}, m_{\pi^-}, j_{\pi^0}, m_{\pi^0} J_{\rho^-}, M_{\rho^-} \rangle$	$-\frac{1}{2}$
$\langle j_{\pi^0}, m_{\pi^0}, j_{\pi^-}, m_{\pi^-} J_{\rho^-}, M_{\rho^-} \rangle$	$\frac{1}{2}$
$\langle j_{\pi^+}, m_{\pi^+}, j_{\pi^0}, m_{\pi^0} J_{\rho^+}, M_{\rho^+} \rangle$	$\frac{1}{2}$
$\langle j_{\pi^0}, m_{\pi^0}, j_{\pi^-}, m_{\pi^-} J_{\rho^-}, M_{\rho^-} \rangle$	$-\frac{1}{2}$

The center-of-mass momentum is given by

$$p_{\text{CMS}} = \frac{1}{2\sqrt{s}} \sqrt{(s - (m_{\pi^+} + m_{\pi^-})^2) \cdot (s - (m_{\pi^+} - m_{\pi^-})^2)}. \quad (\text{C.9})$$

The widths are themselves energy-dependent:

$$\Gamma_{\rho^0 \rightarrow \pi^\pm + \pi^\mp}(\sqrt{s}) = \Gamma_{\rho^0 \rightarrow \pi^\pm + \pi^\mp}^{\text{pole}} \frac{m_\rho}{\sqrt{s}} \left(\frac{p_{\text{CMS}}(\sqrt{s})}{p_{\text{CMS}}(m_\rho)} \right)^{2l+1} \frac{1.2}{1 + 0.2 \left(\frac{p_{\text{CMS}}(\sqrt{s})}{p_{\text{CMS}}(m_\rho)} \right)^{2l}}, \quad (\text{C.10})$$

with an angular momentum l of the decay. We are considering only one decay channel for each process, so $\Gamma_{\text{tot}} = \Gamma_{\text{decay channel}}$. In practical numerical integrations we use a simpler Breit-Wigner parameterization of Eq. (C.8).

D. Lorentz invariance

Lorentz invariance one of the most fundamental principles in relativistic kinematics. Physical laws are valid in every coordinate frame, or, experiments will show the same physical results from every inertial frame. Lorentz invariance of particle distribution functions and related collision probabilities (following from the Boltzmann equation) are however a subtle issue which we shall address here.

D.1. Lorentz invariance of phase-space measures and distribution functions

In this section we define the phase space elements in a Lorentz invariant way.

D.1.1. Momentum space measure

The Lorentz transformation of a momentum 4-vector in x -direction reads,

$$\begin{pmatrix} p^0 \\ p^x \\ p^y \\ p^z \end{pmatrix}' = \begin{pmatrix} \gamma & -\beta\gamma & 0 & 0 \\ -\beta\gamma & \gamma & 0 & 0 \\ 0 & 0 & 1 & 0 \\ 0 & 0 & 0 & 1 \end{pmatrix} \begin{pmatrix} p^0 \\ p^x \\ p^y \\ p^z \end{pmatrix} \quad (\text{D.1})$$

Obviously, p^y, p^z do not transform, neither do dp^y, dp^z . For the transformation of dp^x we compute the Jacobian and find

$$dp'_x = \gamma - \beta_x \gamma \frac{p^x}{p^0} dp^x \equiv \frac{U \cdot P}{p^0} dp^x, \quad (\text{D.2})$$

where we defined the 4-velocity

$$U = (u_\mu) = (\gamma, \beta_x, 0, 0). \quad (\text{D.3})$$

The transformation of the momentum space element of a primed to an unprimed system is simply

$$d^3\vec{p}' = \frac{E'}{E} d^3\vec{p}. \quad (\text{D.4})$$

Space time measure

We consider a space time volume element $d^3\vec{x}^{\text{LAB}}$ that contains two particles, a and b. We consider a boosted frame, whose coordinates and momenta will get a prime. At some time, that we call $t = 0$, the frames coincide, $t = t' = 0$, and the two particles are inside $d^3\vec{x}^{\text{LAB}}$. More precise, their initial positions on the x-axis marks the length measure: $x_a(0) - x_b(0) = dx$. For simplicity, we consider only a boost in x-direction. The two particles have 4-trajectories (world lines)

$$X_a(t_a) = \begin{pmatrix} t_a \\ \frac{p_x}{E} t_a + x_a(0) \\ y_a(0) \\ z_a(0) \end{pmatrix}, \quad X_b(t_b) = \begin{pmatrix} t_b \\ \frac{p_x}{E} t_b + x_b(0) \\ y_b(0) \\ z_b(0) \end{pmatrix}. \quad (\text{D.5})$$

From the primed frame, these vectors are

$$X'_a(t_a) = \begin{pmatrix} \gamma t_a - \beta \gamma x_a(t_a) \\ \gamma x_a(t_a) - \beta \gamma t_a \\ y_a(t_a) \\ z_a(t_a) \end{pmatrix}, \quad X'_b(t_b) = \begin{pmatrix} \gamma t_b - \beta \gamma x_b(t_b) \\ \gamma x_b(t_b) - \beta \gamma t_b \\ y_b(t_b) \\ z_b(t_b) \end{pmatrix}. \quad (\text{D.6})$$

As they belong to the same small volume element, we require that the times of a and b are the same. We call this simultaneity:

$$x_a^{0'} \equiv x_b^{0'}. \quad (\text{D.7})$$

We use Eq. (D.6) in Eq.(D.7) to compute a time difference in the LAB,

$$\begin{aligned} \gamma t_a - \beta \gamma x_a(t_a) &= \gamma t_b - \beta \gamma x_b(t_b) \\ t_a - \beta \frac{p_x}{E} t_a - \beta x_a(0) &= t_b - \beta \frac{p_x}{E} t_b - \beta x_b(0) \\ t_a - t_b &= \beta \frac{x_a(0) - x_b(0)}{1 - \beta \frac{p_x}{E}} = \beta \frac{dx(0)}{1 - \beta \frac{p_x}{E}}. \end{aligned} \quad (\text{D.8})$$

Similarly, the distance of a and b in the primed frame is

$$\begin{aligned} dx' \equiv x'_a - x'_b &= \gamma \left(\frac{p_x}{E} t_a + x_a(0) - \frac{p_x}{E} t_b - x_b(0) - \beta(t_a - t_b) \right) \\ &= \gamma \frac{p_x}{E} \left(\beta \frac{dx(0)}{1 - \beta \frac{p_x}{E}} \right) + \gamma dx(0) - \gamma \beta \left(\beta \frac{dx(0)}{1 - \beta \frac{p_x}{E}} \right) \\ &= \gamma dx(0) \left(1 - \frac{1}{1 - \beta \frac{p_x}{E}} \left(\beta \frac{p_x}{E} - \beta^2 \right) \right) \\ &= \gamma dx(0) \frac{1}{\gamma} \frac{E}{\gamma E - \beta \gamma p_x} = dx(0) \frac{E}{E'}. \end{aligned} \quad (\text{D.9})$$

As a conclusion, if the primed observer chooses the volume element

$$d^3 \vec{x}' = \frac{E}{E'} d^3 \vec{x} \quad (\text{D.10})$$

then the number of particles counted instantaneously inside $d^3 \vec{x}'$ is the same as in $d^3 \vec{x}$.

D.1.2. Lorentz invariant distribution function

Combined with Eq. (D.4) we have a Lorentz invariant phase space measure,

$$d^3 \vec{x} d^3 \vec{p} = d^3 \vec{x}' d^3 \vec{p}', \quad (\text{D.11})$$

provided the $d^3 \vec{x}$ is chosen in the way explained above, with the corresponding transformation, which depends on the particles momentum. Following a specific number of particles, we can define a Lorentz invariant distribution function,

$$f(X, \vec{p}) = \frac{dN}{d^3 \vec{x} d^3 \vec{p}}. \quad (\text{D.12})$$

D.2. Boltzmann equation and stochastic collisions

We write down the Boltzmann equation for $f(X, \vec{p})$,

$$p^\mu \frac{\partial}{\partial x^\mu} f(X, P) = C_{22}(X, P) + \dots \quad (\text{D.13})$$

Here we only consider elastic scattering. Using the notation $dK \equiv d^3k / [(2\pi)^3 2k^0]$ the collision term for $2 \leftrightarrow 2$ collisions reads (\mathcal{C}_{22} is C_{22} up to a factor E)

$$\begin{aligned} C_{22}(X_1, P_1) &= \frac{1}{2E_1} \int dP_2 \frac{1}{\nu} \int dP'_1 \int dP'_2 f'_1 f'_2 |\mathcal{M}|^2 (2\pi)^4 \delta^{(4)}(P'_1 + P'_2 - P_1 - P_2) \\ &\quad - \frac{1}{2E_1} \int dP_2 \frac{1}{\nu} \int dP'_1 \int dP'_2 f_1 f_2 |\mathcal{M}|^2 (2\pi)^4 \delta^{(4)}(P_1 + P_2 - P'_1 - P'_2) \end{aligned} \quad (\text{D.14})$$

The total collision cross section is defined as

$$\sigma_{22} = \frac{1}{2s} \frac{1}{\nu} \int dP'_1 \int dP'_2 |\mathcal{M}|^2 (2\pi)^4 \delta^{(4)}(P_1 + P_2 - P'_1 - P'_2) \quad (\text{D.15})$$

The collision term defines the collision rate, which is the number of collisions in a time interval Δt , for two particles inside a volume element $\Delta^3 \vec{x}$ with momenta in momentum space elements $\Delta^3 \vec{p}_1, \Delta^3 \vec{p}_2$ around the momenta p_1, p_2 ,

$$\frac{\Delta N_{\text{coll}}}{\Delta t \Delta^3 \vec{x}} = \frac{\Delta^3 \vec{p}_1}{2(2\pi)^3 E_1} \frac{\Delta^3 \vec{p}_2}{2(2\pi)^3 E_2} f_1 f_2 2s \sigma_{22}. \quad (\text{D.16})$$

Here we defined the Lorentz invariant distribution function of particle 1, $f_1 \equiv f(X_1, \vec{p}_1)$, and particle 2, $f_2 \equiv f(X_2, \vec{p}_2)$ as in (D.12). As it can be seen here, the right hand side of Eq.(D.16) is Lorentz invariant. Thus, also the left hand side must be Lorentz invariant. But, what is the frame and transformation property of $\Delta t \Delta^3 \vec{x}$? For now, we keep it as an undefined space time element, for which the only thing we know is, that Δt and $\Delta^3 \vec{x}$ belong to the same frame, and the product is Lorentz invariant $\Delta t \Delta^3 \vec{x} = \Delta t' \Delta^3 \vec{x}'$. The collision probability in this space time element is

$$P_{22} \equiv \frac{\Delta N_{\text{coll}}}{\Delta N_1 \Delta N_2} = \frac{\Delta t \Delta^3 \vec{x}}{\Delta^3 \vec{x}_1 \Delta^3 \vec{x}_2} \frac{s}{2E_1 E_2} \sigma_{22}. \quad (\text{D.17})$$

In a boosted frame (prime), we have

$$P'_{22} = \frac{\Delta t' \Delta^3 \vec{x}'}{\Delta^3 \vec{x}'_1 \Delta^3 \vec{x}'_2} \frac{s}{2E'_1 E'_2} \sigma_{22} = \frac{\Delta t \Delta^3 \vec{x}}{\Delta^3 \vec{x}_1 \Delta^3 \vec{x}_2} \frac{E'_1 E'_2}{E_1 E_2} \frac{s}{2E'_1 E'_2} \sigma_{22} = P_{22}, \quad (\text{D.18})$$

and thus, Lorentz invariance of Eq.(D.17) is explicitly guaranteed.

As for now, in BAMPS the Lorentz transformation of $\Delta^3 \vec{x}$ is assumed be the same for all particles, independent of their momentum. Under this assumption it is then justified to cancel the volume elements in Eq. (D.17), to end up with the collision probability

$$P_{22}^{\text{BAMPS}} = \frac{\Delta t}{\Delta^3 \vec{x}} \frac{s}{2E_1 E_2} \sigma_{22}. \quad (\text{D.19})$$

Bibliography

- [1] Moritz Greif, Carsten Greiner, and Gabriel S. Denicol, *Electric conductivity of a hot hadron gas from a kinetic approach*, Phys. Rev. D **93** (2016), 096012, [Erratum: Phys. Rev.D 96 (2017),059902], arXiv:1602.05085, doi:10.1103/PhysRevD.93.096012.
- [2] Moritz Greif, Jan A. Fotakis, Gabriel S. Denicol, and Carsten Greiner, *Diffusion of conserved charges in relativistic heavy ion collisions*, Phys. Rev. Lett. **120** (2018), 242301, arXiv:1711.08680, doi:10.1103/PhysRevLett.120.242301.
- [3] Moritz Greif, Carsten Greiner, and Zhe Xu, *Magnetic field influence on the early time dynamics of heavy-ion collisions*, Phys. Rev. C **96** (2017), 014903, arXiv:1704.06505, doi:10.1103/PhysRevC.96.014903.
- [4] Moritz Greif, Florian Senzel, Heiner Kremer, Kai Zhou, Carsten Greiner, and Zhe Xu, *Nonequilibrium photon production in partonic transport simulations*, Phys. Rev. C **95** (2017), 054903, arXiv:1612.05811, doi:10.1103/PhysRevC.95.054903.
- [5] Moritz Greif, Carsten Greiner, Björn Schenke, Sören Schlichting, and Zhe Xu, *Importance of initial and final state effects for azimuthal correlations in p+Pb collisions*, Phys. Rev. D **96** (2017), 091504, arXiv:1708.02076, doi:10.1103/PhysRevD.96.091504.
- [6] C. Patrignani et al., *Review of Particle Physics*, Chin. Phys. C **40** (2016), 100001, doi:10.1088/1674-1137/40/10/100001.
- [7] Michael E. Peskin and Daniel V. Schroeder, *An introduction to quantum field theory*, Addison-Wesley, Reading, USA, 1995.
- [8] Christof Gattringer and Christian B. Lang, *Quantum Chromodynamics on the Lattice*, Lecture Notes in Physics, vol. 788, Springer Berlin Heidelberg, Berlin, Heidelberg, 2010, available from <http://link.springer.com/10.1007/978-3-642-01850-3>, doi:10.1007/978-3-642-01850-3.
- [9] Wikimedia Commons, *Standard model of elementary particles.svg — wikipedia commons, the free media repository*, 2018, available from https://commons.wikimedia.org/w/index.php?title=File:Standard_Model_of_Elementary_Particles.svg&oldid=308836261.
- [10] William A. Bardeen, A. J. Buras, D. W. Duke, and T. Muta, *Deep Inelastic Scattering Beyond the Leading Order in Asymptotically Free Gauge Theories*, Phys. Rev. D **18** (1978), 3998, doi:10.1103/PhysRevD.18.3998.
- [11] K. A. Olive et al., *Review of Particle Physics*, Chin. Phys. C **38** (2014), 090001, doi:10.1088/1674-1137/38/9/090001.
- [12] David J. Gross and Frank Wilczek, *Ultraviolet Behavior of Nonabelian Gauge Theories*, Phys. Rev. Lett. **30** (1973), 1343, doi:10.1103/PhysRevLett.30.1343.

- [13] H. David Politzer, *Reliable Perturbative Results for Strong Interactions?*, Phys. Rev. Lett. **30** (1973), 1346, doi:10.1103/PhysRevLett.30.1346.
- [14] I. Arsene et al., *Quark gluon plasma and color glass condensate at RHIC? The Perspective from the BRAHMS experiment*, Nucl. Phys. A **757** (2005), 1, arXiv:nucl-ex/0410020, doi:10.1016/j.nuclphysa.2005.02.130.
- [15] K. Adcox et al., *Formation of dense partonic matter in relativistic nucleus-nucleus collisions at RHIC: Experimental evaluation by the PHENIX collaboration*, Nucl. Phys. A **757** (2005), 184, arXiv:nucl-ex/0410003, doi:10.1016/j.nuclphysa.2005.03.086.
- [16] B. B. Back et al., *The PHOBOS perspective on discoveries at RHIC*, Nucl. Phys. A **757** (2005), 28, arXiv:nucl-ex/0410022, doi:10.1016/j.nuclphysa.2005.03.084.
- [17] John Adams et al., *Experimental and theoretical challenges in the search for the quark gluon plasma: The STAR Collaboration's critical assessment of the evidence from RHIC collisions*, Nucl. Phys. A **757** (2005), 102, arXiv:nucl-ex/0501009, doi:10.1016/j.nuclphysa.2005.03.085.
- [18] John C. Collins and M. J. Perry, *Superdense Matter: Neutrons Or Asymptotically Free Quarks?*, Phys. Rev. Lett. **34** (1975), 1353, doi:10.1103/PhysRevLett.34.1353.
- [19] N. Cabibbo and G. Parisi, *Exponential Hadronic Spectrum and Quark Liberation*, Phys. Lett. B **59** (1975), 67, doi:10.1016/0370-2693(75)90158-6.
- [20] Johann Rafelski and Berndt Muller, *Strangeness Production in the Quark - Gluon Plasma*, Phys. Rev. Lett. **48** (1982), 1066, [Erratum: Phys. Rev. Lett. 56 (1986), 2334], doi:10.1103/PhysRevLett.48.1066.
- [21] T. Matsui and H. Satz, *J/ψ Suppression by Quark-Gluon Plasma Formation*, Phys. Lett. B **178** (1986), 416, doi:10.1016/0370-2693(86)91404-8.
- [22] J. D. Bjorken, *Highly Relativistic Nucleus-Nucleus Collisions: The Central Rapidity Region*, Phys. Rev. D **27** (1983), 140, doi:10.1103/PhysRevD.27.140.
- [23] Joseph I. Kapusta, P. Lichard, and D. Seibert, *High-energy photons from quark - gluon plasma versus hot hadronic gas*, Phys. Rev. D **44** (1991), 2774, [Erratum: Phys. Rev. D 47 (1993), 4171], doi:10.1103/PhysRevD.44.2774.
- [24] Ulrich W. Heinz and Maurice Jacob, *Evidence for a new state of matter: An Assessment of the results from the CERN lead beam program*, (2000), arXiv:nucl-th/0002042.
- [25] H. Appelshauser et al., *Hadronic expansion dynamics in central Pb + Pb collisions at 158-GeV per nucleon*, Eur. Phys. J. C **2** (1998), 661, arXiv:hep-ex/9711024.
- [26] J. Bachler et al., *Hadron production in nuclear collisions from the NA49 experiment at 158-GeV/c/A*, Nucl. Phys. A **661** (1999), 45, doi:10.1016/S0375-9474(99)85007-6.
- [27] M. M. Aggarwal et al., *Freezeout parameters in central 158/A-GeV Pb-208 + Pb-208 collisions*, Phys. Rev. Lett. **83** (1999), 926, arXiv:nucl-ex/9901009, doi:10.1103/PhysRevLett.83.926.

-
- [28] I. G. Bearden et al., *Collective expansion in high-energy heavy ion collisions*, Phys. Rev. Lett. **78** (1997), 2080, doi:10.1103/PhysRevLett.78.2080.
- [29] M. C. Abreu et al., *Anomalous J/ψ suppression in Pb - Pb interactions at 158 GeV/c per nucleon*, Phys. Lett. B **410** (1997), 337, doi:10.1016/S0370-2693(97)00915-5.
- [30] M. C. Abreu et al., *Observation of a threshold effect in the anomalous J/ψ suppression*, Phys. Lett. B **450** (1999), 456, doi:10.1016/S0370-2693(99)00178-1.
- [31] M. C. Abreu et al., *Evidence for deconfinement of quarks and gluons from the J/ψ suppression pattern measured in Pb + Pb collisions at the CERN SPS*, Phys. Lett. B **477** (2000), 28, doi:10.1016/S0370-2693(00)00237-9.
- [32] A. Capella, A. B. Kaidalov, and D. Sousa, *Why is the J/ψ suppression enhanced at large transverse energy?*, Phys. Rev. C **65** (2002), 054908, arXiv:nucl-th/0105021, doi:10.1103/PhysRevC.65.054908.
- [33] I. Bearden et al., *Strange meson enhancement in Pb Pb collisions*, Phys. Lett. B **471** (1999), 6, arXiv:nucl-ex/9907013, doi:10.1016/S0370-2693(99)01327-1.
- [34] R. Albrecht et al., *Limits on the production of direct photons in 200-A/GeV S-32 + Au collisions*, Phys. Rev. Lett. **76** (1996), 3506, doi:10.1103/PhysRevLett.76.3506.
- [35] B. Lenkeit et al., *New results on low-mass lepton pair production in Pb-Au collisions at 158 GeV per nucleon*, Nucl. Phys. A **654** (1999), 627c, doi:10.1016/S0375-9474(00)88514-0.
- [36] G. Agakishiev et al., *Low mass e^+e^- pair production in 158/A-GeV Pb - Au collisions at the CERN SPS, its dependence on multiplicity and transverse momentum*, Phys. Lett. B **422** (1998), 405, arXiv:nucl-ex/9712008, doi:10.1016/S0370-2693(98)00083-5.
- [37] I. Arsene et al., *Transverse momentum spectra in Au+Au and d+Au collisions at $s^{1/2} = 200$ -GeV and the pseudorapidity dependence of high $p(T)$ suppression*, Phys. Rev. Lett. **91** (2003), 072305, arXiv:nucl-ex/0307003, doi:10.1103/PhysRevLett.91.072305.
- [38] T. Ludlam, *Experimental results from the early measurements at RHIC: Hunting for the quark-gluon plasma*, Nucl. Phys. A **750** (2005), 9, doi:10.1016/j.nuclphysa.2004.11.005.
- [39] Aleksi Kurkela, Aleksas Mazeliauskas, Jean-François Paquet, Sören Schlichting, and Derek Teaney, *Effective kinetic description of event-by-event pre-equilibrium dynamics in high-energy heavy-ion collisions*, (2018), arXiv:1805.00961.
- [40] Zhe Xu and Carsten Greiner, *Thermalization of gluons in ultrarelativistic heavy ion collisions by including three-body interactions in a parton cascade*, Phys. Rev. C **71** (2005), 064901, arXiv:hep-ph/0406278, doi:10.1103/PhysRevC.71.064901.
- [41] Edward V. Shuryak, *Theory and phenomenology of the QCD vacuum*, Phys. Rept. **115** (1984), 151, doi:10.1016/0370-1573(84)90037-1.

- [42] K. H. Ackermann et al., *Elliptic flow in Au + Au collisions at $(S(NN))^{1/2} = 130$ GeV*, Phys. Rev. Lett. **86** (2001), 402, arXiv:nucl-ex/0009011, doi:10.1103/PhysRevLett.86.402.
- [43] C. Adler et al., *Elliptic flow from two and four particle correlations in Au+Au collisions at $s(NN)^{1/2} = 130$ -GeV*, Phys. Rev. C **66** (2002), 034904, arXiv:nucl-ex/0206001, doi:10.1103/PhysRevC.66.034904.
- [44] S. S. Adler et al., *Scaling properties of proton and anti-proton production in $s(NN)^{1/2} = 200$ -GeV Au+Au collisions*, Phys. Rev. Lett. **91** (2003), 172301, arXiv:nucl-ex/0305036, doi:10.1103/PhysRevLett.91.172301.
- [45] P. Huovinen, P. F. Kolb, Ulrich W. Heinz, P. V. Ruuskanen, and S. A. Voloshin, *Radial and elliptic flow at RHIC: Further predictions*, Phys. Lett. B **503** (2001), 58, arXiv:hep-ph/0101136, doi:10.1016/S0370-2693(01)00219-2.
- [46] S. S. Adler et al., *Absence of suppression in particle production at large transverse momentum in $S(NN)^{1/2} = 200$ -GeV d + Au collisions*, Phys. Rev. Lett. **91** (2003), 072303, arXiv:nucl-ex/0306021, doi:10.1103/PhysRevLett.91.072303.
- [47] B. B. Back et al., *Centrality dependence of charged hadron transverse momentum spectra in d + Au collisions at $S(NN)^{1/2} = 200$ GeV*, Phys. Rev. Lett. **91** (2003), 072302, arXiv:nucl-ex/0306025, doi:10.1103/PhysRevLett.91.072302.
- [48] J. Adams et al., *Evidence from d + Au measurements for final state suppression of high $p(T)$ hadrons in Au+Au collisions at RHIC*, Phys. Rev. Lett. **91** (2003), 072304, arXiv:nucl-ex/0306024, doi:10.1103/PhysRevLett.91.072304.
- [49] A. Majumder and M. Van Leeuwen, *The Theory and Phenomenology of Perturbative QCD Based Jet Quenching*, Prog. Part. Nucl. Phys. **66** (2011), 41, arXiv:1002.2206, doi:10.1016/j.pnpnp.2010.09.001.
- [50] C. Adler et al., *Identified particle elliptic flow in Au + Au collisions at $s(NN)^{1/2} = 130$ -GeV*, Phys. Rev. Lett. **87** (2001), 182301, arXiv:nucl-ex/0107003, doi:10.1103/PhysRevLett.87.182301.
- [51] Raimond Snellings, *Anisotropic flow from RHIC to the LHC*, Eur. Phys. J. C **49** (2007), 87, arXiv:nucl-ex/0610010, doi:10.1140/epjc/s10052-006-0107-4.
- [52] P. Kovtun, Dan T. Son, and Andrei O. Starinets, *Viscosity in strongly interacting quantum field theories from black hole physics*, Phys. Rev. Lett. **94** (2005), 111601, arXiv:hep-th/0405231, doi:10.1103/PhysRevLett.94.111601.
- [53] Ulrich W. Heinz, Huichao Song, and Asis K. Chaudhuri, *Dissipative hydrodynamics for viscous relativistic fluids*, Phys. Rev. C **73** (2006), 034904, arXiv:nucl-th/0510014, doi:10.1103/PhysRevC.73.034904.
- [54] Rudolf Baier and Paul Romatschke, *Causal viscous hydrodynamics for central heavy-ion collisions*, Eur. Phys. J. C **51** (2007), 677, arXiv:nucl-th/0610108, doi:10.1140/epjc/s10052-007-0308-5.
- [55] Paul Romatschke, *Causal viscous hydrodynamics for central heavy-ion collisions. II. Meson spectra and HBT radii*, Eur. Phys. J. C **52** (2007), 203, arXiv:nucl-th/0701032, doi:10.1140/epjc/s10052-007-0354-z.

-
- [56] Ulrich Heinz and Raimond Snellings, *Collective flow and viscosity in relativistic heavy-ion collisions*, *Ann. Rev. Nucl. Part. Sci.* **63** (2013), 123, [arXiv:1301.2826](#), [doi:10.1146/annurev-nucl-102212-170540](#).
- [57] Charles Gale, Sangyong Jeon, and Bjoern Schenke, *Hydrodynamic Modeling of Heavy-Ion Collisions*, *Int. J. of Mod. Phys. A*, Vol. 28, **1340011** (2013), [arXiv:1301.5893](#), [doi:10.1142/S0217751X13400113](#).
- [58] R. Derradi de Souza, Tomoi Koide, and Takeshi Kodama, *Hydrodynamic Approaches in Relativistic Heavy Ion Reactions*, *Prog. Part. Nucl. Phys.* **86** (2016), 35, [arXiv:1506.03863](#), [doi:10.1016/j.ppnp.2015.09.002](#).
- [59] Huichao Song, You Zhou, and Katarina Gajdosova, *Collective flow and hydrodynamics in large and small systems at the LHC*, *Nucl. Sci. Tech.* **28** (2017), 99, [arXiv:1703.00670](#), [doi:10.1007/s41365-017-0245-4](#).
- [60] Harri Niemi, Gabriel S. Denicol, Pasi Huovinen, Etele Molnar, and Dirk H. Rischke, *Influence of the shear viscosity of the quark-gluon plasma on elliptic flow in ultrarelativistic heavy-ion collisions*, *Phys. Rev. Lett.* **106** (2011), 212302, [arXiv:1101.2442](#), [doi:10.1103/PhysRevLett.106.212302](#).
- [61] Harvey B. Meyer, *A Calculation of the shear viscosity in $SU(3)$ gluodynamics*, *Phys. Rev. D* **76** (2007), 101701, [arXiv:0704.1801](#), [doi:10.1103/PhysRevD.76.101701](#).
- [62] Atsushi Nakamura and Sunao Sakai, *Transport coefficients of gluon plasma*, *Phys. Rev. Lett.* **94** (2005), 072305, [arXiv:hep-lat/0406009](#), [doi:10.1103/PhysRevLett.94.072305](#).
- [63] Simon W Mages, Szabolcs Borsányi, Zoltán Fodor, Andreas Schäfer, and Kálmán Szabó, *Shear Viscosity from Lattice QCD*, *PoS LATTICE 2014* (2015), 232.
- [64] C. Wesp, A. El, F. Reining, Z. Xu, I. Bouras, and C. Greiner, *Calculation of shear viscosity using Green-Kubo relations within a parton cascade*, *Phys. Rev. C* **84** (2011), 054911, [arXiv:1106.4306](#), [doi:10.1103/PhysRevC.84.054911](#).
- [65] Zhe Xu, Carsten Greiner, and Horst Stocker, *PQCD calculations of elliptic flow and shear viscosity at RHIC*, *Phys. Rev. Lett.* **101** (2008), 082302, [arXiv:0711.0961](#), [doi:10.1103/PhysRevLett.101.082302](#).
- [66] Andrej El, Francesco Lauciello, Christian Wesp, Zhe Xu, and Carsten Greiner, *Shear viscosity of an ultrarelativistic Boltzmann gas with isotropic inelastic scattering processes*, *Nucl. Phys. A* **925** (2014), 150, [arXiv:1207.5331](#), [doi:10.1016/j.nuclphysa.2014.02.009](#).
- [67] Zhe Xu and Carsten Greiner, *Shear viscosity in a gluon gas*, *Phys. Rev. Lett.* **100** (2008), 172301, [arXiv:0710.5719](#), [doi:10.1103/PhysRevLett.100.172301](#).
- [68] Peter Brockway Arnold, Guy D. Moore, and Laurence G. Yaffe, *Transport coefficients in high temperature gauge theories. 1. Leading log results*, *JHEP* **11** (2000), 001, [arXiv:hep-ph/0010177](#), [doi:10.1088/1126-6708/2000/11/001](#).
- [69] Peter Brockway Arnold, Guy D Moore, and Laurence G. Yaffe, *Transport coefficients in high temperature gauge theories. 2. Beyond leading log*, *JHEP* **05** (2003), 051, [arXiv:hep-ph/0302165](#), [doi:10.1088/1126-6708/2003/05/051](#).

- [70] Nicolai Christiansen, Michael Haas, Jan M. Pawłowski, and Nils Strodthoff, *Transport Coefficients in Yang–Mills Theory and QCD*, Phys. Rev. Lett. **115** (2015), 112002, arXiv:1411.7986, doi:10.1103/PhysRevLett.115.112002.
- [71] Hamza Berrehrah, Elena Bratkovskaya, Thorsten Steinert, and Wolfgang Cassing, *A dynamical quasiparticle approach for the QGP bulk and transport properties*, Int. J. Mod. Phys. E **25** (2016), 1642003, arXiv:1605.02371, doi:10.1142/S0218301316420039.
- [72] Gabriel S. Denicol, Charles Gale, Sangyong Jeon, and Jorge Noronha, *Fluid behavior of a baryon-rich hadron resonance gas*, Phys. Rev. C **88** (2013), 064901, arXiv:1308.1923, doi:10.1103/PhysRevC.88.064901.
- [73] Anton Wiranata, Volker Koch, Madappa Prakash, and Xin Nian Wang, *Shear viscosity of hadrons with K-matrix cross sections*, Phys. Rev. C **88** (2013), 044917, arXiv:1307.4681, doi:10.1103/PhysRevC.88.044917.
- [74] J. B. Rose, J. M. Torres-Rincon, A. Schäfer, D. R. Oliinychenko, and H. Petersen, *Shear viscosity of a hadron gas and influence of resonance lifetimes on relaxation time*, Phys. Rev. **C97** (2018), 055204, arXiv:1709.03826, doi:10.1103/PhysRevC.97.055204.
- [75] Laszlo P. Csernai, Joseph.I. Kapusta, and Larry D. McLerran, *On the Strongly-Interacting Low-Viscosity Matter Created in Relativistic Nuclear Collisions*, Phys. Rev. Lett. **97** (2006), 152303, arXiv:nucl-th/0604032, doi:10.1103/PhysRevLett.97.152303.
- [76] Jaroslav Adam et al., *Direct photon production in Pb-Pb collisions at $\sqrt{s_{NN}}=2.76$ TeV*, Phys. Lett. B **754** (2016), 235, arXiv:1509.07324, doi:10.1016/j.physletb.2016.01.020.
- [77] Shreyasi Acharya et al., *Direct photon elliptic flow in Pb-Pb collisions at $\sqrt{s_{NN}} = 2.76$ TeV*, (2018), arXiv:1805.04403.
- [78] A. Adare et al., *Enhanced production of direct photons in Au+Au collisions at $\sqrt{s_{NN}}=200$ GeV and implications for the initial temperature*, Phys. Rev. Lett. **104** (2010), 132301, arXiv:0804.4168, doi:10.1103/PhysRevLett.104.132301.
- [79] S. Afanasiev et al., *Measurement of Direct Photons in Au+Au Collisions at $\sqrt{s_{NN}} = 200$ GeV*, Phys. Rev. Lett. **109** (2012), 152302, arXiv:1205.5759, doi:10.1103/PhysRevLett.109.152302.
- [80] A. Adare et al., *Centrality dependence of low-momentum direct-photon production in Au+Au collisions at $\sqrt{s_{NN}} = 200$ GeV*, Phys. Rev. C **91** (2015), 064904, arXiv:1405.3940, doi:10.1103/PhysRevC.91.064904.
- [81] O. Linnyk, V. P. Konchakovski, W. Cassing, and E. L. Bratkovskaya, *Photon elliptic flow in relativistic heavy-ion collisions: hadronic versus partonic sources*, Phys. Rev. C **88** (2013), 034904, arXiv:1304.7030, doi:10.1103/PhysRevC.88.034904.
- [82] S. S. Adler et al., *Centrality dependence of direct photon production in $s(NN)^{1/2} = 200$ -GeV Au + Au collisions*, Phys. Rev. Lett. **94** (2005), 232301, arXiv:nucl-ex/0503003, doi:10.1103/PhysRevLett.94.232301.

-
- [83] S. S. Adler et al., *Measurement of direct photon production in $p + p$ collisions at $\sqrt{s^{**}(1/2)} = 200$ -GeV*, Phys. Rev. Lett. **98** (2007), 012002, arXiv:hep-ex/0609031, doi:10.1103/PhysRevLett.98.012002.
- [84] A. Adare et al., *Direct photon production in $d+Au$ collisions at $\sqrt{s_{NN}} = 200$ GeV*, Phys. Rev. C **87** (2013), 054907, arXiv:1208.1234, doi:10.1103/PhysRevC.87.054907.
- [85] Hendrik van Hees, Charles Gale, and Ralf Rapp, *Thermal Photons and Collective Flow at the Relativistic Heavy-Ion Collider*, Phys. Rev. C **84** (2011), 054906, arXiv:1108.2131, doi:10.1103/PhysRevC.84.054906.
- [86] Ralf Rapp, *Dilepton Spectroscopy of QCD Matter at Collider Energies*, Adv. High Energy Phys. **2013** (2013), 148253, arXiv:1304.2309, doi:10.1155/2013/148253.
- [87] Bjorn Schenke, Sangyong Jeon, and Charles Gale, *Elliptic and triangular flow in event-by-event (3+1)D viscous hydrodynamics*, Phys. Rev. Lett. **106** (2011), 042301, arXiv:1009.3244, doi:10.1103/PhysRevLett.106.042301.
- [88] Chun Shen and Ulrich Heinz, *Collision Energy Dependence of Viscous Hydrodynamic Flow in Relativistic Heavy-Ion Collisions*, Phys. Rev. C **85** (2012), 054902, [Erratum: Phys. Rev. C **86** (2012), 049903], arXiv:1202.6620, doi:10.1103/PhysRevC.85.054902.
- [89] Peter F. Kolb and Ulrich W. Heinz, *Hydrodynamic description of ultrarelativistic heavy ion collisions*, (2003), 634, arXiv:nucl-th/0305084.
- [90] D. Teaney, J. Lauret, and Edward V. Shuryak, *Flow at the SPS and RHIC as a quark gluon plasma signature*, Phys. Rev. Lett. **86** (2001), 4783, arXiv:nucl-th/0011058, doi:10.1103/PhysRevLett.86.4783.
- [91] L. Del Zanna, V. Chandra, G. Inghirami, V. Rolando, A. Beraudo, A. De Pace, G. Pagliara, A. Drago, and F. Becattini, *Relativistic viscous hydrodynamics for heavy-ion collisions with ECHO-QGP*, Eur. Phys. J. C **73** (2013), 2524, arXiv:1305.7052, doi:10.1140/epjc/s10052-013-2524-5.
- [92] Iu. Karpenko, P. Huovinen, and M. Bleicher, *A 3+1 dimensional viscous hydrodynamic code for relativistic heavy ion collisions*, Comput. Phys. Commun. **185** (2014), 3016, arXiv:1312.4160, doi:10.1016/j.cpc.2014.07.010.
- [93] Hannu Holopainen, Harri Niemi, and Kari J. Eskola, *Event-by-event hydrodynamics and elliptic flow from fluctuating initial state*, Phys. Rev. C **83** (2011), 034901, arXiv:1007.0368, doi:10.1103/PhysRevC.83.034901.
- [94] Jean-François Paquet, Chun Shen, Gabriel S. Denicol, Matthew Luzum, Björn Schenke, Sangyong Jeon, and Charles Gale, *Production of photons in relativistic heavy-ion collisions*, Phys. Rev. C **93** (2016), 044906, arXiv:1509.06738, doi:10.1103/PhysRevC.93.044906.
- [95] Rupa Chatterjee, Hannu Holopainen, Ilkka Helenius, Thorsten Renk, and Kari J. Eskola, *Elliptic flow of thermal photons from event-by-event hydrodynamic model*, Phys. Rev. C **88** (2013), 034901, arXiv:1305.6443, doi:10.1103/PhysRevC.88.034901.

-
- [96] Rupa Chatterjee, Hannu Holopainen, Thorsten Renk, and Kari J. Eskola, *Enhancement of thermal photon production in event-by-event hydrodynamics*, Phys. Rev. C **83** (2011), 054908, arXiv:1102.4706, doi:10.1103/PhysRevC.83.054908.
- [97] Fu-Ming Liu, Tetsufumi Hirano, Klaus Werner, and Yan Zhu, *Centrality-dependent direct photon $p(t)$ spectra in Au + Au collisions at RHIC*, Phys. Rev. C **79** (2009), 014905, arXiv:0807.4771, doi:10.1103/PhysRevC.79.014905.
- [98] Chun Shen, Jean-François Paquet, Gabriel S. Denicol, Sangyong Jeon, and Charles Gale, *Collectivity and electromagnetic radiation in small systems*, Phys. Rev. C **95** (2017), 014906, arXiv:1609.02590, doi:10.1103/PhysRevC.95.014906.
- [99] Charles Gale, Yoshimasa Hidaka, Sangyong Jeon, Shu Lin, Jean-François Paquet, Robert D. Pisarski, Daisuke Satow, Vladimir V. Skokov, and Gojko Vujanovic, *Production and Elliptic Flow of Dileptons and Photons in a Matrix Model of the Quark-Gluon Plasma*, Phys. Rev. Lett. **114** (2015), 072301, arXiv:1409.4778, doi:10.1103/PhysRevLett.114.072301.
- [100] Ioannis Iatrakis, Elias Kiritsis, Chun Shen, and Di-Lun Yang, *Holographic Photon Production in Heavy Ion Collisions*, JHEP **04** (2017), 035, arXiv:1609.07208, doi:10.1007/JHEP04(2017)035.
- [101] Gojko Vujanovic, Jean-François Paquet, Gabriel S. Denicol, Matthew Luzum, Sangyong Jeon, and Charles Gale, *Electromagnetic radiation as a probe of the initial state and of viscous dynamics in relativistic nuclear collisions*, Phys. Rev. C **94** (2016), 014904, arXiv:1602.01455, doi:10.1103/PhysRevC.94.014904.
- [102] Sanjin Benic and Kenji Fukushima, *Photon from the annihilation process with CGC in the pA collision*, Nucl. Phys. A **958** (2017), 1, arXiv:1602.01989, doi:10.1016/j.nuclphysa.2016.11.003.
- [103] Alejandro Ayala, Jorge David Castano-Yepes, Cesareo A. Dominguez, Luis A. Hernandez, Saul Hernandez-Ortiz, and Maria Elena Tejeda-Yeomans, *Prompt photon yield and elliptic flow from gluon fusion induced by magnetic fields in relativistic heavy-ion collisions*, Phys. Rev. D **96** (2017), 014023, arXiv:1704.02433, doi:10.1103/PhysRevD.96.014023.
- [104] A. Adare et al., *Azimuthally anisotropic emission of low-momentum direct photons in Au+Au collisions at $\sqrt{s_{NN}} = 200$ GeV*, Phys. Rev. C **94** (2016), 064901, arXiv:1509.07758, doi:10.1103/PhysRevC.94.064901.
- [105] Daniel Lohner, *Measurement of Direct-Photon Elliptic Flow in Pb-Pb Collisions at $\sqrt{s_{NN}} = 2.76$ TeV*, J. Phys. Conf. Ser. **446** (2013), 012028, arXiv:1212.3995, doi:10.1088/1742-6596/446/1/012028.
- [106] Charles Gale, Sangyong Jeon, Björn Schenke, Prithwish Tribedy, and Raju Venugopalan, *Event-by-event anisotropic flow in heavy-ion collisions from combined Yang-Mills and viscous fluid dynamics*, Phys. Rev. Lett. **110** (2013), 012302, arXiv:1209.6330, doi:10.1103/PhysRevLett.110.012302.
- [107] Zhi Qiu and Ulrich W. Heinz, *Event-by-event shape and flow fluctuations of relativistic heavy-ion collision fireballs*, Phys. Rev. C **84** (2011), 024911, arXiv:1104.0650, doi:10.1103/PhysRevC.84.024911.

- [108] K. Werner, Iu. Karpenko, T. Pierog, M. Bleicher, and K. Mikhailov, *Event-by-Event Simulation of the Three-Dimensional Hydrodynamic Evolution from Flux Tube Initial Conditions in Ultrarelativistic Heavy Ion Collisions*, Phys. Rev. C **82** (2010), 044904, arXiv:1004.0805, doi:10.1103/PhysRevC.82.044904.
- [109] W. Cassing and E. L. Bratkovskaya, *Parton-Hadron-String Dynamics: an off-shell transport approach for relativistic energies*, Nucl. Phys. A **831** (2009), 215, arXiv:0907.5331, doi:10.1016/j.nuclphysa.2009.09.007.
- [110] O. Linnyk, W. Cassing, and E. L. Bratkovskaya, *Centrality dependence of the direct photon yield and elliptic flow in heavy-ion collisions at $\sqrt{s_{NN}} = 200$ GeV*, Phys. Rev. C **89** (2014), 034908, arXiv:1311.0279, doi:10.1103/PhysRevC.89.034908.
- [111] S. A. Bass et al., *Microscopic models for ultrarelativistic heavy ion collisions*, Prog. Part. Nucl. Phys. **41** (1998), 255, [Prog. Part. Nucl. Phys.41,225(1998)], arXiv:nucl-th/9803035, doi:10.1016/S0146-6410(98)00058-1.
- [112] M. Bleicher et al., *Relativistic hadron hadron collisions in the ultrarelativistic quantum molecular dynamics model*, J. Phys. G **25** (1999), 1859, arXiv:hep-ph/9909407, doi:10.1088/0954-3899/25/9/308.
- [113] Stephan Endres, Hendrik van Hees, Janus Weil, and Marcus Bleicher, *Dilepton production and reaction dynamics in heavy-ion collisions at SIS energies from coarse-grained transport simulations*, Phys. Rev. C **92** (2015), 014911, arXiv:1505.06131, doi:10.1103/PhysRevC.92.014911.
- [114] J. Jalilian-Marian and V. Koch, *Bremsstrahlung dileptons in ultrarelativistic heavy ion collisions*, Phys. Rev. C **58** (1998), 3763, arXiv:nucl-th/9807013, doi:10.1103/PhysRevC.58.3763.
- [115] S. D. Drell and Tung-Mow Yan, *Massive Lepton Pair Production in Hadron-Hadron Collisions at High-Energies*, Phys. Rev. Lett. **25** (1970), 316, [Erratum: Phys. Rev. Lett. 25 (1970),902], doi:10.1103/PhysRevLett.25.316.
- [116] Ralf Rapp and Hendrik van Hees, *Thermal Dileptons as Fireball Thermometer and Chronometer*, Phys. Lett. B **753** (2016), 586, arXiv:1411.4612, doi:10.1016/j.physletb.2015.12.065.
- [117] Hendrik van Hees and Ralf Rapp, *Comprehensive interpretation of thermal dileptons at the SPS*, Phys. Rev. Lett. **97** (2006), 102301, arXiv:hep-ph/0603084, doi:10.1103/PhysRevLett.97.102301.
- [118] G. Agakichiev et al., *Enhanced production of low mass electron pairs in 200-GeV/u S - Au collisions at the CERN SPS*, Phys. Rev. Lett. **75** (1995), 1272, doi:10.1103/PhysRevLett.75.1272.
- [119] M. C. Abreu et al., *Muon pair and vector meson cross-sections in p W and S U collisions at 200-GeV/nucleon*, Phys. Lett. B **368** (1996), 230, doi:10.1016/0370-2693(95)01501-9.
- [120] M. Gonin et al., *Anomalous J / psi suppression in Pb + Pb collisions at 158-A-GeV/c*, Nucl. Phys. A **610** (1996), 404C, doi:10.1016/S0375-9474(96)00373-9.
- [121] R. Rapp and J. Wambach, *Chiral symmetry restoration and dileptons in relativistic heavy ion collisions*, Adv. Nucl. Phys. **25** (2000), 1, arXiv:hep-ph/9909229, doi:10.1007/0-306-47101-9_1.

- [122] R. Rapp, G. Chanfray, and J. Wambach, *Medium modifications of the rho meson at CERN SPS energies*, Phys. Rev. Lett. **76** (1996), 368, arXiv:hep-ph/9508353, doi:10.1103/PhysRevLett.76.368.
- [123] Ralf Rapp, *Thermal lepton production in heavy ion collisions*, 18th Winter Workshop on Nuclear Dynamics (WWND 2002) Nassau, Bahamas, January 20-22, 2002, 2002, arXiv:nucl-th/0204003.
- [124] R. Arnaldi et al., *First measurement of the rho spectral function in high-energy nuclear collisions*, Phys. Rev. Lett. **96** (2006), 162302, arXiv:nucl-ex/0605007, doi:10.1103/PhysRevLett.96.162302.
- [125] Hendrik van Hees and Ralf Rapp, *Dilepton Radiation at the CERN Super Proton-Synchrotron*, Nucl. Phys. A **806** (2008), 339, arXiv:0711.3444, doi:10.1016/j.nuclphysa.2008.03.009.
- [126] L. Adamczyk et al., *Dielectron Mass Spectra from Au+Au Collisions at $\sqrt{s_{NN}} = 200$ GeV*, Phys. Rev. Lett. **113** (2014), 022301, [Addendum: Phys. Rev. Lett. **113** (2014), 049903], arXiv:1312.7397, doi:10.1103/PhysRevLett.113.022301.
- [127] L. Adamczyk et al., *Measurements of Dielectron Production in Au+Au Collisions at $\sqrt{s_{NN}} = 200$ GeV from the STAR Experiment*, Phys. Rev. C **92** (2015), 024912, arXiv:1504.01317, doi:10.1103/PhysRevC.92.024912.
- [128] L. Adamczyk et al., *Energy dependence of acceptance-corrected dielectron excess mass spectrum at mid-rapidity in Au+Au collisions at $\sqrt{s_{NN}} = 19.6$ and 200 GeV*, Phys. Lett. B **750** (2015), 64, arXiv:1501.05341, doi:10.1016/j.physletb.2015.08.044.
- [129] A. Adare et al., *Dielectron production in Au+Au collisions at $\sqrt{s_{NN}}=200$ GeV*, Phys. Rev. C **93** (2016), 014904, arXiv:1509.04667, doi:10.1103/PhysRevC.93.014904.
- [130] Peter F. Kolb, Josef Sollfrank, and Ulrich W. Heinz, *Anisotropic transverse flow and the quark hadron phase transition*, Phys. Rev. C **62** (2000), 054909, arXiv:hep-ph/0006129, doi:10.1103/PhysRevC.62.054909.
- [131] L. Adamczyk et al., *Bulk Properties of the Medium Produced in Relativistic Heavy-Ion Collisions from the Beam Energy Scan Program*, Phys. Rev. C **96** (2017), 044904, arXiv:1701.07065, doi:10.1103/PhysRevC.96.044904.
- [132] Sandeep Chatterjee, Sabita Das, Lokesh Kumar, D. Mishra, Bedangadas Mohanty, Raghunath Sahoo, and Natasha Sharma, *Freeze-Out Parameters in Heavy-Ion Collisions at AGS, SPS, RHIC, and LHC Energies*, Adv. High Energy Phys. **2015** (2015), 349013, doi:10.1155/2015/349013.
- [133] Yukinao Akamatsu, Tetsuo Hatsuda, and Tetsufumi Hirano, *Heavy Quark Diffusion with Relativistic Langevin Dynamics in the Quark-Gluon Fluid*, Phys. Rev. C **79** (2009), 054907, arXiv:0809.1499, doi:10.1103/PhysRevC.79.054907.
- [134] Santosh K. Das, Francesco Scardina, Salvatore Plumari, and Vincenzo Greco, *Heavy-flavor in-medium momentum evolution: Langevin versus Boltzmann approach*, Phys. Rev. C **90** (2014), 044901, arXiv:1312.6857, doi:10.1103/PhysRevC.90.044901.

-
- [135] Paul Romatschke and Ulrike Romatschke, *Viscosity Information from Relativistic Nuclear Collisions: How Perfect is the Fluid Observed at RHIC?*, Phys. Rev. Lett. **99** (2007), 172301, arXiv:0706.1522, doi:10.1103/PhysRevLett.99.172301.
- [136] Peter Brockway Arnold, Caglar Dogan, and Guy D. Moore, *The Bulk Viscosity of High-Temperature QCD*, Phys. Rev. D **74** (2006), 085021, arXiv:hep-ph/0608012, doi:10.1103/PhysRevD.74.085021.
- [137] Dmitri Kharzeev and Kirill Tuchin, *Bulk viscosity of QCD matter near the critical temperature*, JHEP **09** (2008), 093, arXiv:0705.4280, doi:10.1088/1126-6708/2008/09/093.
- [138] Piotr Bozek, *Bulk and shear viscosities of matter created in relativistic heavy-ion collisions*, Phys. Rev. C **81** (2010), 034909, arXiv:0911.2397, doi:10.1103/PhysRevC.81.034909.
- [139] Jacquelyn Noronha-Hostler, Gabriel S. Denicol, Jorge Noronha, Rone P. G. Andrade, and Frederique Grassi, *Bulk Viscosity Effects in Event-by-Event Relativistic Hydrodynamics*, Phys. Rev. C **88** (2013), 044916, arXiv:1305.1981, doi:10.1103/PhysRevC.88.044916.
- [140] Mohammad Nopoush, Radoslaw Ryblewski, and Michael Strickland, *Bulk viscous evolution within anisotropic hydrodynamics*, Phys. Rev. C **90** (2014), 014908, arXiv:1405.1355, doi:10.1103/PhysRevC.90.014908.
- [141] G. S. Denicol, S. Jeon, and C. Gale, *Transport Coefficients of Bulk Viscous Pressure in the 14-moment approximation*, Phys. Rev. C **90** (2014), 024912, arXiv:1403.0962, doi:10.1103/PhysRevC.90.024912.
- [142] S. Ryu, J. F. Paquet, C. Shen, G. S. Denicol, B. Schenke, S. Jeon, and C. Gale, *Importance of the Bulk Viscosity of QCD in Ultrarelativistic Heavy-Ion Collisions*, Phys. Rev. Lett. **115** (2015), 132301, arXiv:1502.01675, doi:10.1103/PhysRevLett.115.132301.
- [143] Sangwook Ryu, Jean-François Paquet, Chun Shen, Gabriel Denicol, Björn Schenke, Sangyong Jeon, and Charles Gale, *Effects of bulk viscosity and hadronic rescattering in heavy ion collisions at energies available at the BNL Relativistic Heavy Ion Collider and at the CERN Large Hadron Collider*, Phys. Rev. **C97** (2018), 034910, arXiv:1704.04216, doi:10.1103/PhysRevC.97.034910.
- [144] Sourendu Gupta, *The Electrical conductivity and soft photon emissivity of the QCD plasma*, Phys. Lett. B **597** (2004), 57, arXiv:hep-lat/0301006, doi:10.1016/j.physletb.2004.05.079.
- [145] P. V. Buividovich, M. N. Chernodub, D. E. Kharzeev, T. Kalaydzhyan, E. V. Luschevskaya, and M. I. Polikarpov, *Magnetic-Field-Induced insulator-conductor transition in $SU(2)$ quenched lattice gauge theory*, Phys. Rev. Lett. **105** (2010), 132001, arXiv:1003.2180, doi:10.1103/PhysRevLett.105.132001.
- [146] Y. Burnier and M. Laine, *Towards flavour diffusion coefficient and electrical conductivity without ultraviolet contamination*, Eur. Phys. J. **C72** (2012), 1902, arXiv:1201.1994, doi:10.1140/epjc/s10052-012-1902-8.
- [147] Gert Aarts, Chris Allton, Alessandro Amato, Pietro Giudice, Simon Hands, and Jon-Ivar Skullerud, *Electrical conductivity and charge diffusion in thermal QCD from the lattice*, JHEP **02** (2015), 186, arXiv:1412.6411, doi:10.1007/JHEP02(2015)186.

- [148] Bastian B. Brandt, Anthony Francis, Benjamin Jäger, and Harvey B. Meyer, *Charge transport and vector meson dissociation across the thermal phase transition in lattice QCD with two light quark flavors*, Phys. Rev. D **93** (2016), 054510, arXiv:1512.07249, doi:10.1103/PhysRevD.93.054510.
- [149] Heng-Tong Ding, Olaf Kaczmarek, and Florian Meyer, *Thermal dilepton rates and electrical conductivity of the QGP from the lattice*, Phys. Rev. D **94** (2016), 034504, arXiv:1604.06712, doi:10.1103/PhysRevD.94.034504.
- [150] Moritz Greif, Ioannis Bouras, Carsten Greiner, and Zhe Xu, *Electric conductivity of the quark-gluon plasma investigated using a perturbative QCD based parton cascade*, Phys. Rev. D **90** (2014), 094014, arXiv:1408.7049, doi:10.1103/PhysRevD.90.094014.
- [151] A. Puglisi, S. Plumari, and V. Greco, *Shear viscosity eta to electric conductivity sigma_{el} ratio for the Quark-Gluon Plasma*, arXiv:1407.2559 (2014), 5, available from <http://arxiv.org/abs/1407.2559>, arXiv:1407.2559.
- [152] Si-Xue Qin, *A divergence-free method to extract observables from correlation functions*, Phys. Lett. B **742** (2015), 358, arXiv:1307.4587, doi:10.1016/j.physletb.2015.02.009.
- [153] Hamza Berrehrah, Wolfgang Cassing, Elena Bratkovskaya, and Thorsten Steinert, *Quark susceptibility in a generalized dynamical quasiparticle model*, Phys. Rev. C **93** (2016), 044914, arXiv:1512.06909, doi:10.1103/PhysRevC.93.044914.
- [154] Stefano I. Finazzo and Jorge Noronha, *Holographic calculation of the electric conductivity of the strongly coupled quark-gluon plasma near the deconfinement transition*, Phys. Rev. D **89** (2014), 106008, arXiv:1311.6675, doi:10.1103/PhysRevD.89.106008.
- [155] D. Fernández-Fraile and A. Gomez Nicola, *The Electrical conductivity of a pion gas*, Phys. Rev. D **73** (2006), 045025, arXiv:hep-ph/0512283, doi:10.1103/PhysRevD.73.045025.
- [156] Gordon Baym and Henning Heiselberg, *The Electrical conductivity in the early universe*, Phys. Rev. D **56** (1997), 5254, arXiv:astro-ph/9704214, doi:10.1103/PhysRevD.56.5254.
- [157] Kirill Tuchin, *Particle production in strong electromagnetic fields in relativistic heavy-ion collisions*, Adv. High Energy Phys. **2013** (2013), 490495, arXiv:1301.0099, doi:10.1155/2013/490495.
- [158] Jean-Marie Paul Robert, *Dileptons, spectral weights, and conductivity in the quark-gluon plasma*, Ph.D. thesis, McGill U., 2006, available from <http://proquest.umi.com/pqdweb?sid=1&Fmt=2&clientId=79356&RQT=309&VName=PQD&did=1441230741>.
- [159] J. Ghiglieri, O. Kaczmarek, M. Laine, and F. Meyer, *Lattice constraints on the thermal photon rate*, Phys. Rev. D **94** (2016), 016005, arXiv:1604.07544, doi:10.1103/PhysRevD.94.016005.
- [160] Romulo Rougemont, Jorge Noronha, and Jacquelyn Noronha-Hostler, *Suppression of baryon diffusion and transport in a baryon rich strongly coupled quark-gluon plasma*, Phys. Rev. Lett. **115** (2015), 202301, arXiv:1507.06972, doi:10.1103/PhysRevLett.115.202301.

-
- [161] Amaresh Jaiswal, Bengt Friman, and Krzysztof Redlich, *Relativistic second-order dissipative hydrodynamics at finite chemical potential*, Phys. Lett. B **751** (2015), 548, arXiv:1507.02849, doi:10.1016/j.physletb.2015.11.018.
- [162] Chun Shen, Gabriel Denicol, Charles Gale, Sangyong Jeon, Akihiko Monnai, and Bjoern Schenke, *A hybrid approach to relativistic heavy-ion collisions at the RHIC BES energies*, Nucl. Phys. A **967** (2017), 796, arXiv:1704.04109, doi:10.1016/j.nuclphysa.2017.06.008.
- [163] W. Cassing, O. Linnyk, T. Steinert, and V. Ozvenchuk, *Electrical Conductivity of Hot QCD Matter*, Phys. Rev. Lett. **110** (2013), 182301, arXiv:1302.0906, doi:10.1103/PhysRevLett.110.182301.
- [164] Simon Caron-Huot, Pavel Kovtun, Guy D. Moore, Andrei Starinets, and Laurence G. Yaffe, *Photon and dilepton production in supersymmetric Yang-Mills plasma*, JHEP **12** (2006), 015, arXiv:hep-th/0607237, doi:10.1088/1126-6708/2006/12/015.
- [165] Gert Aarts, Chris Allton, Justin Foley, Simon Hands, and Seyong Kim, *Spectral functions at small energies and the electrical conductivity in hot, quenched lattice QCD*, Phys. Rev. Lett. **99** (2007), 022002, arXiv:hep-lat/0703008, doi:10.1103/PhysRevLett.99.022002.
- [166] Bastian B. Brandt, Anthony Francis, Harvey B. Meyer, and Hartmut Wittig, *Thermal Correlators in the rho channel of two-flavor QCD*, JHEP **03** (2013), 100, arXiv:1212.4200, doi:10.1007/JHEP03(2013)100.
- [167] Alessandro Amato, Gert Aarts, Chris Allton, Pietro Giudice, Simon Hands, and Jon-Ivar Skullerud, *Electrical conductivity of the quark-gluon plasma across the deconfinement transition*, Phys. Rev. Lett. **111** (2013), 172001, arXiv:1307.6763, doi:10.1103/PhysRevLett.111.172001.
- [168] H. T. Ding, A. Francis, O. Kaczmarek, F. Karsch, E. Laermann, and W. Soeldner, *Thermal dilepton rate and electrical conductivity: An analysis of vector current correlation functions in quenched lattice QCD*, Phys. Rev. **D83** (2011), 034504, arXiv:1012.4963, doi:10.1103/PhysRevD.83.034504.
- [169] G. S. Denicol, H. Niemi, E. Molnar, and D. H. Rischke, *Derivation of transient relativistic fluid dynamics from the Boltzmann equation*, Phys. Rev. D **85** (2012), 114047, [Erratum: Phys. Rev.D 91 (2015), 039902], arXiv:1202.4551, doi:10.1103/PhysRevD.85.114047, 10.1103/PhysRevD.91.039902.
- [170] Gabriel S. Denicol, Jorge Noronha, Harri Niemi, and Dirk H. Rischke, *Origin of the Relaxation Time in Dissipative Fluid Dynamics*, Phys. Rev. D **83** (2011), 074019, arXiv:1102.4780, doi:10.1103/PhysRevD.83.074019.
- [171] G. S. Denicol, J. Noronha, H. Niemi, and D. H. Rischke, *Determination of the Shear Viscosity Relaxation Time at Weak and Strong Coupling*, J. Phys. G **38** (2011), 124177, arXiv:1108.6230, doi:10.1088/0954-3899/38/12/124177.
- [172] S. R. Groot, W.A. van Leeuwen, and van Weert Ch.G., *Relativistic Kinetic Theory-Principles and Applications*, North-Holland, Amsterdam, 1980.
- [173] F. Reif, *Fundamentals of Statistical and Thermal Physics*, Waveland Press, 2009, available from <http://books.google.de/books?id=0bsbAAAAQBAJ>.

- [174] Denes Molnar and Zack Wolff, *Self-consistent conversion of a viscous fluid to particles*, Phys. Rev. **C95** (2017), 024903, arXiv:1404.7850, doi:10.1103/PhysRevC.95.024903.
- [175] J. Weil et al., *Particle production and equilibrium properties within a new hadron transport approach for heavy-ion collisions*, Phys. Rev. C **94** (2016), 054905, arXiv:1606.06642, doi:10.1103/PhysRevC.94.054905.
- [176] Jan Hammelmann, Juan Torres-Rincon, Jean-Bernard Rose, and Hannah Petersen, *Private communication*.
- [177] A. Bazavov et al., *The chiral and deconfinement aspects of the QCD transition*, Phys. Rev. D **85** (2012), 054503, arXiv:1111.1710, doi:10.1103/PhysRevD.85.054503.
- [178] O. Buss, T. Gaitanos, K. Gallmeister, H. van Hees, M. Kaskulov, O. Lalakulich, A. B. Larionov, T. Leitner, J. Weil, and U. Mosel, *Transport-theoretical Description of Nuclear Reactions*, Phys. Rept. **512** (2012), 1, arXiv:1106.1344, doi:10.1016/j.physrep.2011.12.001.
- [179] T. Steinert and W. Cassing, *Electric and magnetic response of hot QCD matter*, Phys. Rev. **C89** (2014), 035203, arXiv:1312.3189, doi:10.1103/PhysRevC.89.035203.
- [180] W. Cassing, V. Metag, U. Mosel, and K. Niita, *Production of energetic particles in heavy ion collisions*, Phys. Rept. **188** (1990), 363, doi:10.1016/0370-1573(90)90164-W.
- [181] Akihiko Monnai, *Dissipative Hydrodynamic Effects on Baryon Stopping*, Phys. Rev. C **86** (2012), 014908, arXiv:1204.4713, doi:10.1103/PhysRevC.86.014908.
- [182] M. M. Aggarwal et al., *An Experimental Exploration of the QCD Phase Diagram: The Search for the Critical Point and the Onset of De-confinement*, (2010), arXiv:1007.2613.
- [183] Bedangadas Mohanty, *STAR experiment results from the beam energy scan program at RHIC*, J. Phys. G **38** (2011), 124023, arXiv:1106.5902, doi:10.1088/0954-3899/38/12/124023.
- [184] Jeffery T. Mitchell, *The RHIC Beam Energy Scan Program: Results from the PHENIX Experiment*, Nucl. Phys. A **904** (2013), 903c, arXiv:1211.6139, doi:10.1016/j.nuclphysa.2013.02.161.
- [185] Grazyna Odyniec, *The RHIC Beam Energy Scan program in STAR and what's next ...*, J. Phys. Conf. Ser. **455** (2013), 012037, doi:10.1088/1742-6596/455/1/012037.
- [186] Akihiko Monnai and Tetsufumi Hirano, *Relativistic Dissipative Hydrodynamic Equations at the Second Order for Multi-Component Systems with Multiple Conserved Currents*, Nucl. Phys. A **847** (2010), 283, arXiv:1003.3087, doi:10.1016/j.nuclphysa.2010.08.002.
- [187] G. S. Denicol, E. Molnár, H. Niemi, and D. H. Rischke, *Derivation of fluid dynamics from kinetic theory with the 14-moment approximation*, Eur. Phys. J. A **48** (2012), 170, arXiv:1206.1554, doi:10.1140/epja/i2012-12170-x.

-
- [188] Lars Onsager, *Reciprocal relations in irreversible processes. i.*, Phys. Rev. **37** (1931), 405, doi:10.1103/PhysRev.37.405.
- [189] Lars Onsager, *Reciprocal relations in irreversible processes. ii.*, Phys. Rev. **38** (1931), 2265, doi:10.1103/PhysRev.38.2265.
- [190] Romulo Rougemont, Renato Critelli, Jacquelyn Noronha-Hostler, Jorge Noronha, and Claudia Ratti, *Dynamical versus equilibrium properties of the QCD phase transition: A holographic perspective*, Phys. Rev. D **96** (2017), 014032, arXiv:1704.05558, doi:10.1103/PhysRevD.96.014032.
- [191] Juan M. Torres-Rincon, *Hadronic Transport Coefficients from Effective Field Theories*, Ph.D. thesis, UCM, Somosaguas, New York, 2012, arXiv:1205.0782, doi:10.1007/978-3-319-00425-9.
- [192] Sydney Chapman and Thomas George Cowling, *The mathematical theory of non-uniform gases: an account of the kinetic theory of viscosity, thermal conduction and diffusion in gases*, Cambridge University Press, 1970.
- [193] G. S. Denicol, *Kinetic foundations of relativistic dissipative fluid dynamics*, J. Phys. G **41** (2014), 124004, doi:10.1088/0954-3899/41/12/124004.
- [194] Alessandro Amato, Gert Aarts, Chris Allton, and Pietro Giudice, *Transport coefficients of the QGP*, arXiv: 1310.7466 (2013), 7, available from <http://arxiv.org/abs/1310.7466>, arXiv:1310.7466.
- [195] V. Skokov, A. Yu. Illarionov, and V. Toneev, *Estimate of the magnetic field strength in heavy-ion collisions*, Int. J. Mod. Phys. A **24** (2009), 5925, arXiv:0907.1396, doi:10.1142/S0217751X09047570.
- [196] Wei-Tian Deng and Xu-Guang Huang, *Event-by-event generation of electromagnetic fields in heavy-ion collisions*, Phys. Rev. C **85** (2012), 044907, arXiv:1201.5108, doi:10.1103/PhysRevC.85.044907.
- [197] Michael L. Miller, Klaus Reygers, Stephen J. Sanders, and Peter Steinberg, *Glauber modeling in high energy nuclear collisions*, Ann. Rev. Nucl. Part. Sci. **57** (2007), 205, arXiv:nucl-ex/0701025, doi:10.1146/annurev.nucl.57.090506.123020.
- [198] B. Alver, M. Baker, C. Loizides, and P. Steinberg, *The PHOBOS Glauber Monte Carlo*, (2008), arXiv:0805.4411.
- [199] C. Loizides, J. Nagle, and P. Steinberg, *Improved version of the PHOBOS Glauber Monte Carlo*, SoftwareX **1** (2015), 13, arXiv:1408.2549, doi:10.1016/j.softx.2015.05.001.
- [200] Adam Bzdak and Vladimir Skokov, *Event-by-event fluctuations of magnetic and electric fields in heavy ion collisions*, Phys. Lett. B **710** (2012), 171, arXiv:1111.1949, doi:10.1016/j.physletb.2012.02.065.
- [201] Hui Li, Xin-li Sheng, and Qun Wang, *Electromagnetic fields with electric and chiral magnetic conductivities in heavy ion collisions*, Phys. Rev. C **94** (2016), 044903, arXiv:1602.02223, doi:10.1103/PhysRevC.94.044903.
- [202] Xu-Guang Huang, *Electromagnetic fields and anomalous transports in heavy-ion collisions — A pedagogical review*, Rept. Prog. Phys. **79** (2016), 076302, arXiv:1509.04073, doi:10.1088/0034-4885/79/7/076302.

- [203] V. Voronyuk, V. D. Toneev, W. Cassing, E. L. Bratkovskaya, V. P. Konchakovski, and S. A. Voloshin, *(Electro-)Magnetic field evolution in relativistic heavy-ion collisions*, Phys. Rev. C **83** (2011), 054911, arXiv:1103.4239, doi:10.1103/PhysRevC.83.054911.
- [204] Umut Gursoy, Dmitri Kharzeev, and Krishna Rajagopal, *Magnetohydrodynamics, charged currents and directed flow in heavy ion collisions*, Phys. Rev. C **89** (2014), 054905, arXiv:1401.3805, doi:10.1103/PhysRevC.89.054905.
- [205] Victor Roy, Shi Pu, Luciano Rezzolla, and Dirk Rischke, *Analytic Bjorken flow in one-dimensional relativistic magnetohydrodynamics*, Phys. Lett. B **750** (2015), 45, arXiv:1506.06620, doi:10.1016/j.physletb.2015.08.046.
- [206] Gabriele Inghirami, Luca Del Zanna, Andrea Beraudo, Mohsen Haddadi Moghadam, Francesco Becattini, and Marcus Bleicher, *Numerical magneto-hydrodynamics for relativistic nuclear collisions*, Eur. Phys. J. C **76** (2016), 659, arXiv:1609.03042, doi:10.1140/epjc/s10052-016-4516-8.
- [207] Santosh K. Das, Salvatore Plumari, Sandeep Chatterjee, Jane Alam, Francesco Scardina, and Vincenzo Greco, *Directed Flow of Charm Quarks as a Witness of the Initial Strong Magnetic Field in Ultra-Relativistic Heavy Ion Collisions*, Phys. Lett. **B768** (2017), 260, arXiv:1608.02231, doi:10.1016/j.physletb.2017.02.046.
- [208] Xingyu Guo, Shuzhe Shi, Nu Xu, Zhe Xu, and Pengfei Zhuang, *Magnetic Field Effect on Charmonium Production in High Energy Nuclear Collisions*, Phys. Lett. B **751** (2015), 215, arXiv:1502.04407, doi:10.1016/j.physletb.2015.10.038.
- [209] Jan Uphoff, Oliver Fochler, Zhe Xu, and Carsten Greiner, *Elliptic Flow and Energy Loss of Heavy Quarks in Ultra-Relativistic heavy Ion Collisions*, Phys. Rev. C **84** (2011), 024908, arXiv:1104.2295, doi:10.1103/PhysRevC.84.024908.
- [210] K. J. Eskola, K. Kajantie, and J. Lindfors, *Quark and Gluon Production in High-Energy Nucleus-Nucleus Collisions*, Nucl. Phys. B. **323** (1989), 37, doi:10.1016/0550-3213(89)90586-5.
- [211] K. Kajantie, P. V. Landshoff, and J. Lindfors, *Minijet Production in High-Energy Nucleus-Nucleus Collisions*, Phys. Rev. Lett. **59** (1987), 2527, doi:10.1103/PhysRevLett.59.2527.
- [212] John Błoczynski, Xu-Guang Huang, Xilin Zhang, and Jinfeng Liao, *Azimuthally fluctuating magnetic field and its impacts on observables in heavy-ion collisions*, Phys. Lett. B **718** (2013), 1529, arXiv:1209.6594, doi:10.1016/j.physletb.2012.12.030.
- [213] Kirill Tuchin, *Time and space dependence of the electromagnetic field in relativistic heavy-ion collisions*, Phys. Rev. C **88** (2013), 024911, arXiv:1305.5806, doi:10.1103/PhysRevC.88.024911.
- [214] Zhe Xu and Carsten Greiner, *Transport rates and momentum isotropization of gluon matter in ultrarelativistic heavy-ion collisions*, Phys. Rev. C **76** (2007), 024911, arXiv:hep-ph/0703233, doi:10.1103/PhysRevC.76.024911.
- [215] Peter Brockway Arnold, *Quark-Gluon Plasmas and Thermalization*, Int. J. Mod. Phys. E **16** (2007), 2555, arXiv:0708.0812, doi:10.1142/S021830130700832X.

- [216] Carlo Cercignani and Gilberto Medeiros Kremer, *The Relativistic Boltzmann Equation: Theory and Applications*, vol. 52 Suppl 3, Springer Basel AG, Boston, March 2002.
- [217] Oliver Fochler, Jan Uphoff, Zhe Xu, and Carsten Greiner, *Radiative parton processes in perturbative QCD: An improved version of the Gunion and Bertsch cross section from comparisons to the exact result*, Phys. Rev. D **88** (2013), 014018, arXiv:1302.5250, doi:10.1103/PhysRevD.88.014018.
- [218] Jan Uphoff, Florian Senzel, Oliver Fochler, Christian Wesp, Zhe Xu, and Carsten Greiner, *Elliptic flow and nuclear modification factor in ultrarelativistic heavy-ion collisions within a partonic transport model*, Phys. Rev. Lett. **114** (2015), 112301, arXiv:1401.1364, doi:10.1103/PhysRevLett.114.112301.
- [219] Jan Uphoff, Oliver Fochler, Zhe Xu, and Carsten Greiner, *Open Heavy Flavor in Pb+Pb Collisions at $\sqrt{s} = 2.76$ TeV within a Transport Model*, Phys. Lett. B **717** (2012), 430, arXiv:1205.4945, doi:10.1016/j.physletb.2012.09.069.
- [220] Jan Uphoff, Oliver Fochler, Zhe Xu, and Carsten Greiner, *Elastic and radiative heavy quark interactions in ultra-relativistic heavy-ion collisions*, J. Phys. G **42** (2015), 115106, arXiv:1408.2964, doi:10.1088/0954-3899/42/11/115106.
- [221] S. Afanasiev et al., *Systematic Studies of Elliptic Flow Measurements in Au+Au Collisions at $s^{*(1/2)} = 200$ -GeV*, Phys. Rev. C **80** (2009), 024909, arXiv:0905.1070, doi:10.1103/PhysRevC.80.024909.
- [222] A. Adare et al., *Azimuthally anisotropic emission of low-momentum direct photons in Au+Au collisions at $\sqrt{s_{NN}} = 200$ GeV*, Phys. Rev. C **94** (2016), 064901, arXiv:1509.07758, doi:10.1103/PhysRevC.94.064901.
- [223] Werner Scheid, Hans Muller, and Walter Greiner, *Nuclear Shock Waves in Heavy-Ion Collisions*, Phys. Rev. Lett. **32** (1974), 741, doi:10.1103/PhysRevLett.32.741.
- [224] A. A. Amsden, G. F. Bertsch, F. H. Harlow, and J. R. Nix, *Relativistic Hydrodynamic Theory of Heavy Ion Collisions*, Phys. Rev. Lett. **35** (1975), 905, doi:10.1103/PhysRevLett.35.905.
- [225] Dirk H. Rischke, Stefan Bernard, and Joachim A. Maruhn, *Relativistic hydrodynamics for heavy ion collisions. 1. General aspects and expansion into vacuum*, Nucl. Phys. A **595** (1995), 346, arXiv:nucl-th/9504018, doi:10.1016/0375-9474(95)00355-1.
- [226] M. Greif, F. Reining, I. Bouras, G. S. Denicol, Z. Xu, and C. Greiner, *Heat conductivity in relativistic systems investigated using a partonic cascade*, Phys. Rev. E **87** (2013), 033019, arXiv:1301.1190, doi:10.1103/PhysRevE.87.033019.
- [227] Bjoern Schenke, Sangyong Jeon, and Charles Gale, *(3+1)D hydrodynamic simulation of relativistic heavy-ion collisions*, Phys. Rev. C **82** (2010), 014903, arXiv:1004.1408, doi:10.1103/PhysRevC.82.014903.
- [228] Bjorn Schenke, Sangyong Jeon, and Charles Gale, *Higher flow harmonics from (3+1)D event-by-event viscous hydrodynamics*, Phys. Rev. C **85** (2012), 024901, arXiv:1109.6289, doi:10.1103/PhysRevC.85.024901.

- [229] E. Molnar, H. Niemi, and D. H. Rischke, *Numerical tests of causal relativistic dissipative fluid dynamics*, Eur. Phys. J. C **65** (2010), 615, arXiv:0907.2583, doi:10.1140/epjc/s10052-009-1194-9.
- [230] Tetsufumi Hirano, Ulrich W. Heinz, Dmitri Kharzeev, Roy Lacey, and Yasushi Nara, *Hadronic dissipative effects on elliptic flow in ultrarelativistic heavy-ion collisions*, Phys. Lett. B **636** (2006), 299, arXiv:nucl-th/0511046, doi:10.1016/j.physletb.2006.03.060.
- [231] P. Braun-Munzinger and J. Stachel, *Particle ratios, equilibration, and the QCD phaseboundary*, J. Phys. G **28** (2002), 1971, arXiv:nucl-th/0112051, doi:10.1088/0954-3899/28/7/355.
- [232] T. S. Biro, E. van Doorn, Berndt Muller, M. H. Thoma, and X. N. Wang, *Parton equilibration in relativistic heavy ion collisions*, Phys. Rev. C **48** (1993), 1275, arXiv:nucl-th/9303004, doi:10.1103/PhysRevC.48.1275.
- [233] Xin-Nian Wang, *pQCD based approach to parton production and equilibration in high-energy nuclear collisions*, Phys. Rept. **280** (1997), 287, arXiv:hep-ph/9605214, doi:10.1016/S0370-1573(96)00022-1.
- [234] G. Baym, *Thermal equilibration in ultrarelativistic heavy ion collisions*, Phys. Lett. B **138** (1984), 18, doi:10.1016/0370-2693(84)91863-X.
- [235] Jefferson Bjoraker and Raju Venugopalan, *From colored glass condensate to gluon plasma: Equilibration in high-energy heavy ion collisions*, Phys. Rev. C **63** (2001), 024609, arXiv:hep-ph/0008294, doi:10.1103/PhysRevC.63.024609.
- [236] Zhe Xu, Kai Zhou, Pengfei Zhuang, and Carsten Greiner, *Thermalization of gluons with Bose-Einstein condensation*, Phys. Rev. Lett. **114** (2015), 182301, arXiv:1410.5616, doi:10.1103/PhysRevLett.114.182301.
- [237] Jan Uphoff, Oliver Fochler, Zhe Xu, and Carsten Greiner, *Heavy quark production at RHIC and LHC within a partonic transport model*, Phys. Rev. C **82** (2010), 044906, arXiv:1003.4200, doi:10.1103/PhysRevC.82.044906.
- [238] J. F. Gunion and G. Bertsch, *Hadronization by color bremsstrahlung*, Phys. Rev. D **25** (1982), 746, doi:10.1103/PhysRevD.25.746.
- [239] Andrej El, Zhe Xu, and Carsten Greiner, *Thermalization of a color glass condensate and review of the 'Bottom-Up' scenario*, Nucl. Phys. A **806** (2008), 287, arXiv:0712.3734, doi:10.1016/j.nuclphysa.2008.03.005.
- [240] Zhe Xu and Carsten Greiner, *Elliptic flow of gluon matter in ultrarelativistic heavy-ion collisions*, Phys. Rev. C **79** (2009), 014904, arXiv:0811.2940, doi:10.1103/PhysRevC.79.014904.
- [241] Andrej El, Azwinndini Muronga, Zhe Xu, and Carsten Greiner, *Shear viscosity and out of equilibrium dissipative hydrodynamics*, Phys. Rev. C **79** (2009), 044914, arXiv:0812.2762, doi:10.1103/PhysRevC.79.044914.
- [242] Felix Reining, Ioannis Bouras, Andrej El, Christian Wesp, Zhe Xu, and Carsten Greiner, *Extraction of shear viscosity in stationary states of relativistic particle systems*, Phys. Rev. E **85** (2012), 026302, arXiv:1106.4210, doi:10.1103/PhysRevE.85.026302.

- [243] I. Bouras, E. Molnar, H. Niemi, Z. Xu, A. El, O. Fochler, C. Greiner, and D. H. Rischke, *Relativistic shock waves in viscous gluon matter*, Phys. Rev. Lett. **103** (2009), 032301, arXiv:0902.1927, doi:10.1103/PhysRevLett.103.032301.
- [244] I. Bouras, E. Molnar, H. Niemi, Z. Xu, A. El, O. Fochler, C. Greiner, and D. H. Rischke, *Investigation of shock waves in the relativistic Riemann problem: A Comparison of viscous fluid dynamics to kinetic theory*, Phys. Rev. C **82** (2010), 024910, arXiv:1006.0387, doi:10.1103/PhysRevC.82.024910.
- [245] G. S. Denicol, H. Niemi, I. Bouras, E. Molnar, Z. Xu, D. H. Rischke, and C. Greiner, *Solving the heat-flow problem with transient relativistic fluid dynamics*, Phys. Rev. **D89** (2014), 074005, arXiv:1207.6811, doi:10.1103/PhysRevD.89.074005.
- [246] K. Gallmeister, H. Niemi, C. Greiner, and D. H. Rischke, *Exploring the applicability of dissipative fluid dynamics to small systems by comparison to the Boltzmann equation*, (2018), arXiv:1804.09512.
- [247] Kai Zhou, Zhe Xu, Pengfei Zhuang, and Carsten Greiner, *Kinetic description of Bose-Einstein condensation with test particle simulations*, Phys. Rev. D **96** (2017), 014020, arXiv:1703.02495, doi:10.1103/PhysRevD.96.014020.
- [248] Oliver Fochler, Zhe Xu, and Carsten Greiner, *Towards a unified understanding of jet-quenching and elliptic flow within perturbative QCD parton transport*, Phys. Rev. Lett. **102** (2009), 202301, arXiv:0806.1169, doi:10.1103/PhysRevLett.102.202301.
- [249] Oliver Fochler, Zhe Xu, and Carsten Greiner, *Energy loss in a partonic transport model including bremsstrahlung processes*, Phys. Rev. C **82** (2010), 024907, arXiv:1003.4380, doi:10.1103/PhysRevC.82.024907.
- [250] Florian Senzel, Oliver Fochler, Jan Uphoff, Zhe Xu, and Carsten Greiner, *Influence of multiple in-medium scattering processes on the momentum imbalance of reconstructed di-jets*, J. Phys. G **42** (2015), 115104, arXiv:1309.1657, doi:10.1088/0954-3899/42/11/115104.
- [251] Jan Uphoff, Oliver Fochler, Zhe Xu, and Carsten Greiner, *Production and elliptic flow of heavy quarks at RHIC and LHC within a partonic transport model*, J. Phys. Conf. Ser. **230** (2010), 012004, arXiv:1004.4091, doi:10.1088/1742-6596/230/1/012004.
- [252] Jan Uphoff, Florian Senzel, Zhe Xu, and Carsten Greiner, *Momentum imbalance of D mesons in ultra-relativistic heavy-ion collisions at LHC*, Phys. Rev. C **89** (2014), 064906, arXiv:1310.1340, doi:10.1103/PhysRevC.89.064906.
- [253] Florian Senzel, Jan Uphoff, Zhe Xu, and Carsten Greiner, *The different energy loss mechanisms of inclusive and b-tagged reconstructed jets within ultra-relativistic heavy-ion collisions*, Phys. Lett. B **773** (2017), 620, arXiv:1602.05086, doi:10.1016/j.physletb.2017.09.022.
- [254] Michel Le Bellac, *Thermal Field Theory*, Cambridge University Press, 2011.
- [255] J. I. Kapusta and Charles Gale, *Finite-temperature field theory: Principles and applications*, Cambridge Monographs on Mathematical Physics, Cambridge University Press, 2011, doi:10.1017/CB09780511535130.

- [256] Eric Braaten and Robert D. Pisarski, *Soft Amplitudes in Hot Gauge Theories: A General Analysis*, Nucl. Phys. B. **337** (1990), 569, doi:10.1016/0550-3213(90)90508-B.
- [257] Robert D. Pisarski, *Computing Finite Temperature Loops with Ease*, Nucl. Phys. B. **309** (1988), 476, doi:10.1016/0550-3213(88)90454-3.
- [258] Robert D. Pisarski, *Scattering Amplitudes in Hot Gauge Theories*, Phys. Rev. Lett. **63** (1989), 1129, doi:10.1103/PhysRevLett.63.1129.
- [259] Charles Gale and Joseph I. Kapusta, *Vector dominance model at finite temperature*, Nucl. Phys. B. **357** (1991), 65, doi:10.1016/0550-3213(91)90459-B.
- [260] Victor Ilisie, *Concepts in Quantum Field Theory*, UNITEXT for Physics, Springer, 2016, doi:10.1007/978-3-319-22966-9.
- [261] R. E. Cutkosky, *Singularities and discontinuities of Feynman amplitudes*, J. Math. Phys. **1** (1960), 429, doi:10.1063/1.1703676.
- [262] Gerardus 't Hooft and Martinus J G Veltman, *Diagrammar*, CERN Yellow Reports: Monographs, CERN, Geneva, 1973, available from <https://cds.cern.ch/record/186259>.
- [263] Margaret E. Carrington and Stanislaw Mrowczynski, *Transport theory beyond binary collisions*, Phys. Rev. D **71** (2005), 065007, arXiv:hep-ph/0406097, doi:10.1103/PhysRevD.71.065007.
- [264] S. M. H. Wong, *Disentangling the imaginary time formalism at finite temperature*, Phys. Rev. D **64** (2001), 025007, arXiv:hep-ph/0007212, doi:10.1103/PhysRevD.64.025007.
- [265] M. E. Carrington, Hou Defu, and R. Kobes, *Scattering amplitudes at finite temperature*, Phys. Rev. D **67** (2003), 025021, arXiv:hep-ph/0207115, doi:10.1103/PhysRevD.67.025021.
- [266] H. Arthur Weldon, *Simple Rules for Discontinuities in Finite Temperature Field Theory*, Phys. Rev. D **28** (1983), 2007, doi:10.1103/PhysRevD.28.2007.
- [267] R. L. Kobes and G. W. Semenoff, *Discontinuities of Green Functions in Field Theory at Finite Temperature and Density*, Nucl. Phys. B. **260** (1985), 714, doi:10.1016/0550-3213(85)90056-2.
- [268] A. Majumder and Charles Gale, *On the imaginary parts and infrared divergences of two loop vector boson selfenergies in thermal QCD*, Phys. Rev. C **65** (2002), 055203, arXiv:hep-ph/0111181, doi:10.1103/PhysRevC.65.055203.
- [269] R. Baier, H. Nakkagawa, A. Niegawa, and K. Redlich, *Production rate of hard thermal photons and screening of quark mass singularity*, Z. Phys. C **53** (1992), 433, doi:10.1007/BF01625902.
- [270] Chun Shen, Jean-Francois Paquet, Ulrich Heinz, and Charles Gale, *Photon Emission from a Momentum Anisotropic Quark-Gluon Plasma*, Phys. Rev. C **91** (2015), 014908, arXiv:1410.3404, doi:10.1103/PhysRevC.91.014908.
- [271] A. P. Contogouris, S. Papadopoulos, and C. Papavassiliou, *Large p_T Direct Photon Production and Opposite Side Photon - Hadron Correlations in QCD*, Nucl. Phys. B **179** (1981), 461, doi:10.1016/0550-3213(81)90014-6.

- [272] Peter Brockway Arnold, Guy D. Moore, and Laurence G. Yaffe, *Photon emission from quark gluon plasma: Complete leading order results*, JHEP **12** (2001), 009, arXiv:hep-ph/0111107, doi:10.1088/1126-6708/2001/12/009.
- [273] Peter Brockway Arnold, Guy D. Moore, and Laurence G. Yaffe, *Photon emission from ultrarelativistic plasmas*, JHEP **11** (2001), 057, arXiv:hep-ph/0109064, doi:10.1088/1126-6708/2001/11/057.
- [274] Guy D. Moore, *Transport coefficients in large $N(f)$ gauge theory: Testing hard thermal loops*, JHEP **05** (2001), 039, arXiv:hep-ph/0104121, doi:10.1088/1126-6708/2001/05/039.
- [275] G. Baym, H. Monien, C. J. Pethick, and D. G. Ravenhall, *Transverse Interactions and Transport in Relativistic Quark - Gluon and Electromagnetic Plasmas*, Phys. Rev. Lett. **64** (1990), 1867, doi:10.1103/PhysRevLett.64.1867.
- [276] G. Baym, H. Monien, C. J. Pethick, and D. G. Ravenhall, *Transverse interactions and transport in quark gluon and QED plasmas*, Nucl. Phys. A **525** (1991), 415C, doi:10.1016/0375-9474(91)90355-A.
- [277] Alex Meistrenko, Andre Peshier, Jan Uphoff, and Carsten Greiner, *Collisional energy loss of heavy quarks*, Nucl. Phys. A **901** (2013), 51, arXiv:1204.2397, doi:10.1016/j.nuclphysa.2013.02.012.
- [278] Peter Brockway Arnold, Guy D. Moore, and Laurence G. Yaffe, *Effective kinetic theory for high temperature gauge theories*, JHEP **01** (2003), 030, arXiv:hep-ph/0209353, doi:10.1088/1126-6708/2003/01/030.
- [279] Peter Brockway Arnold, Guy D. Moore, and Laurence G. Yaffe, *Photon and gluon emission in relativistic plasmas*, JHEP **06** (2002), 030, arXiv:hep-ph/0204343, doi:10.1088/1126-6708/2002/06/030.
- [280] Hualong Gervais and Sangyong Jeon, *Photon Production from a Quark-Gluon-Plasma at Finite Baryon Chemical Potential*, Phys. Rev. C **86** (2012), 034904, arXiv:1206.6086, doi:10.1103/PhysRevC.86.034904.
- [281] H. Stöcker et al., *Under-saturation of quarks at early stages of relativistic nuclear collisions: The hot glue initial scenario and its observable signatures*, Astron. Nachr. **336** (2015), 744, arXiv:1509.07682, doi:10.1002/asna.201512252.
- [282] Dinesh K. Srivastava, Rupa Chatterjee, and Munshi G. Mustafa, *Initial temperature and extent of chemical equilibration of partons in relativistic collisions of heavy nuclei*, J. Phys. G **45** (2018), 015103, arXiv:1609.06496, doi:10.1088/1361-6471/aa9421.
- [283] Dinesh Kumar Srivastava, Munshi Golam Mustafa, and Berndt Muller, *Chemical equilibration of an expanding quark - gluon plasma*, Phys. Lett. B **396** (1997), 45, arXiv:hep-ph/9608424, doi:10.1016/S0370-2693(97)00090-7.
- [284] V. Vovchenko, M. I. Gorenstein, L. M. Satarov, I. N. Mishustin, L. P. Csernai, I. Kisel, and H. Stöcker, *Entropy production in chemically nonequilibrium quark-gluon plasma created in central pb+pb collisions at energies available at the cern large hadron collider*, Phys. Rev. C **93** (2016), 014906, arXiv:1510.01235, doi:10.1103/PhysRevC.93.014906.

- [285] Edward V. Shuryak and L. Xiong, *Dilepton and photon production in the 'hot glue' scenario*, Phys. Rev. Lett. **70** (1993), 2241, arXiv:hep-ph/9301218, doi:10.1103/PhysRevLett.70.2241.
- [286] Duncan M. Elliott and Dirk H. Rischke, *Chemical equilibration of quarks and gluons at RHIC and LHC energies*, Nucl. Phys. A **671** (2000), 583, arXiv:nucl-th/9908004, doi:10.1016/S0375-9474(99)00840-4.
- [287] Christoph T. Traxler and Markus H. Thoma, *Photon emission from a parton gas at chemical nonequilibrium*, Phys. Rev. C **53** (1996), 1348, arXiv:hep-ph/9507444, doi:10.1103/PhysRevC.53.1348.
- [288] Yuri L. Dokshitzer, G. Marchesini, and B. R. Webber, *Dispersive approach to power behaved contributions in QCD hard processes*, Nucl. Phys. B. **469** (1996), 93, arXiv:hep-ph/9512336, doi:10.1016/0550-3213(96)00155-1.
- [289] P. B. Gossiaux and J. Aichelin, *Towards an understanding of the RHIC single electron data*, Phys. Rev. C **78** (2008), 014904, arXiv:0802.2525, doi:10.1103/PhysRevC.78.014904.
- [290] A. Peshier, *Running coupling and screening in the (s)QGP*, (2006), arXiv:hep-ph/0601119.
- [291] R. Baier, Yuri L. Dokshitzer, Alfred H. Mueller, S. Peigne, and D. Schiff, *Radiative energy loss of high-energy quarks and gluons in a finite volume quark - gluon plasma*, Nucl. Phys. **B483** (1997), 291, arXiv:hep-ph/9607355, doi:10.1016/S0550-3213(96)00553-6.
- [292] Simon Turbide, Charles Gale, Sangyong Jeon, and Guy D. Moore, *Energy loss of leading hadrons and direct photon production in evolving quark-gluon plasma*, Phys. Rev. C **72** (2005), 014906, arXiv:hep-ph/0502248, doi:10.1103/PhysRevC.72.014906.
- [293] Sangyong Jeon and Guy D. Moore, *Energy loss of leading partons in a thermal QCD medium*, Phys. Rev. C **71** (2005), 034901, arXiv:hep-ph/0309332, doi:10.1103/PhysRevC.71.034901.
- [294] Sigtryggur Hauksson, Sangyong Jeon, and Charles Gale, *Photon emission from quark-gluon plasma out of equilibrium*, Phys. Rev. C **97** (2018), 014901, arXiv:1709.03598, doi:10.1103/PhysRevC.97.014901.
- [295] Simon Turbide, *Electromagnetic radiation from matter under extreme conditions*, Ph.D. thesis, McGill U., 2006, available from <http://wwwlib.umi.com/dissertations/fullcit?pNR25272>.
- [296] F. Arleo et al., *Hard probes in heavy-ion collisions at the LHC: Photon physics in heavy ion collisions at the LHC*, (2004), arXiv:hep-ph/0311131.
- [297] P. Aurenche, F. Gelis, G. D. Moore, and H. Zaraket, *Landau-Pomeranchuk-Migdal resummation for dilepton production*, JHEP **12** (2002), 006, arXiv:hep-ph/0211036, doi:10.1088/1126-6708/2002/12/006.
- [298] P. Aurenche, F. Gelis, and H. Zaraket, *A Simple sum rule for the thermal gluon spectral function and applications*, JHEP **05** (2002), 043, arXiv:hep-ph/0204146, doi:10.1088/1126-6708/2002/05/043.

- [299] Bjoern Schenke, Charles Gale, and Sangyong Jeon, *MARTINI: An Event generator for relativistic heavy-ion collisions*, Phys. Rev. C **80** (2009), 054913, arXiv:0909.2037, doi:10.1103/PhysRevC.80.054913.
- [300] Ante Bilandzic, Raimond Snellings, and Sergei Voloshin, *Flow analysis with cumulants: Direct calculations*, Phys. Rev. C **83** (2011), 044913, arXiv:1010.0233, doi:10.1103/PhysRevC.83.044913.
- [301] Jean-Yves Ollitrault, Arthur M. Poskanzer, and Sergei A. Voloshin, *Effect of flow fluctuations and nonflow on elliptic flow methods*, Phys. Rev. C **80** (2009), 014904, arXiv:0904.2315, doi:10.1103/PhysRevC.80.014904.
- [302] Simon Turbide, Charles Gale, and Rainer J. Fries, *Azimuthal Asymmetry of Direct Photons in High Energy Nuclear Collisions*, Phys. Rev. Lett. **96** (2006), 032303, arXiv:hep-ph/0508201, doi:10.1103/PhysRevLett.96.032303.
- [303] Torbjorn Sjostrand, Stephen Mrenna, and Peter Z. Skands, *PYTHIA 6.4 Physics and Manual*, JHEP **05** (2006), 026, arXiv:hep-ph/0603175, doi:10.1088/1126-6708/2006/05/026.
- [304] Martin Wilde, *Measurement of Direct Photons in pp and Pb-Pb Collisions with ALICE*, Nucl. Phys. A **904** (2013), 573c, arXiv:1210.5958, doi:10.1016/j.nuclphysa.2013.02.079.
- [305] Betty Abelev et al., *Suppression of high transverse momentum D mesons in central Pb-Pb collisions at $\sqrt{s_{NN}} = 2.76$ TeV*, JHEP **09** (2012), 112, arXiv:1203.2160, doi:10.1007/JHEP09(2012)112.
- [306] Maxime Dion, Jean-Francois Paquet, Bjorn Schenke, Clint Young, Sangyong Jeon, and Charles Gale, *Viscous photons in relativistic heavy ion collisions*, Phys. Rev. C **84** (2011), 064901, arXiv:1109.4405, doi:10.1103/PhysRevC.84.064901.
- [307] Patrick Aurenche, Michel Fontannaz, Jean-Philippe Guillet, Eric Pilon, and Monique Werlen, *A New critical study of photon production in hadronic collisions*, Phys. Rev. D **73** (2006), 094007, arXiv:hep-ph/0602133, doi:10.1103/PhysRevD.73.094007.
- [308] J. F. Owens, *Large Momentum Transfer Production of Direct Photons, Jets, and Particles*, Rev. Mod. Phys. **59** (1987), 465, doi:10.1103/RevModPhys.59.465.
- [309] P. Aurenche, R. Baier, M. Fontannaz, and D. Schiff, *Prompt Photon Production at Large p(T) Scheme Invariant QCD Predictions and Comparison with Experiment*, Nucl. Phys. B. **297** (1988), 661, doi:10.1016/0550-3213(88)90553-6.
- [310] F. Aversa, P. Chiappetta, Mario Greco, and J. P. Guillet, *QCD Corrections to Parton-Parton Scattering Processes*, Nucl. Phys. B. **327** (1989), 105, doi:10.1016/0550-3213(89)90288-5.
- [311] Daniel Stump, Joey Huston, Jon Pumplin, Wu-Ki Tung, H. L. Lai, Steve Kuhlmann, and J. F. Owens, *Inclusive jet production, parton distributions, and the search for new physics*, JHEP **10** (2003), 046, arXiv:hep-ph/0303013, doi:10.1088/1126-6708/2003/10/046.
- [312] K. J. Eskola, H. Paukkunen, and C. A. Salgado, *EPS09: A New Generation of NLO and LO Nuclear Parton Distribution Functions*, JHEP **04** (2009), 065, arXiv:0902.4154, doi:10.1088/1126-6708/2009/04/065.

- [313] L. Bourhis, M. Fontannaz, and J. P. Guillet, *Quarks and gluon fragmentation functions into photons*, Eur. Phys. J. **C2** (1998), 529, arXiv:hep-ph/9704447, doi:10.1007/s100520050158.
- [314] O. Linnyk, V. Konchakovski, T. Steinert, W. Cassing, and E. L. Bratkovskaya, *Hadronic and partonic sources of direct photons in relativistic heavy-ion collisions*, Phys. Rev. C **92** (2015), 054914, arXiv:1504.05699, doi:10.1103/PhysRevC.92.054914.
- [315] K. Kajantie, Joseph I. Kapusta, Larry D. McLerran, and A. Mekjian, *Dilepton Emission and the QCD Phase Transition in Ultrarelativistic Nuclear Collisions*, Phys. Rev. D **34** (1986), 2746, doi:10.1103/PhysRevD.34.2746.
- [316] J. Cleymans, J. Fingberg, and K. Redlich, *Transverse Momentum Distribution of Dileptons in Different Scenarios for the QCD Phase Transition*, Phys. Rev. D **35** (1987), 2153, doi:10.1103/PhysRevD.35.2153.
- [317] Radoslaw Ryblewski and Michael Strickland, *Dilepton production from the quark-gluon plasma using (3+1)-dimensional anisotropic dissipative hydrodynamics*, Phys. Rev. D **92** (2015), 025026, arXiv:1501.03418, doi:10.1103/PhysRevD.92.025026.
- [318] Eric Braaten, Robert D. Pisarski, and Tzu-Chiang Yuan, *Production of Soft Dileptons in the Quark - Gluon Plasma*, Phys. Rev. Lett. **64** (1990), 2242, doi:10.1103/PhysRevLett.64.2242.
- [319] M. Laine, *NLO thermal dilepton rate at non-zero momentum*, JHEP **11** (2013), 120, arXiv:1310.0164, doi:10.1007/JHEP11(2013)120.
- [320] I. Ghisoiu and M. Laine, *Interpolation of hard and soft dilepton rates*, JHEP **10** (2014), 83, arXiv:1407.7955, doi:10.1007/JHEP10(2014)083.
- [321] Jacopo Ghiglieri and Guy D. Moore, *Low Mass Thermal Dilepton Production at NLO in a Weakly Coupled Quark-Gluon Plasma*, JHEP **12** (2014), 029, arXiv:1410.4203, doi:10.1007/JHEP12(2014)029.
- [322] N. Borghini, R. S. Bhalerao, and J. Y. Ollitrault, *Anisotropic flow from Lee-Yang zeroes: A Practical guide*, J. Phys. **G30** (2004), S1213, arXiv:nucl-th/0402053, doi:10.1088/0954-3899/30/8/092.
- [323] Betty Abelev et al., *Long-range angular correlations on the near and away side in p-Pb collisions at $\sqrt{s_{NN}} = 5.02$ TeV*, Phys. Lett. B **719** (2013), 29, arXiv:1212.2001, doi:10.1016/j.physletb.2013.01.012.
- [324] Georges Aad et al., *Observation of Associated Near-Side and Away-Side Long-Range Correlations in $\sqrt{s_{NN}} = 5.02$ TeV Proton-Lead Collisions with the ATLAS Detector*, Phys. Rev. Lett. **110** (2013), 182302, arXiv:1212.5198, doi:10.1103/PhysRevLett.110.182302.
- [325] Georges Aad et al., *Measurement with the ATLAS detector of multi-particle azimuthal correlations in p+Pb collisions at $\sqrt{s_{NN}} = 5.02$ TeV*, Phys. Lett. B **725** (2013), 60, arXiv:1303.2084, doi:10.1016/j.physletb.2013.06.057.
- [326] Georges Aad et al., *Measurement of long-range pseudorapidity correlations and azimuthal harmonics in $\sqrt{s_{NN}} = 5.02$ TeV proton-lead collisions with the ATLAS detector*, Phys. Rev. C **90** (2014), 044906, arXiv:1409.1792, doi:10.1103/PhysRevC.90.044906.

-
- [327] Serguei Chatrchyan et al., *Observation of long-range near-side angular correlations in proton-lead collisions at the LHC*, Phys. Lett. B **718** (2013), 795, arXiv:1210.5482, doi:10.1016/j.physletb.2012.11.025.
- [328] Serguei Chatrchyan et al., *Multiplicity and transverse momentum dependence of two- and four-particle correlations in pPb and PbPb collisions*, Phys. Lett. B **724** (2013), 213, arXiv:1305.0609, doi:10.1016/j.physletb.2013.06.028.
- [329] Betty Bezverkhny Abelev et al., *Multiplicity dependence of the average transverse momentum in pp, p-Pb, and Pb-Pb collisions at the LHC*, Phys. Lett. B **727** (2013), 371, arXiv:1307.1094, doi:10.1016/j.physletb.2013.10.054.
- [330] Vardan Khachatryan et al., *Observation of Long-Range Near-Side Angular Correlations in Proton-Proton Collisions at the LHC*, JHEP **09** (2010), 091, arXiv:1009.4122, doi:10.1007/JHEP09(2010)091.
- [331] Vardan Khachatryan et al., *Evidence for Collective Multiparticle Correlations in p-Pb Collisions*, Phys. Rev. Lett. **115** (2015), 012301, arXiv:1502.05382, doi:10.1103/PhysRevLett.115.012301.
- [332] Albert M Sirunyan et al., *Pseudorapidity and transverse momentum dependence of flow harmonics in pPb and PbPb collisions*, (2017), arXiv:1710.07864.
- [333] Kevin Dusling, Wei Li, and Björn Schenke, *Novel collective phenomena in high-energy proton-proton and proton-nucleus collisions*, Int. J. Mod. Phys. E **25** (2016), 1630002, arXiv:1509.07939, doi:10.1142/S0218301316300022.
- [334] Piotr Bozek and Wojciech Broniowski, *Correlations from hydrodynamic flow in p-Pb collisions*, Phys. Lett. B **718** (2013), 1557, arXiv:1211.0845, doi:10.1016/j.physletb.2012.12.051.
- [335] Heikki Mäntysaari, Björn Schenke, Chun Shen, and Prithwish Tribedy, *Imprints of fluctuating proton shapes on flow in proton-lead collisions at the LHC*, Phys. Lett. B **772** (2017), 681, arXiv:1705.03177, doi:10.1016/j.physletb.2017.07.038.
- [336] Sören Schlichting and Prithwish Tribedy, *Collectivity in Small Collision Systems: An Initial-State Perspective*, Adv. High Energy Phys. **2016** (2016), 8460349, arXiv:1611.00329, doi:10.1155/2016/8460349.
- [337] Kevin Dusling, Mark Mace, and Raju Venugopalan, *Parton model description of multiparticle azimuthal correlations in pA collisions*, Phys. Rev. D **97** (2018), 016014, arXiv:1706.06260, doi:10.1103/PhysRevD.97.016014.
- [338] Bjoern Schenke, Soeren Schlichting, Prithwish Tribedy, and Raju Venugopalan, *Mass ordering of spectra from fragmentation of saturated gluon states in high multiplicity proton-proton collisions*, Phys. Rev. Lett. **117** (2016), 162301, arXiv:1607.02496, doi:10.1103/PhysRevLett.117.162301.
- [339] Paul Romatschke, *Do nuclear collisions create a locally equilibrated quark-gluon plasma?*, Eur. Phys. J. C **77** (2017), 21, arXiv:1609.02820, doi:10.1140/epjc/s10052-016-4567-x.
- [340] Bjoern Schenke, Prithwish Tribedy, and Raju Venugopalan, *Fluctuating Glasma initial conditions and flow in heavy ion collisions*, Phys. Rev. Lett. **108** (2012), 252301, arXiv:1202.6646, doi:10.1103/PhysRevLett.108.252301.

- [341] Bjoern Schenke, Prithwish Tribedy, and Raju Venugopalan, *Event-by-event gluon multiplicity, energy density, and eccentricities in ultrarelativistic heavy-ion collisions*, Phys. Rev. C **86** (2012), 034908, arXiv:1206.6805, doi:10.1103/PhysRevC.86.034908.
- [342] Alex Krasnitz and Raju Venugopalan, *The Initial energy density of gluons produced in very high-energy nuclear collisions*, Phys. Rev. Lett. **84** (2000), 4309, arXiv:hep-ph/9909203, doi:10.1103/PhysRevLett.84.4309.
- [343] Alex Krasnitz and Raju Venugopalan, *The Initial gluon multiplicity in heavy ion collisions*, Phys. Rev. Lett. **86** (2001), 1717, arXiv:hep-ph/0007108, doi:10.1103/PhysRevLett.86.1717.
- [344] T. Lappi, S. Srednyak, and R. Venugopalan, *Non-perturbative computation of double inclusive gluon production in the Glasma*, JHEP **01** (2010), 066, doi:10.1007/JHEP01(2010)066.
- [345] Björn Schenke, Sören Schlichting, and Raju Venugopalan, *Azimuthal anisotropies in p+Pb collisions from classical Yang–Mills dynamics*, Phys. Lett. B **747** (2015), 76, arXiv:1502.01331, doi:10.1016/j.physletb.2015.05.051.
- [346] Francois Gelis, Edmond Iancu, Jamal Jalilian-Marian, and Raju Venugopalan, *The Color Glass Condensate*, Ann. Rev. Nucl. Part. Sci. **60** (2010), 463, arXiv:1002.0333, doi:10.1146/annurev.nucl.010909.083629.
- [347] Francois Gelis and Bjoern Schenke, *Initial State Quantum Fluctuations in the Little Bang*, Ann. Rev. Nucl. Part. Sci. **66** (2016), 73, arXiv:1604.00335, doi:10.1146/annurev-nucl-102115-044651.
- [348] Heikki Mäntysaari and Björn Schenke, *Evidence of strong proton shape fluctuations from incoherent diffraction*, Phys. Rev. Lett. **117** (2016), 052301, arXiv:1603.04349, doi:10.1103/PhysRevLett.117.052301.
- [349] Juergen Berges, Kirill Boguslavski, Soeren Schlichting, and Raju Venugopalan, *Universal attractor in a highly occupied non-Abelian plasma*, Phys. Rev. D **89** (2014), 114007, arXiv:1311.3005, doi:10.1103/PhysRevD.89.114007.
- [350] R. Baier, Alfred H. Mueller, D. Schiff, and D. T. Son, *'Bottom up' thermalization in heavy ion collisions*, Phys. Lett. B **502** (2001), 51, arXiv:hep-ph/0009237, doi:10.1016/S0370-2693(01)00191-5.
- [351] Aleks Kurkela and Yan Zhu, *Isotropization and hydrodynamization in weakly coupled heavy-ion collisions*, Phys. Rev. Lett. **115** (2015), 182301, arXiv:1506.06647, doi:10.1103/PhysRevLett.115.182301.
- [352] T. Lappi, *Azimuthal harmonics of color fields in a high energy nucleus*, Phys. Lett. B **744** (2015), 315, arXiv:1501.05505, doi:10.1016/j.physletb.2015.04.015.
- [353] S. Schlichting, *Initial state and pre-equilibrium effects in small systems*, Nucl. Phys. A **A956** (2016), 216, arXiv:1601.01177, doi:10.1016/j.nuclphysa.2016.02.026.
- [354] Bernd A. Kniehl, G. Kramer, and B. Potter, *Fragmentation functions for pions, kaons, and protons at next-to-leading order*, Nucl. Phys. B. **582** (2000), 514, arXiv:hep-ph/0010289, doi:10.1016/S0550-3213(00)00303-5.

-
- [355] Kevin Dusling, Mark Mace, and Raju Venugopalan, *Multiparticle collectivity from initial state correlations in high energy proton-nucleus collisions*, Phys. Rev. Lett. **120** (2018), 042002, [arXiv:1705.00745](https://arxiv.org/abs/1705.00745), [doi:10.1103/PhysRevLett.120.042002](https://doi.org/10.1103/PhysRevLett.120.042002).
- [356] R. Mertig, M. Bohm, and Ansgar Denner, *FEYN CALC: Computer algebraic calculation of Feynman amplitudes*, Comput. Phys. Commun. **64** (1991), 345, [doi:10.1016/0010-4655\(91\)90130-D](https://doi.org/10.1016/0010-4655(91)90130-D).

Declaration

I herewith declare that I have not previously participated in any doctoral examination procedure in a mathematics or natural science discipline.

Frankfurt am Main,(Date)(Signature)

Author's Declaration

I herewith declare that I have produced my doctoral dissertation on the topic of

“Electromagnetic probes in Heavy-Ion Collisions”

independently and using only the tools indicated therein. In particular, all references borrowed from external sources are clearly acknowledged and identified. I confirm that I have respected the principles of good scientific practice and have not made use of the services of any commercial agency in respect of my doctorate.

Frankfurt am Main,(Date).....(Signature)

